



Virginia Commonwealth University
VCU Scholars Compass

Theses and Dissertations


Graduate School

2017

Investigations into structure and properties of atomically-precise transition metal-chalcogenide clusters of CrTe and ligated Cr₆Te₈(PEt₃)₆

Anthony F. Pedicini
Virginia Commonwealth University

Follow this and additional works at: <https://scholarscompass.vcu.edu/etd>

 Part of the [Atomic, Molecular and Optical Physics Commons](#), [Materials Chemistry Commons](#), and the [Physical Chemistry Commons](#)

© The Author

Downloaded from

<https://scholarscompass.vcu.edu/etd/4963>

This Dissertation is brought to you for free and open access by the Graduate School at VCU Scholars Compass. It has been accepted for inclusion in Theses and Dissertations by an authorized administrator of VCU Scholars Compass. For more information, please contact libcompass@vcu.edu.

© Copyright by Anthony F. Pedicini, 2017
All Rights Reserved

Investigations into structure and properties of atomically-precise transition metal-chalcogenide clusters of CrTe and ligated $\text{Cr}_6\text{Te}_8(\text{PEt}_3)_6$

A Dissertation Submitted in Partial Fulfillment of the Requirements for the Degree of Doctor of Philosophy in Nanoscience & Nanotechnology at
Virginia Commonwealth University

by

Anthony Filippo Pedicini

B.S., Physics & B.S. Applied Mathematics

Virginia Commonwealth University, 2011

M.S. Physics

Virginia Commonwealth University, 2013

Director: Shiv N. Khanna, Ph.D.

Chairman and Commonwealth Professor, Department of Physics

Virginia Commonwealth University

Richmond, Virginia

July, 2017

Contents

List of Figures.....	iv
Abstract.....	viii
1 Introduction.....	1
1.1 Novel Materials and Magic Clusters.....	1
1.2 Transition Metal—Chalcogenides: Filled Electronic Valence in Periodic Systems.....	7
1.3 Periodic Solids with Ligated Transition Metal—Chalcogenides.....	10
1.3.1 Motivation.....	10
1.3.2 Superatomic Clusters and Their Solids.....	10
1.3.3 Alterations Upon Electronic Properties of Superatomic Clusters.....	14
1.4 Transition Metal-Chalcogenides at The Extremum: Chromium and Tellurium, Purpose of the Present Study.....	15
1.5 Organization of This Thesis.....	18
2 Computational Approach.....	20
2.1 Overview.....	20
2.2 Background.....	20
2.2.1 The Electronic Problem & The Born—Oppenheimer Approximation.....	20
2.2.2 Pauli.....	24
2.2.3 The Hartree—Fock Approximation.....	25
2.3 Density Functional Theory.....	27
2.3.1 Overview.....	27
2.3.2 The Hohenberg—Kohn Theorems.....	28
2.3.3 The Kohn—Sham Formulation.....	31
2.3.4 Exchange—Correlation Functionals.....	34
2.3.5 Mulliken Population and Hirschfeld Charge Analyses.....	35
2.4 Computational Methods.....	37
3 Atomically-Precise Binary Cr _x Te _y Clusters.....	40
3.1 Overview & Two-Dimensional CrTe.....	40
3.2 Pure Systems of Chromium, and Tellurium.....	42
3.2.1 Overview.....	42
3.2.2 Tellurium Clusters.....	42
3.2.3 A Brief History of Small Chromium Clusters.....	43

3.2.4	Small Clusters of Pure Chromium	47
3.2.5	Summary	49
3.3	The Cr_xTe_y Clusters.....	51
3.3.1	Overview	51
3.3.2	Geometries & Structure.....	52
3.3.3	Summary	64
3.4	Cr_xTe_y Series Properties.....	66
3.4.1	Hirshfeld Charge Density, Average Bond Distances, and “Malleability” of Chromium.....	68
3.4.2	Removal Energies & Fragmentation Pathways.....	70
3.4.3	Summary	74
3.5	Cr_xTe_y Electronic Properties	76
3.5.1	Overview	76
3.5.2	Cr_1Te_y ($y = 1 - 4$).....	77
3.5.3	Cr_2Te_y ($y = 1 - 4$).....	81
3.5.4	Cr_3Te_y ($y = 1 - 5$).....	85
3.5.5	Cr_4Te_y ($y = 1 - 6$).....	87
3.5.6	Cr_5Te_y ($y = 1 - 7$).....	96
3.5.7	Cr_6Te_y ($y = 1 - 6$).....	99
3.5.8	Cr_6Te_y ($y = 7, 8$).....	102
3.6	Discussion & Conclusions	108
4	Electronic Properties of ${}^7\text{Cr}_6\text{Te}_8(\text{PET}_3)_6$ and Alteration Through Ligand Exchange	110
4.1	Overview	110
4.2	Change of Basis Set.....	110
4.3	The ${}^7\text{Cr}_6\text{Te}_8$ Metal Core: QZ4P vs. TZ2P (Frozen Core).....	112
4.4	The ${}^7\text{Cr}_6\text{Te}_8(\text{PET}_3)_6$ Cluster.....	116
4.4.1	Robustness of ${}^7\text{Cr}_6\text{Te}_8(\text{PET}_3)_6$	121
4.5	Ligand Exchange.....	123
4.6	Discussion & Conclusions	131
5	Summary & Future Directions.....	132
Appendix A	Cr_x Bond Lengths	135
Appendix B	Cr_xTe_y Bond Distances.....	137
References	147

List of Figures

Figure 1-1. Etching reaction of aluminum anions ($Al_5^- - Al_{24}^-$) with oxygen.	5
Figure 1-2. Superatomic Orbitals and Al_{13}^-	5
Figure 1-3. Ligated Transition Metal-Chalcogenide Clusters and Their Assemblies.	11
Figure 1-4. Magnetic behavior of the $[Ni_9Te_6(PEt_3)_8][C_{60}]$ cluster assembly.	12
Figure 1-5. Inverse magnetic susceptibility versus temperature measurements.	16
Figure 1-6. The evolution of the ZFC-FC magnetization vs. temperature for $Sm_2Ba_3Fe_5O_{15-\delta}$. ..	17
Figure 3-1. Magnetic moments per atom μ for chromium clusters of $N = 20 - 133$	44
Figure 3-2. Groundstate clusters of pure Cr_n , $n = 1 - 6$	48
Figure 3-3. Groundstate structures of Cr_1Te_{1-4}	52
Figure 3-4. Groundstate structures of Cr_2Te_{1-4}	53
Figure 3-5. Groundstate structures of Cr_3Te_{1-5}	54
Figure 3-6. Groundstate structures of Cr_4Te_{1-6}	56
Figure 3-7. Groundstate structures of Cr_5Te_{1-7}	59
Figure 3-8. Groundstate structures of Cr_6Te_{1-6}	62
Figure 3-9. Groundstate structures of $Cr_6Te_{7,8}$	63
Figure 3-10. Basic properties of the Cr_xTe_y binary clusters.	66
Figure 3-11. Magnetic moments for the Cr_xTe_y cluster series.	67
Figure 3-12. Hirshfeld Charge Deviation and Bond Distance Averages.	69
Figure 3-13. Removal Energies for solitary, and complexed, Chromium and Tellurium.	71
Figure 3-14. Mulliken spin populations for Cr_1Te_{1-4}	77
Figure 3-15. Level diagrams for $CrTe_n$, $n = 1 - 4$	78

Figure 3-16. $^3\text{CrTe}_3$ Atomic Orbital (AO) level diagram.	79
Figure 3-17. $^3\text{CrTe}_4$ Atomic Orbital (AO) level diagram.	80
Figure 3-18. Density of States (DOS) for $\text{Cr}_1\text{Te}_{3,4}$	80
Figure 3-19. Mulliken spin populations for $\text{Cr}_2\text{Te}_{1-4}$	82
Figure 3-20. $^1\text{Cr}_2\text{Te}_3$ Atomic Orbital (AO) level diagram.	83
Figure 3-21. $^1\text{Cr}_2\text{Te}_4$ Atomic Orbital (AO) level diagram.	83
Figure 3-22. Density of States for Cr_2Te_3	84
Figure 3-23. Density of States (DOS), and OPDOS for $^1\text{Cr}_2\text{Te}_4$	84
Figure 3-24. Mulliken spin populations for $\text{Cr}_3\text{Te}_{1-5}$	85
Figure 3-25. $^7\text{Cr}_3\text{Te}_3$ Atomic Orbital (AO) level diagram.	86
Figure 3-26. Density of States (DOS) & OPDOS for $^7\text{Cr}_3\text{Te}_3$	87
Figure 3-27. Mulliken spin populations for $\text{Cr}_4\text{Te}_{1-3}$	88
Figure 3-28. Mulliken spin populations for $\text{Cr}_4\text{Te}_{4-6}$	88
Figure 3-29. Mulliken spin populations for the Cr_4Te_4 and Cr_4Te_6 geometries.	90
Figure 3-30. $^7\text{Cr}_4\text{Te}_4$ & $^9\text{Cr}_4\text{Te}_5$ Atomic Orbital (AO) level diagrams.	91
Figure 3-31. Atomic Orbital (AO) level diagram for Cr_4Te_6	92
Figure 3-32. Atomic Orbital (AO) level diagrams for Cr_4Te_y , $y = 4 - 6$	92
Figure 3-33. Density of States (DOS) & OPDOS for $^7\text{Cr}_4\text{Te}_4$	94
Figure 3-34. Density of States (DOS) for $^9\text{Cr}_4\text{Te}_5$	94
Figure 3-35. Density of States (DOS) for $^3\text{Cr}_4\text{Te}_6$	95
Figure 3-36. Mulliken spin populations for $\text{Cr}_5\text{Te}_{1-7}$	96
Figure 3-37. Atomic Orbital (AO) level diagram for $^7\text{Cr}_5\text{Te}_5$	97
Figure 3-38. Density of States (DOS) & OPDOS for $^7\text{Cr}_5\text{Te}_5$	98

Figure 3-39. Mulliken spin populations for $\text{Cr}_6\text{Te}_{1-8}$	99
Figure 3-40. $^1\text{Cr}_6\text{Te}_5$ Atomic Orbital (AO) level diagram.....	100
Figure 3-41. $^9\text{Cr}_6\text{Te}_6$ Atomic Orbital (AO) level diagram.....	101
Figure 3-42. Density of States (DOS) & OPDOS for $^9\text{Cr}_6\text{Te}_6$	101
Figure 3-43. Groundstate geometries of $^1\text{Cr}_6\text{Te}_7$ and $^7\text{Cr}_6\text{Te}_8$	102
Figure 3-44. Geometry of the central Cr_4 subunits for $^1\text{Cr}_6\text{Te}_7$ and $^7\text{Cr}_6\text{Te}_8$ clusters.....	103
Figure 3-45. Mulliken spin populations for $^1\text{Cr}_6\text{Te}_7$ and $^7\text{Cr}_6\text{Te}_8$	103
Figure 3-46. $^1\text{Cr}_6\text{Te}_7$ Atomic Orbital (AO) level diagram.....	105
Figure 3-47. $^7\text{Cr}_6\text{Te}_8$ Atomic Orbital (AO) level diagram.....	105
Figure 3-48. Density of States for unligated $^7\text{Cr}_7\text{Te}_8$	106
Figure 3-49. Cluster energetics for $^{(x+1)}\text{Cr}_6\text{Te}_8$ across various values of total μ_B	107
Figure 4-1. Groundstate geometries of $^7\text{Cr}_6\text{Te}_8$ utilizing different Basis Sets.....	113
Figure 4-2. Mulliken spin populations per QZ4P and TZ2P (Large Core) basis set computed groundstates of the $^7\text{Cr}_6\text{Te}_8$ cluster.....	114
Figure 4-3. Atomic Orbital (AO) level diagram for $^7\text{Cr}_6\text{Te}_8$ as computed using the TZ2P (Large Core) basis set.	115
Figure 4-4. Density of States for the $^7\text{Cr}_6\text{Te}_8$ cluster as computed using the TZ2P (Large Core) basis set.....	115
Figure 4-5. The groundstate structure of the $^7\text{Cr}_6\text{Te}_8(\text{PEt}_3)_6$ cluster.....	116
Figure 4-6. Groundstate geometries for $^7\text{Cr}_6\text{Te}_8$, and core of the $^7\text{Cr}_6\text{Te}_8(\text{PEt}_3)_6$ cluster.	117
Figure 4-7. Mulliken spin populations for $^7\text{Cr}_6\text{Te}_8(\text{PEt}_3)_6$	117
Figure 4-8. $^7\text{Cr}_6\text{Te}_8(\text{PEt}_3)_6$ Atomic Orbital (AO) level diagram, total.....	118
Figure 4-9. $^7\text{Cr}_6\text{Te}_8(\text{PEt}_3)_6$ Atomic Orbital (AO) level diagram, scaled.....	119

Figure 4-10. Density of states (DOS) for the Bare and PEt_3 ligated ${}^7\text{Cr}_6\text{Te}_8$ clusters.	120
Figure 4-11. Starting and final Cr spin moment arrangements for the two singlet state permutations of ${}^1\text{Cr}_6\text{Te}_8(\text{PEt}_3)_6$	121
Figure 4-12. Cluster energetics for ${}^x\text{Cr}_6\text{Te}_8(\text{PEt}_3)_6$ across various values of total μ_B	122
Figure 4-13. Mulliken spin populations for individual chromium atoms within the ligated systems of $\text{L} = \text{PH}_3, \text{CO},$ and CN	124
Figure 4-14. Average bond distances, HOMO-LUMO level positions, Hirshfeld Charge Density, Adiabatic Ionization Potential and Electron Affinity energies, for none and various ligands.	125
Figure 4-15. Atomic Orbital (AO) level diagrams for Bare and Ligated ${}^x\text{Cr}_6\text{Te}_8$ cluster cores.	128
Figure 4-16. Density of States for various ligated $\text{Cr}_6\text{Te}_8(\text{L})_6$ clusters.	130

Abstract

INVESTIGATIONS INTO STRUCTURE AND PROPERTIES OF ATOMICALLY-PRECISE TRANSITION METAL-CHALCOGENIDE CLUSTERS OF CRTE AND LIGATED CR₆TE₈(PET₃)₆

By Anthony Filippo Pedicini, Ph.D.

A dissertation submitted in partial fulfillment of the requirements for the degree of Doctor of Philosophy in Nanoscience & Nanotechnology at Virginia Commonwealth University.

Virginia Commonwealth University, 2017

Major Director: Shiv N. Khanna, Ph.D.
Commonwealth Professor and Chairman, Department of Physics

The complete understanding of a clusters electronic structure, the primary mechanisms for its properties and stabilization is necessary in order to functionalize them for use as building blocks within novel materials. First principle theoretical studies have been carried out upon the electronic properties of Cr_xTe_y ($x = 1 - 6$, $y = 0 - 8$, $x + y \leq 14$), as well as for the larger triethylphosphine (PEt₃) ligated cluster system of Cr₆Te₈(PEt₃)₆. Together, we aim to use the information garnered from the smaller clusters to address the underlying behavior of the ligated Cr₆Te₈(PEt₃)₆. Additionally, the properties of this larger cluster will be used to further understand its role when paired with C₆₀ within the binary cluster assembled material. The stability and macroscopic properties of the Cr₆Te₈(PEt₃)₆ cluster, have been found to be sensitive to type of passivating ligand.

As will be shown, the ground state structures of Cr_n atoms are sensitive to both the number and position of bonded Te atoms. Moreover, that this sensitivity carries over into larger cluster sizes, and at several size intervals produces clusters with high magnetization. To this, we add the

investigation into the manipulation of the Cr_6Te_8 cluster geometry and its properties through various ligands, such as PH_3 , CO , and CN . It will show, that in altering these ligands there is a modification to the clusters valence shell count, which in turn alters its ionization potential and electron affinity. Additionally, although the ionization potential and electron affinity have changed for the $\text{Cr}_6\text{Te}_8(\text{PEt}_3)_6$ cluster, it has been found that its high magnetization does not.

1 Introduction

1.1 Novel Materials and Magic Clusters

Systematic study of atomic clusters offers a gateway to understanding the complexity in their properties and the unique phenomena that are present only at these small sizes. The next challenge, is to protect and magnify these properties into large, periodic, systems. Novel materials built in this manner, are purposely synthesized and optimized for the harnessing of a specific property, or function. Materials for specialized microelectronic devices such as spintronics, and new types of computer processors. As well as, new applications within superconductivity, photocatalysis, and nonlinear optical materials.

The building blocks of matter commonly found in nature are atoms or molecules. Depending on their chemistry and the physical conditions present, including pressure and temperature, these atoms/molecules frequently arrange themselves into crystalline solids of well-defined arrays. The properties of the crystals often depend strongly on the chemical nature of the atoms as well as on their arrangement. Consider, as a simple example, two such crystals- diamond, and graphite. Although both of these materials are built from carbon atoms, their mechanical, electronic, chemical and optical properties are very different due their atomic structure. Molecular crystals, on the other hand, exhibit unique properties because molecules and not atoms are the fundamental building blocks. An example of this is that of ice, that is even though neither hydrogen nor oxygen condenses at 0°C, H₂O molecules will freeze together. While the examples above demonstrate that by changing the building blocks and/or their

arrangements one can create new materials, nature however does not offer pathways to synthesize all such materials.

Advances in experimental techniques over the past three decades have enabled researchers to make clusters of atoms containing few to thousands of atoms. The properties of these sub-nanoscale units are found to be different from the bulk, and change with size and composition. For example, while bulk gold is a noble element, small clusters of Au_n are found to be highly effective catalysts for a variety of reactions including conversion of CO to CO_2 .¹ Additionally, while bulk aluminum is highly reactive with oxygen, an Al_{13}^- cluster is found to be resistant to etching by oxygen.² Also, while bulk Rh is paramagnetic, small Rh_n clusters are found to display ferromagnetic coupling with appreciable moments.³ What is important is that the properties can change significantly with size. In fact, the reactivity of Fe_n clusters has been found to change by orders of magnitude by adding just a single atom.⁴⁻⁶

The above findings have led to a new and promising direction within nanoscience, namely, using clusters as the basis for new materials, instead of atoms, is the very idea behind Cluster-Assembled Materials (CAMs).¹²⁻¹⁷ Like molecular crystals, it is expected that cluster-crystals may possess unique properties hitherto unknown to man. The use of clusters as the main building block, or *motif*, introduces yet another method for tuning properties within a periodic solid. Moreover, since the properties of clusters themselves can be controlled by size, composition, and the charge state, cluster assemblies offer a unique prospect in constructing tailored materials.⁷⁻¹¹ This idea of custom materials encompasses a great deal and offers even more, but creating small clusters is often a difficult task on the road to realizing these materials. Thus, two fundamental hurdles are to be surmounted before continuing; (1), formation and characterization of the cluster motif itself, pure or ligated; and (2), understanding its interactions,

stability, preferred arrangement, and orientation, within a periodic system. Addressing both of these points, to identify new and stable species of interest, as well as facilitate the formation of novel materials, is of the utmost importance.

A major downfall in the synthesis of materials using clusters is their intrinsic instability, and desire to coalesce. At these larger sizes, the novel properties seen in smaller versions are then destroyed. One approach to realizing the possibility of novel materials is therefore to identify clusters that are stable and would maintain their identity when assembled. These stable clusters have become known as *Superatoms*, and the prospect of making cluster materials has started a vigorous search for these species.^{2,14,18-28} The first step in this direction is to identify the factors that control the stability of clusters themselves.

Just over two decades ago, Khanna and Jena discussed the possibility of designing these stable metallic clusters.¹³ Their arguments were derived from the experiments on the mass spectra of simple metal clusters.²⁹ Specifically, the mass spectra of small sodium clusters observed by Knight and co-workers showed that clusters containing 2, 8, 18, 20, 34, 40... atoms were more prominent than the other sizes. In order to explain the enhanced stability of these *magic* clusters, Knight and co-workers then proposed the *spherical jellium model*.²⁹⁻³¹ In brief, one imagines that the positive charge of all ions present in the cluster is distributed uniformly over a sphere. The electronic levels associated with this charge distribution correspond to $1S^21P^61D^{10}2S^21F^{14}2P^6$, etc., much like the electronic states of an atom.^{19,31-34}

Like noble gas atoms, the magic numbers (2, 8, 18, etc.) thus correspond to filled electronic shells, thereby indicating the role of electronic counts on the stability. The possibility of describing the electronic structure of clusters, in terms of electronic shells, raised the interesting possibility that clusters themselves could be regarded as superatoms, as well. There

are several reasons for such an analogy. The ionization potentials of simple metal clusters were found to exhibit peaks at sizes corresponding to filled electronic shells much in the same way as atoms. In another series of experiments, it was quite surprisingly found that the chemical behavior of clusters could also be predicted by the shell model.³⁵⁻³⁸

Further proof of this concept came from the experiments by Leuchtner, Harms, and Castleman, who studied the reactivity of Al_n^- clusters with oxygen.³⁹ They showed that while other sizes were etched away by oxygen, the mass spectra of the reacted species exhibited a marked peak at Al_{13}^- , as well as Al_{23}^- and Al_{37}^- . **Figure 1-1** below shows the observed mass spectra, while **Figure 1-2** shows the groundstate structure of Al_{13}^- . Since Al_{13}^- has 40 valence electrons, its inertness can be understood in terms of a closed electronic shell, (as well as the 23- and 37-atom containing systems that also have closed electronic configurations).

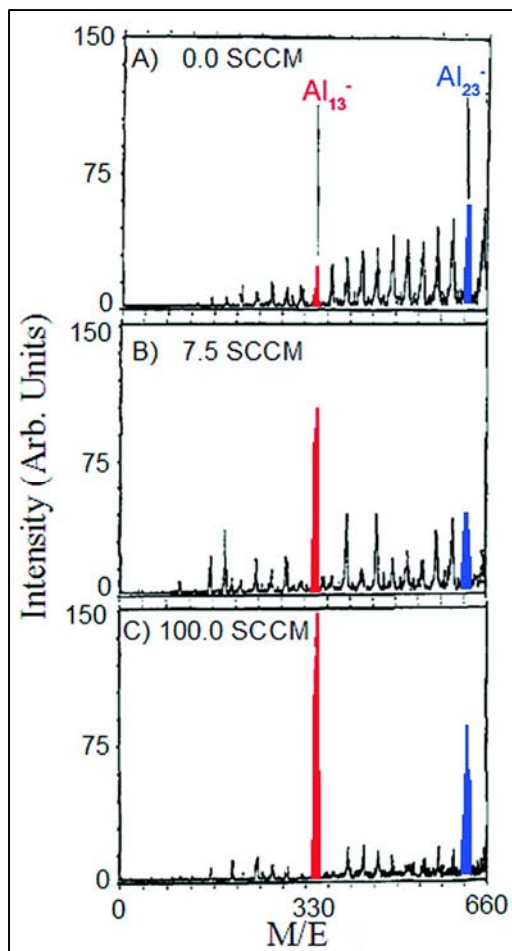


Figure 1-1. Etching reaction of aluminum anions ($Al_5^- - Al_{24}^-$) with oxygen. (A) 0.0 sccm oxygen, (B) 7.5 sccm oxygen, (C) 100.0 sccm oxygen.^{16,39}

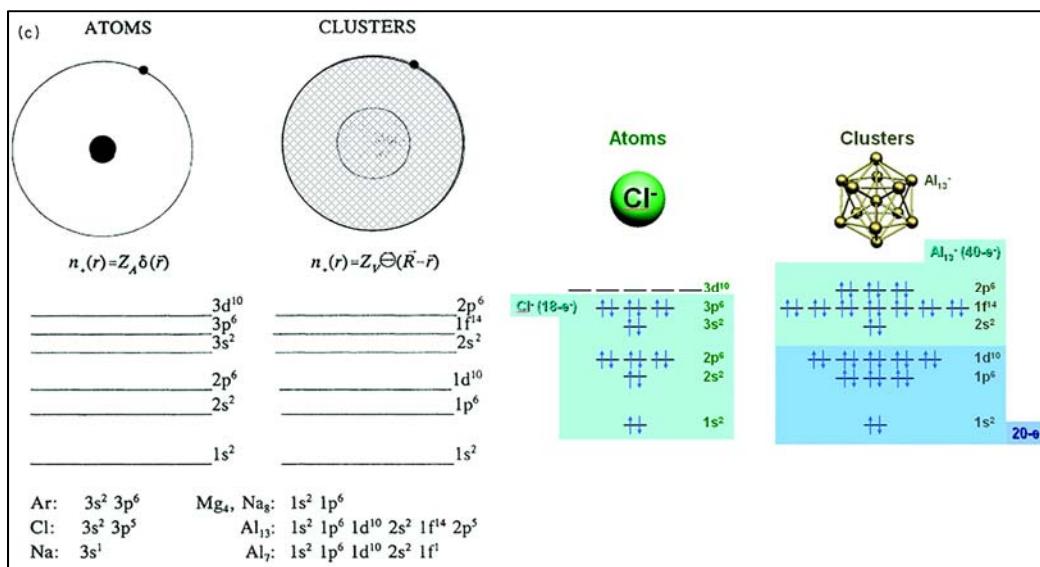


Figure 1-2. Superatomic Orbitals and Al_{13}^- . Similarities between atomic and superatomic orbital levels (left), Closed shell Cl^- compared to Al_{13}^- groundstate with closed shell and 40 electron count (right). (Reproduced with permission.)¹⁶

These and other observations have shown that the jellium picture, though extremely simplistic, is amazingly successful in describing many of the globally observed electronic features in a variety of systems and that certain metallic clusters could be described as superatoms. Moreover, later experiments and companion theoretical calculations have proven that aluminum clusters can also behave as halogens and alkaline earth metals, enabling the possibility of forming a class of superatoms with analogies to various elements of the periodic table.^{2,37,40-42} It is important to emphasize that although the electronic shells were introduced via the jellium model, the existence of electronic shells of fermionic systems is known to occur for a far wider range of potentials.

1.2 Transition Metal—Chalcogenides: Filled Electronic Valence in Periodic Systems

A full valence shell is not only used to understand the stability of free clusters, but also within solid state systems as well. Specifically, systems of crystalline and amorphous semiconductors, where valence shell properties have a large influence on a materials macroscopic electronic behavior. Alterations upon these intrinsic properties are more readily seen when applied to amorphous semiconductors, which they themselves can be divided into two classifications. The first, being the *chalcogenide glasses*; and second, *hydrogenated amorphous silicon* (a-Si:H) and other related solids.⁴³ (Here, we discuss materials and solids based on the former; and comprising one, or several, chalcogenides.) The term *chalcogenides* denote dianionic elements from group 16 (VIA), of the periodic table; namely, sulfur, S²⁻; selenium, Se²⁻; and tellurium, Te²⁻. Oxygen, while still a chalcogen, and along with other oxide based materials, is not discussed here. Moreover, the term “ideal *glass*” is often given to a material in which within it “all atoms satisfy their valence requirements”. In this definition, valence is referred to classically; the number of single covalent bonds an atom requires to complete its outer shell. From the context, an atom that completes its shell of eight electrons is obeying the 8-*N* rule when $N > 4$, and *N* is equal to the number of valence electrons. Binary chalcogenides are typically of two forms, As-Chalcogenide and amorphous (e.g. As₂Se₃); or Ge-Chalcogenide and crystalline (e.g. GeSe₂). Of course, this “ideal” situation is only perfectly suited to describe short-range ordering when long-range (i.e. crystalline) ordering is absent. However, the 8-*N* rule was first proposed for chalcogenide glasses in an effort to account for the observation that these glasses were insensitive to alteration upon their electronic structure from a third element, purposely introduced into the system, i.e. doping. The term “8-*N* rule” is often interchanged

with that of “*Mott rule*”, attributed to the first person to observe this phenomena, Sir Nevill F. Mott.^{44,45}

Knowing the intrinsic nature of chalcogenides, the intention now is to create novel materials based on them. Exercising their high dependence of the 8-N rule, and deviations upon it, we can now begin to discuss using an elemental pairing with the chalcogenides alternative to those of group 15 (VI), i.e. the pnictogens. In doing so, introduces a method of manipulating coordination through choice of that second element, which leads to interesting stoichiometric modifications upon the original concept of these materials and its properties. Along these lines, chalcogenides have been paired with elements from, and studied, across all areas of the periodic table, including; the lanthanides, actinides, transition metals, and other main group elements.

The versatility in creating new materials with transition-metals and chalcogenides, rather than oxides, stems from several advantages present at the atomic level between chalcogens and oxygen. The major differences can be stated simply that chalcogens are: larger and heavier, less electronegative, and further down the group, possess inner *d*-orbitals. This alternate bonding pattern displays; a more covalent bond between metal-chalcogen than metal-oxygen; bonds that may involve *d*-orbitals of the chalcogen; within a compound, oxygen is in its formal oxidation state (-2), while the chalcogen is less negative (-1); and, the chalcogenide ions are more polarizable.⁴⁶ This covalent nature of the bonds between metal and chalcogen produces a material which possesses broad valence and conduction bands, while still maintaining a band gap. This gap grows smaller, and may even close, as the chalcogen element of choice moves down the group, from sulfur to tellurium.⁴⁶

The specific choice in using high-spin 3*d* transition-metals paired with chalcogenides is deliberate. As a result, numerous pairings have produced compounds that each vary wildly in

optical, magnetic, and electronic properties, all sensitive to impurities and/or vacancies.⁴⁷ Within these compounds, the mixing between the metal d -orbitals with the s and p of the chalcogen can no longer be ignored. Because, after mixing, the degeneracy in d -orbitals between metal and chalcogen has been lifted, and the exact separation between those orbitals is now dependent upon the geometry of the chalcogen. Moreover, the orbital involvement of the chalcogenide in covalent bonding also introduces effects upon the coordination of the chalcogenide, as well. It has been shown previously, that chalcogenides in the d^0 (and even d^1 , or the spin-paired d^2) configuration prefer a trigonal-prismatic configuration.^{46,48} Thus, in conjunction with a particular metal, this type of bonding is seen in many MCs, and often produces a NiAs-type crystal (or, something close to it) when bonded to many of the transition-metals and/or lanthanides.⁴⁹ This type of bonding also gives rise to individual cluster units with formula M_6E_8 (M = transition-metal; E = chalcogenide)⁵⁰, formed through combination of a transition-metal octahedron surrounded by an X_8 cube.⁵¹ Each of these units are often described as a (distorted) fragment of its associated periodic compound.

As mentioned previously, in order to create novel materials based on solitary clusters, a degree of stabilization is required in order to prevent agglomeration. Additionally, a form of isolation from its surroundings as a means to stop growth at a particular cluster size and maintain its properties. Production of ligated-TMC (LTMC) cluster was first completed in an effort to understand the pathways in which reagents combined together to form an extended solid.^{51,52-64} This marked something of a beginning in an effort to understand how macroscopic properties of these elemental combinations are transformed, or altered, after ligation at small sizes; resulting in a new type of cluster family with formula $M_6E_8L_6$ (L = phosphine ligand), (LTMCs, MEL-686, or simply MELs).^{60-63,65}

1.3 Periodic Solids with Ligated Transition Metal—Chalcogenides

1.3.1 Motivation

One form of constructing larger systems using molecular clusters is through binary stabilization. An example of this can already be seen in every day table salt, NaCl. This *binary-system* method is not new, and can be found throughout the literature.^{12,13,15,40,66–69} However, building regularly periodic systems comprised of ligated clusters, who they themselves are composed of transition metal-chalcogenides (TMCs), is a new direction.

1.3.2 Superatomic Clusters and Their Solids

As mentioned above, the first foray into ligated TMCs began with the desire to understand the exact nature of how the bonding between metals and its associated chalcogenide created a periodic network.⁶³ Investigations into a close relative of the LTMCs are the unligated ternary metal-chalcogenides, with 868 stoichiometry, better known as the *Chevrel Phase* clusters, and formula $M_xMo_6X_8$ ($X = S, Se, Te; M = \text{cation}$).^{57,70–76} These have been a source of special attention as they were considered to be the first superconducting ternary system to possess high critical temperatures.^{72,77} The overlap, if not similarity, between these two cluster types is not difficult to miss as they have sometimes been discussed together, in explaining the transition from bare cluster to extended system.^{57–59,65,72,75}

Below, **Figure 1-3** highlights some recent developments along these lines, into novel binary solids, undertaken by Roy *et al.*⁷⁸ Within this study, they have resynthesized a selection of LTMCs taken from the literature, specifically $Co_6Se_8(PEt_3)_8$, $Cr_6Te_8(PEt_3)_8$, and $Ni_9Te_6(PEt_3)_8$, with the express intention of using them as motifs in construction of novel binary solids. Pairing these clusters with fullerenes, i.e. C_{60} , as their counterion, forms two different

ionic solids. The clusters of $\text{Co}_6\text{Se}_8(\text{PET}_3)_6$ and $\text{Cr}_6\text{Te}_8(\text{PET}_3)_6$ will form a structure resembling CdI_2 , while $\text{Ni}_9\text{Te}_6(\text{PET}_3)_8$ forms the classic NaCl type structure.

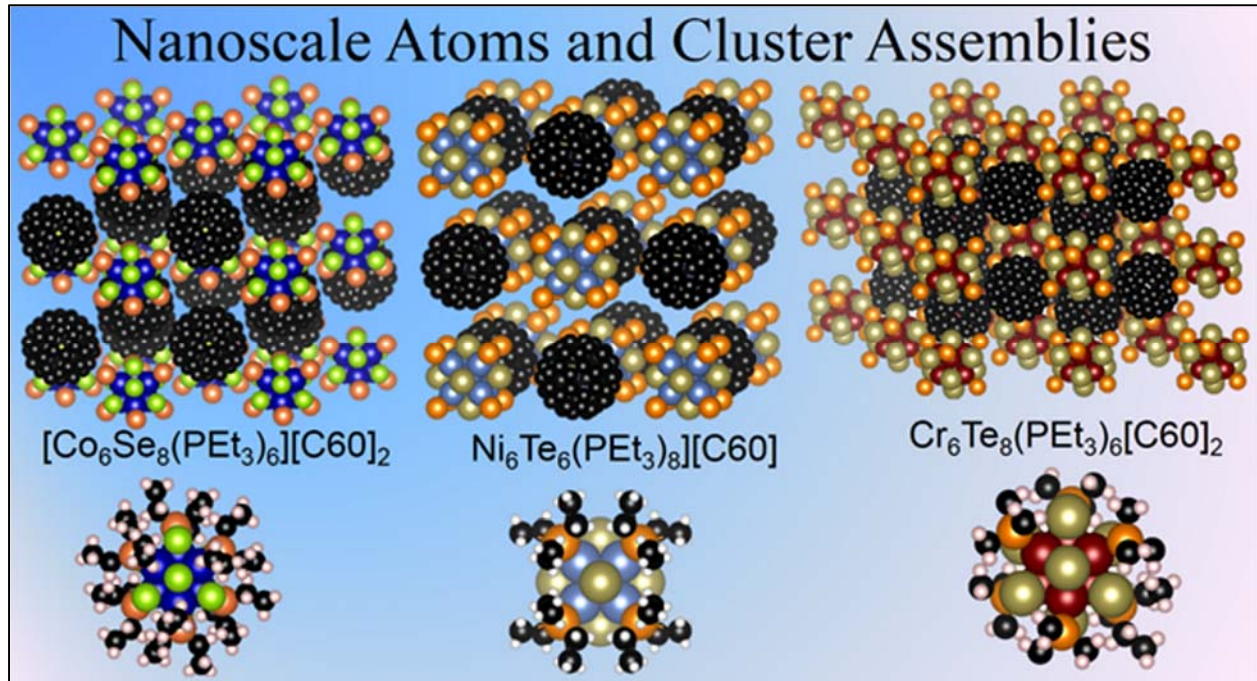


Figure 1-3. Ligated Transition Metal-Chalcogenide Clusters and Their Assemblies. Atomistic representations of the three metal-chalcogenide clusters, and combinations with the C_{60} fullerene complex, left to right. The systems of $\text{Co/Se} \cdot 2\text{C}_{60}$, $\text{Ni/Te} \cdot \text{C}_{60}$, and $\text{Cr/Te} \cdot \text{C}_{60}$. (Reproduced and edited with permission.)⁷⁸

These assemblies, built from different transition metal-chalcogenides and counterions, offer a new avenue within areas of photovoltaics, spintronics, and single molecule electrical circuits. Moreover, their electronic and magnetic properties raise new and intriguing questions. Consider the $[\text{Ni}_9\text{Te}_6(\text{PET}_3)_8][\text{C}_{60}]$ assembly, which consists of $\text{Ni}_9\text{Te}_6(\text{PET}_3)_8$ clusters, built from a Ni_9Te_6 core decorated with eight tri-ethylphosphine ligands bonded to the Ni sites. This cluster had been previously isolated as an intermediate species during the synthesis of bulk NiTe from organometallic precursors serving as sources for Ni and Te. However, Roy *et al.* have demonstrated, for the first time, that $\text{Ni}_9\text{Te}_6(\text{PET}_3)_8$ forms a rock-salt (i.e. NaCl) structure, where the ligated cluster takes on the role of electron donor when combined with C_{60} as an electron acceptor. Experiments indicate that this ionic solid is magnetic and undergoes a ferromagnetic

phase transition at low temperatures (4 K), while exhibiting Curie-Weiss behavior at higher temperatures ($T > 10$ K), both can be seen below in **Figure 1-4**, left and right respectively.

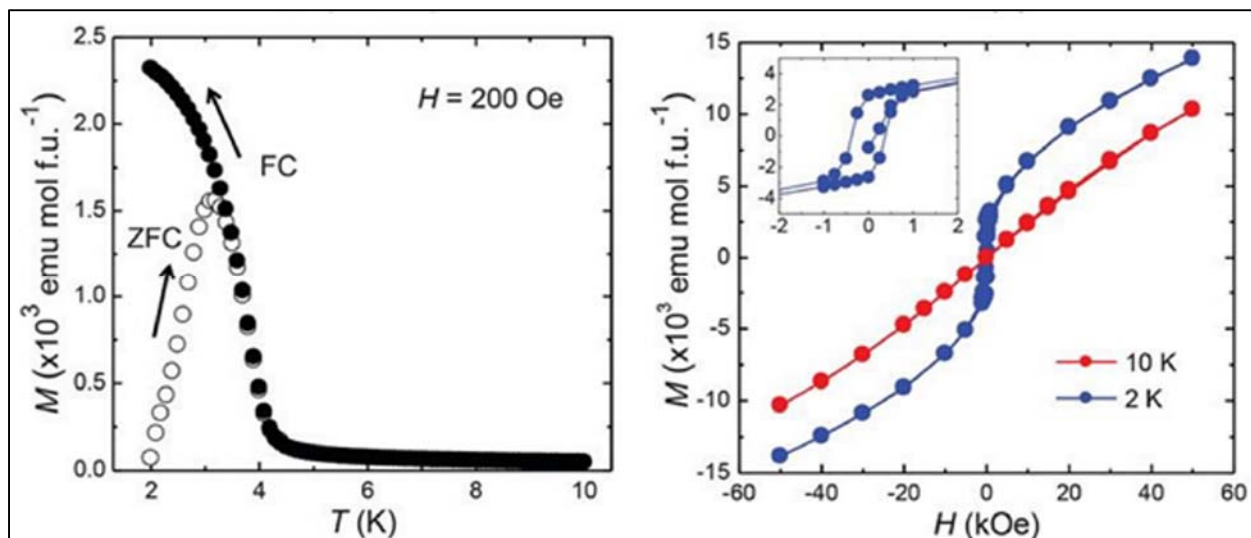


Figure 1-4. Magnetic behavior of the $[\text{Ni}_9\text{Te}_6(\text{PEt}_3)_8][\text{C}_{60}]$ cluster assembly. Temperature dependence of the ZFC and FC magnetization (left), and magnetization as a function of applied field (right). (Reproduced with permission.)⁷⁸

Later, Lee *et al.* experimentally synthesized this binary cluster assembled material again in order to further examine the magnetic behavior at these small temperatures. Results obtained from Superconducting Quantum Interface Device (SQUID) and Muon spin relaxation (MuSR) measurements have shown that these individual clusters behave like isolated magnets, with magnetic moment around $5.4 \mu_B$ per functional unit in an applied field of 1 Tesla.⁷⁹ Moreover, that static ordering of the magnetic moments occurs at a temperature of ~ 4 K.

First-principles theoretical investigations by Chauhan *et al.* have provided an electronic and magnetic characterization of the $[\text{Ni}_9\text{Te}_6(\text{PEt}_3)_8][\text{C}_{60}]$ ionic assembly.⁸⁰ This study has shown that despite the large ionization potentials of both cluster and ligand, there exist a charge transfer from ligand to the cluster. Consequently, the PEt_3 ligands create an internal, coulombic, potential-well that lifts the quantum states of the Ni_9Te_6 cluster, in turn lowering its ionization energy to 3.39 eV, creating a superalkali motif. The metallic core has a magnetic spin moment

of $5.3 \mu_B$, in agreement with experiments. But, the cluster is marked by a low Magnetic Anisotropy Energy (MAE) of 2.72 meV and a larger intra-exchange coupling, which exceeds 0.2 eV. These results showed that the observed paramagnetic behavior around 10 K is due to superparamagnetic relaxations. Additionally, these magnetic cluster motifs, separated by C_{60} , experience a weak superexchange that stabilizes in a ferromagnetic groundstate around 2 K. The calculated MAE was sensitive to the charge state (multiplicity), which could account for the observed change in magnetic transition temperature due to the size of the ligands or anions.

All of these properties, and across all binary types of cores, can be considered macroscopic, to which are then used as the starting point for development in an upward fashion toward larger materials. With an eye toward a new functionality for these, and many other, LTMC clusters, it is also necessary to fill the newly formed gap that has emerged between the understanding of atomically precise clusters and these LTMCs. That is, despite their size, a 14-element binary-core with six ligands, studies into the exciting properties expected of small-numbered clusters seems nonexistent, and neither its modifications due to the passivating ligand. Moreover, alternatively to the discussions of the preceding paragraphs, study into the origins of the central bare clusters electronic stability and its formation routes, are rarely, if ever, discussed. The discussions typically found regarding the properties of those smaller cluster variants are completed only in context, as a supportive step for their parent, extended solid, and bulk versions in an “upwards” fashion.

What remains to be seen is the reverse connection, the origin of properties found at the LTMC scale based from the point of view and study of binary cluster growth. In that regard, we aim to answer a few questions, namely; Are the properties of these ligated clusters simply taken

to be a given, as result of their size? Or, are they all that remain after growth and ligation? We shall see below, in chapter 3 and 4, that it is the latter.

1.3.3 Alterations Upon Electronic Properties of Superatomic Clusters

Above, we briefly mentioned the alteration of a TMC clusters macroscopic properties due to ligand exchange. The sequence of events in the synthesis procedure of LTMCs can vary from system to system, however post synthesis procedures offer another variable in the building of periodic systems. The alteration of the capping ligand in question upon a metal cluster is done to stabilize the metal core, and specifically control the total number of valence electrons. In manipulating this electron count, one can alter the system's ability to donate or accept charge to the external environment, that is, the clusters ionization potential and electron affinity. Such a procedure has been studied and verified on several occasions within the literature.^{13,14,16,29,68} Ionization potential and electronic affinity, together, are two of the most fundamental properties in any system. Clusters with full electronic shells exhibit large ionization potentials and a lower electron affinity. Alternatively, clusters deviating from a full valence by one electron, either lacking or in excess, experience the opposite effect, a lowered ionization potential and high electron affinity. The stability of these cluster species is often described within the superatomic framework.^{13,16,23}

The triethylphosphine (PEt₃) ligands attached to metal sites of these LMTC clusters, highlighted above, bond by creating a charge transfer complex. The cluster and ligand, once together, form an ionic compound when paired with C₆₀, with the LMTC clusters serving as the electron donors.⁷⁸ Some clusters have an open electronic shell, and stability is dictated by their geometric structure rather than a closed electronic shell. Because of this, the addition of a ligand may not close the electronic shell in question, but does change the electronic spectrum of the

cluster itself.⁸¹ The idea of altering the TMC core electronics through ligand exchange arose through the investigations into the $[\text{Ni}_9\text{Te}_6(\text{PEt}_3)_8][\text{C}_{60}]$ system, where previous studies have shown the Ni_9Te_6 core and $\text{Ni}_9\text{Te}_6(\text{PEt}_3)_8$ to possess the same magnetic moment; with the core becoming superalkali when passivated with ligands.^{80,81} Moreover, the magnetic solid undergoes a ferromagnetic phase transition at extremely low temperatures (4 K), but then exhibits Curie—Weiss behavior upon temperature increase.⁷⁹

The argument described above for the Ni/Te clusters system is the same for that based upon chromium. How does the underlying electronic behavior change with respect to the use of different capping ligands? Moreover, can Cr_6Te_8 be described in a similar fashion to Ni_9Te_6 ? That is, in the process of stabilization, do both geometry and electronic structure, dictate the overall properties of the system; or only electronic?

1.4 Transition Metal-Chalcogenides at The Extremum: Chromium and Tellurium, Purpose of the Present Study

Using the preceding sections for the line of inquiry, it is necessary to now understand how two elements at the extremum of the transition metal-chalcogenide bonding argument, chromium and tellurium, can vary so wildly from its TMC molecular cluster compatriots. The same magnetic measurements performed by Roy *et al.* upon the systems $\text{Co}_6\text{Se}_8(\text{PEt}_3)_6$ and $\text{Cr}_6\text{Te}_8(\text{PEt}_3)_6$ based solids displayed a drastically smaller, if almost nonexistent, magnetic moment for the $\text{Cr}_6\text{Te}_8(\text{PEt}_3)_6^{2+}$ system.⁷⁸ The inverse magnetic susceptibility measurements shown in **Figure 1-5** highlights the differences between these two cluster assemblies. While the $\text{Co}_6\text{Se}_8(\text{PEt}_3)_6$ based assembly shows Curie-Weiss behavior, $\text{Cr}_6\text{Te}_8(\text{PEt}_3)_6$ displays an initial increase followed by saturation. Previous magnetic susceptibility measurements have shown that the solid constructed solely of the $\text{Cr}_6\text{Te}_8(\text{PEt}_3)_6^{2+}$ cluster to be paramagnetic, with an effective

moment, μ_{eff} , of $\sim 2.6 - 2.8 \mu_B$ between 100 and 300 K, but the electronic structure yielding this moment was not detailed.⁵¹

It was surmised by Hessen *et al.* that the $\text{Cr}_6\text{Te}_8(\text{PEt}_3)_6$ cluster is the solid-state relative of Cr_3Te_4 , whose periodic structure is indeed a distorted metal-deficient NiAs type. The periodic solid of Cr_3Te_4 itself has been studied extensively for many years^{82–86} and has been found to be one of many stoichiometric combinations of chromium and tellurium to form a periodic solid, each forming their own macroscopic, 2D, properties.^{87–110}

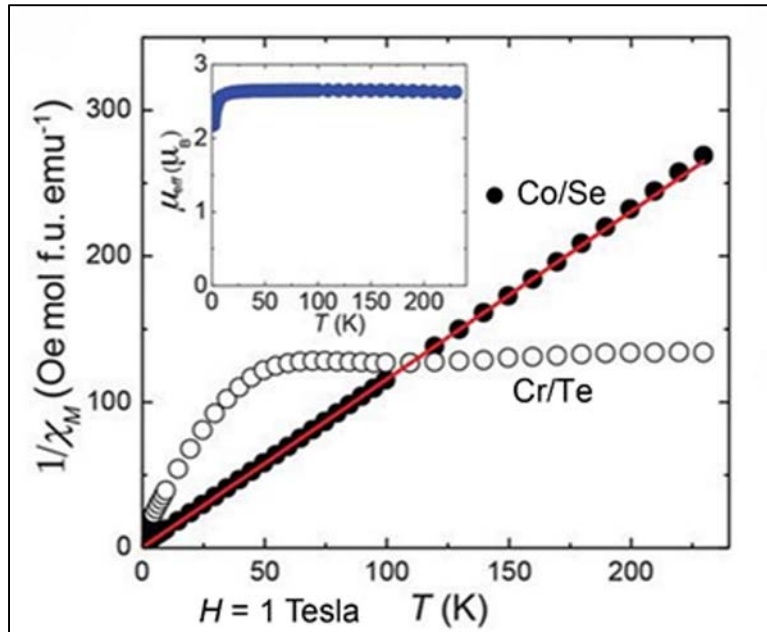


Figure 1-5. Inverse magnetic susceptibility versus temperature measurements. The Co/Se cluster assembly (black circles) and Cr/Te cluster assembly (open circles) in an applied external field $H = 1T$. Curie-Weiss fit for Co/Se in red. Inset shows effective moment versus temperature for Co/Se. (Reproduced with permission.)⁷⁸

While the literature details the properties of these numerous stoichiometries of chromium and tellurium in the two-dimensional solid form, there is little to no discussion as to the origin of said properties based upon smaller constituents.^{82–85,87–91,93–113} As such, the precise nature of free, binary CrTe clusters has not been established and is to be remedied.

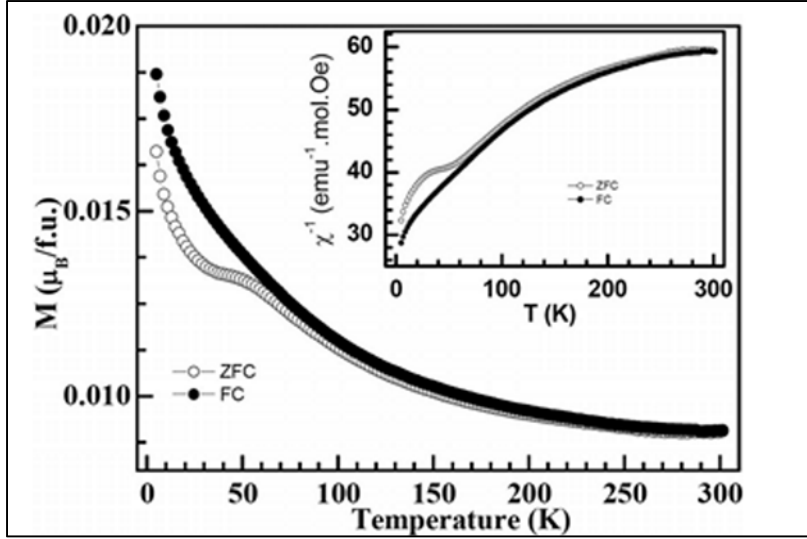


Figure 1-6. The evolution of the ZFC-FC magnetization vs. temperature for $Sm_2Ba_3Fe_5O_{15-\delta}$. Inset shows the inverse magnetization vs. temperature in question. (Figure 12. of Reproduced.)¹¹⁴

The shape of the inverse magnetic susceptibility plot in **Figure 1-5** for $Cr_6Te_8(PEt_3)_6$ is something that has been seen before within the work of Raveau and Seikh, pertaining to magnetic perovskites. The plots of Zero Field Cooled – Field Cooled (ZFC-FC) and inverse magnetic susceptibility vs temperature measurements (inset) for the quintuple perovskite of $Sm_2Ba_3Fe_5O_{15-\delta}$ are shown above in **Figure 1-6**.¹¹⁴ The behavior of this perovskite phase as seen in its ZFC magnetization plot shows a large irreversibility as well as an unusual hump at 50 K. This was investigated and from the linear behavior of the $M(H)$ vs temperature plot (not shown) it was determined that the ZFC results do not originate from superparamagnetism. The total of this collected data showed that the magnetization of the perovskite does not involve ferromagnetism, but is in fact due to intra- and interdomain antiferromagnetic interactions. This point was confirmed by the fact that there was no linear dependence in the inverse magnetic susceptibility vs temperature plot (inset, **Figure 1-6**). The behavior of this plot reflects the absence of free spins through the probed temperature range.

With this information, we can deduce that our system of $Cr_6Te_8(PEt_3)_6$ and C_{60} is behaving in the same manner. That the magnetic behavior of individual $Cr_6Te_8(PEt_3)_6$ and its

arrangement within the larger solid dictates the overall behavior seen experiment. Thus, we aim to investigate and establish, if any, the clusters magnetic properties.

Furthermore, the present study seeks to determine if the high magnetization of solitary chromium, and the alternating pattern of magnetization present within its small cluster sizes, is hindered, maximized, or indifferent to the introduction of tellurium. This will be determined through the systematic search of groundstate structures after the sequential addition of both elemental chromium and tellurium atoms. Additionally, we aim to investigate the mechanisms which alter the ionization potential, electronic affinity, and overall magnetic moment in the final Cr_6Te_8 metal core through the exchange with various ligands.

The resultant clusters will be compared to one another, using their electronic stability to determine any fragmentation pathways. Furthermore, analysis of the bonding between the elements, using alterations upon the Hirshfeld Charge densities, as well as molecular orbital (MO) analysis of particularly interesting clusters. Moreover, the oxidation of chromium and movement of electronic charge, which can be seen through the diagrams of both the MOs, and the Mulliken Population charge density graphs of the chromium orbitals.

1.5 Organization of This Thesis

In Chapter 2, an outline of the theoretical basis behind Density Functional Theory (DFT) is presented, as well as some specifics regarding electronic methods to further investigate binary and ligated CrTe. Chapter 3 will be divided into four portions; the first, overall details of the entire Cr_xTe_y binary cluster systems. Here, we discuss results pertaining to magnetic moments of the total system, as well as the individual chromium atoms. Additionally, the change of other macroscopic properties, such as bond-lengths, charge movements, and some fragmentation pathways. Within parts two, three, and four, the stability, electronic properties, charge, and

molecular orbital analysis of systems Cr_xTe_y ($x = 1 - 2$, $y = 1 - 4$); ($x = 3$, $y = 0 - 5$) & ($x = 4$, $y = 0 - 6$); and, ($x = 5$, $y = 0 - 7$) & ($x = 6$, $y = 0 - 8$), respectively. Chapter 4 discusses the properties discovered for the ligated $\text{Cr}_6\text{Te}_8(\text{PEt}_3)_6$, as well as how those properties change through substitution of the triethyl-phosphine (PEt_3) vs. PH_3 , Carbon Monoxide (CO), and Cyanide (CN). Finally, Chapter 5 summarizes the preceding chapters and discusses future directions.

2 Computational Approach

2.1 Overview

The methods of theoretically calculating the properties, characteristics of, and interactions between solitary atoms, clusters, compounds, molecules, and solids has been formulated, expanded upon, and refined over a very long period of time. These calculations are performed for two reasons: (1), to establish the origins of intrinsic properties seen in those various systems; and (2), to predict those properties within new materials. The very basis behind these powerful methods and tools rests upon the accurate representation of electrons moving in and around a group of point nuclei.

Calculating basic properties, through a process which has been termed in the past and shall be referred to again here as “the electronic problem”, is the cornerstone of quantum chemistry and the origins of its most widely used tool today, Density Functional Theory (DFT). This chapter is intended to give a brief introduction to the history, and overview of, the theoretical methods behind DFT and its origins. We conclude this chapter with a discussion regarding the implementation taken within this present study.

2.2 Background

2.2.1 The Electronic Problem & The Born—Oppenheimer Approximation

The usage of DFT in finding basic properties of chemicals and compounds arises from the need to approximately solve the time-independent Schrödinger Equation,

$$\hat{H}\Psi = E\Psi , \quad (2.1)$$

a partial differential equation of order two, where in this context \hat{H} is the Hamiltonian operator for a system of nuclei and electrons. From this equation, we can solve for the energy E given some wavefunction Ψ . The Hamiltonian itself contains five terms, each incorporating different aspects of the overall system, and has the form

$$\hat{H} = -\frac{\hbar^2}{2m_e} \sum_i \nabla_i^2 - \frac{\hbar^2}{2} \sum_a \frac{1}{m_a} \nabla_a^2 + \sum_a \sum_{b>a} \frac{Z_a Z_b e^2}{4\pi\epsilon_0 r_{ab}} - \sum_a \sum_i \frac{Z_a e^2}{4\pi\epsilon_0 r_{ia}} + \sum_j \sum_{i>j} \frac{e^2}{4\pi\epsilon_0 r_{ij}}, \quad (2.2)$$

where indices a and b denote nuclei, while i and j , the electrons. The terms specifically, moving left to right in Equation (2.2), are the kinetic energy of the electrons, kinetic energy of the nuclei, nuclei-nuclei repulsion, Coulombic attraction between nuclei and electrons, and finally, the electron-electron repulsion.^{115,116} The solution to this Hamiltonian operator involves a wavefunction of which depends on the explicit knowledge in the position of every electron in the system, as well as parametric dependence of the positions of every nucleus. Our problem is further complicated, in three-dimensions, with N total number of electrons, and M total nuclei; the wavefunction Ψ for our system is then dependent upon $3N$ coordinates of space for the electrons, N coordinates of spin, and $3M$ spatial coordinates for the nuclei. One can immediately deduce that calculating the interactions between every subatomic unit with their counterparts using this wavefunction can become quite large and solving for the groundstate of such a system grows uncontrollably, even with today's computational resources.

In order to scale computations of this kind we can make a simplification, in exercising the fact that nuclei are significantly heavier than the electrons. Knowing this, we consider the electrons around the nuclei to be in their optimal, lowest energy, configuration, which then allows us claim the nuclei are stationary. The motions of both can now, in effect, be considered decoupled from one another and the system in question can be treated as a group of electrons in motion around a group of point nuclei. The procedure we have outlined here is referred to as the

Born—Oppenheimer approximation, and with this we can effectively shorten Equation (2.2).

With stationary nuclei, the second term can be set equal to zero, the terms of their kinetic energy and interactions between one another. Furthermore, the third term detailing the interactions between the nuclei is simply now a constant. What remains of Equation (2.2) is called the electronic Hamiltonian,

$$\hat{H}_{el} = -\frac{\hbar^2}{2m_e} \sum_i \nabla_i^2 - \sum_a \sum_i \frac{Z_a e^2}{4\pi\epsilon_0 r_{ia}} + \sum_j \sum_{i>j} \frac{e^2}{4\pi\epsilon_0 r_{ij}} = \hat{T} + \hat{V}_{Ne} + \hat{V}_{ee} , \quad (2.3)$$

and operates on the electronic wavefunction Ψ_{el} to obtain energy E_{el} . If we include coordinates for the electrons q_i along with those of the nuclei q_a , the wavefunction can be written as

$$\Psi_{el} = \Psi_{el,n}(q_i; q_a) . \quad (2.4)$$

The total energy of the system being calculated can be found by simply summing together Equation (2.3) with the constant potential for the interacting nuclei,

$$V_{NN} = \sum_a \sum_{b>a} \frac{Z_a Z_b e^2}{4\pi\epsilon_0 r_{ab}} , \quad (2.5)$$

which produces

$$\begin{aligned} (\hat{H}_{el} + V_{NN}) \Psi_{el} &= (E_{el} + V_{NN}) \Psi_{el} = U \Psi_{el} \\ U &= E_{el} + V_{NN} \end{aligned} . \quad (2.6)$$

It has been proven in the past, that omission of a constant from the Hamiltonian does not change the wavefunction, so we can now rewrite the Schrödinger Equation as

$$\hat{H}_{el} \Psi_{el} = E_{el} \Psi_{el} . \quad (2.7)$$

Once we find E_{el} and V_{NN} , we can then obtain U of Equation (2.6), and finally reincorporate the nuclear motion into these equations. We know the nuclei are in some position q_a , then change their configuration slightly and move to position q'_a , and again to position q''_a , etc. Together, the total number of these motions can be considered strictly as one, i.e.

$$q_a \xrightarrow{\Delta} q'_a \xrightarrow{\Delta} q''_a \Rightarrow q_a \xrightarrow{\Delta} q''_a . \quad (2.8)$$

From the picture we have constructed in the previous paragraphs, the electrons move much more rapidly than the nuclei. When the nuclei change slightly in the manner as shown in Equation 2.8, the electrons immediately adjust to this change, altering the electronic wavefunction, $\Psi(q_i; q_a) \Rightarrow \Psi(q_i; q''_a)$, as well as the electronic energy, $U(q_a) \Rightarrow U(q''_a)$. Thus, as nuclei move, the electronic energy changes smoothly, with $U(q_a)$ effectively becoming a form of potential energy. Taking this nuclear potential energy and adding it to the kinetic from Equation (2.2), we obtain the nuclear Hamiltonian

$$\hat{H}_N = -\frac{\hbar^2}{2} \sum_a \frac{1}{m_a} \nabla_a^2 + U(q_a) \quad (2.9)$$

which is used to calculate the energy of the moving nuclei within

$$\hat{H}_N \Psi_N = E \Psi_N , \quad (2.10)$$

termed the nuclear Schrödinger Equation.

Compiling together the information from our discussion above, we see that the electronic wavefunction can now be treated as the product between electron and nuclear parts, as originally prescribe by Born and Oppenheimer. Their treatment of the mathematics in calculating properties of molecules have shown that the true wavefunction can be approximated as,

$$\Psi(q_i, q_a) = \Psi_{el}(q_i; q_a) \Psi_N(q_a) , \quad (2.11)$$

if $(m_e / m_a)^{1/4} \ll 1$.¹¹⁶ Justifications of, and corrections to, the Born—Oppenheimer approximation are outside the scope of this document, and can be found elsewhere. Moreover, those arguments do not address the omissions inherent of the approximation itself. Specifically, one will notice that there is no discussion above regarding the explicit position or coupling of the electrons around and between their individual nuclei. Additionally, there has been no discussion involving the interactions between the electrons themselves, or how those interactions are varied when we incorporate their spin. Thus, the Born—Oppenheimer Approximation is only the beginning when discussing molecular calculations, as we shall see below in subsequent sections.

2.2.2 Pauli

The inclusion of an electrons spin into the calculation of the energy, $E[\Psi]$, further expands the wavefunction through necessity. From here, we must address the obvious nature in the physical interactions involving two electrons, with or without the same spin, alternating positions with one another in space. Recalling from above, the electronic Hamiltonian involves only the spatial coordinates of the electrons. We now introduce an additional variable ω to accommodate the spin direction, up or down, and further combine this with the electrons three spatial coordinates (\vec{r}) into one new variable, denoted as $\vec{x} = \{\vec{r}, \omega\}$. In creating this new variable, we can now write an N -electron wavefunction simply as

$$\Psi(\vec{x}_1, \dots, \vec{x}_i, \dots, \vec{x}_j, \dots, \vec{x}_N) . \quad (2.12)$$

For electrons to maintain their indistinguishability from one another requires that their total probability density to not change through the exchange in position, (\vec{r}), between any two said electrons. Fermions, all particles with $1/2$ spin, including electrons, possess an antisymmetric wavefunction, thus any change in the state between two electrons further necessitates a change of

sign to the total wavefunction. This was first outlined by Wolfgang Pauli, and is now known as The Pauli Exclusion Principle, which states that no two electrons may occupy the same state.

We can write this in terms of equations as

$$\Psi(\vec{x}_1, \dots, \vec{x}_i, \dots, \vec{x}_j, \dots, \vec{x}_N) = -\Psi(\vec{x}_1, \dots, \vec{x}_j, \dots, \vec{x}_i, \dots, \vec{x}_N), \quad (2.13)$$

and it is the antisymmetry principle that thereby enforces the exclusion principle.

2.2.3 The Hartree—Fock Approximation

Searching for the wavefunction of a system that yields its groundstate, the minimum energy (E_0), is an impossible task. The methods as outlined by Hartree and Fock, provide a practical method to approximate the wavefunction and solve the Schrödinger equation. Within this method the incorporation and enforcement of the antisymmetry principle into the wavefunction is done through the use of a Slater Determinant. Defining the spatial orbital to be $\psi_i(\vec{r})$, and the spin orbital $\chi(\vec{x})$ as the product between spatial orbital and spin functions, $\psi_i(\vec{r})\alpha(\omega)$ or $\psi_i(\vec{r})\beta(\omega)$. Using these, we can write the Slater determinant in matrix form as

$$\Psi_0(\vec{x}_1, \vec{x}_2, \dots, \vec{x}_N) \cong \Psi_{SD} = (N!)^{-1/2} \begin{vmatrix} \chi_i(\vec{x}_1) & \chi_j(\vec{x}_1) & \cdots & \chi_k(\vec{x}_1) \\ \chi_i(\vec{x}_2) & \chi_j(\vec{x}_2) & \cdots & \chi_k(\vec{x}_2) \\ \vdots & \vdots & \ddots & \vdots \\ \chi_i(\vec{x}_N) & \chi_j(\vec{x}_N) & \cdots & \chi_k(\vec{x}_N) \end{vmatrix}. \quad (2.14)$$

The antisymmetric nature of the determinant arises from the property that exchanging either two rows or columns, the determinant changes its sign.¹¹⁷

The Hartree—Fock energy is obtained through calculating the expectation value of the Hamiltonian constructed using the Slater determinant. This expression for the molecular electronic energy of the system in question can be written as

$$E_{HF} = \langle \Psi_{SD} | \hat{H}_{el} + V_{NN} | \Psi_{SD} \rangle = 2 \sum_{i=1}^{n/2} H_{ii}^{CORE} + \sum_{i=1}^{n/2} \sum_{j=1}^{n/2} (2J_{ij} - K_{ij}) + V_{NN} , \quad (2.15)$$

where

$$H_{ii}^{CORE} = \langle \phi(1) | \hat{H}^{CORE}(1) | \phi(1) \rangle = \left\langle \phi_i(1) \left| -\frac{1}{2} \nabla_1^2 - \sum_{\alpha} \frac{Z_{\alpha}}{r_{1\alpha}} \right| \phi_i(1) \right\rangle , \quad (2.16)$$

$$J_{ij} = \left\langle \phi_i(1) \phi_j(2) \left| \frac{1}{r_{12}} \right| \phi_i(1) \phi_j(2) \right\rangle , \quad (2.17)$$

and

$$K_{ij} = \left\langle \phi_i(1) \phi_j(2) \left| \frac{1}{r_{12}} \right| \phi_j(1) \phi_i(2) \right\rangle . \quad (2.18)$$

Equation (2.16) is the sum of electron kinetic energy and electron-nuclear attraction terms.

Equations (2.17) and (2.18) represent the Coulomb and Exchange integrals, respectively. Both equations sum together to form the Hartree—Fock potential, V_{HF} , experienced by the electron.

The Coulomb term describes the energy between interacting electrons i and j in their respective positions and spin states. While the Exchange term is due to the possibility of an exchange occurring between those two electrons into their respective partners position and state. We must note that orthonormality of the spin orbitals renders this term zero for electrons in different spin states, and electron exchange only exists for electrons with similar spin. Moreover, the convenient removal within the equations above of the *self-interaction* term, when $i = j$. In this situation, Equations (2.17) and (2.18) cancel out one another within (2.15). This *self-interaction* is not completely absent within DFT, and can even lead to errors in certain calculations.^{115,118–120}

The Hartree—Fock Approximation offers a practical method for solving the Schrödinger equation in a simplified and reasonable representation of the wavefunction. Using the Slater determinant within this approximation, the problem of calculating the interactions between all N

electrons is reduced to simply one involving those electrons interacting with their surrounding environment. Finally, this HF method introduces the concept of the self-consistent field (SCF) approximation for iteratively solving the HF equations. Where an initial guess to the wavefunction is successively made more exact through calculation of the energy and continual update. This process serves at the very heart of DFT, and both will be outlined in the following section.

2.3 Density Functional Theory

2.3.1 Overview

From above, we recall that the wavefunction of an N electron molecule depends on $3N$ coordinates and N spin coordinates. However, the electronic Hamiltonian involves only one- and two-electron spatial terms. This implies that the molecular energy of the system can be written in terms of integrals involving only six spatial coordinates. This leaves us with some disturbing facts, namely, that the many-electron wavefunction contains more information than we need, and it lacks any direct physical significance. Resolving this has led to the search of new wavefunctions, and has even introduced the concept of replacing the wavefunction as the primary construct with that of the electron density $\rho(\vec{r})$. We shall see below that the density can be used to construct everything necessary within a calculation, and solved self consistently to reach a unique groundstate energy. There is no universal method for computing a groundstate from the electron density, however the purpose of DFT is to approximate it.

The electron density is defined as

$$\rho(\vec{r}) = N \int \cdots \int |\Psi(\vec{x}_1, \vec{x}_2, \vec{x}_3, \dots, \vec{x}_N)|^2 d\vec{x}_1 d\vec{x}_2 d\vec{x}_3 \cdots d\vec{x}_N, \quad (2.19)$$

and represents the probability of finding the i^{th} electron at any point within the volume of total electrons $d\vec{r}$. It has the property of

$$\int \rho(\vec{r}) d\vec{r} = N , \quad (2.20)$$

which states that integration over the volume elements yields the total number of electrons N .

A precursor to DFT, and one of the first examples to outline calculation methods based upon the density, was the work of Thomas and Fermi in 1927, the Thomas—Fermi Model.¹²¹ Based upon the model of a Uniform Electron Gas (UEG), they proposed a description for the kinetic energy of electrons to be

$$T_{TF}[\rho(\vec{r})] = \frac{3}{10} (3\pi^2)^{2/3} \int \rho^{5/3}(\vec{r}) d\vec{r} , \quad (2.21)$$

and the total energy of an atom by the equation

$$E_{TF}[\rho(\vec{r})] = \frac{3}{10} (3\pi^2)^{2/3} \int \rho^{5/3}(\vec{r}) d\vec{r} - Z \int \frac{\rho(\vec{r})}{r} d\vec{r} + \iint \frac{\rho(\vec{r}_1)\rho(\vec{r}_2)}{r_{12}} d\vec{r}_1 d\vec{r}_2 . \quad (2.22)$$

The first term is the kinetic energy, and is derived from the statistical behavior of interacting electrons. The second and third terms describe the interactions of nuclei-electron and electron-electron repulsion. Within the third term above, one can see that there is no incorporation of the exchange between electrons. In addition to this, the Thomas—Fermi Model itself is not very accurate. However, our concern here is not with its accuracy, but with the fact that the model has now shown it to be possible to use the electron density as a parameter in performing calculations.

2.3.2 The Hohenberg—Kohn Theorems

The next point in the history of DFT first began with the two theorems of Hohenberg and Kohn, in 1964, which together establish the basic framework for describing exactly how the electron density can be incorporated into a variational procedure.^{122,123} Their work proved for a

molecule with non-degenerate (only one) groundstate, that the energy, wavefunction, and all other properties, are uniquely determined by its electron probability density.

The first theorem states:

The external potential, $V_{ext}(\vec{r})$, (to within some trivial additive constant) is determined by the electron density $\rho(\vec{r})$; because this potential fixes a particular Hamiltonian, and one can find that the full many particle groundstate is a functional of the density.

Establishing this point solidifies the use of the density as a parameter for determining the interaction potential between nuclei and electrons. The Hamiltonian this theorem applies to can be written as

$$\hat{H} = -\frac{1}{2} \sum_{i=1}^n \nabla_i^2 + \sum_{i=1}^n v(\vec{r}_i) + \sum_j \sum_{i>j} \frac{1}{r_{ij}}, \quad (2.23)$$

where

$$v(\vec{r}_i) = V_{ext}(\vec{r}_i) = -\sum_{\alpha} \frac{Z_{\alpha}}{r_{i\alpha}} \equiv V_{Ne}(\vec{r}), \quad (2.24)$$

and using the property described in Equation (2.20), we can determine this external potential of Equation (2.24). From here, we can now find the remaining properties of the system, such as kinetic and potential energies, and the total energy E_V^{HK} for some potential V , all utilizing the density as a variable, written as

$$E_V^{HK}[\rho] = E_{Ne}[\rho] + T[\rho] + E_{ee}[\rho] = \int \rho(\vec{r}) V_{Ne}(\vec{r}) d\vec{r} + F_{HK}[\rho], \quad (2.25)$$

where

$$F_{HK}[\rho] = T[\rho] + V_{ee}[\rho] \quad (2.26)$$

is Hohenberg—Kohn functional. When this functional operates upon a given density, it produces values for the kinetic \hat{T} and electron-electron repulsion \hat{V}_{ee} within the groundstates wavefunction.

The Hohenberg—Kohn functional is what one would need to solve the Schrödinger equation exactly. However, the explicit form of the two terms on the righthand side of Equation (2.26) are completely unknown and must be found. But, we can rewrite the latter term in its classical analogue form of

$$V_{ee}[\rho] = \frac{1}{2} \iint \frac{\rho(\vec{r}_1)\rho(\vec{r}_2)}{r_{12}} d\vec{r}_1 d\vec{r}_2 + V_{ncl}[\rho], \quad (2.27)$$

$$V_{ee}[\rho] = J[\rho] + V_{ncl}[\rho]$$

where the $V_{ncl}[\rho]$ term encapsulates the non-classical contributions within electron-electron interaction, such as the self-interaction correction, exchange, and Coulomb correlation.

The second theorem states:

The functional that delivers the groundstate energy of a system, that energy is the groundstate if-and-only-if the input density is the actual groundstate.

This means that for some trial electron density which is greater than zero and associated with some external potential, the energy obtained using Equation (2.25) will be an upper-bound to the true groundstate. That is, the particular density that minimizes this energy obtained will then be the exact groundstate.

These two theorems developed by Hohenberg and Kohn solidify the usefulness of the electron density as a viable construct and parameter to replace the explicit wavefunction when computing the groundstate energy through the variational principle. However, these two theorems do not establish a routine in which to solve the Schrödinger Equation, and it was not

until later, in 1965, within the work of Kohn and Sham where they would devise a solution to this problem, through the use of a universal functional.¹²⁴

2.3.3 The Kohn—Sham Formulation

Modern density functional theory holds its origins in the implementation of the procedures as outlined by Kohn and Sham, where calculation of many-body properties can be completed through independent particle methods. Within their work they replace the many-particle interacting system with that of an auxiliary system, comprised of non-interacting particles, specifically the electrons. This fictitious auxiliary system then effectively allows one to split the behavior of the electrons into two components which can be treated individually: the first, where their kinetic energy is computed exactly; the second, the electron correlation, and repulsion, which is to be approximated.

To elaborate, let us suppose a system of N electrons. Furthermore, that they do not interact with the surrounding nuclei, but with some potential $V_s(\vec{r})$. We intentionally create this potential in a manner that fosters a density that does not change, i.e. $\rho = \rho_0$. Assuming this potential exists, we can find ρ . This density is constructed from single electron orbitals, the Kohn—Sham spinorbitals, to form the Slater determinant in a similar fashion to that of the Hartree—Fock approximation, and is written

$$\rho = \sum_i^N |\psi_i^{KS}|^2 . \quad (2.28)$$

Now, because the electrons do not interact with one another, we only need to iteratively solve for the energy of the individual one-electron Hamiltonians as an eigenvalue problem of the form

$$\hat{h}_i^{KS} \psi_i^{KS} = \epsilon_i^{KS} \psi_i^{KS} , \quad (2.29)$$

where this describes the energy of a particular electron in orbital i . The total number of one-electron orbitals, their Hamiltonians, and energies, are summed together to effectively obtain that of the total system, and can be seen in the expressions of

$$\hat{H}_S = \sum_{i=1}^n \left[-\frac{1}{2} \nabla_i^2 + V_s(\vec{r}_i) \right] \equiv \sum_{i=1}^n \hat{h}_i^{KS}, \quad (2.30)$$

$$\Psi_{s,0} = \left| u_1^{KS} u_2^{KS} \cdots u_n^{KS} \right|, \text{ with } u_i^{KS} = \psi_i^{KS}(\vec{r}_i) \sigma_i$$

where σ_i is the spin coordinate of the i^{th} electron, and ϵ_i^{KS} the *Kohn—Sham energy eigenvalues*.

The total energy for the groundstate as computed under the Kohn—Sham formalism can be written as

$$E_{KS} = T_0[\rho] + E_{Ne}[\rho] + J[\rho] + E_{xc}[\rho], \quad (2.31)$$

where

$$T_0[\rho] = -\frac{1}{2} \sum_{i=1}^N \langle \psi_i^{KS} | \nabla \psi_i^{KS} \rangle, \quad (2.32)$$

is the exact kinetic energy of the auxiliary system,

$$E_{Ne}[\rho] = \int V(\vec{r}) \rho(\vec{r}) d\vec{r} = \sum_i^N \int \sum_A^M \frac{Z_A}{r_{1A}} |\psi_i^{KS}(\vec{r}_1)|^2 d\vec{r}_1 \quad (2.33)$$

represents the Coulomb Nuclear-electron attraction, and

$$J[\rho] = \frac{1}{2} \iint \frac{\rho(\vec{r}_1) \rho(\vec{r}_2)}{|\vec{r}_1 - \vec{r}_2|} d\vec{r}_1 d\vec{r}_2, \quad (2.34)$$

is the Coulomb repulsion integral.

The final term in Equation (2.31), $E_{xc}[\rho]$, is termed the exchange-correlation energy,

which can be written as

$$E_{xc}[\rho] \equiv \Delta T[\rho] + \Delta J[\rho], \quad (2.35)$$

and represents the sum of two separate discrepancies. The first is the inherent difference in energy between this fictitiously constructed one-electron schematic and the actual kinetic energy of the system in question, $\Delta T[\rho] \equiv \bar{T}[\rho] - T_0[\rho]$. The second, is the energy that arises between interacting electrons, termed the *correlation* energy or Hartree Energy (as calculated by the Coulomb repulsion and interaction term), $\Delta J[\rho] \equiv \bar{J}[\rho] - J[\rho]$.

The utility of the Kohn—Sham approach is in the ability to turn the problem of solving a complicated many-particle system into an independent-particle one, despite these discrepancies. The exact contributions of the kinetic and potential energies are readily calculated, while the remaining contributions arising from these discrepancies are placed within E_{xc} , whose exact form is unknown and must be approximated at the time of calculation. Much progress has gone into devising new and all-encompassing forms for the E_{xc} term, resulting in many available choices, and improving them is a continual effort.

Iteratively solving for a systems electron density and energy using the Kohn—Sham formalism (the SCF procedure) can be outlined as follows; (1) Choose a Basis-Set (detailed below), an *exchange-correlation functional*, and calculate the electronic density of the system; (2) Using this density, calculate the exchange—correlation potential of the system, and all of the one-electron Hamiltonians with their individual energies; (3) calculate the Kohn—Sham (KS) matrix elements (i.e. the interactions between orbitals); (4) Solve the KS equations for their coefficients and the total energy of the system; (5) Use the coefficients to update and improve upon the previously calculated electron density; (6) Return to (2), and continue until the density and energy of the system does not change with appreciable difference. This energy difference is termed the *convergence criterion*, and is often taken to be 1E-3 eV (electron-volts). Specifically,

a system is deemed isolated, or *converged*, when the difference between its calculated energy of the previous cycle and energy from that of the current one, is less than or equal to 0.001 eV.¹²⁵

2.3.4 Exchange—Correlation Functionals

The Kohn-Sham equations, since their publication, have served as the starting point for any and all DFT calculations, and has proven itself time and time again. What remains, is to further devise an appropriate exchange-correlation functional which eliminates all the unknowns within a calculation. The true analytical form of the functional is itself unknown, but over the decades, there have been numerous undertakings in the derivation of new functionals, each aimed specifically at further refinement or the inclusion of another aspect in the behavior of electrons. This have given rise to functionals that vary wildly in theory and extent, and dependent upon a functionals complexity it can be classified with its counterparts in what has affectionately been termed the “Jacob’s Ladder” of functionals.¹²⁶ The first rung being the simplest, with the top rung reserved for functionals deemed closest to representing the actual electronic density of a system, found in nature.

Within the first rung of this ladder resides the basis for all exchange—correlation functionals, the *Local Density Approximation* (LDA). The functional describes the reduction of the complex arrangement of molecules within a system to a simpler argument, to one involving a uniform electron gas within a known fixed volume. This approximation assumes homogeneity, and divides the volume containing the electronic gas into smaller regions. This division then reduces the calculation of determining the exchange—correlation energy contribution to the overall system into nothing more than the multiplicative product of the small volumes and the density within them. The algebraic expression for the exchange portion was originally derived by Bloch and Dirac, and the correlation originally fitted through Quantum-Monte Carlo

simulation by Vosko, Wilk, and Nusair (VWN), with several variants upon it in later years.^{125,127–}

¹³¹ The properties of systems obtained using LDA have made it insufficient for many applications in chemistry, however. It has been shown to give reasonable ionization, dissociation, and cohesive energies to within 10-20 %. But, bond lengths of molecules and solids to an accuracy of ~2%. The functional cannot be relied upon for use in systems that are dominated by electron-electron interaction effects, such as transition metal-oxides, as well.

An improvement upon LDA, on the next rung upwards of our ladder, resides the *generalized gradient approximation* (GGA) functionals. Functionals here add an extra term to their exchange portion, to include not only the position of the electrons of the one-electron system, but also their gradient. Such an inclusion effectively reduces the errors of LDA by a factor of 3 when calculating atomization energies for small molecules. Moving up in complexity, we highlight the Hybrid functionals. These functionals marriage together the exchange portion derived separately, or taken from another functional, with the correlation of yet another (derived or taken from). The exact procedure for creating functionals is beyond the scope of this dissertation, but Scuderia and Staroverov give a detailed outline and brief overview of the complexity at each level of formalism and provide starting points for review of the literature.¹³²

2.3.5 Mulliken Population and Hirschfeld Charge Analyses

Using the capabilities of first-principles DFT, or rather “onsite” DFT, which involves computation at the atomic orbital level, we can compute a number of useful electronic values. In doing so, we aim to complete two aspects in this investigation. The first, is to understand the emergence and eventual collapse of magnetization in the progression from small, binary, Cr-Te clusters, up to the larger ligated $\text{Cr}_6\text{Te}_8(\text{PET}_3)_6$ system. The second, to establish basic electronic

information that can be used to describe behavior of these clusters on the macroscopic level; either in a large periodic system, where onsite DFT is impossible, or in a top-down approach through experimental measurements. We bridge these two ideas together through the methods of *Mulliken Population Analysis* (MPA), *Hirshfeld Charge Analysis* (HCA).

Briefly mentioned above, Mulliken Population Analysis is the oldest and best-known definition in describing atomic charge. It is completed using the optimized atomic orbitals and their coefficients, found during the calculation, which are then used to form the resultant electron “density matrix”. Thus, this density matrix possesses all the information of the system, specifically with regards to every atom, its orbitals, electron occupations, and orbital overlap with its neighbors.^{133–137} Because MPA involves such detail, we can obtain information regarding both, the density of charge present on an atomic site, as well as the spin direction and number of electrons. Within this study, we shall only concern ourselves with the population of spin for each element, and how that spin population is distributed across all of its orbitals. We can easily deduce that applying MPA to large systems can become computationally taxing, very quickly, and only applied to onsite DFT. But, we can continue with methods of charge analysis which are based on the electron density, as a function of space, regardless of how that density is computed.

Hirshfeld Charge Analysis, involves effectively two densities, one for the total molecule itself, and a fictitious density constructed from each of the elements within that molecule. Atomic charges obtained by this method are a result of distributing, among all the atoms in the molecule, the total electronic probability density, which can be seen in

$$\rho_A(x, y, z) = \frac{\rho_A^0(x, y, z)}{\sum_A \rho_A^0(x, y, z)} \rho_{mol}(x, y, z) , \quad (2.36)$$

where $\rho_{mol}(x, y, z)$ is the electronic probability density at some point, $\rho_A(x, y, z)$ the amount of density at (x, y, z) being assigned to atom A , $\rho_A^0(x, y, z)$ is the electronic density of the isolated atom A (which has been calculated using the same method and basis set to obtain $\rho_{mol}(x, y, z)$), and the sum in the denominator of Equation (2.36) is over all the probability densities of the isolated atom types found within the molecule. Finally, the Hirshfeld Charge for an atom A can be written as

$$Q_A = Z_A - \int_{-\infty}^{\infty} \int_{-\infty}^{\infty} \int_{-\infty}^{\infty} \rho_A dx dy dz , \quad (2.37)$$

where Z_A is the atomic number of atom A .^{116,137-142} Doing this analysis allows one to view density movement on a larger scale, across the entire molecule. Moreover, the individual Hirschfeld charges on each atom provides the means to view a molecules effective dipole strength and its direction.

2.4 Computational Methods

All geometries below have been found, and their properties calculated, under the framework of DFT utilizing the exchange and correlation components of the generalized-gradient approximation (GGA) functional as derived and outlined by Perdew, Burke, and Ernzerhof (PBE).^{127,143} All calculations and property investigations are completed using the *Amsterdam Density Functional* (ADF 2016.104) set of codes.¹⁴⁴⁻¹⁴⁶ Here, the molecular orbitals are represented as linear combinations of atomic orbitals (LCAO) centered on the atomic sites. These onsite one-electron orbitals are generated in the fashion outlined by John C. Slater, the Slater-type orbitals (STOs).¹⁴⁷⁻¹⁴⁹ Moreover, geometry optimizations have been done under

ADFs *Zeroth-Order Regular Approximation* (ZORA) representation, a modification to the solution of the four-component Dirac equation, to effectively treat relativistic effects.^{150–154}

In addition to the choice of exchange-correlation functional, one is also afforded a choice in the size of the Basis-Set, or simply *basis*, to use within a calculation. The Basis Set file is nothing more than a table, or list, of which there is one file for each element on the periodic table, with a minimum of one pair of numbers, one for each orbital of that element. The first number is the fitting constant, designed to calibrate that particular orbitals behavior and contribution to the overall wavefunction. The second number in this Basis file is the “Slater orbital exponent”, ζ (zeta), which is a fitting constant used to accurately represent the long-range behavior of the orbital it is associated with. Of course, there are a fixed number of physical orbitals, but there is no limit to the number orbitals we can use in order to construct the full MO of a particular system. Thus, depending on the calculation, one can choose a basis set with a single zeta coefficient (SZ) (one orbital coefficient, and one zeta parameter) to represent atomic orbitals, or as many as four, quadruple-zeta (QZ) (eight coefficients, and eight zeta parameters), for every element. Obviously, the choice of basis set size has a direct effect on the final Molecular-Orbital (MO) representation. As such, when using local atomic orbitals to build a larger MO, the basis plays a very important role in calculating individual electron contributions to the system. Moreover, all charge analysis methods upon the system in question will involve one or several aspects of the basis and the final computed coefficients.

Within ADF, the various geometries of Cr_xTe_y stoichiometry outlined below (unless otherwise noted) have been computed using the QZ4P basis set (Quadruple Zeta, Quadruple Polarized; all-electron) basis.¹⁵⁵ This basis consists of 13S, 8P, 5D, and 3F functions for Cr; and 18S, 15P, 8D, and 3F functions for Te. The 4P designation represents the addition of functions

(coefficients and zeta exponents) to the basis in order to appropriately represent the stretching, or polarization, and modification of orbitals due to bonding and other effects.

These atoms within the clusters will be moved in the direction of forces until those forces are reduced to 0.001 Hartree (0.027 eV) per Å, and total bonding energy reduced to 0.001 eV per geometry iteration, at which time the cluster is considered to have converged and thus reached its groundstate. Converged geometries are visualized using the Discovery Studio Client as provided by Dassault Systems, Inc. (Formerly Accelrys), and the ADF Graphical User Interface (ADF GUI). The ADF GUI will be used to visualize molecular orbitals, and help in detailing other properties such as Hirshfeld and Mulliken Populations (HPA and MPA). Both of these analysis techniques are employed in order to ascertain the spin density of individual atoms as well as the underlying charge movement between the various atoms, and cluster fragments. An isosurface value varying between 0.01 and 0.03 electrons will be applied and used throughout to better view the molecular orbitals.

The structures found in the search for binary atomically-precise CrTe, in addition to their Mulliken Populations, Hirshfeld Charges, and other basic cluster properties, will be discussed during the presentation of results in Chapter 3. And similarly, for ligated versions of Cr₆Te₈ within Chapter 4.

3 Atomically-Precise Binary Cr_xTe_y Clusters

3.1 Overview & Two-Dimensional CrTe

While small binary clusters of chromium and tellurium are nonexistent in the literature, there are several reports describing the fundamental unit cells of various two-dimensional, periodic systems. Chevreton, amongst a handful of others, were first to describe the magnetic behavior and crystallographic properties within systems containing the basic units of CrTe and Cr_3X_4 ($X = \text{S}, \text{Se}, \text{Te}$).⁸²⁻⁸⁵ Around this time it was first proposed by Khoi & Veillet in their study of Cr_3Te_4 , and later seen in the NMR studies of Hashimoto & Yamaguchi upon Cr_7Te_8 , the presence of two different kinds of internal electric fields.^{85,87} It was inferred that both systems were comprised of two chromium oxidation states, specifically Cr^{2+} and Cr^{3+} . Moreover, in addition to Cr_3Te_4 and Cr_7Te_8 , Chevreton also discovered that the Cr-Te umbrella encapsulates another homogeneous compound, Cr_2Te_3 .⁸² That same year, Van Con & Suchet would go further and state that the Cr-Te family possessed more than three homogeneous compounds, but many more nonstoichiometric counterparts in the composition range of 52-61 at.% Te.⁸³

The very early studies of Cr_7Te_8 showed its fundamental unit cell to be of the NiAs-structure with associated Cr-vacancies. The NiAs crystal structure is hexagonal, with a layering scheme between the two element types representative of an ABABAB... stacking, with atom A in the octahedral coordination, and atom B in the trigonal prismatic. The vacancies described are the literal absence of an element within the lattice, typically chromium, and tends to occur every two layers within the superstructure. In a two-step thermal treatment procedure of this crystal, Hashimoto & Yamaguchi succeeded in producing two phases, an ordered, monoclinic; and

disordered, hexagonal. Each with a different arrangement of those vacancies. Their saturation magnetization experiments reported a slightly higher Curie temperature and effective Bohr magneton number for the disordered phase than that of the ordered; 361 K vs. 350 K, and 2.5 μ_B vs. 1.8 μ_B .⁸⁷

Obviously, this opened the door for many more studies into the Cr-Te systems, in both strictly pure binary forms, and even doped^{108,113} versions. Early investigations delved into the magnetic properties of $\text{Cr}_{2-\delta}\text{Te}_3$ ^{88,89}, as well as further studies into previously known structures and into newly found compositions, such as; CrTe, $\text{Cr}_{23}\text{Te}_{24}$, Cr_7Te_8 , Cr_5Te_6 , and Cr_3Te_4 ⁹⁰. Within the same year of this comprehensive magnetism study, Klepp & Ipsier in 1982, report their discovery of the never before seen CrTe₃ crystal phase.⁹¹ Its electronic structure, and underlying role of tellurium, was not detailed until five years later.⁹⁴ Some years prior, in 1987 Yuzuri *et al.* detail their findings involving the effects of pressure upon the magnetic properties of Cr_2S_3 and Cr_2Te_3 .⁹² In 1989 with Dijkstra *et al.* they discuss band-structure, magnetism, and transport within CrTe, Cr_3Te_4 , and Cr_2Te_3 .⁸⁶ A year later, yet another phase, CrTe₂, is newly discovered.⁹³ Finally, in 1991 through the work of Steigerwald *et al.*, a report appears detailing the differences between our cluster, $\text{Cr}_6\text{Te}_8(\text{PEt}_3)_6$, and the connection to its periodic ancestry of Chevrel clusters and the NiAs structure.⁵⁷ Later, a discussion of the clusters' synthesis and its connection to the two-dimensional Cr_3Te_4 system by Hessen *et al.* in 1993.⁵¹ The study of Cr-Te systems continues, up until today, with literature discussing everything from solidifying the nature of its crystal structure⁹⁶, pressure induced transformations⁹⁷⁻¹⁰⁰, and underlying magnetic origins and overall electronic behavior.^{95,101-104,106,109,110,112}

Despite the vast number of investigations into periodic CrTe, the magnetism, structural behavior, and electronic subsystem of atomically-precise CrTe clusters has yet to be understood.

To fully understand the complications in theoretically finding groundstate structures, electronic, and magnetic properties for CrTe based systems, it is necessary to first discuss and highlight a few previous results, and difficulties, when finding those same properties within pure clusters of those elements.

3.2 Pure Systems of Chromium, and Tellurium

3.2.1 Overview

Firstly, to establish a unifying and overall framework in which to discuss new clusters based on chromium, a gap appears that must be addressed. Specifically, in regards to chromium clusters, between i) the computational results within this document; and ii), those of both theoretical computation and experiments previously completed. To bridge this gap, groundstates for pure chromium clusters, Cr_n $n = 1 - 6$, have been obtained within the formalism as outlined above in Chapters 2, namely; PBE GGA functional, (Scalar Relativistic) ZORA, QZ4P Basis, and without symmetry constraints. Thus, before introducing clusters of binary CrTe, we first briefly introduce pure tellurium clusters, followed by discussion of chromium. Finally, address the newly obtained small clusters of chromium.

3.2.2 Tellurium Clusters

The inherent complexity needed for chromium cluster calculations can be easily transferred to those for pure tellurium, as well. Stable structures formed from elements of group-16 on the periodic table display transformations from diatomic species of oxygen, up through rings of sulfur, selenium chains, and tellurium helices, with an increase in strength of single bonds versus double.^{156,157} Elements of this group are known to have two lone electrons; each the sole occupant of a non-bonding orbital. These orbitals are directional, and lie at the top of

the valence band, with divalent tendencies and a preference for twofold coordination. The behavior of these elements with regards to their orbital interactions, results in various groundstate geometries of ring and/or chain-like structures, which is exemplified by the small clusters of tellurium.^{158–163}

Specific cluster isomers for Te_n $n = 6$ were obtained by Igel-Mann *et al.* in 1993 under Hartree-Fock methods, and found changes in the ordering of these isomers after inclusion of correlation and configuration interactions.¹⁶⁴ Additionally, density functional calculations of Te_n ($n = 2 - 4$) clusters completed by Goddard *et al.* in 1999 displayed a high dependence on the choice of basis-set used (more about this below) on the resultant structure and vibrational frequencies. But, in all instances, the isomers of Te_3 (C_{2v}) and Te_3 (D_{3h}) were found to be almost degenerate, and similarly for the isomers of Te_4 (C_{2v}) and Te_4 (D_{2h}).^{159,160} Subsequent theoretical studies into geometries and frequencies by Pan in 2002, $n = 2 - 8$, was completed using three different types of *xc*-functionals to complete their calculations, in turn finding several isomers for $n = 4 - 6$.¹⁶¹ This dependence on *xc*-functional was also accounted for in the work of Akola & Jones, while investigating amorphous tellurium and clusters $n \leq 16$. Using four different *xc*-functionals, they showed the energy difference between two- and threefold coordination of tellurium atoms to be sensitive to the particular *xc*-functional used, as well.¹⁵⁷ We do not delve further into the nature of tellurium or its clusters, but the references mentioned here (and those therein) do provide sufficient introduction.¹⁶⁵

3.2.3 A Brief History of Small Chromium Clusters

Chromium, for many years has been known to be an antiferromagnetic substance. However, even within large cluster systems, chromium behavior is very complex and has drawn a lot of interest. Thanks to the work of Payne *et al.*¹⁶⁶ just over a decade ago, they have

measured the magnetic moments of free Cr_n clusters reaching over 100 atoms in size showing there are two different magnetic behaviors that develop as a function of size. This can be seen below in **Figure 3-1**, which for the clusters Cr_{30} , and $\text{Cr}_{34} - \text{Cr}_{133}$ have two magnetically distinguishable isomers, hence the two plots. However, at the small scale, the antiferromagnetic character does not persist and on some occasions, leads to systems possessing a ferromagnetic high spin polarization.^{167,168} It is this ferromagnetism that is to be harnessed and maintained into the macroscopic regime. But, obtaining systems of this type can be difficult, due to the tendency of transition metals with a nearly half-filled shell, i.e. Mn_n and Cr_n , to align in an antiparallel manner with the nearest neighbor.¹⁶⁹ Understanding these findings is still somewhat of a challenge, with many theoretical investigations having already been conducted to study magnetism as related to structure, and vice versa.¹⁷⁰⁻¹⁷⁴

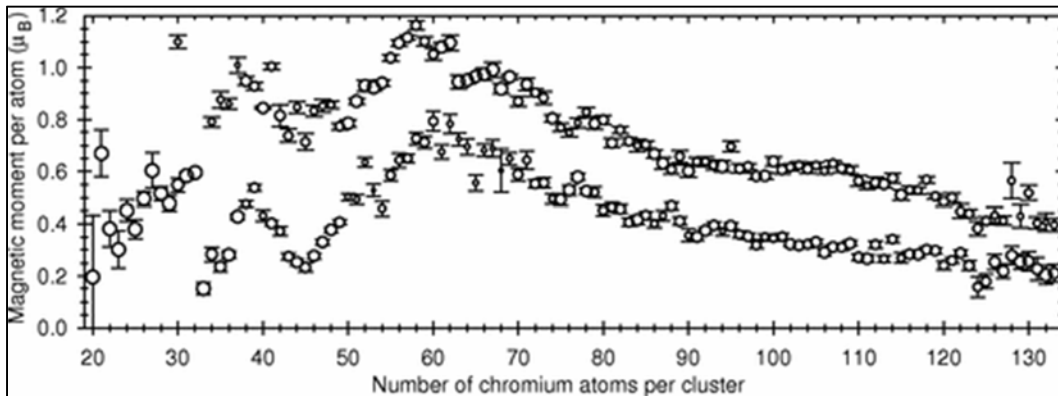


Figure 3-1. Magnetic moments per atom μ for chromium clusters of $N = 20 - 133$.
(Reused with permission, Copyright American Physical Society)¹⁶⁶

At the smaller scale, it has been confirmed in experiments of solitary Cr that it possesses a groundstate of 7S_3 , in a $3d^54s^1$ configuration.¹⁷⁵⁻¹⁷⁷ A configuration found similarly within the present study. Additionally, in the investigation of chromium clusters, extensive attention has been placed upon that of Cr_2 , both theoretically and experimentally.^{171,178-185} Across these studies it has been experimentally found that the groundstate is formed by two chromium atoms coupling antiferromagnetically. This bond is comprised entirely between the s - and d -orbitals,

with length of 1.6788 Å; drastically shorter than found in bulk, 2.50 Å.^{172,186} Ideally, with each Cr atom supplying six unpaired electrons, this should in principle produce a dimer with six bonds. Due to the size difference between the 4s and 3d orbitals, as well as the influence from exchange energy, this bond is very weak and has a low binding energy (1.53 ± 0.05 eV).^{187,188} Accordingly, it has been found through bond order analysis that the dimer has an effective bond order of 3.5, instead of the ideal six.¹⁸⁹ In this present investigation, the Cr₂ cluster has a calculated bond length of 1.71 Å, and dissociation energy of $D_e = 0.735$ eV, both in fair agreement with experimental data.

The extensive studies into the electronic properties of Cr₂ have often been used as a benchmark when discussing the specific magnetic and bonding characteristics of larger, polyatomic chromium. This understanding of Cr₂ has lead Cheng & Wang in 1996 to propose a dimeric growth route for clusters up to Cr₁₁, in an effort to explain the widely alternating spin multiplicities between even and odd numbered clusters, as well as antiferromagnetic ordering and structural transitions.¹⁷² Later calculations at a higher level of theory by Wang *et al.*, in search of Cr_n ($n = 2 - 5$) equilibrium geometries, have reported small chromium clusters are antiferromagnetically coupled, and found no dimer-growth route for clusters larger than $n = 3$.^{174,190} This was confirmed later in 2010 by Ge *et al.*, reporting no dimeric-growth for metastable isomers of Cr_n ($n = 2 - 9$), under the same, higher level, of theory.¹⁹¹

Clearly, as computational methods become more complex and encompassing, it is advantageous to determine, at these higher levels of theory, what exactly is the behavior of small chromium. This lack of complexity in formalism and/or availability of adequate orbital representation can be followed up into the present day, as told through previous literature reports. The wealth of information from these studies has yielded a multitude results that are extremely

diverse. Moreover, some of the claims made in regards to the electronic properties of small chromium are drastically different from the experimental data, in regards to bond lengths and dissociation energies.

It is important to remember, and bears some emphasis, in the desire to create new materials with novel properties and use clusters to do so, calculation of fundamental properties must obviously be of the utmost of quality. Thus, choice of *xc*-functional and matching basis-set are the two main variables for these calculations. Within this study, the choice of PBE functional was based upon its history of successful usage in predicting and verifying both properties and structure of various clusters, as well as periodic solids and CAMs. Moreover, the basis-set of QZ4P was chosen not only for its completeness in numerical representation and optimization for use with the ZORA formalism within ADF, but also as a type of benchmark. Performing these cluster optimizations in this manner serves as a useful reference for comparing past results, as well as future DFT calculations of this type. Specifically, those utilizing GGA or meta-GGA functionals and/or *Slater-type orbitals* (STO); despite the concentration of this investigation placed solely upon neutral species with collinear spins.

A modern investigation into the most suitable combination between the DFT functionals of GGA PBE and meta-GGA TPSS, and various basis sets was undertaken recently by López-Estrada *et al.* in 2016.¹⁹² This was done in search for the best description to verify experimental findings regarding the properties of Cr_n , $n = 1 - 4$, and highlighted a Cr_4 cluster with $S = 6$ spin state. Prior to this, a more comprehensive investigation into the most suitable functional and basis pairing was performed by Würdemann *et al.*¹⁹³ Within that study, a compendium of information derived from numerous basis set combinations with functionals from GGA and meta-GGA levels was undertaken in order to solidify the electronic properties of Cr_2 and Cr_3 ,

which is then compared with vast amounts of experimental data found in the literature. Furthermore, these newly found results are applied upwards toward larger sized chromium in an effort to put all calculated Cr_n data on the same footing.

3.2.4 Small Clusters of Pure Chromium

The groundstate structures of pure chromium clusters found in this study are shown below, in **Figure 3-2**, while their respective bond lengths and level diagrams are given in Appendix A. Interestingly enough, their total magnetic moments vary between 0 and $6 \mu_B$, depending on even or odd number of Cr atoms, respectively. Macroscopic properties of the Cr_2 dimer have already been discussed above, and we shall save the remainder of its analysis until reaching the sections of Te addition.

Thus, we begin with the trimer which we can see below. Different possible geometries without symmetry constraints, and across several spin states were considered initially, but only the groundstate geometry is given below. The lowest energy geometry is in the septuplet spin state, $M = 7$. The local moment for each chromium is listed (negative = downward). The first isomer appearing at higher energy is the quintuplet, and at a difference in energy of ~ 0.46 eV. A competition between $M = 5$ and $M = 7$ groundstates has been seen before.¹⁹² López-Estrada *et al.* have performed computations upon small chromium and have claimed their energy difference to be ~ 0.2 eV. Within that report, the authors have also deemed the cluster of $M = 7$ to be groundstate, based upon previous experimental results.

With regards to geometry, the triangle formed below follows along the lines of previously reported geometries for the trimer, possessing a right triangle shape formed as a dimer plus adatom formation. The presence of a lengthened bond exists between Cr_2 and Cr_3 at 1.803 \AA , and is slightly larger than other geometries whom report lengths closer to the original dimer

when using GGA functions. Together, this bond, along with the Cr2-Cr3 bond of 2.432 Å, form an angle at 91.19°.

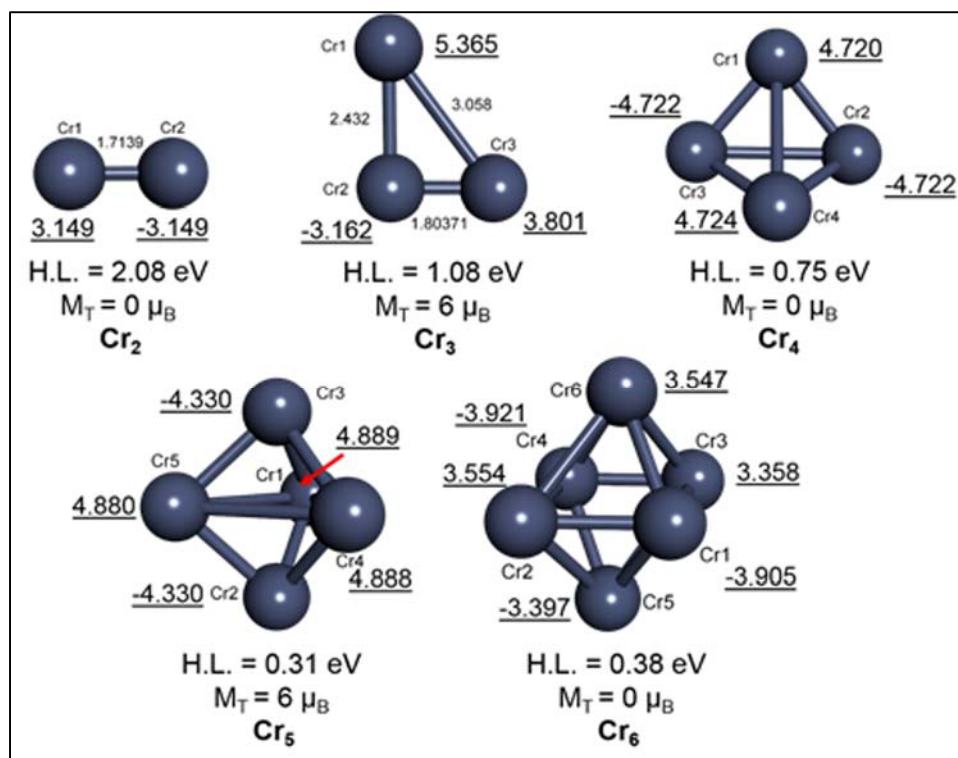


Figure 3-2. Groundstate clusters of pure Cr_n, n = 1 – 6. With HOMO-LUMO gap, and magnetic moments for individual Cr, and total cluster (M_T).

The chromium tetramer has been obtained from various initial geometries and spin states. The groundstate is a singlet, M = 1, with three atoms forming a right triangle base and the fourth atom bonding similarly to share the hypotenuse. From there, this structure remains as a distorted tetrahedron, as the fourth atom does not reach an apex above the remaining three. The resultant dihedral formed has angle of 113.24°. The bond distances between Cr1 and Cr4, & Cr2 and Cr3 are ~3.01 Å, while the remaining bonds are ~2.35 Å. In this arrangement, the chromium atoms are antiferromagnetically arranged, with near equal charge density. The next geometry higher in energy can be found at ~0.60 eV away, however there is a competition between structures in the triplet spin state and that with higher multiplicity of M = 13; with the triplet state only ~24 meV lower in energy. This again has been reported on previously¹⁹², but in that publication the

position of the fourth Cr atom at the apex does not yield any singlet spin state geometry and has brought the groundstate to a discussion between the triplet and $M = 13$ states. The competition between those two spin states has been attributed to their close geometries, which facilitates a spin-flip due to spin-orbit coupling.

Trends of this type, based on differences in energy, bond distances, and magnetic coupling continue upwards into the larger size of chromium. The pentamer of chromium begins to display a form of regularity with respect to bond distances. The triangle formed of Cr1, 4, and 5, have lengths of $\sim 3.03 \text{ \AA}$; with the remaining distances at $\sim 2.40 \text{ \AA}$. Apex atoms together are antiferro with respect to the central triangle, but sum total of spin moments results in a ferrimagnetic cluster with septuplet multiplicity. Additionally, the cluster of Cr₆ is highly distorted from an ideal tetragonal bipyramid structure with all bond distances lying within the range of $2.33 - 2.77 \text{ \AA}$, with the shortest being found joining the four atoms of the center square. The distortion appears now to be a result of the individual moments of the atoms, and despite their differing magnitudes the overall cluster is in the singlet state. This is affirmed, as the next highest pair of geometries are $\sim 0.33 \text{ eV}$ higher in energy. Here, the two geometries in question are those with multiplicity of $M = 9$, and $M = 11$. Both geometries are highly similar in structure, with only minute differences in bond lengths.

3.2.5 Summary

Together, all the clusters above are in reasonably good agreement with current, modern, literature reports and serve as suitable starting points for comparison with their tellurium paired variants. Using these new results, as well as our knowledge of elemental tellurium behavior from the prior discussions, we begin to address binary CrTe. Specifically, what we now lack is a concrete formulation detailing the transition of properties between the two; small clusters of

chromium, and those of tellurium, together. More importantly, how their overall magnetic and electronic behavior change when moving into the macroscopic scale. Moreover, despite the large magnetic moment of elemental chromium, and its small clusters, how and why does that magnetic moment enhance, stabilize, or diminish in the presence of tellurium. The apparent lack of any robust magnetism on a large scale regarding the $\text{Cr}_6\text{Te}_8(\text{PEt}_3)_6$ cluster, and overall solid itself as shown in experiment, can be traced back to these small cluster sizes of binary Cr/Te, and shall be addressed in the next section.

3.3 The Cr_xTe_y Clusters

3.3.1 Overview

We further divide the remainder of this chapter effectively into three parts. The first, discusses the clusters, their structures, bond distances, etc. Within the second, overall properties pertaining to the entire series. Electronic properties such as HOMO-LUMO Gap, trends of the individual bond distances, magnetism, Hirshfeld Charge analysis, and removal energies. Lastly, the bonding patterns between chromium and surrounding tellurium, as seen through levels diagrams, the density of states, and Mulliken spin density movement. All cluster geometries can be seen below in **Figure 3-3** through **Figure 3-9**, with labels and associated labels bond lengths in Appendix B.

It should be noted, that although there are numerous interpretations and results for small chromium geometries and associated isomers, that number pales in comparison to those of small CrTe. For each groundstate shown below, there are numerous higher energy isomers within 1.00 eV. One can deduce, this number grows even larger depending on the total number of Cr and Te atoms within a cluster. For example, smaller CrTe systems have approximately five higher energy isomers; while the larger can have upwards of eight or more. For the groundstate and low-lying isomers, full convergence was guaranteed through frequency analysis. After such analysis, any geometry displaying a frequency which is negative, in any vibrational mode, would subsequently be reoptimized under a tighter geometry convergence criterion; 10^{-5} eV, rather than the standard, 10^{-3} . Tests involving geometry optimizations incorporating both a tighter convergence criterion and integration grid (ADF 2016.104: “verygood” vs “good”) have shown the modified geometry criterion (10^{-5}) to be sufficient when used alone.

3.3.2 Geometries & Structure

3.3.2.1 Cr_1Te_y ($y = 1 - 4$)

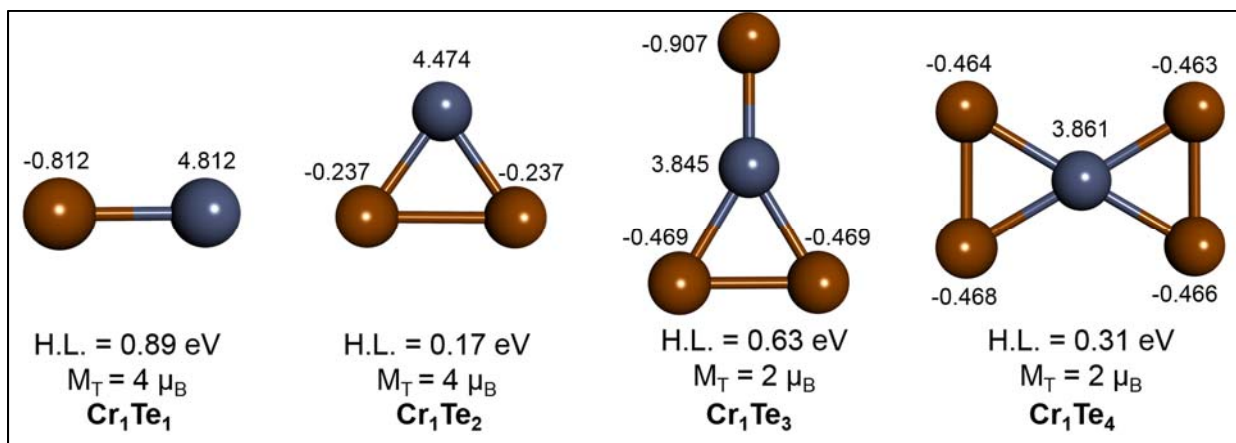


Figure 3-3. Groundstate structures of $\text{Cr}_1\text{Te}_{1-4}$.
With HOMO-LUMO gap, individual Mulliken Spin Density, and total magnetic moment, M_T . (Cr:Blue; Te:Beige)

Ascertaining the effect of bonded tellurium is best understood through its imposition upon the free atom and dimer of chromium. The groundstate geometries for $\text{Cr}_1\text{Te}_{1-4}$ are shown in **Figure 3-3**, accompanied by their total magnetic moment, M_T , as well as individual spin moment contributions from chromium and tellurium. What can be seen immediately is the systematic decline of spin density of the central chromium atom, and the fall of the total moment. The bond length within Cr_1Te_1 is 2.453 Å. The closest geometry higher in energy to CrTe is in the septuplet state, at a difference of 0.55 eV. For CrTe_2 , the two tellurium atoms bonded to solitary Cr form an isosceles triangle with a bond length of 2.874 Å between the tellurium. As the number of Te atoms increase, we can see they take on something close to a square planar arrangement around Cr. Bond lengths now are ~2.62 Å between Cr and Te, and ~2.70 Å between the Te. The nearest geometry higher in energy to CrTe_2 is in the triplet state, and <60 meV away. Similarly, the first isomer of CrTe_3 is 0.17 eV higher and in the quintuplet state; while for CrTe_4 , the first isomer is ~0.13 eV higher, but still in the triplet state.

3.3.2.2 Cr_2Te_y ($y = 1 - 4$)

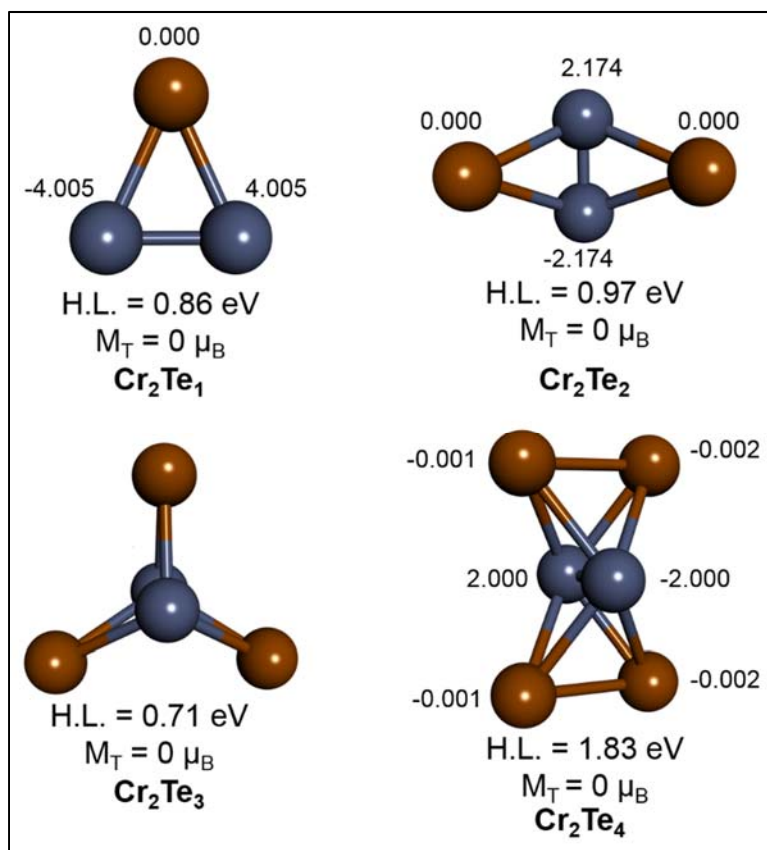


Figure 3-4. Groundstate structures of $\text{Cr}_2\text{Te}_{1-4}$.
With HOMO-LUMO gap, individual Mulliken Spin Density, and total magnetic moment, M_T . (Cr:Blue; Te:Beige)

Interesting geometrical effects can be seen on the dimer of chromium through the sequential addition of Te atoms in **Figure 3-4**. Firstly, all geometries are in the singlet state, with virtually no spin density in the Te atoms. Placing a single Te atom upon Cr_2 stretches the bond from 1.7138 Å to 2.102 Å, and this Te atom is now closer to both Cr atoms at a distance of 2.555 Å. A second Te atom reduces the Cr_2 bond back downward to 1.838 Å. Both Te atoms are in a butterfly position, out of plane in the dihedral, but each maintain bond lengths of 2.559 Å and 2.561 Å. A third Te atom in Cr_2Te_3 now brings the Cr dimer to a bond length to 1.769 Å, and all Te atoms are in the range of 2.565 – 2.570 Å. More importantly, the spin moments on both Cr atoms are now completely quenched. Finally, a total of four Te atoms, in Cr_2Te_4 , encircling the central Cr_2 leaves the metal bond at 1.792 Å, bonds between Cr and Te are now in the range

of 2.708 – 2.715 Å, with Te atoms forming two dimers, each with length of 2.781 Å. Here, the spin moments are antiferromagnetic to one another.

3.3.2.3 Cr_3Te_y ($y = 1 - 5$)

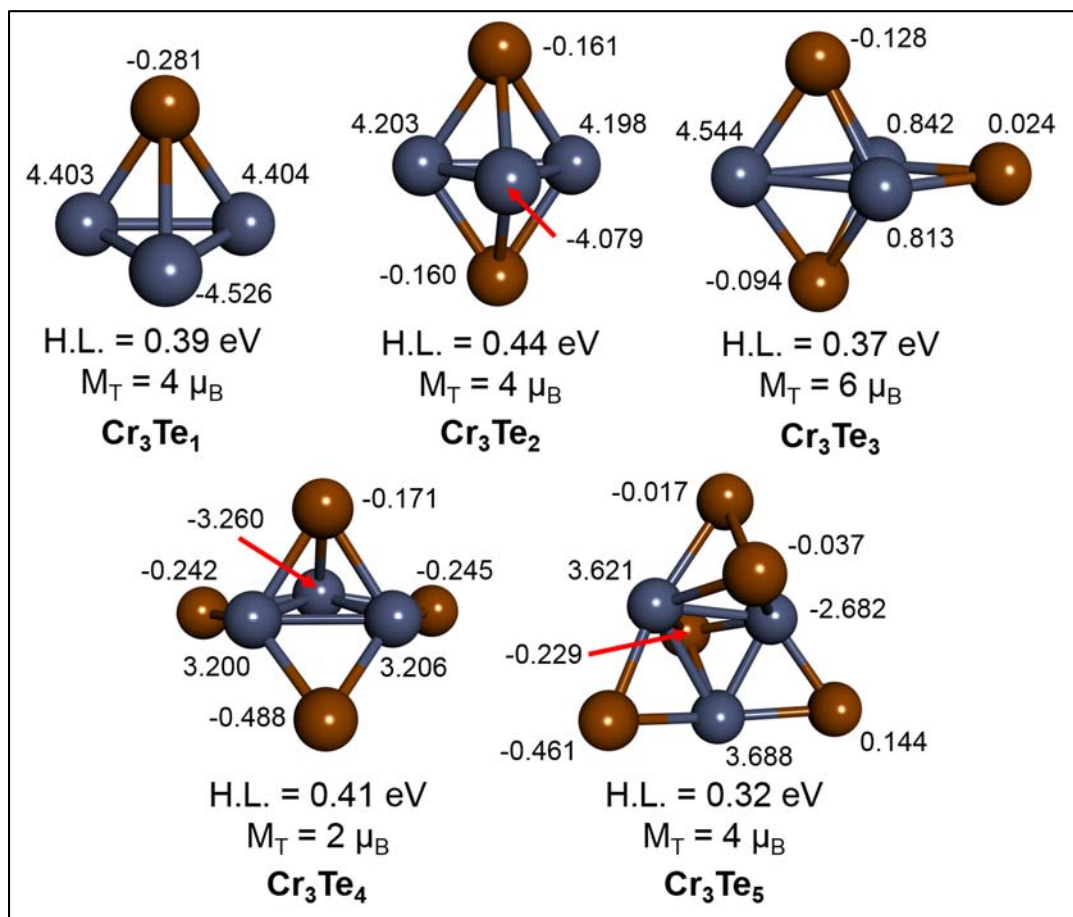


Figure 3-5. Groundstate structures of $\text{Cr}_3\text{Te}_{1-5}$.
With HOMO-LUMO gap, individual Mulliken Spin Density, and total magnetic moment, M_T . (Cr:Blue; Te:Beige)

Groundstate geometries for the chromium trimer series can be seen in **Figure 3-5**. All structures possess a quintuplet multiplicity, with the exceptions of Cr_3Te_3 ($M = 7$) and Cr_3Te_4 ($M = 3$). The central Cr_3 atoms remain in their isosceles formation throughout the series, with varying degrees of bond length, except for Cr_3Te_5 when all Cr atoms are stretched to their furthest positions. Each central trimer takes on the behavior of the pure Cr_3 structure, in that there remains one Cr with downward spin, excluding Cr_3Te_3 .

A single Te atom atop Cr_3 effectively takes the position of the fourth Cr atom of the pure Cr_4 geometry. It resides 2.594 Å away from the spin-up Cr atoms, but 2.903 Å from the Cr of downward spin. The Cr bond distances are 2.921 Å between the spin-up chromium, and 2.312 Å between spin-up and spin-down chromium. The spin density of the lone Te atom reaches -0.281. Addition of two Te atoms to Cr_3 stretches the metal bonds only slightly, ~ 0.05 Å for each bond. However, each Te atoms is mirrored by its partner, both are a distance of ~ 2.66 Å from the spin-up Cr atoms, but ~ 2.72 Å from the spin-down. The two Te atoms are effectively balancing their distances across of all bond lengths.

The geometry of Cr_3Te_3 can be best described as Cr_2Te_3 with a third Cr atom attached. In adding this Cr, only one Te atom remains with two-coordination. Moreover, the triangle formed by Cr_3 becomes highly irregular. The two Cr atoms which are bonded to the total number of tellurium, compress their bond distance to 1.821 Å. These two Cr bond to the third with distances of 2.839 Å, and 2.846 Å, respectively. The two-coordinated Te atom forms bond distances of ~ 2.54 Å, while the remaining two Te atoms bond within the range of 2.652 Å – 2.678 Å. The spin density analysis shows that the entire system is a ferromagnet, with the majority of spins located upon the least coordinated Cr atom.

The Cr_3Te_4 complex effectively rearranges itself to accommodate the increase in Te number. Only the Te atom forming the apex above Cr_3 forms three bonds, while the remaining three are two-coordinated on the edges. When compared to complexes of Cr_3Te_1 and Cr_3Te_2 , four Te atoms move the central Cr_3 complex closer to an equilateral triangle, with the least coordinated Cr atom forming the peak. This atom is 2.421 Å and 2.424 Å away from the remaining two Cr atoms, which are separated by a length of 2.829 Å. The Te atom bonded to both these Cr has spin-down density of 0.488, the maximum of all Te atoms across the Cr_3 series.

Further addition of Te produces a complex with a Te-Te bond, Cr_3Te_5 . The central Cr₃ has bonds of all different length, with the shortest located between the Cr atom that is spin-down and Cr atom that is least coordinated to Te, at 2.457 Å. Opposite this bond, between the spin-up Cr atoms, the length reaches 2.859 Å. The third is at length 2.604 Å. Once again, the lone two-coordinated Te atom bonded to two ferromagnetically coupled Cr atoms has the largest amount of spin density.

3.3.2.4 Cr_4Te_y ($y = 1 - 6$)

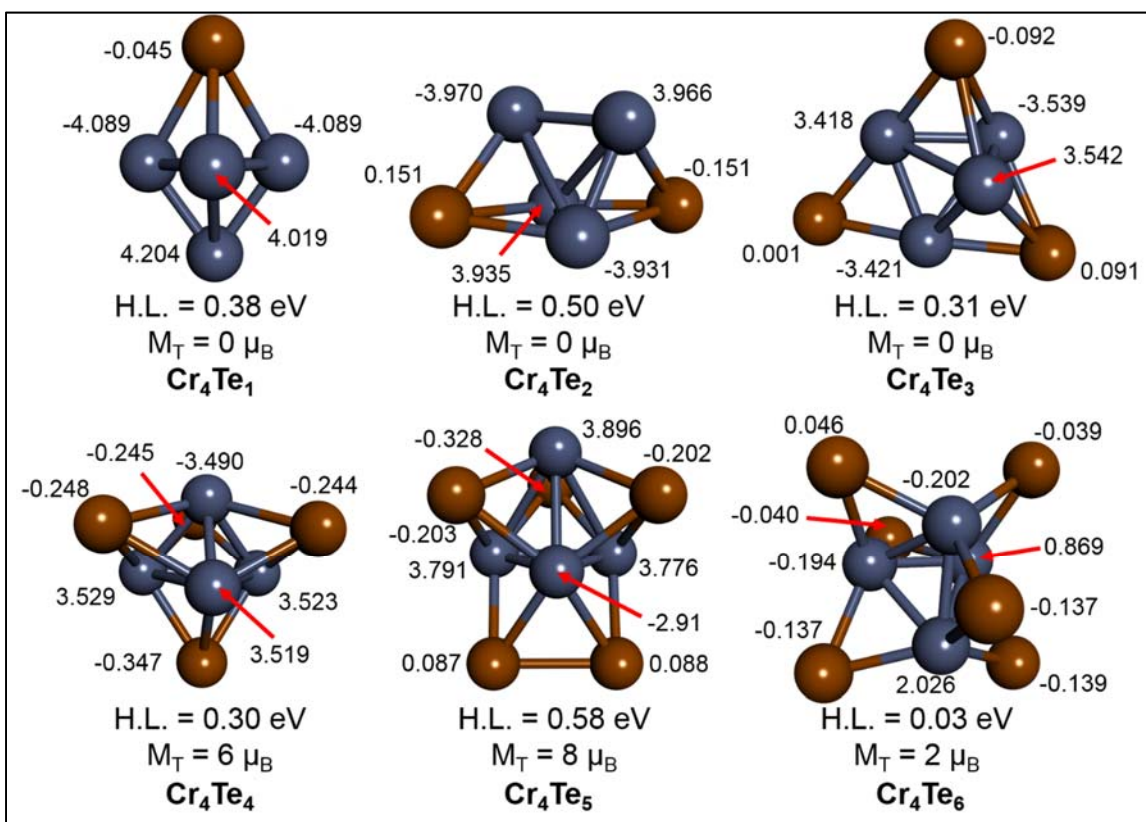


Figure 3-6. Groundstate structures of $\text{Cr}_4\text{Te}_{1-6}$.
With HOMO-LUMO gap, individual Mulliken Spin Density, and total magnetic moment, M_T . (Cr: Blue; Te: Beige)

Geometries for the Cr_4Te_y ($y = 1 - 6$) series are found in above in **Figure 3-6**. For Cr_4Te_1 , the first Te atom forms the second apex of the trigonal bipyramid, is bonded to both the spin-down Cr atoms at 2.74 Å, and forms the third bond at 2.640 Å. The system is in the singlet state. The pure Cr_4 geometry has a larger average bond length between Cr atoms, thus lending

evidence to the idea of Te absorbing charge and manipulating the underlying chromium.

Moreover, the local spin moments have diminished through the bonding of Te versus pure Cr₄.

In Cr₄Te₂ the two Te atoms are bonded in the furthest possible positions from one another, and heavily distorting the underlying Cr₄ pyramid. Despite only two Te atoms, the longest bonds between Cr atoms have reached lengths of ~3.01 Å, while the remainder fall in the range of 2.270 – 2.465 Å. The three-coordinated Te atoms bond onto their nearest Cr₃ triangle, and of the Cr atoms forming this triangle, only one is opposite in spin to the other two. The four Cr atoms are antiferromagnetically arranged, leaving the total cluster in the singlet state.

What is interesting to see, with regards to the spin moment localized on the Te atoms, as the cluster size grows the effect of the Te atom varies with this size, as well. This results in clusters that have Te atoms all in the spin down state, or a mixture of both up and down, depending on the total number and arrangement of those Te atoms. In Cr₄Te₂, we can see both Te atoms have the same amount of spin density, but in opposite directions. This continues into Cr₄Te₃, where the maximally coordinated Te atoms are equal and opposite, while the third possesses virtually no change in spin density.

The Cr₄Te₃ geometry, as stated above, two Te atoms that are maximally coordinated and a third which is doubly so. The three-coordinated Te atoms have bond distances within 2.650 – 2.716 Å, and the two-coordinated bonds are of length 2.575 Å, each. The addition of a third Te atom has diminished the effective spin moments on all Cr atoms, but the system remains in the singlet state. The overall geometry of the Cr₄ structure is now less distorted than that of Cr₄Te₂, but bond distances remain elongated, ranging between 2.238 – 2.748 Å.

The structure of Cr₄Te₄ marks the beginning of a rise in the total magnetic moment of the Cr₄ series. The triangle formed by the spin-up Cr atoms can be considered equilateral, with

distances 2.847 – 2.852 Å. The apex, spin-down, Cr atom bonds effectively equally, in the range 2.449 – 2.458 Å. Moreover, all Te atoms are now maximally coordinated, with the Te atom bonded to the spin-up Cr₃ triangle possessing the maximum amount of downward spin density. Contrary to Cr₄Te₂ and Cr₄Te₃, all Te atoms herein have spin-down (negative spin) density. Together, the Cr atoms are ferrimagnetic, producing a system in the septuplet state. What is interesting within this particular size of clusters is the Cr₄Te₄ groundstate, and up to the fifth highest isomer, is all Cr atoms form a tetrahedron with the Te atoms on the faces. The major difference between them are the bond lengths between the Cr atoms, creating isomers that are +0.08 eV, +0.16 eV, +0.38 eV, and +0.39 eV, with total magnetic moments of 0 μ_B, 8 μ_B, 2 μ_B, and 4 μ_B, respectively.

This magnetization further increases in the groundstate system of Cr₄Te₅. The fifth Te atom bonds to two Cr atom sites, and effectively moves the fourth into the same position opposite itself. Together, forming a Te-Te bond at 2.809 Å. This has had a negative effect upon the Cr-Cr bonds. The Cr₃ base triangle has two shortened bonds at ~2.35 Å, and although two Cr atoms have increased in spin density the third has fallen drastically and flipped downward, -2.91. The distortion of the system has increased the spin density, and changed the direction, of the apex Cr atom. As a result, the total system now has multiplicity of M = 9. The next geometry is 0.31 eV higher in energy, and in the septuplet state.

Following this, the Cr₄Te₆ cluster system now loses this high magnetization, and is in the triplet state. From the figure, we can see that there is little area remaining for the Te atoms, and for each to be separated from one another all must bond in the two-coordination on the edges of the Cr₄ pyramid. As a result, large amounts of charge transfer between Te and Cr cannot occur, leaving all atoms with a diminished localized spin moment. Moreover, the Cr-Cr bond distances

have contracted, into the range of 2.277 – 2.575 Å, with the largest bond distance between the spin-up Cr atoms. The next geometry is 0.38 eV higher in energy, in the quintuplet state.

3.3.2.5 Cr_5Te_y ($y = 1 - 7$)

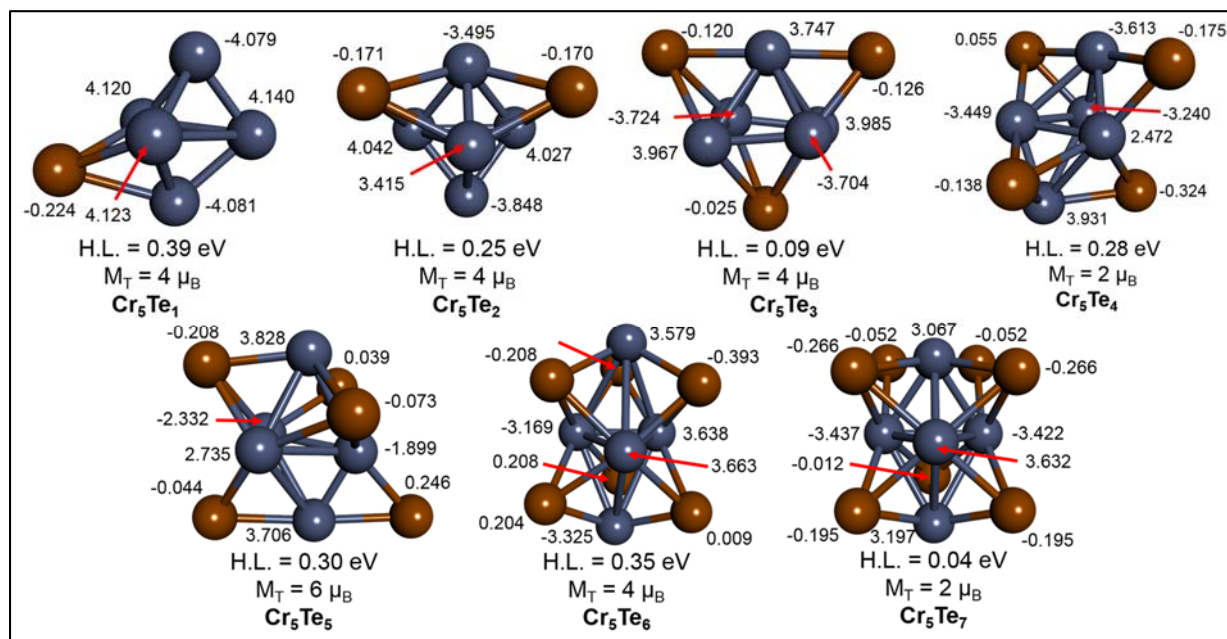


Figure 3-7. Groundstate structures of $\text{Cr}_5\text{Te}_{1-7}$.

With HOMO-LUMO gap, individual Mulliken Spin Density, and total magnetic moment, M_T . (Cr: Blue; Te: Beige)

Groundstates pertaining to the Cr_5Te_y ($y = 1 - 7$) series are shown in **Figure 3-7**. A glance over the entire figure shows the numerous contortions of the underlying Cr_5 structure. For most, this structure remains as a trigonal bipyramid with the exception of Cr_5Te_3 when it takes on the shape of tetragonal pyramid. Moreover, due to the larger number of bonding sites for Te, only within Cr_5Te_4 and Cr_5Te_5 does a two-coordinated Te atom appear. In all other geometries, Te atoms are three-coordinated, either with Cr, or both Cr and Te atoms. The Cr_5Te_5 cluster also has the highest multiplicity of the entire series, at $M = 7$.

The Cr_5Te geometry displays a similar behavior to the pure Cr_5 geometry, with three spin-up Cr atoms forming the center Cr_3 substructure and two spin-down Cr atoms bonded on the opposing faces. Albeit, these moments are lower than found in pure Cr_5 . The movement of spin

density toward the adatom of Te contracts all Cr-Cr bonds, bringing average bond length down from 2.611 Å to 2.52 Å, while the three bonds of Te are 2.656 Å, 2.654 Å, and 2.787 Å. What is most interesting, is the spin-up Cr atoms form a near perfect equilateral triangle, at 2.839 Å, 2.831 Å, and 2.843 Å, respectively.

The geometry of Cr_5Te_2 continues in the same manner as that of Cr_5Te_1 , maintain the quintuplet multiplicity, and with the average bond distances between Cr atoms contracting further, to 2.49 Å, while Cr-Te bond distances persist. Here, the central Cr_3 substructure containing the spin-up chromium, forms its own equilateral triangle, at 2.750 Å, 2.753 Å, and 2.780 Å, respectively. With the remaining Cr atoms bonding at the apex's in the range of 2.299 – 2.448 Å. Both Te atoms are now equal in spin density, and spin down. The spin density of the Cr atoms occurs in pairs, with the exception of the fifth Cr which has spin density valued near the average per chromium. Addition of three Te to Cr_5 subsequently breaks one of the Cr-Cr bonds, and produces a cluster whose center region is effectively open, and exposed. This is done by Te to obtain a coordination of three. Subsequently, Cr average bond distances are now enlarging, and equal that of Cr_5Te_1 . Moreover, the Cr_4 center effectively forms a rectangle that has been elongated in the direction of the apex bonded Te atoms. A feature producing two antiferromagnetically coupled dimers held together by an apex Cr, and equally spaced perimeter of Te.

The presence of four Te atoms produces a cluster geometry with one of the smallest multiplicities of the Cr_5 series, $M = 3$. In an effort to maintain their distance from one another, there are equal number of Te atoms in the two- and three-coordinated patterns. As a result, spin density uptake by the surrounding Te is uneven and incomplete. This then produces an arrangement where the Cr atoms involved in three-coordinated Te bonding elongate their

distance from the Cr atoms of the two-coordinated. The maximum of such elongation, between lower apex and equatorial Cr atoms, has a bond length of 2.972 Å. Additionally, between equatorial and upper apex Cr, the maximum bond is 2.836 Å.

The situation seen in Cr_5Te_4 reproduces itself within Cr_5Te_5 , but to the opposite effect. The system is in the septuplet multiplicity, with majority spin density contribution from the apex Cr atoms. The bonding pattern of the surrounding Te atoms now increases the number of three-coordinated atoms to four, with the fifth in a two-coordinated scheme. This increase in Te count now brings the average Cr-Cr bond distance to 2.64 Å. We can also see the spin density of individual Te are occurring in near antiferromagnetic pairings.

It is not until reaching Cr_5Te_6 in which all Te atoms bond in the three-coordinate scheme, occupying all the faces. This produces a central Cr_3 triangle with bond distances on average to those seen previously, but apex Cr bond distances in the range of 3.016 – 3.296 Å. These large bond distances further support the notion that the Cr-Cr interactions are managed through the bonded Te. Upon arriving at the structure for Cr_5Te_7 , in the triplet multiplicity, it can be seen that the additional Te atom must form its third bond with the neighboring Te. In doing so, breaks the symmetry of the cluster. Once completed, each Te atom, with the exception of one, has a partner with equal spin density. The redistribution of charge has now allowed the structure to compress along the z-axis, bringing the apex Cr atoms closer to the center. This results in an average Cr-Cr bond distance of 2.75 Å.

3.3.2.6 Cr_6Te_y ($y = 1 - 6$) & ($y = 7 - 8$)

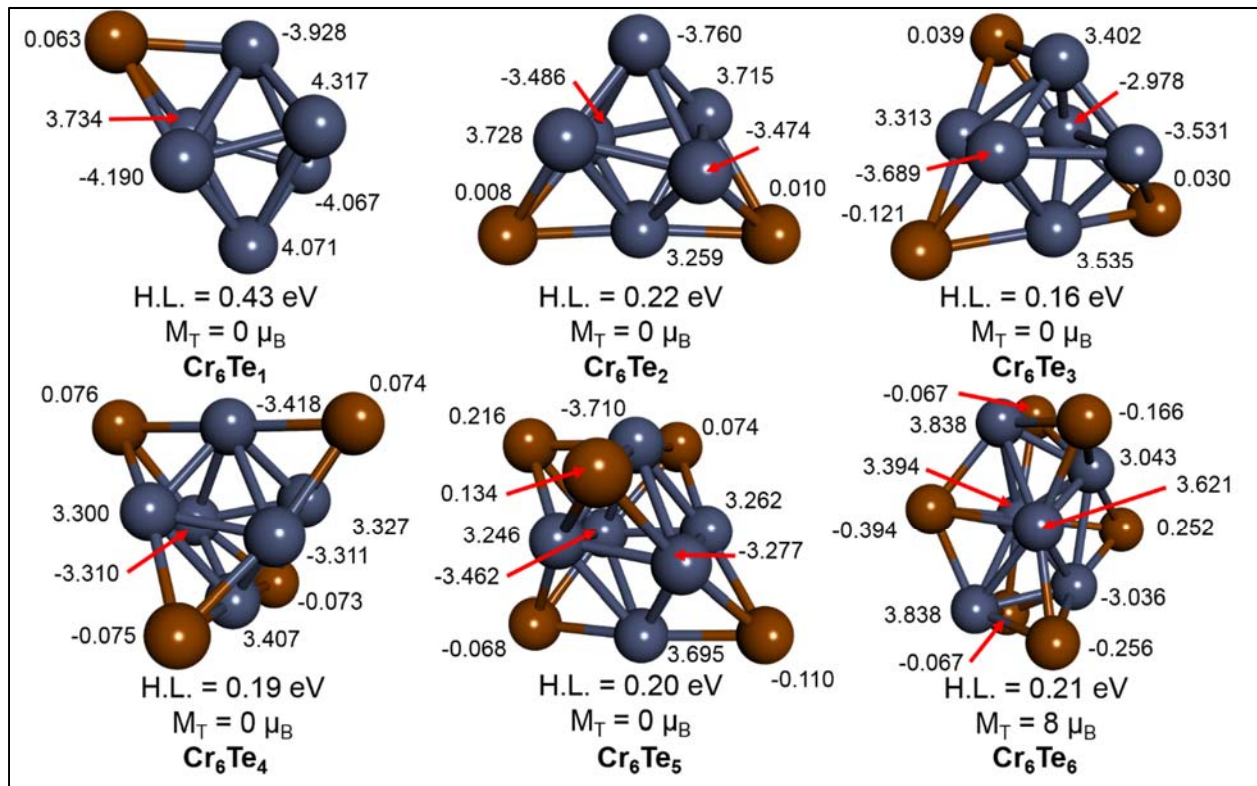


Figure 3-8. Groundstate structures of $\text{Cr}_6\text{Te}_{1-6}$.
With HOMO-LUMO gap, individual Mulliken Spin Density, and total magnetic moment, M_T . (Cr:Blue; Te:Beige)

The series of Cr_6Te_y , $y = 1 - 6$ above in **Figure 3-8**, takes on a similar tone with regards to structural deformation and spin density through the increase of Te atoms, as we have seen above in smaller geometries. The major difference here is the tetragonal bipyramid structure persists, resulting in antiferromagnetic clusters in the singlet state. The exception to this occurs in the system of Cr_6Te_6 , when the center Cr_4 subunit contracts and bonds. This then allows an increased number of Cr atoms to ferromagnetically couple, and produce a geometry with $M = 9$ multiplicity. The likelihood of such a geometry to maintain itself in this high magnetic state is very small, the next geometry is <0.14 eV higher in energy, is in the singlet state, and has the tetragonal bipyramid form.

It is easier to see within this series, that the Te atoms are sharing and balancing their effect upon the Cr structure. This can be seen plainly within the geometry of Cr_6Te_4 , in which all

spin densities are nearly equal and divided between spin-up and spin-down. Moreover, their overall effect is now maximized, as each Te atom is able to bond with its preferred bonding site on the face formed by three Cr atom, due to the fact that a compact geometry for Cr₆ is now less likely. The result, there is an alteration between odd and even numbered of Te atoms in the average bond lengths of Cr which continues into larger numbers of Te. However, after Cr₆Te₄ this average bond distance never falls again below 2.55 Å; Cr₆Te₄, 2.552 Å; Cr₆Te₅, 2.637 Å; Cr₆Te₆, 2.717 Å; Cr₆Te₇, 2.678 Å; Cr₆Te₈, 2.783 Å.

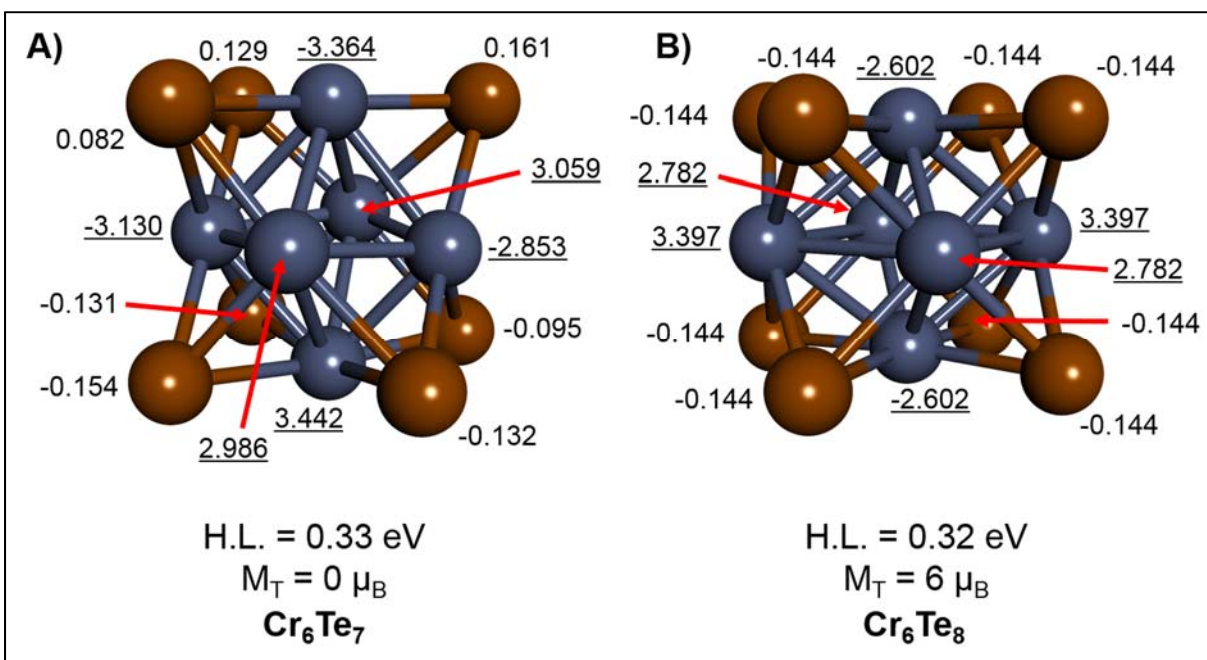


Figure 3-9. Groundstate structures of $\text{Cr}_6\text{Te}_{7,8}$.
 Te = 7 (A), 8 (B). With HOMO-LUMO gap, individual Mulliken Spin Density, and total magnetic moment, M_T . (Cr:Blue; Te:Beige)

Above in **Figure 3-9**, we find the structures for Cr_6Te_7 (**A**) and Cr_6Te_8 (**B**). We can clearly see that the necessity for the Cr₆ geometry to maintain its high multiplicity rests not only upon the distance between the individual Cr atoms, but also on a form of symmetry in the structure itself. The addition of another Te atom to Cr_6Te_7 rearranges the overall spin density, forming a Cr₆ structure comprised of four spin-up Cr atoms in the center, capped by two spin-

down Cr atoms in the apex positions. Moreover, the spin density of all Te atoms within Cr_6Te_8 are equal and in the spin-down configuration.

Higher energy isomers for Cr_6Te_7 begin at a difference of only 0.03 eV, and is in the quintuplet state. This very small distance between ground and first isomer highlights the ease in which the chromium complex can distort to remove any kind of electronic frustration from the overall system. The second isomer is 0.08 eV higher in energy (0.11 eV higher than ground), with triplet multiplicity. There is a marked increase in stability in the Cr_6Te_8 cluster due to the extra Te atom. The first isomer is 0.07 eV higher in energy, and in a higher magnetic state of $M = 9$. Again, due to the cooperative effects of all Te atoms balanced across the entire cluster, an even number in this arrangement would better restrict movement of the Cr atoms.

3.3.3 Summary

Upon closer examination of all geometries above, we can see that the behavior of pure chromium persists until a small number of Te are bonded. Moreover, this number changes depending on the size of the Cr cluster. With this now made obvious, the effect of said Te atoms can be varied to view a host of changes upon the underlying Cr complex. In pure chromium clusters, after complexation, to effectively reduce the distance between two Cr atoms back toward its free Cr_2 bond length, one must remove all electronic effects which drive the two atoms apart. This is rather difficult to do, and as the total number of Cr atoms increase, so do the number of d -orbitals and their degeneracies. Thus, introducing atoms of Te, the two incoming lone-pair orbitals in $5p^4$ covalently bond to Cr (d) and in doing so can effectively weaken, or remove, the local spin moment on the Cr atom. Such a scheme is made apparent within the Cr_2Te_3 cluster, and broken in the Cr_2Te_4 geometry. The modification of spin density and

bonding lead the rearrangement of an already weakly bound chromium atoms into vastly different geometric shapes, seen in the above.

As the number of chromium atoms increase, the role of tellurium changes as well. Not only does it continue withdrawing charge from Cr, but also begins to play a key role in stabilizing the overall structure. The removal of charge from Cr drives their bond distances upwards, and becomes reliant upon the nearby Te atoms to balance the overall structure. With that process complete, Cr can now take on different arrangements in spin. The sensitivity of the underlying Cr system to the decorated Te varies at all scales, and these overall properties are something we discuss in the next section.

3.4 Cr_xTe_y Series Properties

An overview of electronic properties for the entirety of the Cr_xTe_y series can be best summarized using **Figure 3-10**, and **Figure 3-11**. At first glance, we can immediately see special characteristics and traits in numerous Cr/Te combinations and sizes. Specifically, beginning with their total magnetic moments of **Figure 3-10 (A)**, moving left-to-right, that the overall magnetic moments mimic those of bare chromium clusters, in their alteration between high and no magnetization.^{166,169,194,195} However, this pattern is broken, and magnetization appears to even be enhanced, beginning with clusters comprised of equal, or greater, number chromium vs. tellurium atoms. The clusters of Cr₃Te₃, Cr₄Te₄, and Cr₅Te₅, each display a total magnetic moment, M_T, of 6 μ_B; as well as the Cr₆Te₈ cluster core of Cr₆Te₈(PEt₃)₆, discussed later. This moment continues to increase within the clusters of Cr₄Te₅ and Cr₆Te₆, whose M_T both equal 8 μ_B.

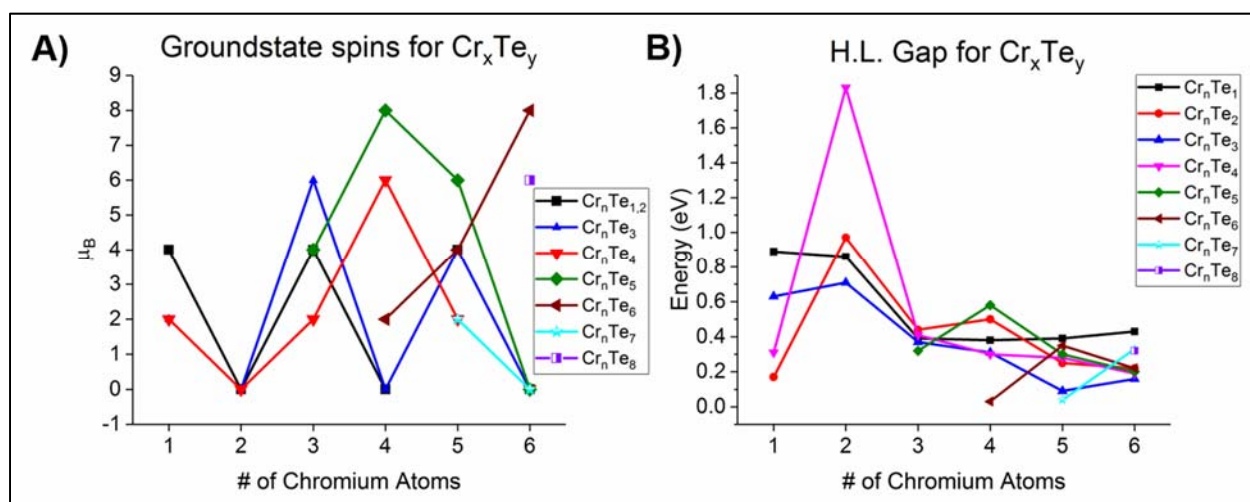


Figure 3-10. Basic properties of the Cr_xTe_y binary clusters.

(A) Total magnetic moments, and (B) Distance between Highest Occupied Molecular Orbital (HOMO) and Lowest Unoccupied Molecular Orbital (LUMO), i.e. the HOMO-LUMO Gap.

The large magnetic moments are expected within odd numbered chromium, as often with those of the even numbered the magnetic moments of individual chromium atoms are

antiferromagnetically couple to one another, yielding an overall moment of $0 \mu_B$. However, this scheme no longer holds within (44) or (66), something we shall discuss in Secs. 3.5.4 and 3.5.6. Another interesting discovery is that of the HOMO-LUMO gap energies for the Cr/Te series, shown in **Figure 3-10 (B)**. Specifically, for that of the chromium dimer which is enhanced from solitary chromium, when decorated with two or more atoms of tellurium.

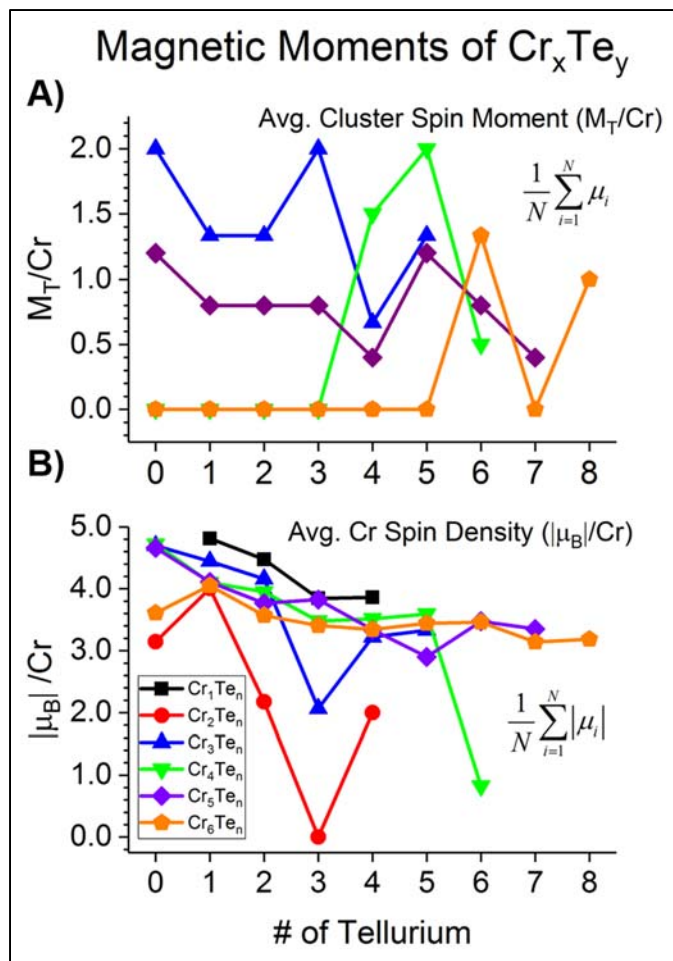


Figure 3-11. Magnetic moments for the Cr_xTe_y cluster series. Averages tabulated under two different schemes; Total cluster moment divided by number of Cr atoms (A), and summed absolute value of individual Cr atoms by different schemes. (Insets show equation used: N , total number of Cr; μ_i , local spin of the i^{th} Cr)

In an effort to link the results presented to those of previous theoretical and experimental investigations, magnetic moments are presented in two different forms within **Figure 3-11**.

Panel (A) highlights the total magnetic moment of a particular cluster, M_T , as divided over the total number of Cr atoms present. In (B), to fully understand the sequential addition of tellurium

upon the individual chromium atoms within a cluster, the same procedure of panel (A) is carried out using the absolute value of each individual Cr atom. Together, provide a better overall picture as to the electronic and magnetic behavior. Panel (A) highlights our discussion of the previous sections, in that major changes to the total magnetic moment are not likely to occur until there are equal or greater number of Te atoms when counted against the number of Cr, and similarly for the conservation, creation, or enhancement of any magnetic moment within a cluster. Within panel (B), each individual chromium appears to maintain a large magnetic moment, with the exception of a few cluster species; namely, Cr_2Te_3 , Cr_3Te_3 , and Cr_4Te_6 . Moreover, clusters with a very high magnetization are void of any symmetry and whose total magnetic moments are closely linked with arrangement of tellurium around chromium.

3.4.1 Hirshfeld Charge Density, Average Bond Distances, and “Malleability” of Chromium

The idea that individual tellurium decorates chromium and affects the underlying metal system can be further illustrated in **Figure 3-12**, below. Atop shows the effective average Hirshfeld Charge density change, for both chromium (black) and tellurium (red), within each cluster combination. Additionally, the bottom portion shows the average bond distances between chromium's and chromium-tellurium.

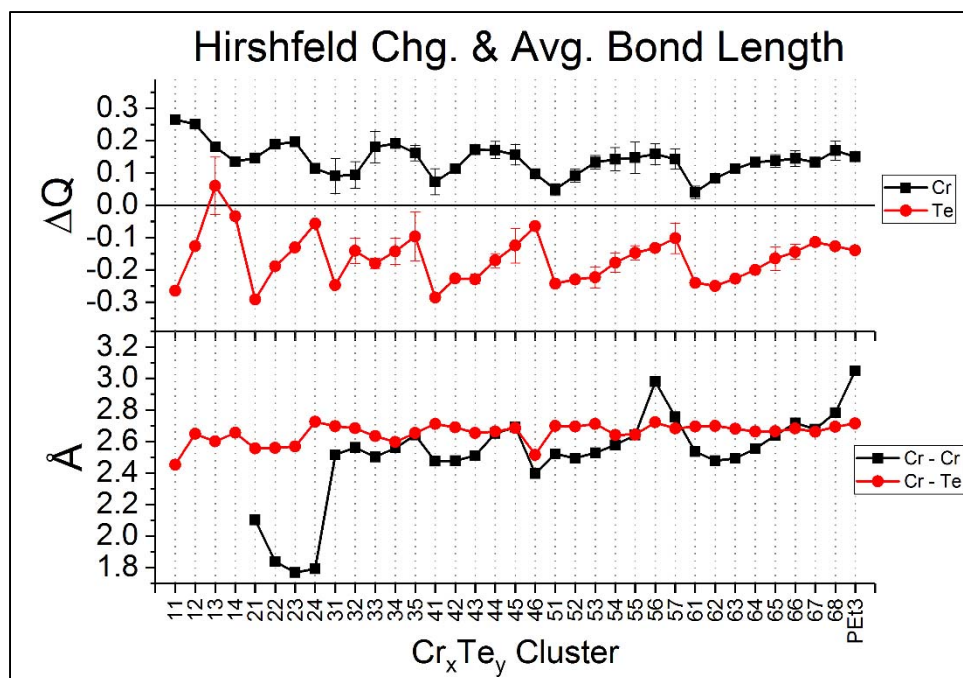


Figure 3-12. Hirshfeld Charge Deviation and Bond Distance Averages. Deviations for individual chromium and tellurium atoms (top), average Cr—Cr and Cr—Te distances (bottom); for $Cr_1Te_1 - Cr_6Te_8$, $Cr_6Te_8(PEt_3)_6$. (First number:x, Second:y)

We can see, in all clusters, that chromium is losing charge to tellurium, with the exception of $CrTe_3$. Specifically, the amount of charge density possessed by a free, solitary chromium atom is larger when compared to that amount found upon a chromium atom within its associated cluster complex. Thus, chromium bonded with tellurium results in a positive change to its Hirshfeld charge density; and, vice versa for tellurium. Additionally, and most notably, the effect of tellurium removing charge from chromium is balanced across all the tellurium present within the complex itself. This can readily be seen by choosing any number of chromium, and sequentially adding tellurium atoms. In doing so, produces a graph of the saw-tooth variety.

This charge balancing and movement has also a noticeable effect upon the bond distances within each cluster. Across the entire series, bond distances between Cr and Te deviated only minutely after Cr_3Te_x , with the exception of Cr_4Te_6 . However, this is the opposite case for Cr—Cr bond distances, and especially so when discussing $Cr_1Te_1 - Cr_2Te_4$. If we call from above,

from experimental studies, it has been proven that the Cr₂ dimer has an equilibrium bond length of ~1.678 Å.^{185,186} Additionally, and despite this close bond distance, Cr₂ has a dissociation energy of 0.72 eV/atom.¹⁹⁶

Previous experiments have shown Cr₂ to possess a potential energy surface with an unusual shape (see, for example, Figure 1 of *Bauschlicher*¹⁷¹), with a broad shoulder on its outerwall.¹⁸⁵ Subsequent calculations have proven that this outer wall portion corresponds to 4s orbitals bonding with the 3d electrons on each center; while the inner portion to be the region corresponding to 3d orbital bonding.^{170,187,197} The energy difference between these two regions is on the order of ~0.4 eV. Thus, one can expect that unless the 4s and 3d are both participating in a bond or bonding pattern, the distance between the chromium atoms will be significantly greater than 1.678 Å. It is precisely this scheme and mechanism behind the widely different properties, seen above, for the Cr₂Te_x series, which we shall discuss below, in Sec. 3.5.3. Similarly, due to the weak bonding nature inherent between chromium's, post the Cr₂Te_x series, this bond remains at the upper limit in the range of the chromium bond lengths and on some occasions, is driven even further due to the increased number of tellurium.

3.4.2 Removal Energies & Fragmentation Pathways

Alluding to our discussion of weakly bonding chromium, there is however an increase in stability of the overall cluster system due an increasing Te number, with the slight exception of the Cr₆Te_x series, readily seen in **Figure 3-13 (A)**. At first glance, the increasing Cr removal energies appears to occur in a regular fashion for clusters of Cr_n $n = 2 - 4$ clusters when compared to those of $n = 5$ & 6. Upon closer inspection, this is not the case for any number of Cr atoms. However, the most stable complexes are those with an even number of Cr. Specifically, Cr₂Te₃ & Cr₂Te₄, Cr₄Te₄ & Cr₄Te₅, and Cr₆Te_x ($x = 4 - 7$).

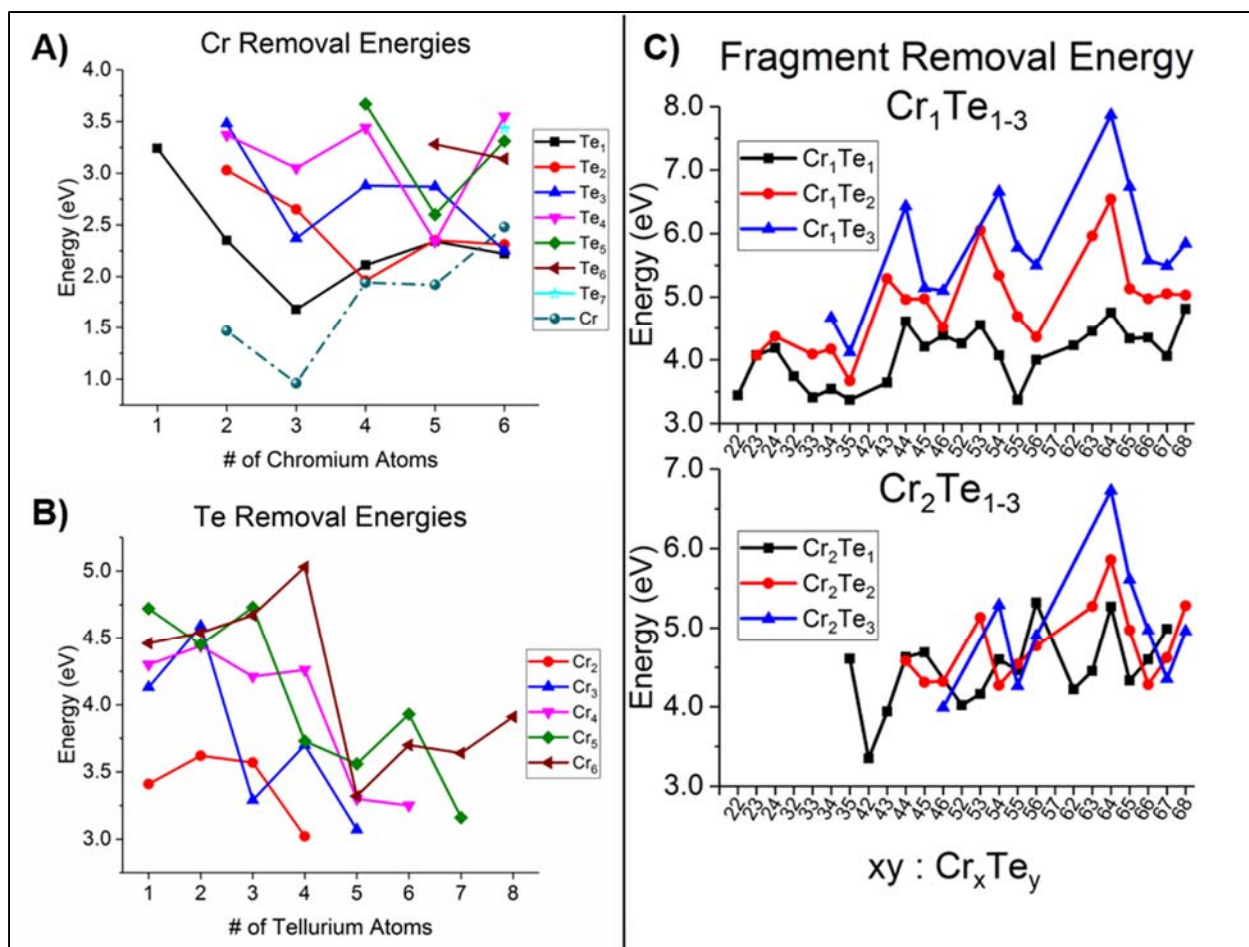


Figure 3-13. Removal Energies for solitary, and complexed, Chromium and Tellurium. Solitary chromium (A), and tellurium (B). Fragmentation energies of Cr/Te complexes at various sizes (C).

The bonding of one Te atom effectively smooths the graph of removal energy versus that of pure Cr, and raises this energy for all clusters with the exception of Cr₆Te. A second Te atom raises this bond energy within Cr₆Te, but not to the level of the pure case. Adding another Te has virtually no effect upon Cr₅Te, and actually reduces the effective bond energy for Cr₄Te₂ back to that of pure Cr₄. Increasing the number of Te atoms however does further stabilize Cr₂Te and Cr₃Te clusters by approximately 0.65 eV and 1.00 eV, respectively. Comparing this increased stability with the figure of average bond lengths, **Figure 3-12**, we can see that through sequential addition of Te to the Cr₂Te_x series, the Cr – Cr bond is becoming shorter and approaches approximately the same value for that of pure Cr₂. With the exception of Cr₃Te₃ and

Cr_6Te_3 , the presence of three Te atoms raises the stability of pure Cr clusters even further. Cr_3Te_2 is weakened, versus Cr_3Te_3 , through the addition of Te by ~ 0.28 eV. Continuing this process, the clusters of Cr_3Te_y , Cr_6Te_y all reach a maximum in their respective series when $y = 4$. While within Cr_4Te_y , for $y = 4$, this cluster reaches nearly 3.50 eV in removal energy, and then proceeds to increase that number for $y = 5$.

Of course, the increase in decoration of bare chromium with tellurium does raise its overall stability. However, this stability is only maximized when each Cr series reaches a certain number of Te atoms. Moreover, in achieving this stability, across the entire series of Cr_xTe_y , there is first a point within each cluster where its overall stability falls before increasing again. For example, the Cr_2 series reaches a maximum at Cr_2Te_3 , which is then diminished through addition of another Te atom. Similarly, in the Cr_3 series as mentioned above, and Cr_3Te_3 is less stable than Cr_3Te_2 . But, neither are as stable when compared to Cr_3Te_4 . Within Cr_4 , its stability immediately begins an upward increase after Cr_4Te_2 .

This sequence becomes obvious when discussing Cr_5Te_y and Cr_6Te_y . For Cr_5Te_y , there is virtually no change in energy between $y = 1 - 2, 4$. However, a spike in stability appears for $y = 3$, and removal energy continues upwards for $y = 5, 6$. In the Cr_6Te_y case, after $y = 1$, energy remains at approximately 2.30 eV. Not until $y = 4$, when this series reaches its maximum, does the Cr_6 series raise this energy into the region of 3.00 – 3.50 eV, for $y = 4 - 7$. Moreover, within both of these Cr_6Te_y subseries, the apparent rise-and-fall of the energy value occurs within each of them, thus effectively twice for the entire Cr_6Te_y series. We can see from the figure, for $y = 1 - 3$, Cr_6Te_2 is a maximum, and again within $y = 4 - 7$, Cr_6Te_4 is the dominant species. From careful analysis of Cr removal energies, it can be readily deduced that there is a delicate balance between the number of Cr and Te atoms. Thus, in sequentially adding Te, it has been found that

there is what can effectively be called a tipping point in stabilization within each of the pure Cr series.

In turning our attention to the Te removal energies of **Figure 3-13 (B)**, there is additional evidence highlighting the delicate stability within these clusters. What can immediately be seen is the scale of the graph itself, where all Te removal energies are above 3.0 eV. Moreover, the effective reduction of the Te removal energy within all clusters falls below 4.0 eV upon reaching $y = 5$. Most importantly, for many chromium sizes, after a certain number of tellurium have been added, their removal energies become lower than that for removing solitary tellurium from pure chromium clusters.

The sequence of events upon how these clusters all diminish below these thresholds occurs differently depending upon the exact number of Cr present. For Cr_2 , Te removal energy peaks at Cr_2Te_2 and then falls for subsequent Te, but always remains within the window of 3.10 – 3.60 eV. This almost gentle illustration is again seen of the Cr_4 series, but is not maintained across the entire series. For $y = 1 - 4$, energies remain in the region of approximately 4.25 eV. However, upon addition of five tellurium's, this binding energy falls nearly an entire electron-volt downward to ~ 3.30 eV. The drastic alteration of Te binding energy seen in the Cr_4 series marks only the beginning. Within the cluster series of Cr_3 and Cr_5 , stability of tellurium removal rises and falls on two occasions. For Cr_3 , stability is maximized with two and six Te atoms. While for Cr_5 , that number is three and six tellurium. The largest of tellurium removal energy occurs for C_6Te_4 . Within this cluster, each tellurium forms three bonds upon one of the Cr_6 octahedron faces, in a staggered configuration.

These wildly varying binding energies, and across various numbers of tellurium, can be explained as a matter of the underlying geometry of the Cr atoms. Depending on that geometry,

the cluster can only accommodate a fixed number of Te on its surface. This is further made true due to the inherent behavior of Te to first form two bonds, using its two lone-pair orbitals, and in the case of Cr clusters, often followed by yet another bond, into three-coordination.

Additionally, the apparent balancing across all Te atoms present in the charge removal from the central Cr cluster results in CrTe mixed clusters groundstates with Te atoms that are as far away from one another as possible. Exceptions to this are the clusters of Cr_2Te_2 , Cr_5Te_2 , and Cr_6Te_2 , where electronic effects of the Cr cluster dictate that the second Te atom be bonded nearby to the first. We shall see below, clusters decorated with Te atoms that are two-coordinated, three-coordinated, as well as those with a mixture of both.

Continuing along these lines of cluster stability, we turn our attention to the fragment removal energies of **Figure 3-13 (C)**. Here, it can be seen the various possible avenues for a particular cluster to dissociate into two smaller complexes. In comparing upper and lower panels, a particular cluster is more likely to lose Te atoms when Te is also accompanied by a single Cr, shown in the upper panel (black line). With this in mind, the most stable clusters are those that possess the most aligned graph peaks. Specifically, the clusters of Cr_4Te_4 and Cr_6Te_4 . And, when looking to the discussion above with regards to individual atomization, are the two clusters which have the highest removal energies. In Cr_4Te_4 , the Cr atoms are bonded in a compacted pyramid structure, with each Te atom forming three bonds on the faces, effectively protecting Cr_4 from dissociation.

3.4.3 Summary

Across all of the macroscopic properties discussed thus far for small clusters of CrTe, it has been shown that stability and magnetic properties are highly dependent on both numbers of atoms. Moreover, as we shall see below, these properties are closely linked and can be modified,

or supported, through their individual arrangements. The overall effect of introducing Te atoms onto pure Cr clusters is this, the Te pulls and modifies the nearby charge distribution of chromium by specifically bonding to the *d*-orbitals. As a result, it drives the expansion of the bond distance of those involved chromium's. This then allows the individual Cr atoms to maintain their large spin density, and produces binary clusters with higher overall magnetization than their pure cluster variants. What we shall see below, is this effect produced by additional tellurium has a very large and noticeable effect on the smaller clusters of chromium. This charge modification performed by tellurium continues upwards into the larger clusters, and further solidifies itself as both a key structural and electrical component.

3.5 Cr_xTe_y Electronic Properties

3.5.1 Overview

The above results outlined the modification of chromium clusters through sequential addition of tellurium atoms. Moreover, until a cluster is decorated with a larger number of tellurium only minute effects will be witnessed. In witnessing such effects, we can directly view the contribution to the total magnetic moment through the alteration of each Cr atom, individually. Additionally, within each atom, we can view the change to the individual spin moment through the contributions and changes within each orbital. We do this by graphing the spin density of each cluster, with respect to each chromium, as calculated using Mulliken Population Analysis (MPA). Although MPA may not be the most suitable method for population analysis, it does serve as a very useful tool in ascertaining any changes and deviations from the ideal representation of the orbitals in question. And, because of our strict use of QZ4P in the search for groundstate geometries, we can be assured that the representation below captures any and all information, due to MPAs high dependence on the Basis Set. Because of such a large Basis Set is used throughout these calculations, it is expected that results obtained using other methods of population analysis based on the electronic density, namely that of Natural Population Analysis (NPA), should not deviate too far from those presented.^{198–204}

For the graphs below, each chromium population has been normalized to valence. That is, in this representation, the sum of alpha and beta spin populations reaches a maximum of six electrons, representing the 4s¹3d⁵ orbitals. With the 3p⁶ orbitals of chromium taken to be part of the core electrons, any deviation from these maximums in the population density will be readily noticeable and traceable.

3.5.2 Cr₁Te_y (y= 1 – 4)

The Mulliken populations for the Cr₁Te₁₋₄ series are shown below in **Figure 3-14**. What can be seen immediately is the slow decline and leveling of the alpha spin channel and slow increase in the beta spin, of Cr (d). Additionally, the slow decline of Cr (s) and increase in the hybridization of Cr (p). The decline of population in Cr (s) can be attributed to its increased use in hybridization when the lone Cr atom is accommodating additional Te atoms. What is also evident, is the persistence of the Cr (d) orbital. This is due to the fact that, although tellurium does pull charge from chromium, it cannot do so alone. To that effect, the increase in beta channel population only manifests itself when there are four Te atoms present, creating a total of four Cr-Te bonds.

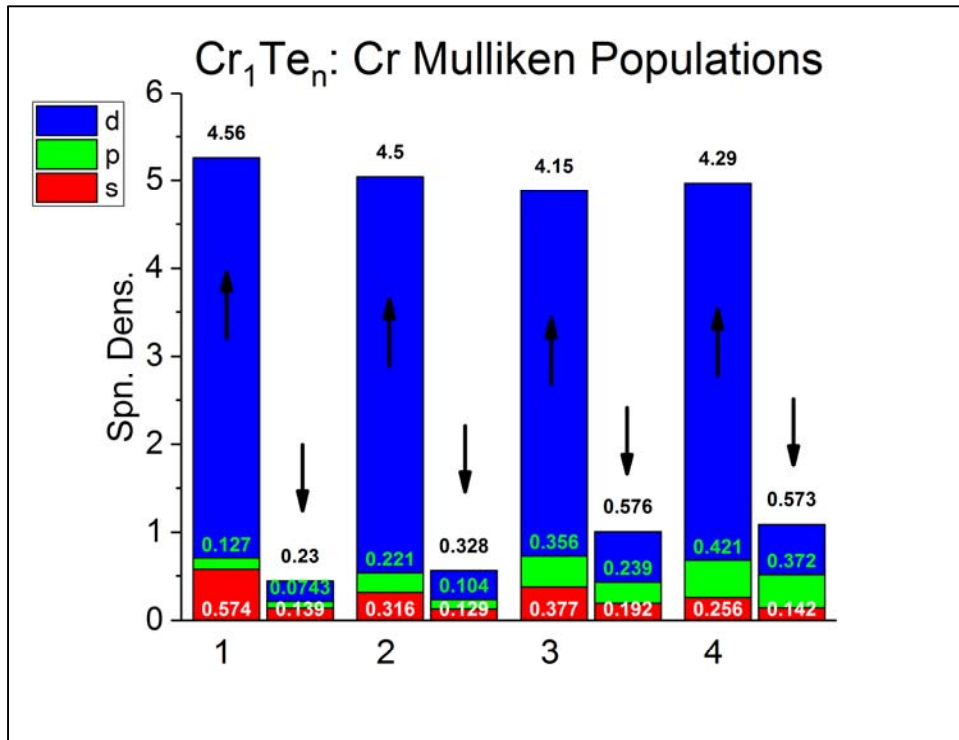


Figure 3-14. Mulliken spin populations for Cr₁Te₁₋₄.
(For each n; Arrows mark direction of both spin channels for each Cr atom.)

Furthermore, the atomic orbital level diagrams for the Cr₁ series can be found in **Figure 3-15**. Within it, we can see the splitting of the Cr (d) levels to varying degrees and across all

sizes. The HOMO level of Cr_1Te_1 is formed by a degenerate, half-empty, Te (p) orbital, and is the reason for the overlap of HOMO and LUMO levels. The Cr (d) levels of HOMO-1 through HOMO-3 form bonds directly with two of the remaining Te (p) orbitals. A similar situation arises within the Cr_1Te_2 cluster, where the second Te atom splits the Cr (d) orbitals even further, and bonds to both Cr and Te. Subsequent addition of three Te atoms continues to drive downward the total number of Te (p) orbitals in both the alpha and beta spin channels. The central Cr atom is now flanked by a Te dimer on one side, and a lone Te on the other. The fourth Te atom effectively forms a bond with its neighbor Te and the central Cr, and whose orbitals are subsequently pushed further downward and increases the hybridization of the Cr atom.

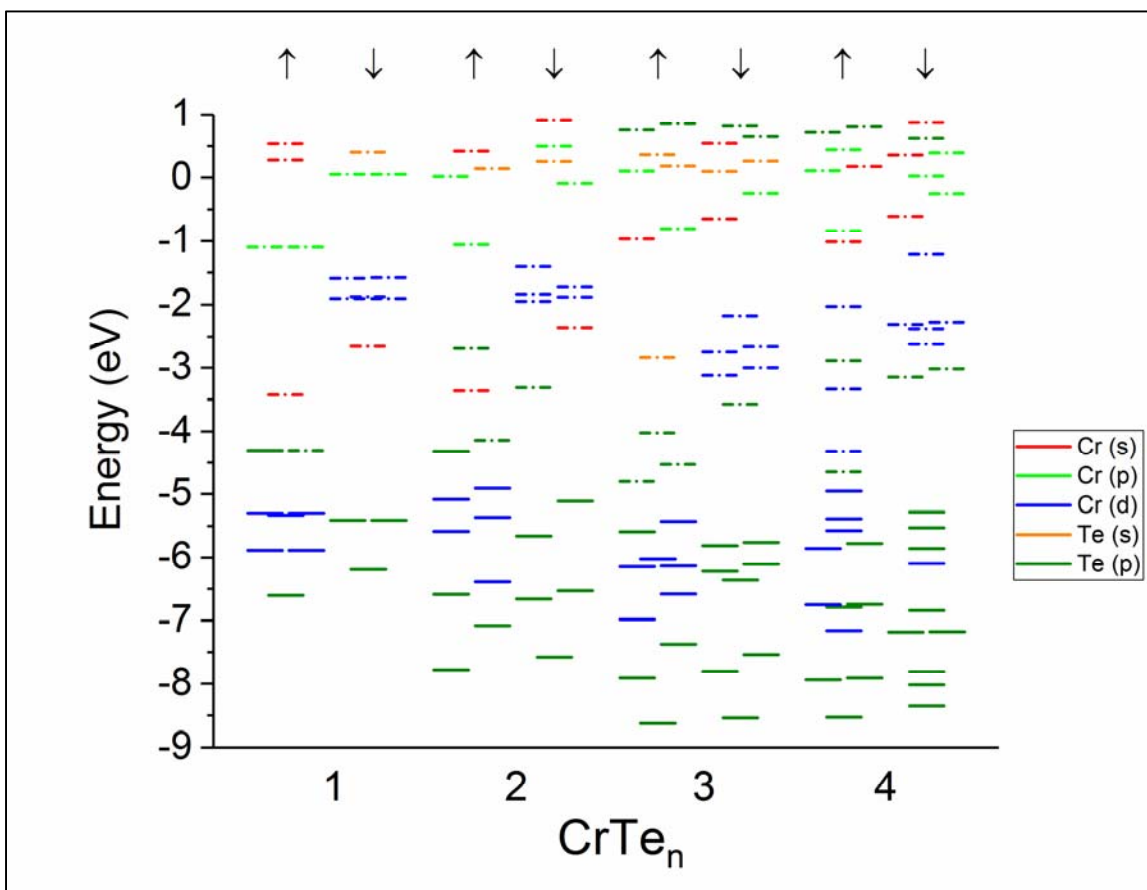


Figure 3-15. Level diagrams for CrTe_n , $n = 1 - 4$. Spin-up and Spin-down channels labelled with associated arrows

The atomic orbitals for CrTe₃ and CrTe₄ are further elaborated upon in **Figure 3-16** and **Figure 3-17**, respectively, as well as plots for their density of states (DOS) in **Figure 3-18**. Within both figures are the levels diagrams found within **Figure 3-15**, but now contain diagrams of the associated molecular orbitals (MO) for a selection of levels. Within **Figure 3-16** we can see that Te does not form the requisite number of bonds to fully quench the Cr atom, the HOMO-5 level is comprised solely of Cr d_{z^2} . Bonds around the HOMO level and comprised of Te (p) and Cr (d) are antibonding. This continues within the structure of CrTe₄, in **Figure 3-17**. For HOMO through HOMO-3, Cr (d) and Te (p) in the alpha spin channel are antibonding, while Te (p) in the beta channel are driven further downward in energy.

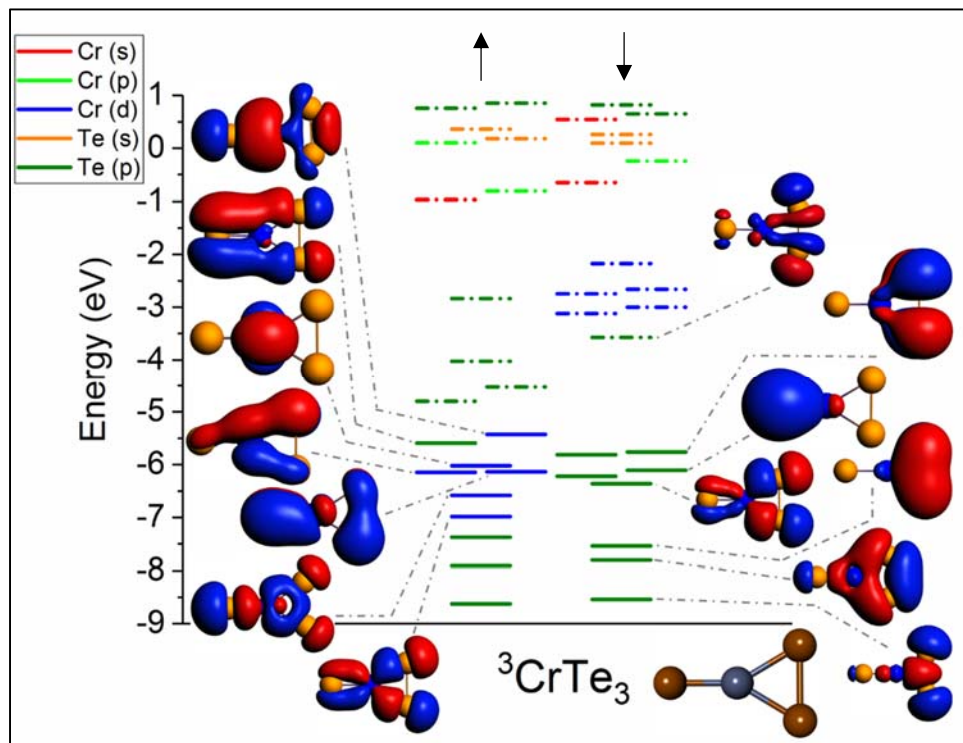


Figure 3-16. ³CrTe₃ Atomic Orbital (AO) level diagram. Left column represents spin-up (alpha) channel. Right; spin-down (beta).

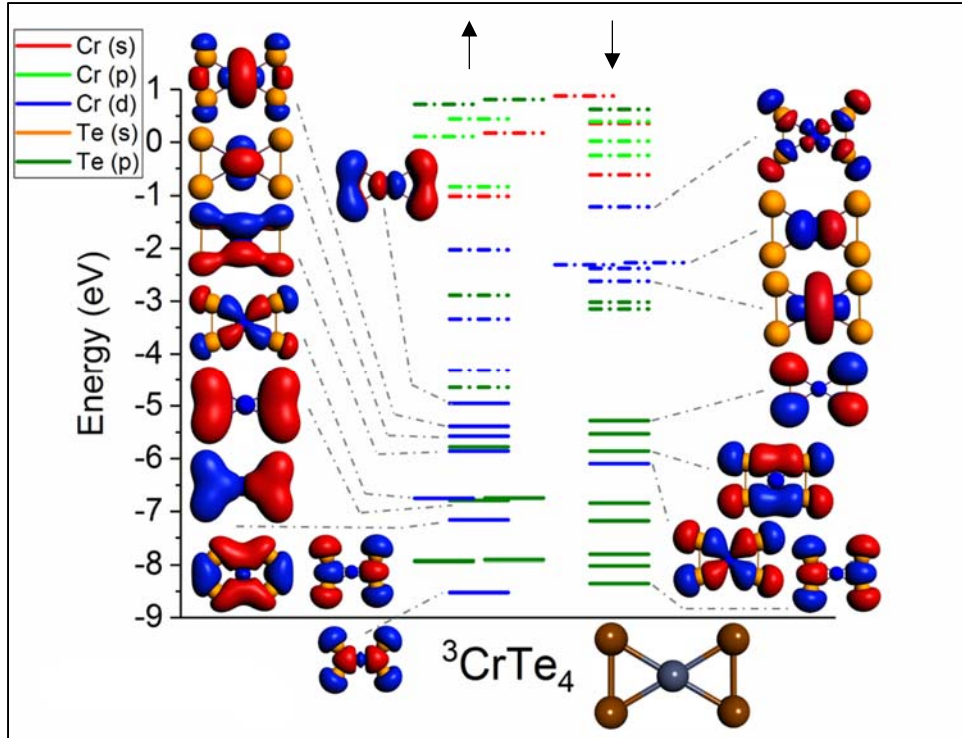


Figure 3-17. ${}^3\text{CrTe}_4$ Atomic Orbital (AO) level diagram. Left column represents spin-up (alpha) channel. Right; spin-down (beta).

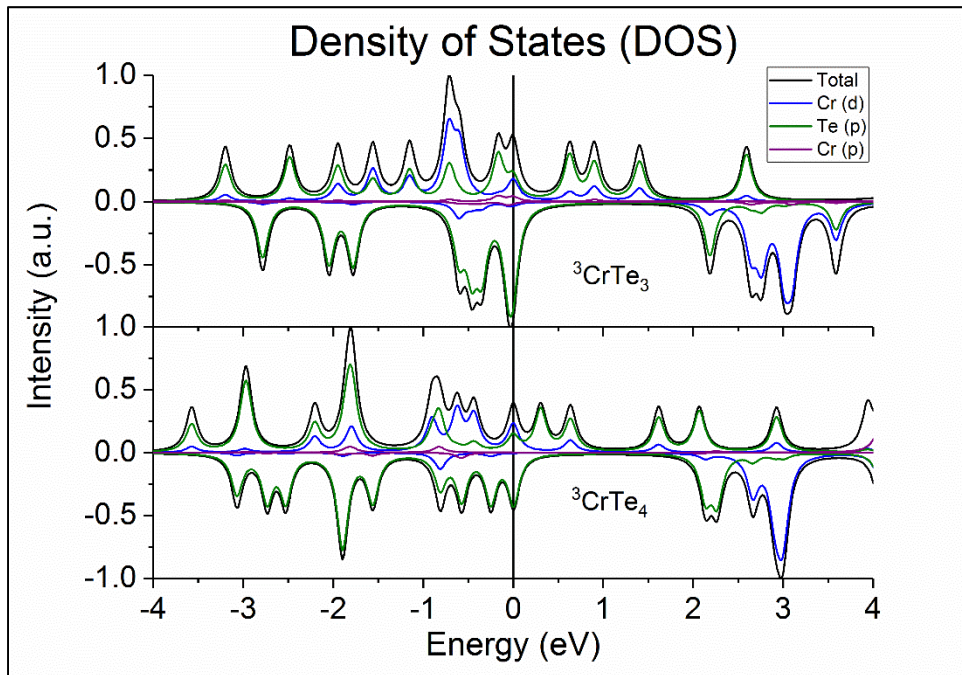


Figure 3-18. Density of States (DOS) for $\text{Cr}_1\text{Te}_{3,4}$.

3.5.3 Cr_2Te_y ($y = 1 - 4$)

The Mulliken spin populations for the Cr_2 series is shown in **Figure 3-19**. Here we can watch a drastic change occur to the central Cr_2 dimer with increasing number of Te atoms. Within Cr_2Te , we know from previously that the bond is stretched beyond equilibrium, thus the increase in spin density for each Cr atoms alpha and beta channel, respectively. Moreover, there is still a quite sizeable amount of Cr (s) remaining on each atom, and virtually no Cr (p) involvement. The second Te atom bonds to Cr (d), driving both populations slightly downward, as well as those of Cr (s). It is the third Te atom which fully quenches the total spin density of Cr_2Te_3 . The central Cr_2 forms a total of two bonds between each Cr atom, while the remaining orbitals bond directly to the incoming Te (p) lone-pairs or are now diffused over the surface of the cluster. In adding the fourth Te atom, the spin density on both chromium atoms reemerges. The Cr_2 dimer now forms three bonds between the two chromium atoms, leaving the incoming Te (p) orbitals bond and hybridize with the remaining orbitals and opening the HOMO-LUMO gap.

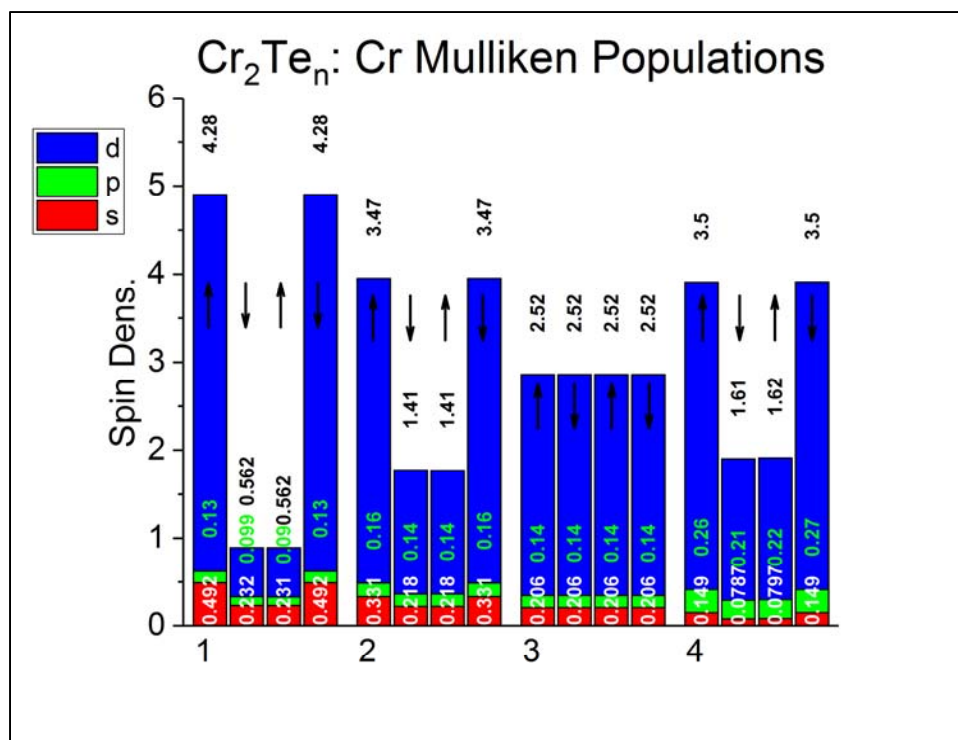


Figure 3-19. Mulliken spin populations for Cr₂Te₁₋₄.
(For each n; Arrows mark direction of both spin channels for each Cr atom.)

All of the charge movement and bonding within the Cr₂Te₃ and Cr₂Te₄ cluster systems can be seen in the level and molecular orbital diagrams, as well as the density of states found in **Figure 3-20** through **Figure 3-23**, we can see the HOMO for Cr₂Te₃ is highly delocalized and primarily comprised of Te lone-pair orbitals. Additionally, many orbitals are antibonding in nature, for both Cr₂Te₃ and Cr₂Te₄. This is made clear in **Figure 3-21**, in which orbitals as far down as 1 eV below the HOMO are antibonding, and between Cr (d) and Te (p) orbitals specifically. This is confirmed in the plot of the Overlap Population Density of States (OPDOS), seen in **Figure 3-23**.

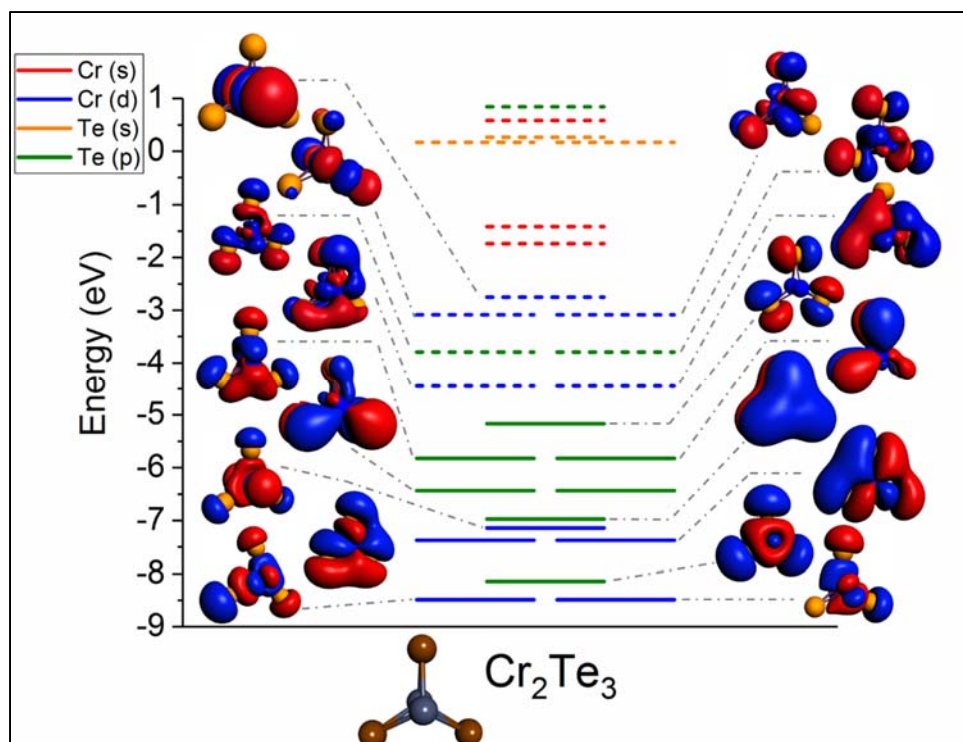


Figure 3-20. ${}^1\text{Cr}_2\text{Te}_3$ Atomic Orbital (AO) level diagram.

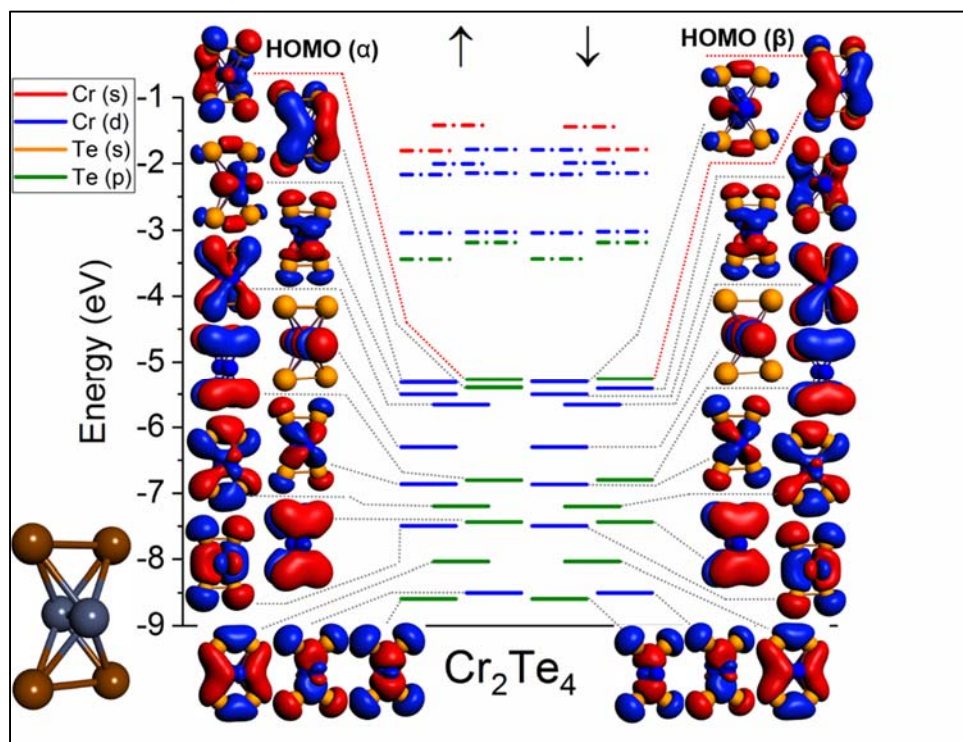


Figure 3-21. ${}^1\text{Cr}_2\text{Te}_4$ Atomic Orbital (AO) level diagram. Left column represents spin-up (alpha) channel. Right; spin-down (beta).

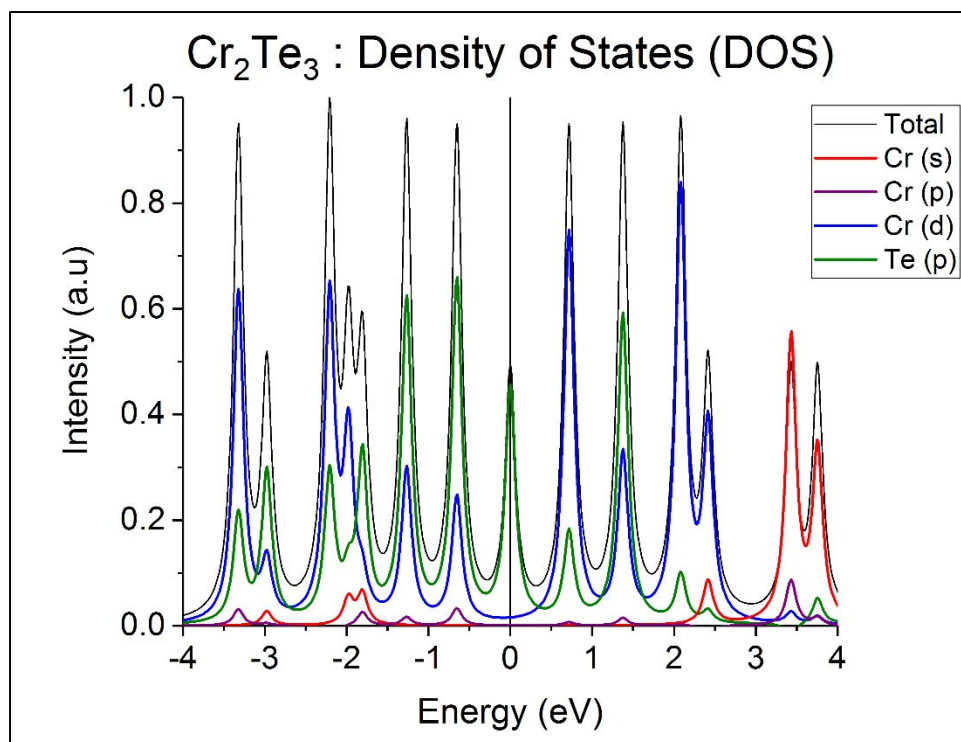


Figure 3-22. Density of States for Cr_2Te_3 .

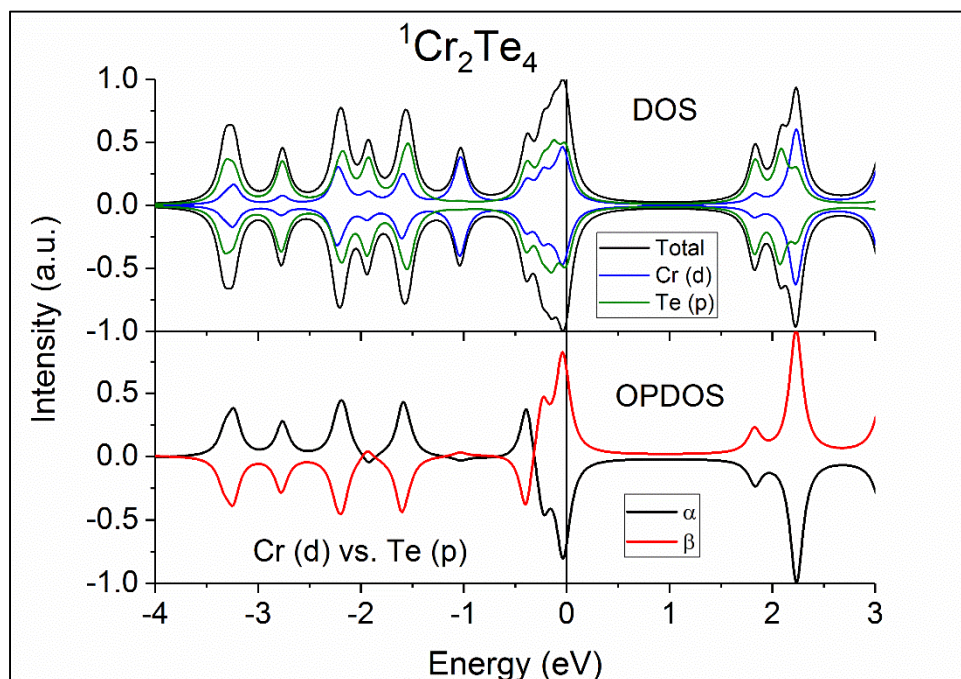


Figure 3-23. Density of States (DOS), and OPDOS for $^1\text{Cr}_2\text{Te}_4$.

(OPDOS: Overlap Population Density of States. Positive indicates bonding; Negative: antibonding. Beta inverted for clarity.)

3.5.4 Cr₃Te_y (y = 1 – 5)

In turning our attention to the Cr₃ series, the Mulliken populations are shown in **Figure 3-24**. The Cr₃ series marks the first that experiences fluctuations in the Cr-Cr bond distance due to excess Te atoms, but fluctuations that do not vary wildly as compared to the later Cr series. Sequential addition of Te atoms does not modify greatly the amount Cr (d) spin density, with the exception of Cr₃Te₃, until reaching Cr₃Te₅. The modification of the Cr (p) orbitals slowly increase through successive addition of Te, while the Cr (s) contribution decreases substantially.

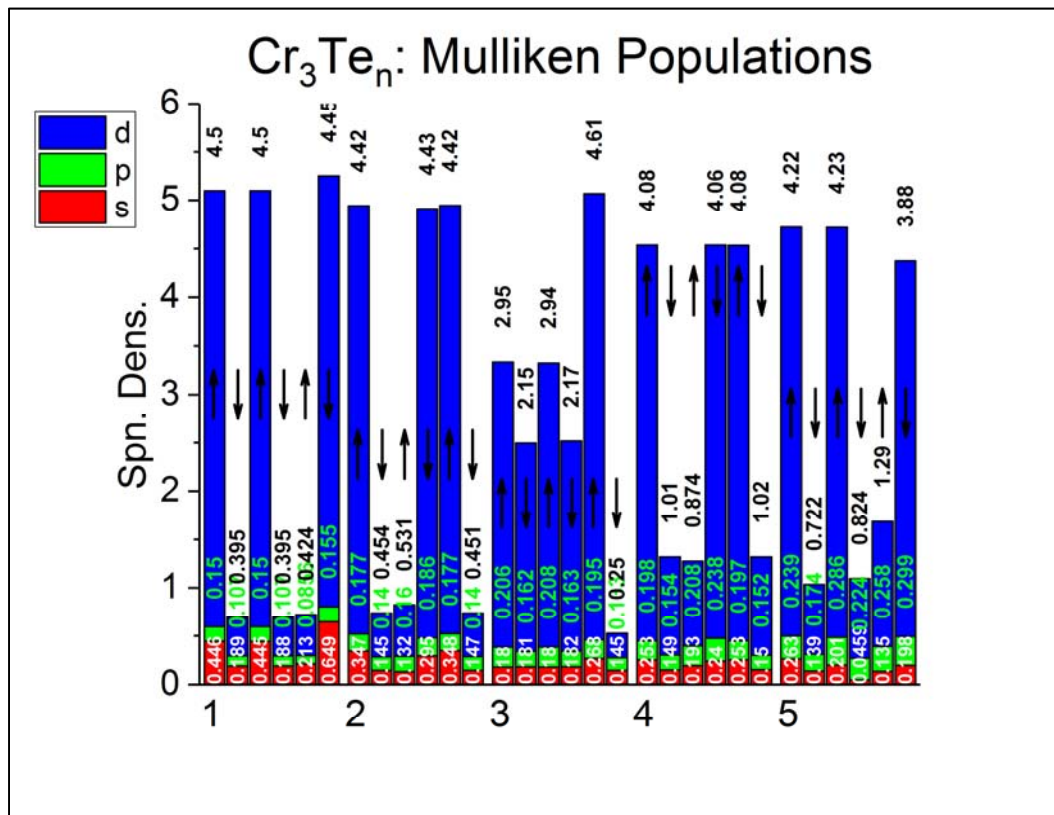


Figure 3-24. Mulliken spin populations for Cr₃Te₁₋₅.
(For each n; Arrows mark direction of both spin channels for each Cr atom.)

The total magnetic moment reaches a maximum in the cluster of Cr₃Te₃, which has the majority of its spin localized on the third Cr atom, seen in **Figure 3-24**. This structure is closely linked with that of Cr₂Te₃, where the third Cr atom bonds within one of that clusters open

regions. The third Cr atom introduces a change in the bonding pattern, away from the perfectly quenched Cr_2Te_3 , and into a structure where all Cr atoms are spin-up.

Comparing the level diagram of Cr_2Te_3 in **Figure 3-20**, with that of Cr_3Te_3 in **Figure 3-25**, we can see that the alpha channel of Cr_3Te_3 is becomes densely more populated due to the additional Cr (d) states, combined with a significant amount of shifting in the *s* and *p* levels.

This addition and shifting can also be seen in the Density of States, between **Figure 3-22** and **Figure 3-26**. Of the Cr_2Te_3 cluster, the region around the HOMO level is devoid of Cr (d) states, contrary to the HOMO region of Cr_3Te_3 . This region within Cr_3Te_3 is also antibonding in nature, and has expanded into the range of 1.5 eV below the HOMO level, as seen in the OPDOS of **Figure 3-26**, indicating very weak bonds.

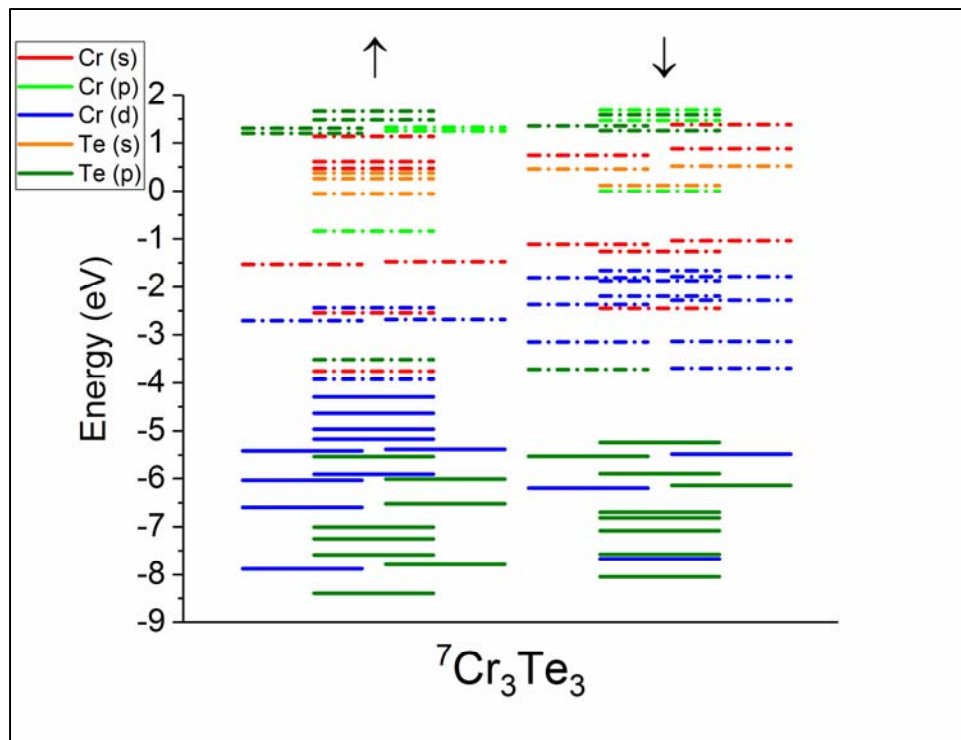


Figure 3-25. ${}^7\text{Cr}_3\text{Te}_3$ Atomic Orbital (AO) level diagram. Left column represents spin-up (alpha) channel. Right; spin-down (beta).

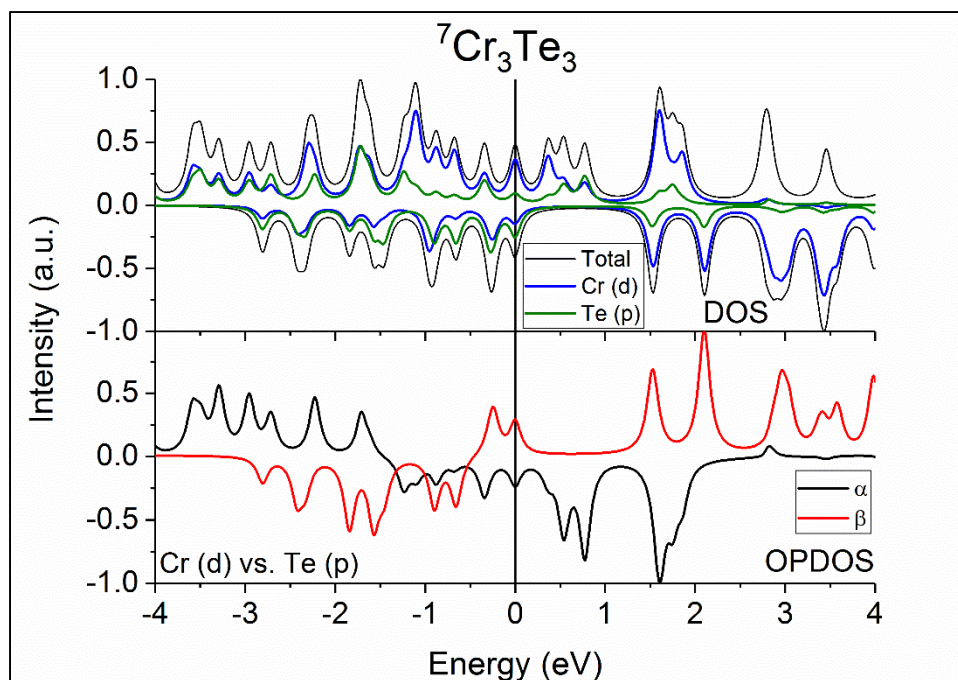


Figure 3-26. Density of States (DOS) & OPDOS for ${}^7\text{Cr}_3\text{Te}_3$.
(OPDOS: Overlap Population Density of States. Positive indicates bonding; Negative: antibonding. Beta inverted for clarity.)

3.5.5 Cr_4Te_y ($y = 1 - 6$)

As our chromium cluster grows larger, the overall effects of bonded Te on the Cr cluster become weaker and necessitates more Te to effect change. This is seen in the population densities of $\text{Cr}_4\text{Te}_{1-3}$ and $\text{Cr}_4\text{Te}_{4-6}$, within **Figure 3-27** and **Figure 3-28**, respectively. The increase in Te atoms elongates the Cr-Cr bonds and reduces the presence of localized Cr (s) orbitals on the participating Cr atoms. This then allows the Cr (s) to further hybridize with the nearby orbitals. The only exception to this is that of Cr_4Te_6 , which returns the Cr (s) orbitals back and then participate in the intermetallic bonding process. Moreover, what we now see is the total absence of the Cr p -orbitals. This is something that we must address now, and will further our discussion with regards to the choice of Basis Set and mainly the analysis method based upon it.

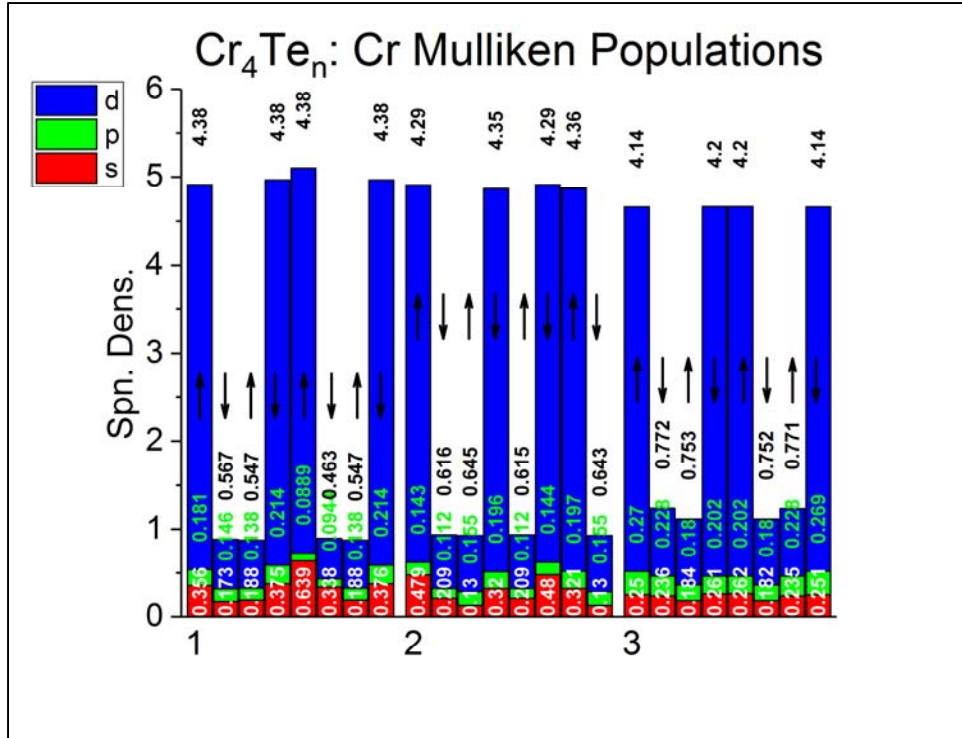


Figure 3-27. Mulliken spin populations for Cr₄Te₁₋₃.
(For each n; Arrows mark direction of both spin channels for each Cr atom.)

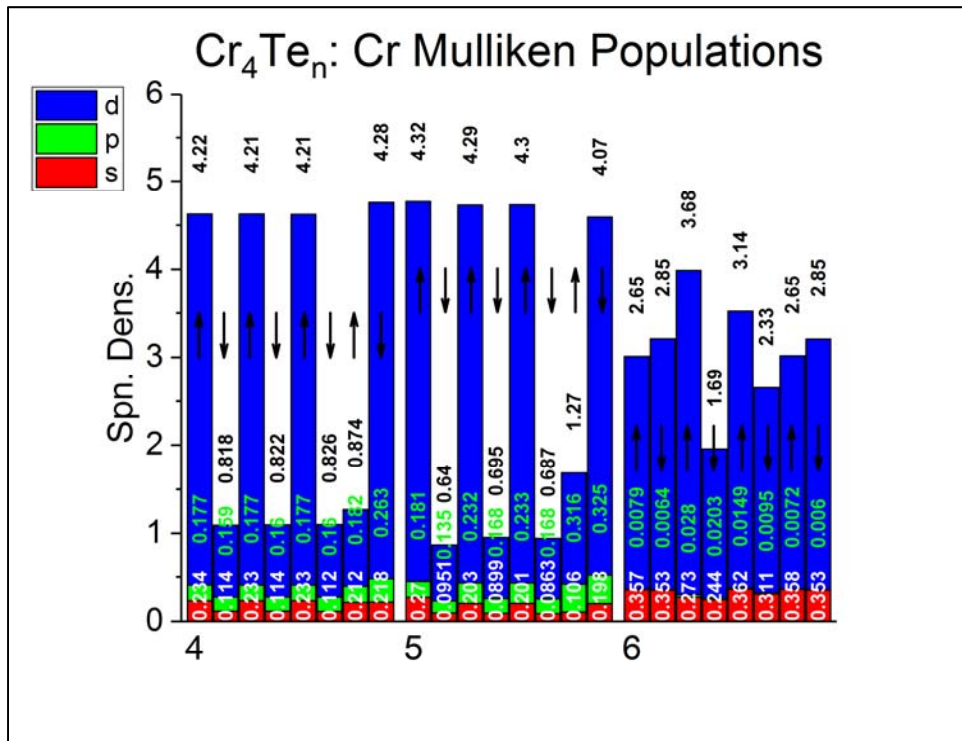


Figure 3-28. Mulliken spin populations for Cr₄Te₄₋₆.
(For each n; Arrows mark direction of both spin channels for each Cr atom.)

This apparent depletion within the Cr (p) orbitals, specifically within the geometry of Cr₄Te₆, can be associated primarily with two sources. The first of which is that the Cr (p) orbitals are no longer needed for bonding with Te. The second, an often scenario that arises when using Mulliken Population Analysis (MPA), where the Cr (p) orbitals have been overestimated, lets evaluate. If we look back upon the geometry Cr₄Te₄ we see all Te atoms are three-coordinated to the faces of the pyramid formed by Cr₄. Alternatively, the geometry of Cr₄Te₆ shows that all Te atoms are all two-coordinated, and strictly bonding with the *d* orbitals of chromium. We detail the overall effect of Te on the Cr₄ substructure, and vice versa, in both these clusters within the upper and lower panels of **Figure 3-29**, respectively.

Below, the valence orbitals for the chromium are taken in the usual manner, 3d⁵4s¹. However, for tellurium we go a step further. Instead of the traditional 5p⁴ we separate alpha and beta spin channels into two electron counts. The total electron count within the *p* orbitals in a solitary Te atoms is 22, the alpha channel consists of twelve electrons, while there are ten electrons in beta. From here, if we were to subtract nine electron pairs from the *p* orbitals of Te, we would obtain the typical 5p⁴ valence scheme. However, below we subtract a total of ten electrons from each channel, all of the electrons which are paired, producing an effective 5p¹p¹ valence. In doing so, we can strictly discuss the modification of the empty, unoccupied, lone-pair orbitals of Te (p). Similar to our earlier outline for treatment of the chromium spin populations, we now sum the alpha and beta spins of Te. This number will reach a maximum of two electrons in the alpha spin channel, and zero in the beta. A completely filled 5p orbital of tellurium in this scheme would thus be represented below as both alpha and beta channels equal to a spin density value of two (together then totaling four electrons, i.e. p_y²p_z²). Deviations from these totals display the contribution of Te (p) to the overall system.

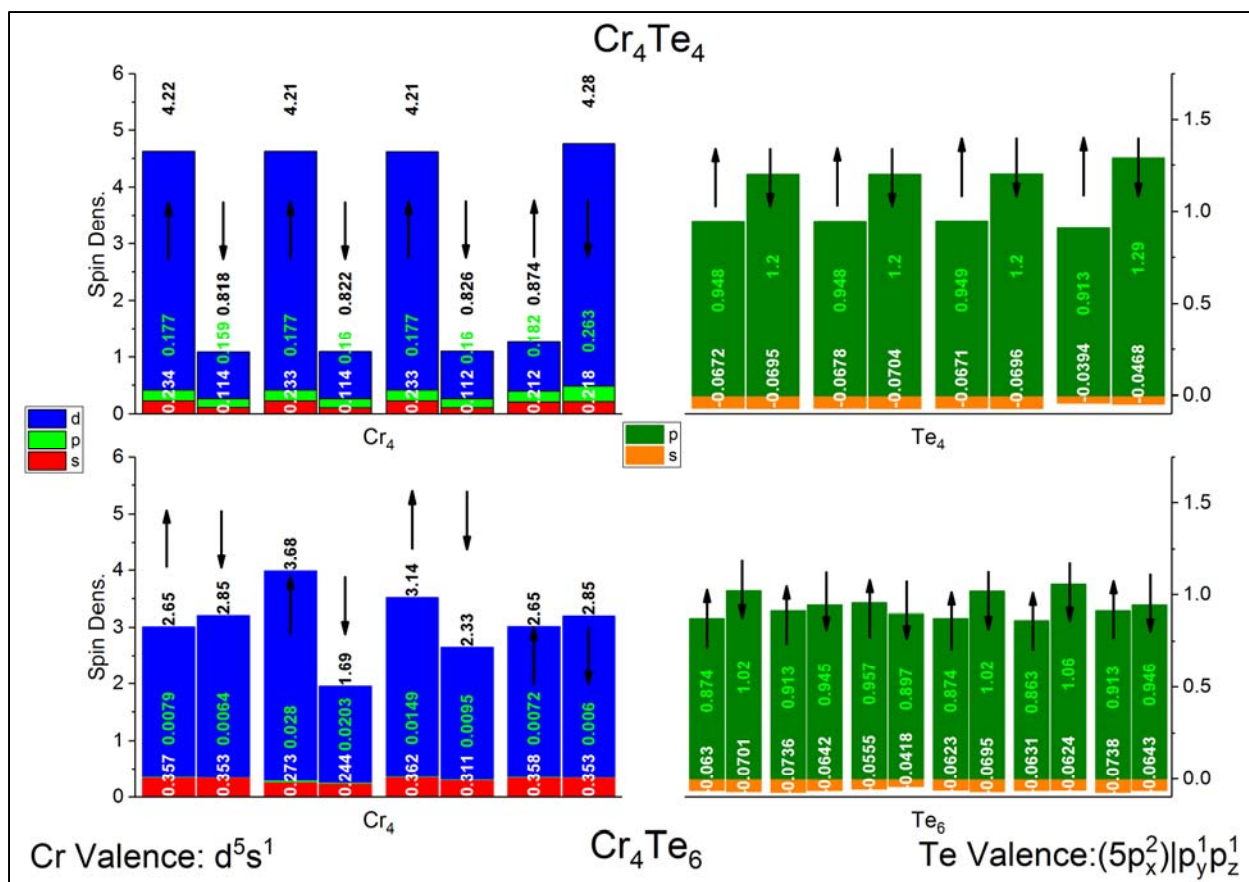


Figure 3-29. Mulliken spin populations for the Cr_4Te_4 and Cr_4Te_6 geometries. Upper and Lower, respectively. (Arrows mark direction of both spin channels for every Cr and Te atom, respectively.) (Te valence taken to be the two electrons of the lone-pair orbitals, $5p_y^1p_z^1$)

For Cr_4Te_4 (upper) there is a significant amount of Te (p) spin density increased as a result of additional bonding with Cr, in the beta channel. While for Cr_4Te_6 (lower), the Te (p) density is maintaining approximately its original valence electron count. The movement between Cr (p) levels, across all the geometries outlined in this document, can be best described as the involvement of Cr (p) in the bonding scheme, and as an attempt of the calculation to fully represent the interactions between Te (p) and Cr (d).

Without too much elaboration, the presence of this artifact in calculations arises from using a finite sized basis set to describe (supra)molecular orbitals (i.e. from using localized orbitals in describing and constructing diffuse, molecular orbitals). This approach amplifies

these shortcomings when computing the interaction energy between two subspecies of a molecule. Or, as in our case between two atoms. That subspecies will then attempt to improve upon this by effectively “borrowing” basis functions from another subspecies (tellurium) within that system.^{205,206} Thus, the Cr (p) Mulliken Spin Densities graphed for these clusters, those previous and those below in subsequent sections, are slightly increased (10^{-3}) in their totals. This slight increase in the Cr (p) is not enough to alter their description, but warrants a brief mention.

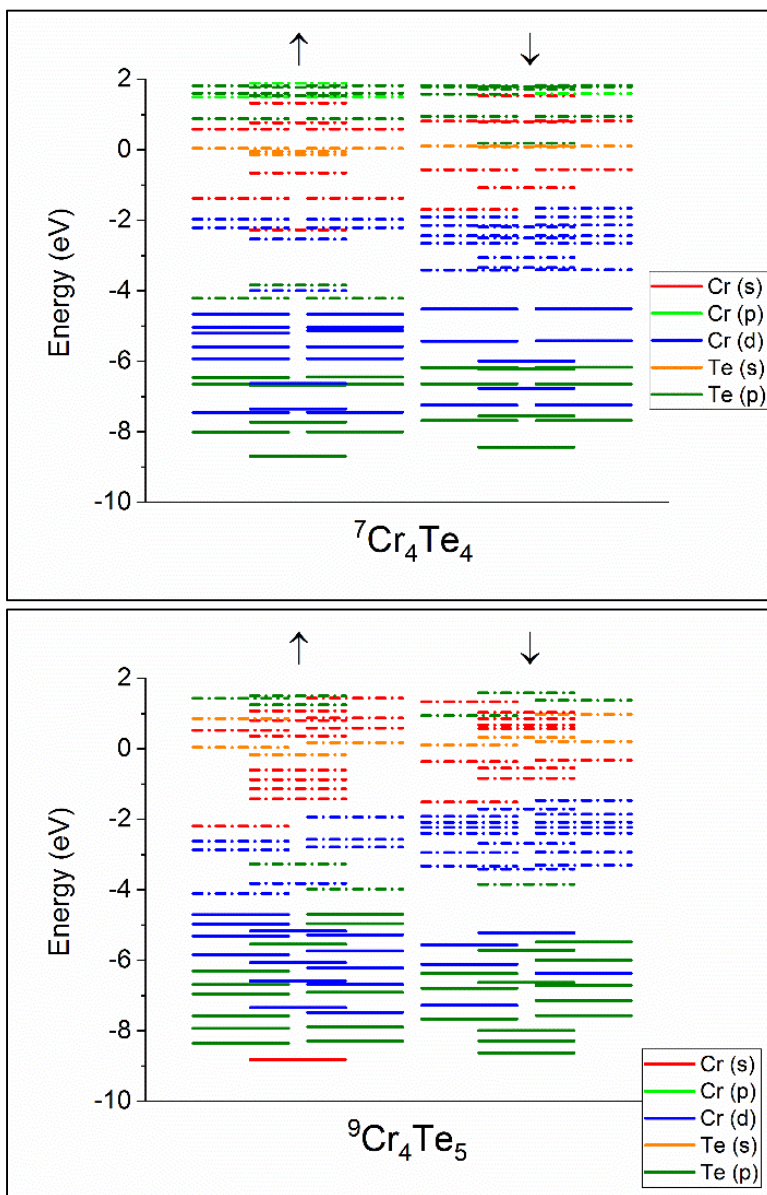


Figure 3-30. ${}^7\text{Cr}_4\text{Te}_4$ & ${}^9\text{Cr}_4\text{Te}_5$ Atomic Orbital (AO) level diagrams. Left column represents spin-up (alpha) channel. Right; spin-down (beta).

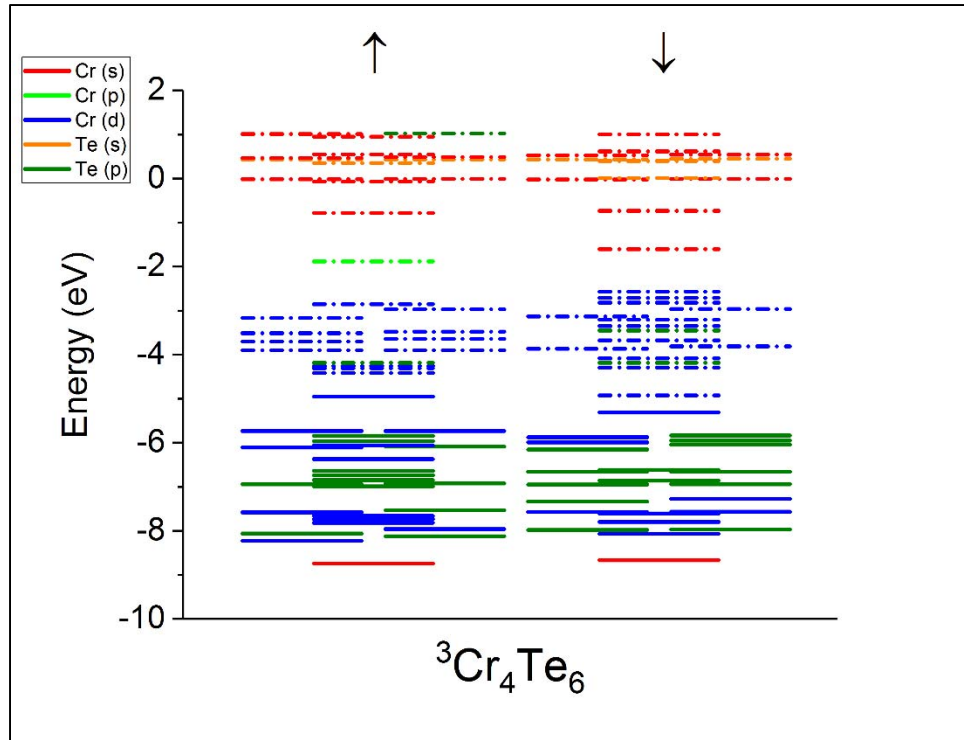


Figure 3-31. Atomic Orbital (AO) level diagram for Cr_4Te_6 .

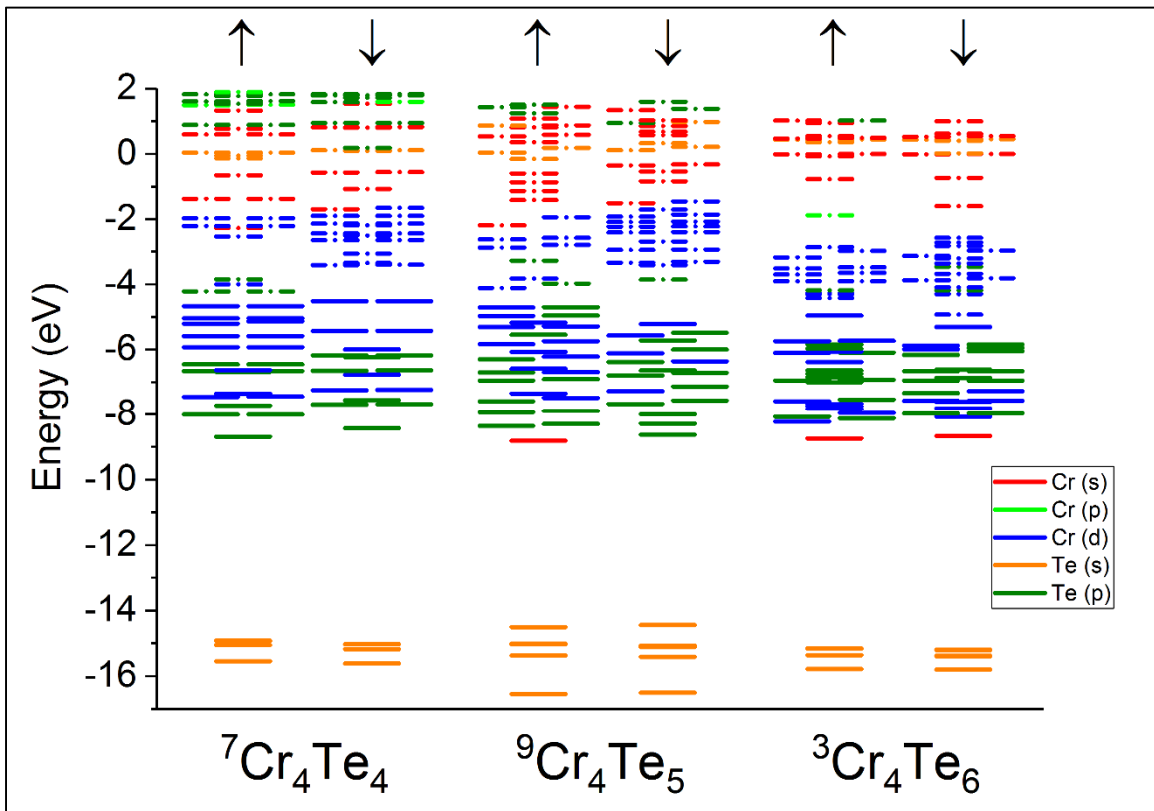


Figure 3-32. Atomic Orbital (AO) level diagrams for Cr_4Te_y , $y = 4 - 6$.
(left to right, respectively.)

The atomic orbital (AO) level diagrams for Cr_4Te_4 and Cr_4Te_5 are shown in **Figure 3-30** and Cr_4Te_6 in **Figure 3-31**. Additionally, all are shown together in series, with corresponding Te (s) orbitals, within **Figure 3-32**. The density of states for these clusters are shown below in **Figure 3-33** through **Figure 3-35**. Across all of these figures can be highlighted the distortion of Cr, and rearrangement of the Te atoms. With a diminished bond order between the orbitals of Cr (d) and Te (p), the chromium atoms are now forming stronger bonds between each other. This results in structures with chromium arrangements and bond lengths that closely mimic those found within the pure clusters of chromium of the same number. This behavior can be seen between the structures of Cr_4 in **Figure 3-2** and Cr_4Te_6 in **Figure 3-6**.

Furthermore, if we recall the graphs of Average Bond Distances and the change in Hirshfeld Charge densities from **Figure 3-12**. From that figure, we can see that the absence of a third bond from Te has allowed the average bond distances between the Cr atoms to fall to the lowest of all geometries composed of three or more chromium. Additionally, compared to the previous Cr_4Te_x clusters, both chromium and tellurium atoms within Cr_4Te_6 experience the least amount of change to their Hirshfeld charge densities. The bonding of Te (p) with Cr (d) across all of these clusters can be seen below in their respective DOS. For Cr_4Te_4 and Cr_4Te_5 , **Figure 3-33** and **Figure 3-34**, we can see that the Te (p) do not completely eliminate the spins of Cr (d). Alternatively, for Cr_4Te_6 , Te (p) primarily bonds to Cr (d) and drives the total magnetic moment of the cluster downward.

Thanks in part to its size, the continual addition of Te atoms onto Cr_4 produces clusters with an alternating bonding scheme for the Te atoms. That is, for an even number of Te each bond in the three-coordination, and for odd number all will be three-coordinated with the exception of one Te. This occurs in a few of the smaller sized chromium structures, but becomes

a regularity and more apparent within Cr_4Te_y . Especially so for the clusters of Cr_4Te_3 , Cr_4Te_4 , and Cr_4Te_5 . The cluster of Cr_4Te_6 is thus a special case.

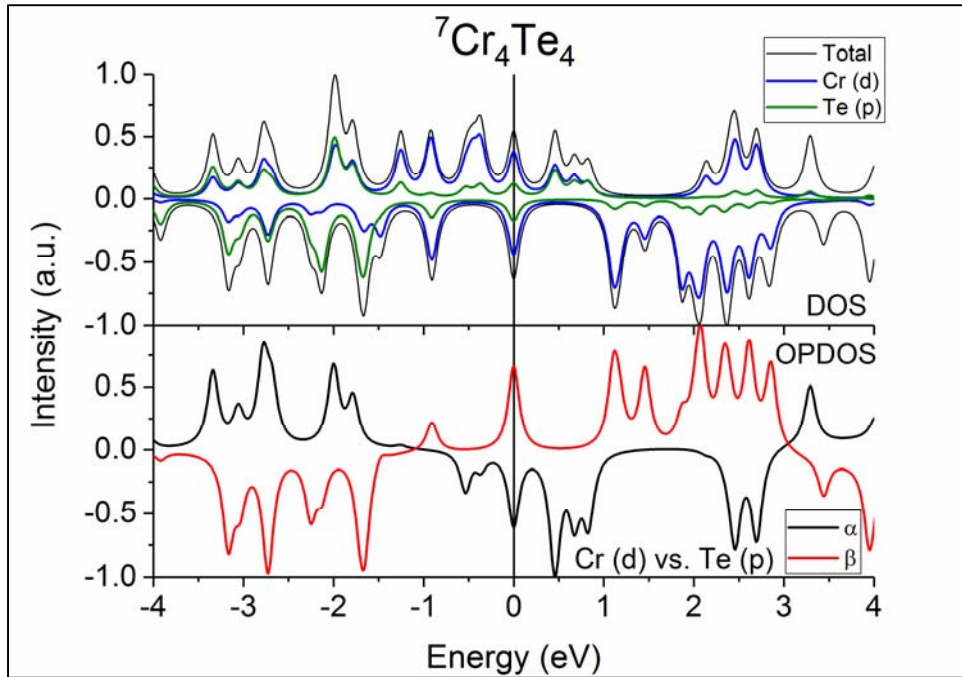


Figure 3-33. Density of States (DOS) & OPDOS for ${}^7\text{Cr}_4\text{Te}_4$. (OPDOS: Overlap Population Density of States. Positive indicates bonding; Negative: antibonding. Beta inverted for clarity.)

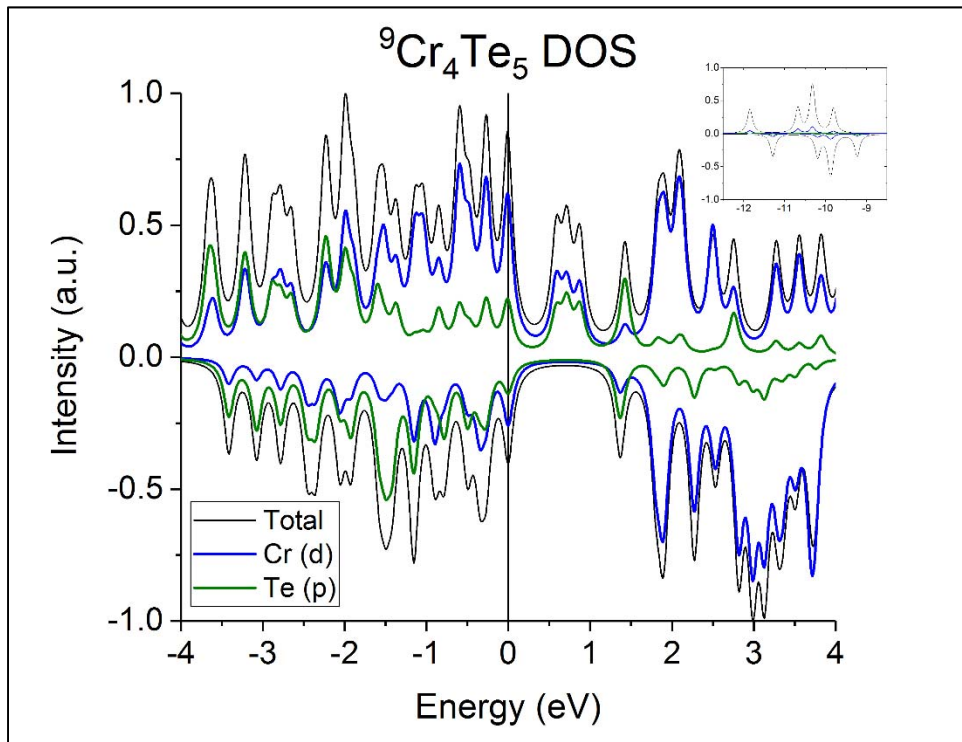


Figure 3-34. Density of States (DOS) for ${}^9\text{Cr}_4\text{Te}_5$.

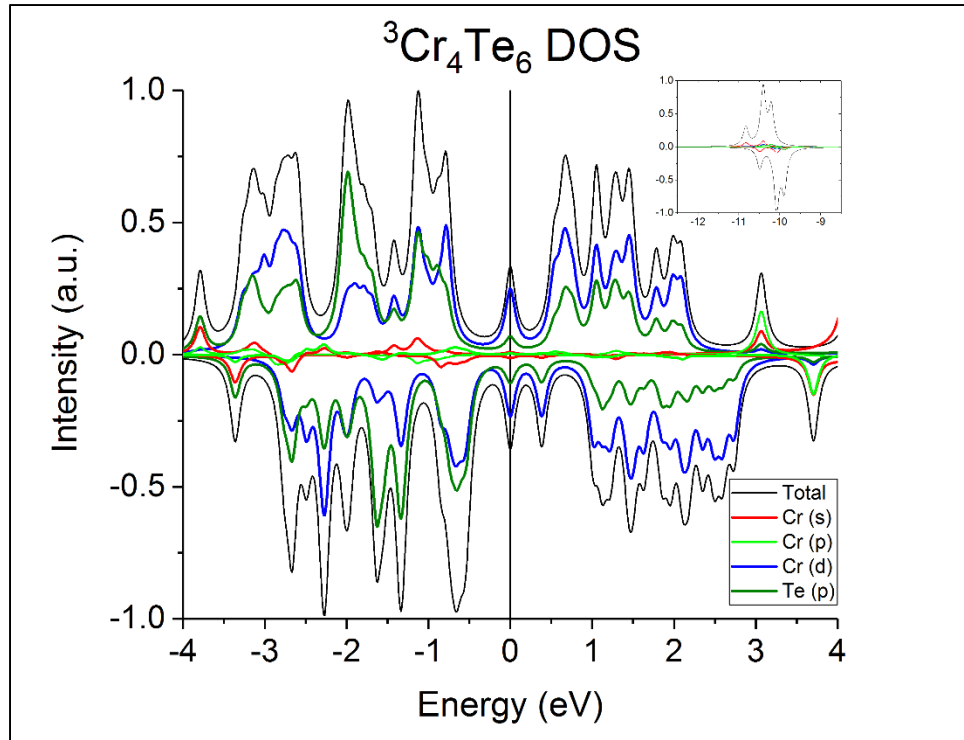


Figure 3-35. Density of States (DOS) for ${}^3\text{Cr}_4\text{Te}_6$.

3.5.6 Cr₅Te_y (y = 1 – 7)

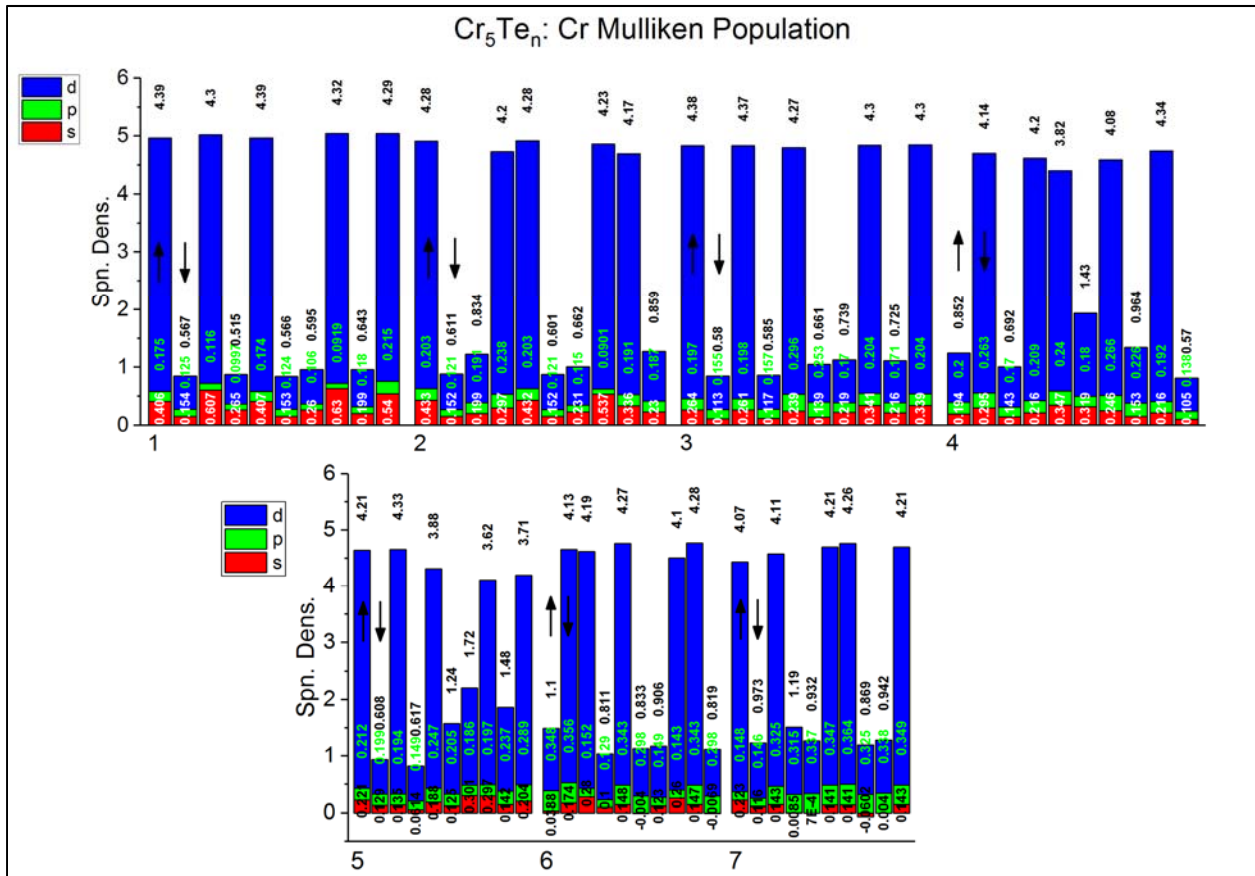


Figure 3-36. Mulliken spin populations for Cr₅Te₁₋₇. (Arrows mark direction of both spin channels for each Cr atom, respectively. For clarity, only the first atom is marked.)

The Mulliken spin populations for each Cr atom within the Cr₅Te₇ series can be seen in **Figure 3-36**. Here we can clearly see on a larger scale both the total effect of added Te atoms, as well as the diminishment in population density of the Cr (s) orbitals, as well as the slight increase in the filling of the Cr (d) beta channel. In this series, as in all others, the bond lengths between the Cr atoms increases. In addition to this, the result of odd numbered Cr atoms further increases the likelihood of their distortion and rearrangement through sequential addition of Te atoms. Furthermore, increased distortion and bond lengths grow in accordance with the number of Te present.

Because of the odd number of Te, the underlying Cr₅ structure is not entirely decorated by three-coordinated Te, but possess a single Te in the two-coordination. This occurs as a matter of necessity, as the Te atoms desire to be farthest away from one another. The result of which is an arrangement of the Cr in a manner that the apex atoms are both spin-up, with a minimal loss of their spin densities. The large number of Cr (d) orbitals involved in this process can be seen in the alpha channel of **Figure 3-37**. Moreover, this effect can be seen within the DOS of **Figure 3-38**, where Te (p) is not fully occupying all available Cr (d) between the HOMO level and down to -1 eV below HOMO. Within this region, we find that the Overlap Population Density of States (OPDOS) between Te (p) and Cr (d) again, as we have seen before in these clusters, to be antibonding in nature, plotted in the lower panel of **Figure 3-38**.

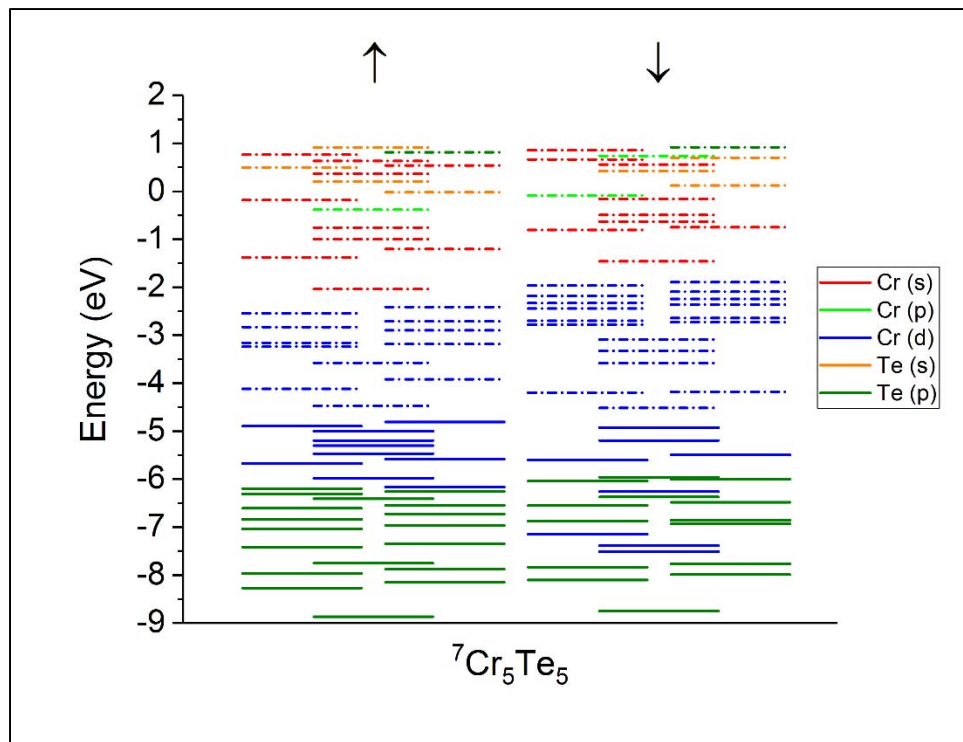


Figure 3-37. Atomic Orbital (AO) level diagram for ⁷Cr₅Te₅.

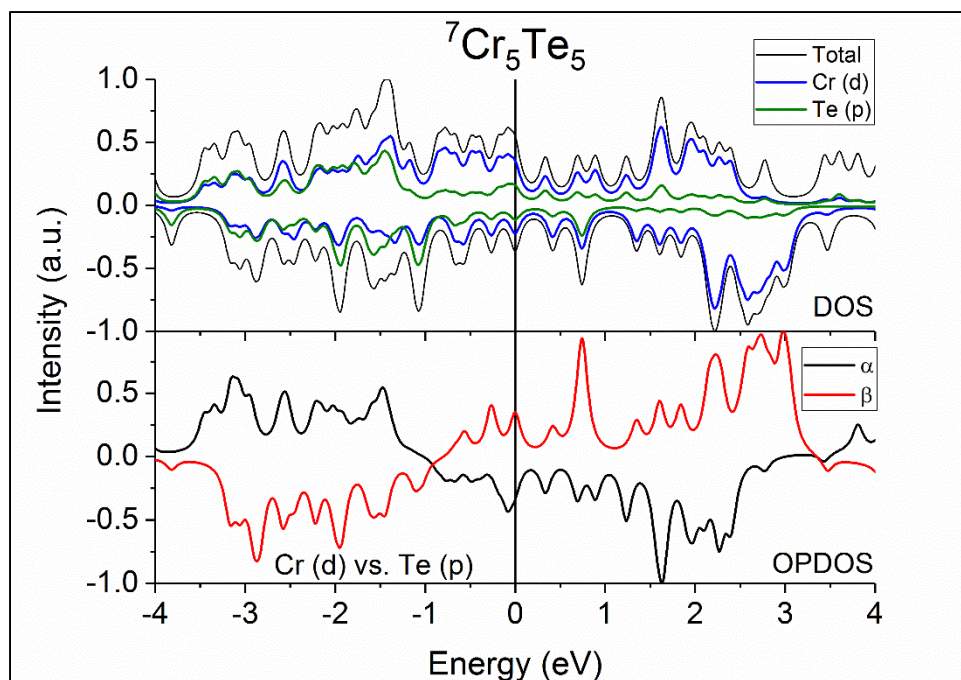


Figure 3-38. Density of States (DOS) & OPDOS for ${}^7\text{Cr}_5\text{Te}_5$.
(OPDOS: Overlap Population Density of States. Positive indicates bonding; Negative: antibonding. Beta inverted for clarity.)

The Cr_5 series can effectively be thought of as marking a transition between the compact structures of Cr_4 and those of the larger Cr_6 . This transition not only highlights the continual influence of Te within the cluster, but also changes within the Cr_xTe_y series arising due to this newly achieved cluster size specifically. A persistent property seen at all cluster sizes is the effective decrease in the total number of Te atoms that can be supported. However, the current Cr_5 series marks the beginning of the geometries in which all the added Te atoms, with the exception of Cr_5Te_5 , are bonded with three-coordination. This may seem trivial, but this added coordination, and with fewer Te atoms, allows the larger cluster to now become effectively closed and reduces the number of open sites which further protects the cluster from the environment. Moreover, the remaining active sites begin to enforce a form of directionality in the cluster, as their locations dictate the positions available for ligand bonding upon the surface. All of these properties and concepts can be found within the Cr_6Te_y series as well, in the following section.

3.5.7 Cr₆Te_y (y = 1 – 6)

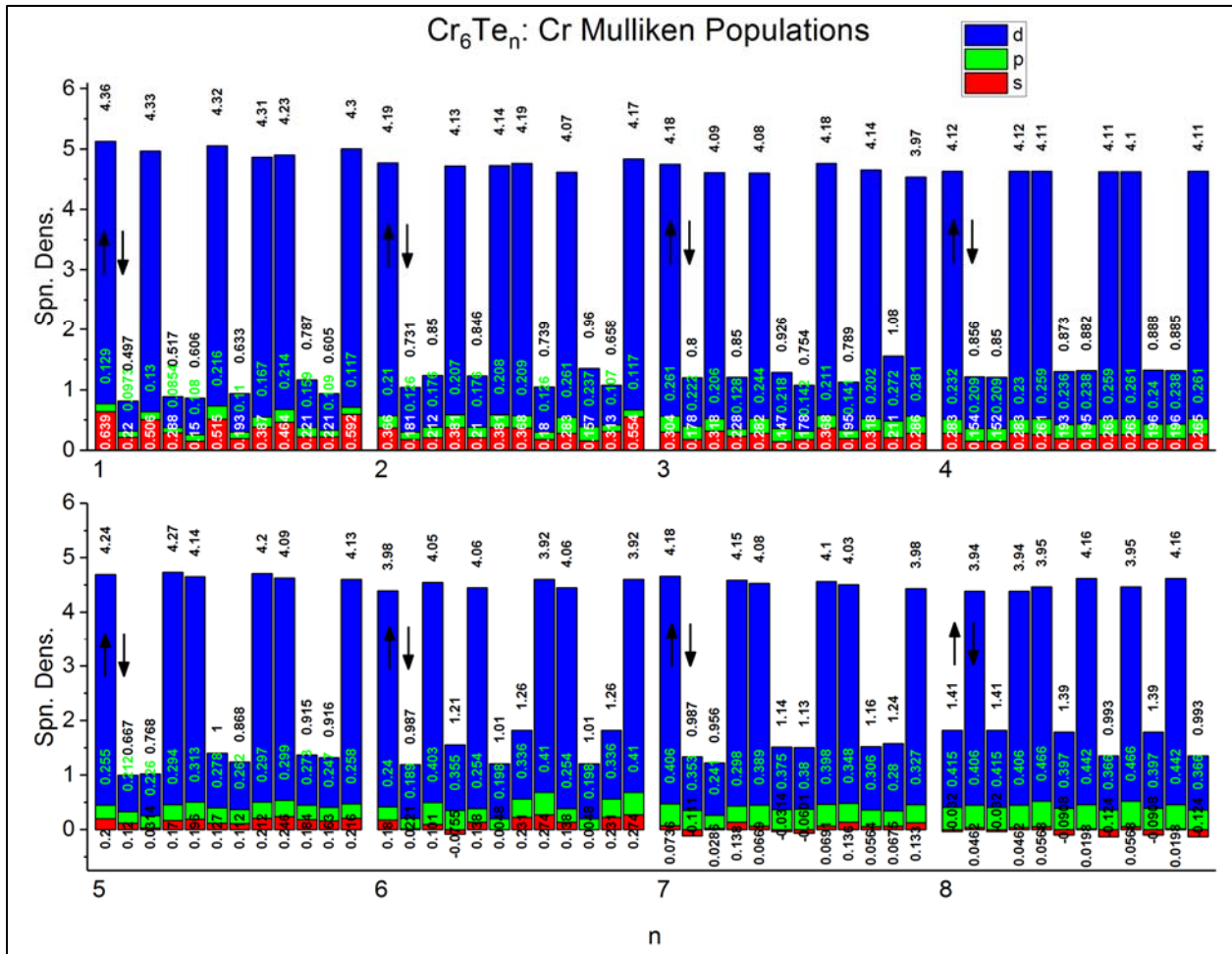


Figure 3-39. Mulliken spin populations for Cr₆Te₁₋₈. (Arrows mark direction of both spin channels for each Cr atom, respectively. For clarity, only the first atom is marked.)

As we have discussed above in regards to the Cr₅Te_y series, when viewing the Mulliken spin populations of Cr₆Te_y in **Figure 3-39** the same effects can be seen. The increased decoration of Te atoms driving the Cr atoms away from one another, changing the overall contributions and bonding patterns of the Cr orbitals. Additionally, over the entire series, we can see again the slight increase in filling of the beta channel in the Cr (d) orbitals. As we have noted above, in Section 3.3.2.6, all Cr atoms within the Cr₆ series bond together to form an antiferromagnetic cluster in the singlet state, with the exception of Cr₆Te₆ which has fundamentally altered its geometry to avoid this. We can compare the clusters of ¹Cr₆Te₅ and

${}^7\text{Cr}_6\text{Te}_6$ below using their level diagrams within **Figure 3-40** and **Figure 3-41**, respectively. In **Figure 3-40**, we can see the Cr (d) orbitals near the HOMO level to be bonding with each other, facilitating the antiferromagnetic behavior of the total cluster. In the compact geometry of ${}^7\text{Cr}_6\text{Te}_6$, all Cr atoms are maximally coordinated with the surrounding Te atoms as well as each other. This then allows the Cr atoms to arrange their spins in a manner similar to what we have seen above in the smaller CrTe clusters, and maximize the total magnetic moment of the cluster. The level diagram of **Figure 3-41** shows the number of Cr (d) orbitals of the alpha channel densely populated near the HOMO level, without equal number to those of the beta channel. Moreover, **Figure 3-42** shows us, again, that Te (p) does not entirely fill the Cr (d) orbitals within the cluster, and as far as one electron-volt below the HOMO level the antibonding behavior persists, as well.

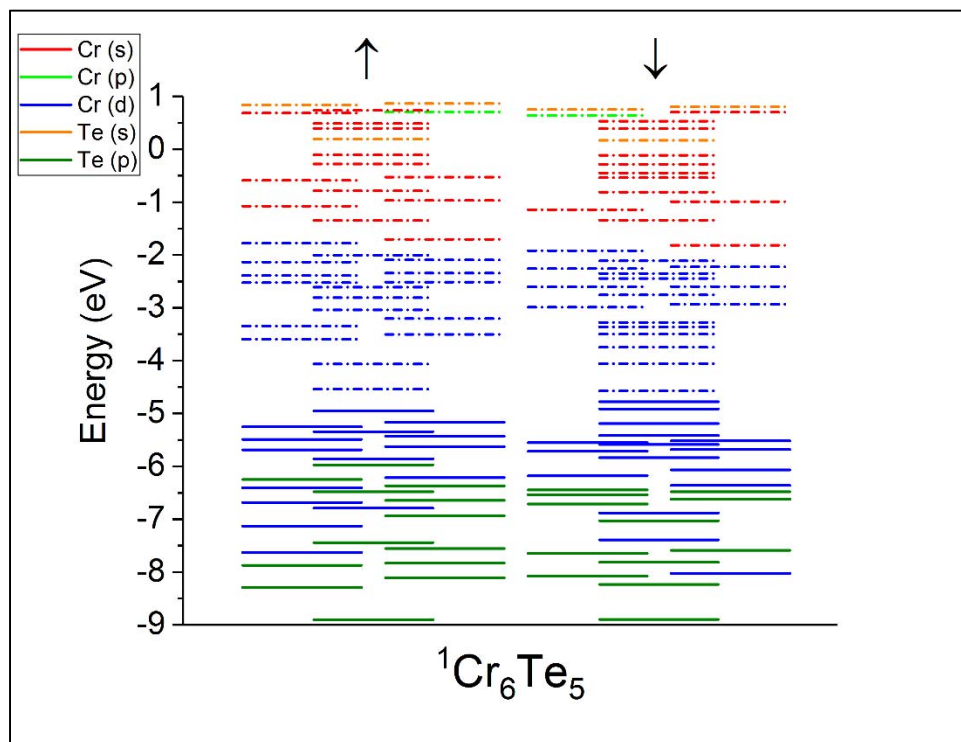


Figure 3-40. ${}^1\text{Cr}_6\text{Te}_5$ Atomic Orbital (AO) level diagram.

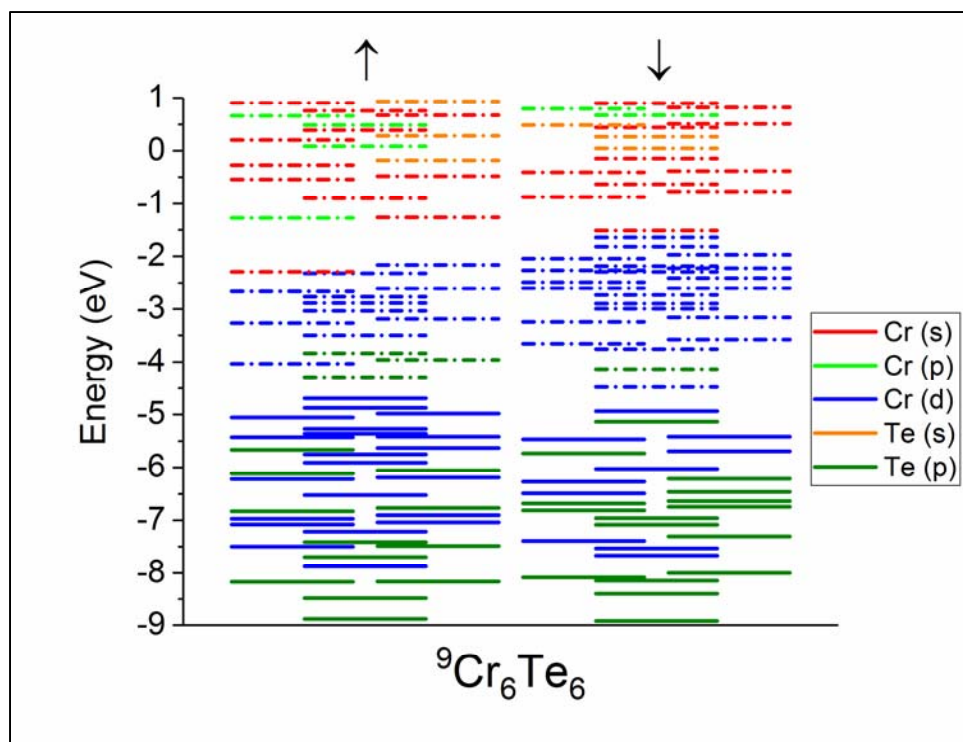


Figure 3-41. ${}^9\text{Cr}_6\text{Te}_6$ Atomic Orbital (AO) level diagram.

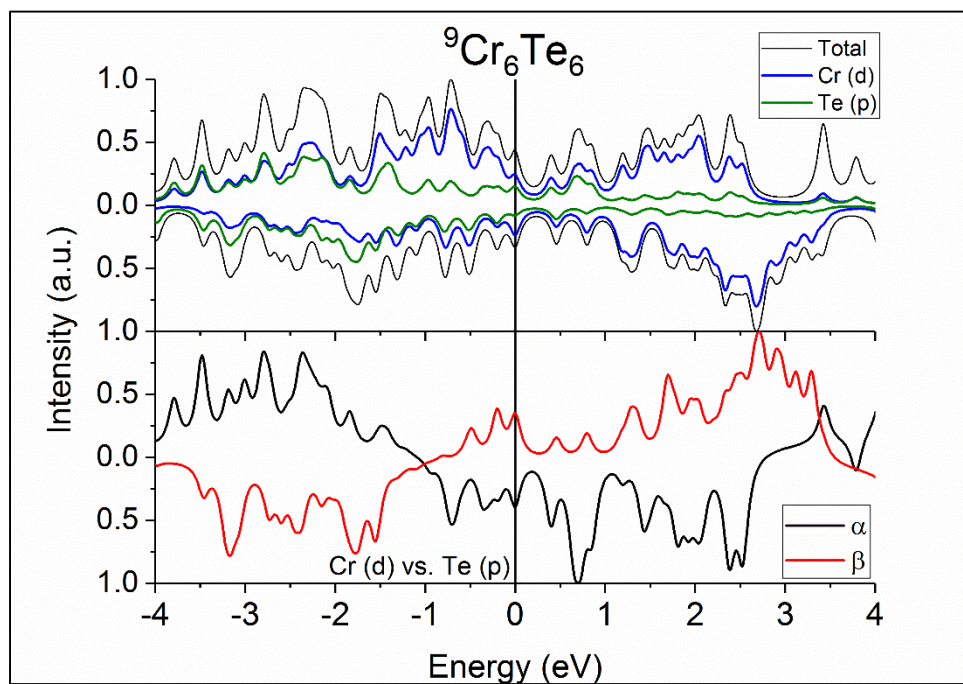
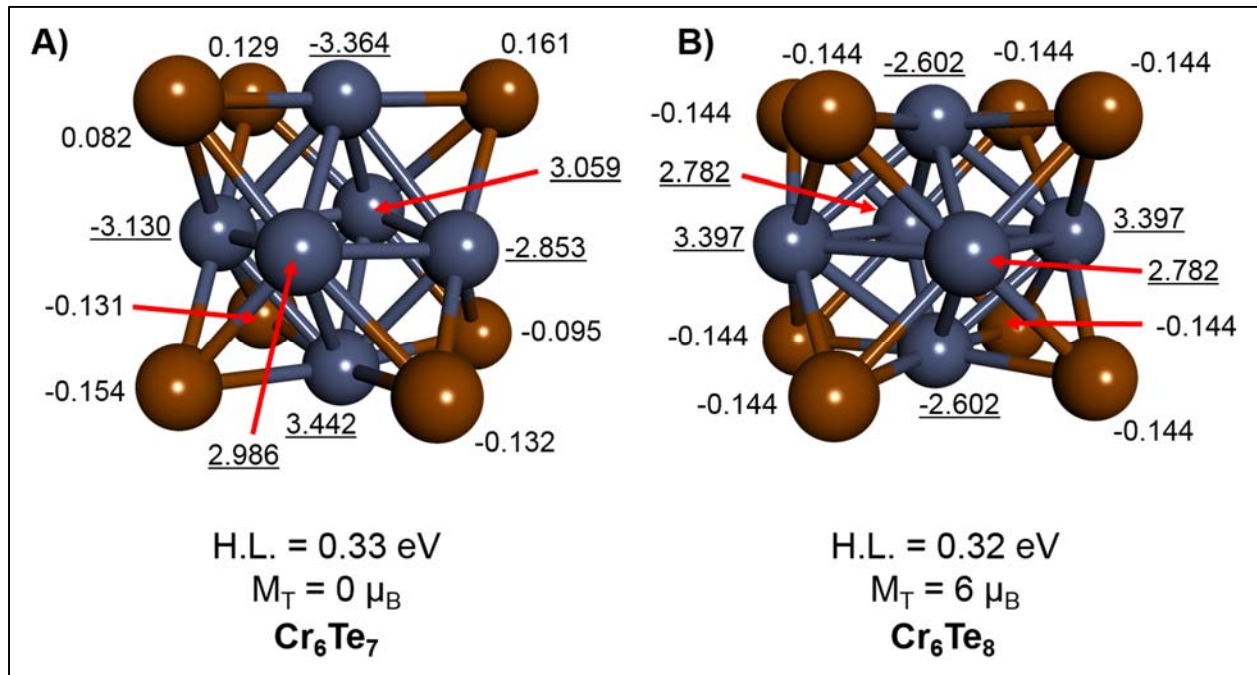


Figure 3-42. Density of States (DOS) & OPDOS for ${}^9\text{Cr}_6\text{Te}_6$.

(OPDOS: Overlap Population Density of States. Positive indicates bonding; Negative: antibonding. Beta inverted for clarity.)

3.5.8 Cr₆Te_y (y = 7, 8)

We conclude our discussions of small binary CrTe clusters by further examining Cr₆Te₇ and Cr₆Te₈. Geometries for both clusters are shown in **Figure 3-43 (A)** and **(B)**. The major difference between these two can be first be seen in their spin states, $M = 1$ and $M = 7$, respectively. Without the addition of the eighth Te atom, Cr₆Te₇ takes on a configuration which is highly distorted. This configuration is exemplified in the central Cr₄ substructure of both clusters, seen in **Figure 3-44**, left and right, respectively. For Cr₆Te₇, all central Cr bonds are of different length and, because these four atoms are out-of-plane in the dihedral with angle 168.69°, can maintain bonding angles close or very near to 90°. Alternatively, the Cr₆Te₈ central Cr₄ unit remains planar, and with near equal bond lengths of ~2.902 Å. However, to maintain this configuration the atoms are merely deformed, forming two pairs of angles 81.98° and 98.02°.



*Figure 3-43. Groundstate geometries of ¹Cr₆Te₇ and ⁷Cr₆Te₈.
(Reproduced from above.)*

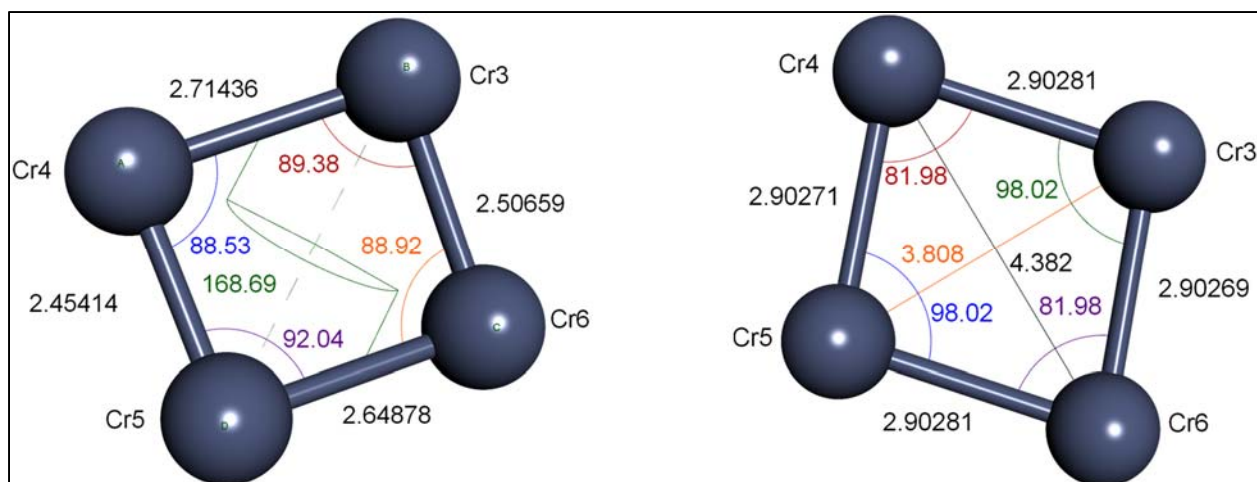


Figure 3-44. Geometry of the central Cr_4 subunits for 1Cr_6Te_7 and 7Cr_6Te_8 clusters. (left and right, respectively.)

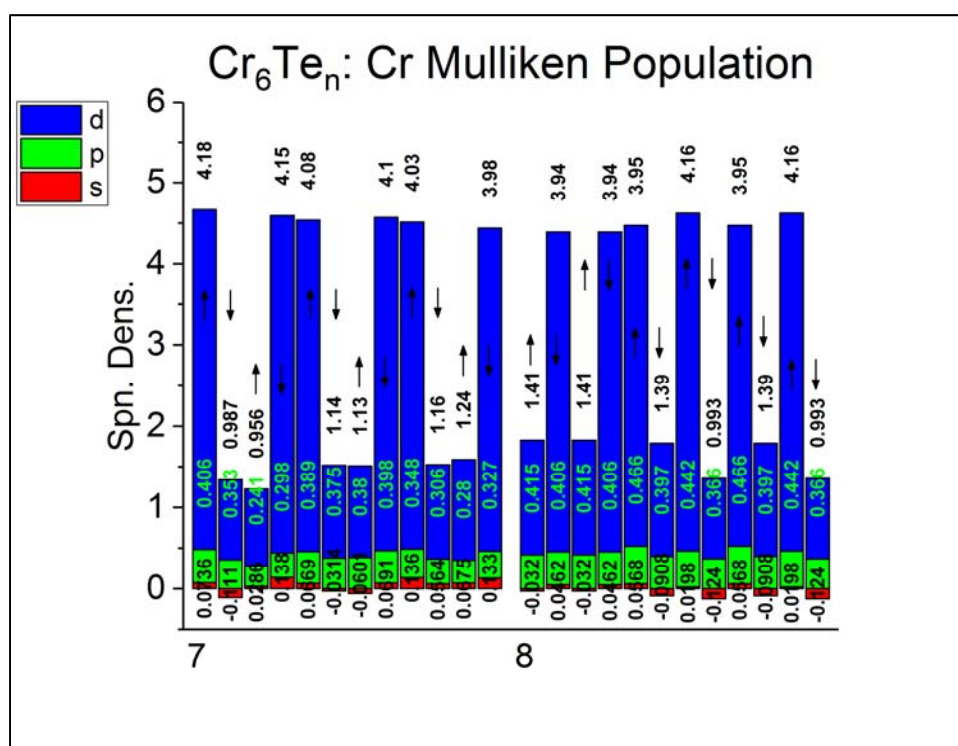


Figure 3-45. Mulliken spin populations for 1Cr_6Te_7 and 7Cr_6Te_8 . (Arrows mark direction of both spin channels for each Cr atom, respectively.)

Furthermore, the Cr_6Te_7 cluster can be described easily with an argument typically found previously in the literature for describing this type of cluster; as the antiferromagnetic result of the union between two ferromagnetic *nido*- clusters, Cr_3Te_3 and Cr_3Te_4 . The addition of the eighth Te atom, in Cr_6Te_8 , slightly relieves the distortion of the central Cr_4 geometry, which

alters the arrangements of the nearby Cr atoms. This results in a cluster with a total magnetic moment of $6 \mu_B$, constructed by Cr atoms in a ferrimagnetic arrangement formed across three separate regions of the cluster, the apex Cr of top and bottom, both spin down, and the middle Cr_4 , all spin up. All of this has been labelled above in **Figure 3-43**, and can be seen in the spin density graph of **Figure 3-45**.

The change in the bonding of nearby chromium atoms through addition of tellurium can be seen below in the level diagrams of **Figure 3-46** and **Figure 3-47**. Structural deformation is apparent in both figures. The Cr_6Te_7 cluster employs nearby Cr (p) and Cr (s) orbitals, and as mentioned in the Cr_4Te_6 cluster, near mimicking the properties found in the pure Cr_6 cluster variant. The Cr_6Te_8 cluster is not only distorted in its Cr_4 subunit, but also compressed along the z-axis direction. Much of the deformation in both of these clusters can be attributed to Jahn-Teller distortion, where the numerous *d*-orbitals must break their degeneracy through either modification of the electronic shells, or the structure itself.²⁰⁷⁻²¹³ The result of all of this rearrangement drives both average Cr and Cr-Te bond lengths in Cr_6Te_8 upwards, and drastically so for Cr-Cr. This then allows underlying orbitals to participate in bonding, while Cr (d) maintain their spin densities, and can be seen in the density of states of **Figure 3-48**.

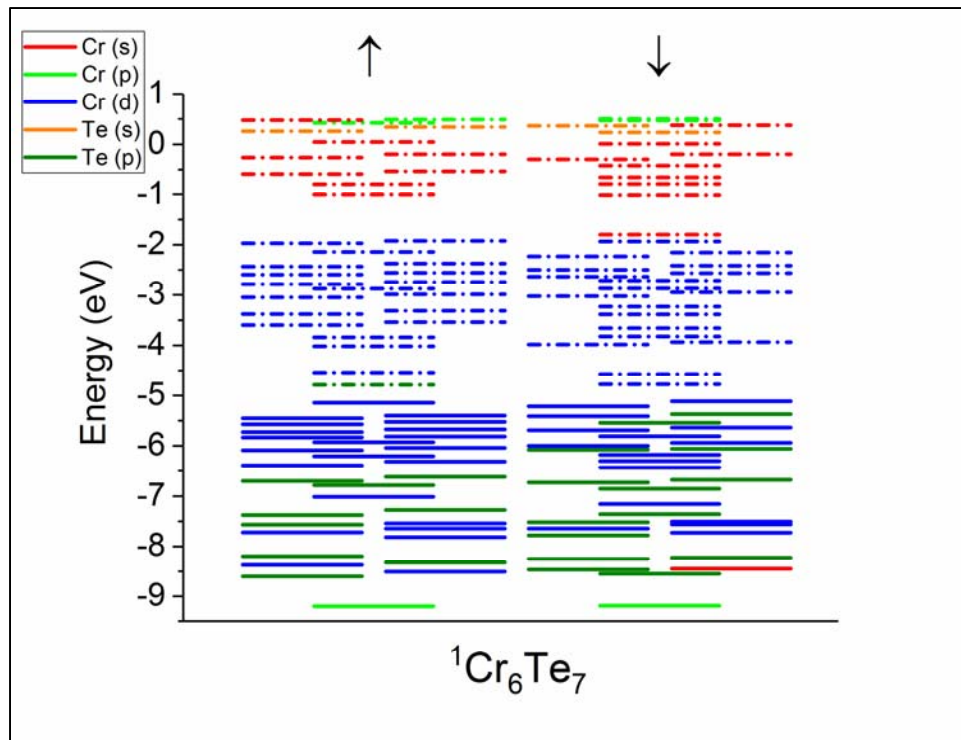


Figure 3-46. $^1\text{Cr}_6\text{Te}_7$ Atomic Orbital (AO) level diagram.

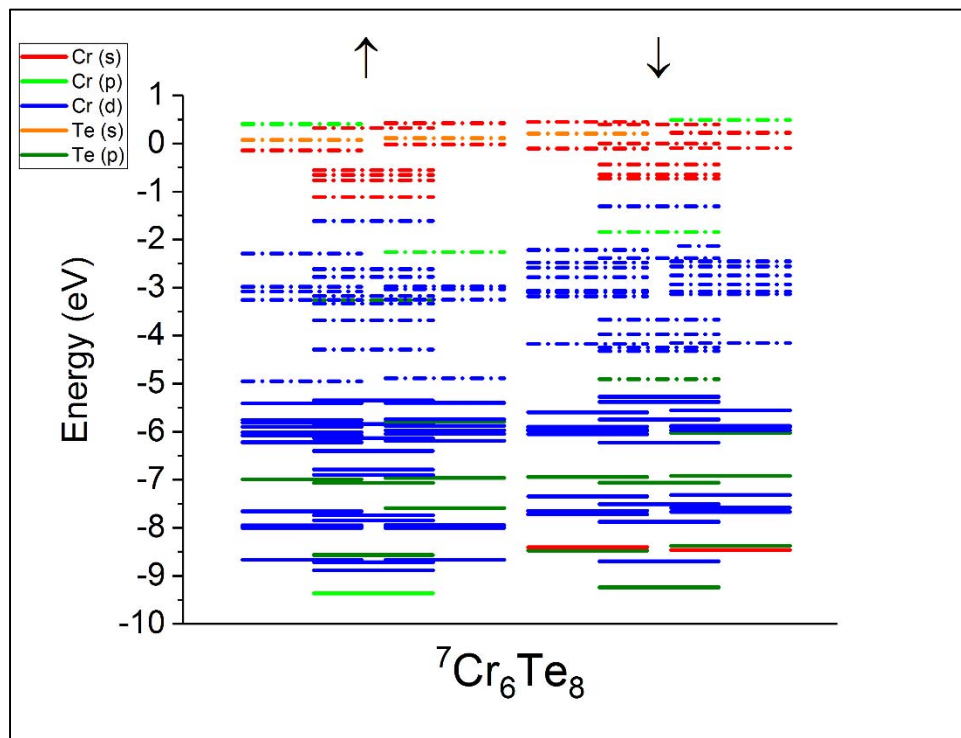


Figure 3-47. $^7\text{Cr}_6\text{Te}_8$ Atomic Orbital (AO) level diagram.

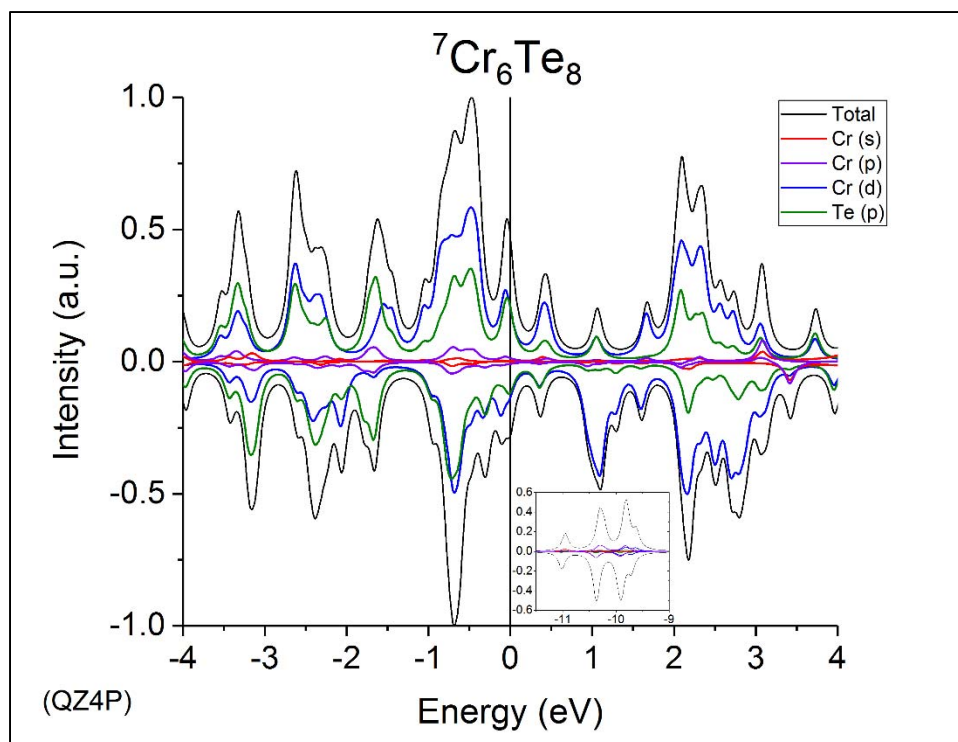


Figure 3-48. Density of States for unligated ${}^7\text{Cr}_6\text{Te}_8$.
Inset shows location of the lower Te (s) orbitals

The stability of the bare Cr_6Te_8 can be further expressed using the information within **Figure 3-49**, below. Here, we have plotted the lowest energy geometry for each magnetic moment, with inset showing the average Cr-Cr and Cr-Te bond distances. The groundstate magnetic moment for the Cr_6Te_8 is the septuplet, as shown above in previous sections. From the plot, we can deduce that to deviate from this magnetic moment, the Cr_6Te_8 cluster would favor the $M = 9$ multiplicity. However, even though this is energetically favorable, it is not structurally, as the bond distance between Cr atoms would need to be elongated to a drastic degree to produce such a charge state. Knowing this information regarding the Cr_6Te_8 cluster further confirms that the septuplet multiplicity is correct.

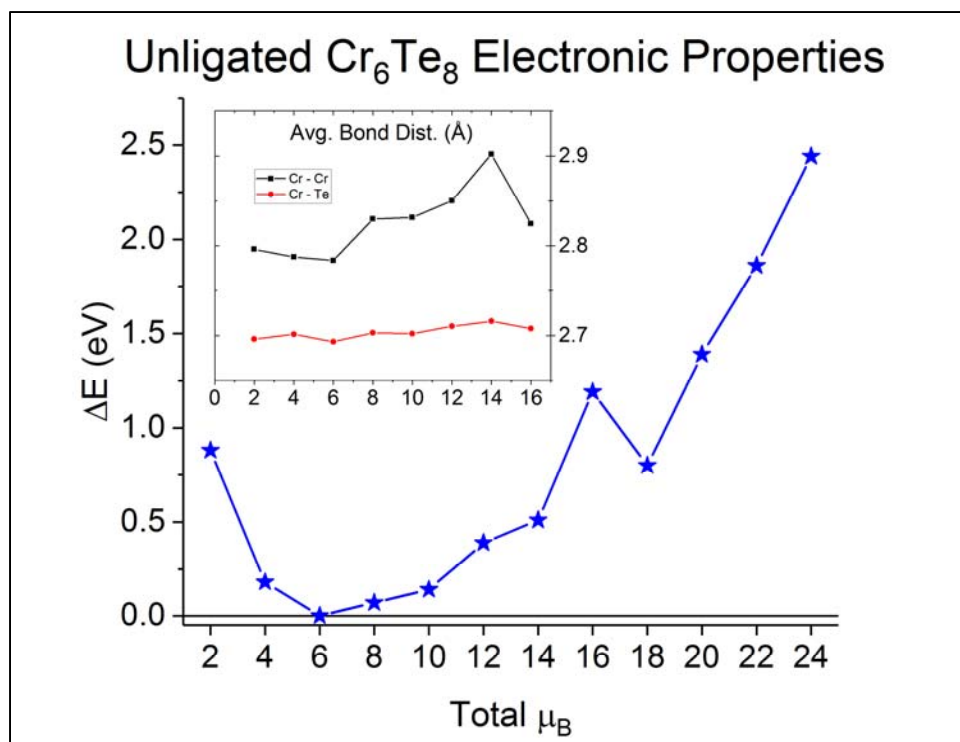


Figure 3-49. Cluster energetics for $(x+1)\text{Cr}_6\text{Te}_8$ across various values of total μ_B . Cluster energies have been normalized to groundstate. Inset shows average Cr-Cr and Cr-Te bond distances.

3.6 Discussion & Conclusions

From the analysis and results above, ranging across all sizes in the combination of chromium and tellurium, we can make definitive conclusions on a number points. The first of these is in regard to the overall structures. The weakness of the chromium bond is made more apparent and exploited through addition of tellurium, but the overall cluster is made stronger as a result. Additionally, within all clusters, chromium atoms still prefer to bond with each other, of course, and structurally, comprise the main clusters component.

The effect of Te on the underlying properties of Cr is apparent at all sizes. However, this effect is made especially noticeable between the two species when Cr has yet to be decorated with sufficient number of Te. This situation is typical of the intermediate cluster sizes, where the number of bonding sites is lacking. It is within those clusters we can see an attempt, and some success, of the chromium atoms to return to properties found in their pure versions. In regards to Te bonding, pure tellurium is known for its ability to form two- and three-coordinated configurations, and the effect of Te itself is not maximized until it engages this third bond upon the cluster, further influencing the underlying chromium.

Secondly, growing to larger cluster sizes, the resulting expansion of bond lengths between chromium atoms is due in part to the bonded tellurium atoms. Because of this expansion, the Cr bonds are driven to lengths that can be considered an extremum. These extended lengths seen between the metal atoms has led previous experimental reports in the literature on 686-cluster types to describe the metal-metal bonds as mediated by the nearby, capping, atom. From what we have shown above in previous sections, this description lacks conclusiveness, can be misleading, and fails to highlight the underlying cluster behavior. We saw above in describing the Cr_6Te_8 cluster, that all bonds formed are covalent, and the bonding

of Te upon the faces of the Cr₆ octahedron deform the structure and thus becomes another structural component. This indicates that the added Te atoms are integral to the stability of the overall cluster, more than merely dictating the behavior of the underlying metal-metal bond. This role of bonded Te atoms has been seen at all sizes of cluster, and is not applicable strictly to the cluster of Cr₆Te₈.

Using the information and results of this chapter we now carry forward an understanding of the Cr₆Te₈ structure as necessary for our discussion in utilizing it as a cluster motif. We can further the discussion of ligated atomically precise binary transition metal—chalcogenides as it pertains to the union between the elements at the extremums of both these classifications. Thus, in Chapter 4, below, we describe the alteration of properties in the pure ⁷Cr₆Te₈ through ligation with triethylphosphine (PEt₃), whose structure has been experimentally reported in the literature previously. Moreover, how these properties are varied through passivation of the cluster with alternate ligands; specifically, PH₃, CN, and CO.

4 Electronic Properties of ${}^7\text{Cr}_6\text{Te}_8(\text{PEt}_3)_6$ and Alteration Through Ligand Exchange

4.1 Overview

If we recall from chapter one, the passivation of a bare metal cluster is first done to stop its the growth into larger sizes, and preserve any atomic scale properties. Moreover, we also know that is it is possible to manipulate these properties by adjusting the electron count of its valence shell through the use of various ligands. We shall see below that the attachment of triethylphosphine (PEt_3) ligands alters both the structure and electronic properties of the Cr_6Te_8 core, while also preserving its overall magnetic moment in the septuplet state. But, before moving into the ligated cluster, we must first discuss briefly about DFT formalism.

4.2 Change of Basis Set

Calculations upon the larger ligated cluster were again performed utilizing the methods describe in the previous chapters. However, in the interest of time and resources, the basis set has been changed from the original all-electron quadruple-zeta with four added polarization terms (QZ4P). The new basis set utilized below, for the ligated core, is the triple-zeta with double polarization (TZ2P), and under the frozen core approximation. The “frozen core” approximation allows one to hold fixed the coefficients and exponents that construct an atomic orbital comprised within a chosen basis set. Keeping the values constant will thus mean they do not update during the SCF cycles between geometry updates (i.e. not computed), and translates to a reduced computation time. The “frozen core approximation” itself and how it is

implemented within ADF will not be detailed here, but can be found within the literature for those interested.¹⁵⁴

To assuage any doubt or discrepancy between this switch in formalism, we compute the Cr₆Te₈ core yet again with an additional two basis sets, and maintaining the PBE functional, to finally obtain the core geometry most comparable to the ligated version. The basis set list is as follows; (1) QZ4P (from above), (2) TZ2P (All Electron, without frozen core), (3) PBE:TZ2P (Large Frozen Core). A keen eye will immediately see the reduction in basis set size when moving from (1) to (2), followed by the reduction in the number of basis set coefficients to compute, from (2) to (3).

The sizes of these basis sets vary between each element, of course, depending on the number of orbitals it possesses. Thus, for the chromium atom ($1s^2 2s^2 2p^6 3s^2 3p^6 4s^1 3d^5$), the ZORA QZ4P basis is constructed using coefficients totaling 13S 8P 5D 3F, for their respective orbitals. That is, 13 coefficients for the total number of *s* orbitals, eight for *p*, five for *d*, and three for *f*. For tellurium ($1s^2 2s^2 2p^6 3s^2 3p^6 4s^2 3d^{10} 4p^6 5s^2 4d^{10} 5p^4$), 18S 15P 8D 3F. Under ZORA TZ2P, all electron; chromium, 9S 6P 3D 1F; and tellurium, 12S 10P 7D 1F.

In ADFs frozen core approximation, one is afforded three options; small, medium, large. Each choice utilizes a different basis, adjusting the number of atomic orbital coefficients to hold fixed. For a few elements, some of these choices have similar effect. For example, for both Cr and Te atoms the “medium” and “large” options perform in the same manner. However, for an element such as phosphorus, all options are equal. Specifically, when choosing a “large” frozen core when calculating Cr, the coefficients representing the orbitals $1s^2 2s^2 2p^6 3s^2 3p^6$ are kept fixed, effectively making them the “core” orbitals, while $4s^1 3d^5$ are then treated as “valence”.

The TZ2P large frozen core basis set now reads as 3S 2P | 3S 1P 3D 1F, where 3S 2P terms have

been used to represent the “core”. In tellurium, $1s^2 2s^2 2p^6 3s^2 3p^6 4s^2 3d^{10} 4p^6 5s^2 4d^{10}$ are treated as the “core”, and only $5p^4$ as “valence”. The basis for this configuration is 4S 3P 2D | 3S 3P 1D 1F.

After all of these changes, it should be noted that the groundstate geometry and isomer series of the Cr_6Te_8 cluster remains unchanged. That is geometry, across all calculations, is in the $M = 7$ multiplicity. Within the next section we shall highlight any differences that should arise when changing the basis, and maintain that there are a larger number of similarities between them.

4.3 The ${}^7\text{Cr}_6\text{Te}_8$ Metal Core: QZ4P vs. TZ2P (Frozen Core)

The groundstate structure for Cr_6Te_8 , as computed with QZ4P and Large Frozen Core TZ2P, can be seen below in **Figure 4-1 (A)** and **(B)**, respectively. Major differences between the two can first be seen in the spin moments of the individual Cr atoms, specifically those of the apex atoms. In moving from a sizeable all-electron basis to the smaller, and then utilizing the “frozen core approximation” there is an increase in magnitude by approximately $0.5 \mu_B$ in each atom. Although not to the same magnitude, there is also an increase in the spin moments of the individual chromium atoms comprising the central Cr_4 square structure. Additionally, a decrease in the magnitude all the Te atoms, -0.144 to -0.106 . Moreover, an increase in average bond distances between Cr-Cr and Cr-Te, 2.713 \AA to 2.783 \AA , and 2.651 \AA to 2.693 \AA , respectively.

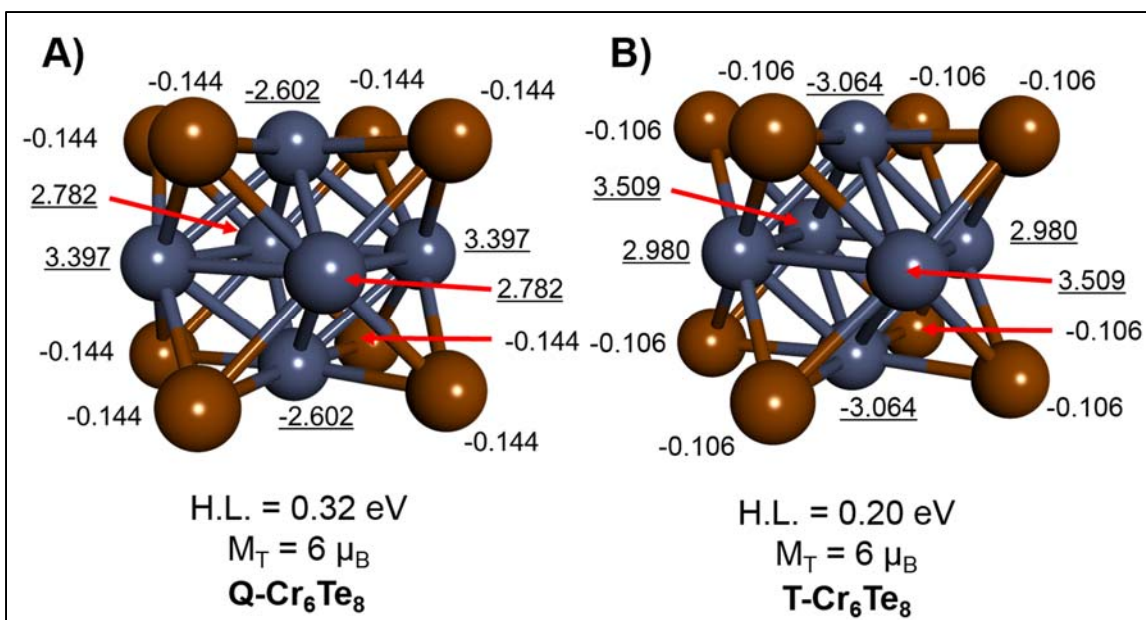


Figure 4-1. Groundstate geometries of ${}^7\text{Cr}_6\text{Te}_8$ utilizing different Basis Sets. QZ4P (A), TZ2P Large Frozen Core (B).

All of these changes can be attributed mainly to the restriction of the involved Cr (s) orbitals within the computation below the $4s^1$ level, and to a smaller degree the Cr (p) orbitals. The distortion and charge movement can be attributed to the behavior of the individual Cr atoms, and placing this restriction upon them effectively disallows further s (p) orbital movement to participate in bonding. Thus, the presence of Cr (s) from the TZ2P calculation can be seen in both its level diagram and density of states, **Figure 4-3** and **Figure 4-4**. The change in basis set and orbital involvements can also be easily seen in the spin populations of **Figure 4-2**.

Moreover, calculations utilizing the TZ2P basis without the frozen core approximation, TZ2P all-electron, have yielded a cluster with similar results and properties to that of QZ4P. This then confirms not the size of the basis set, but correct overall treatment and representation of the orbitals in the calculation to be of more importance. However, in our current context, the differences between the two cluster representations becomes mute due to the fact that upon ligation of the Cr_6Te_8 cluster this distortion is removed(!). Given the required computation time, ligated Cr_6Te_8 clusters as computed with QZ4P can be expected to achieve a representation

similar to that found with the TZ2P Large Core. Thus, making the Cr₆Te₈ cluster and its ligated counterparts as computed below sufficiently represented.

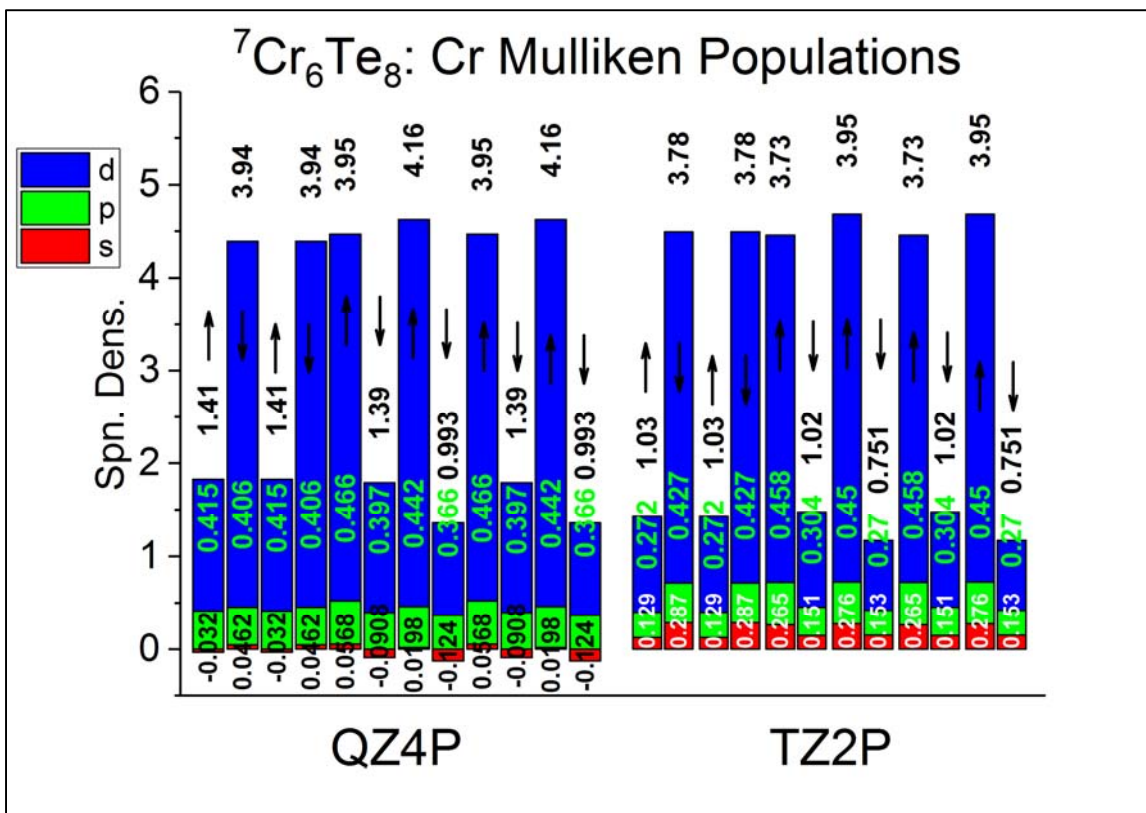


Figure 4-2. Mulliken spin populations per QZ4P and TZ2P (Large Core) basis set computed groundstates of the ⁷Cr₆Te₈ cluster. (Arrows mark direction of the both spin channels for each Cr atom, respectively.)

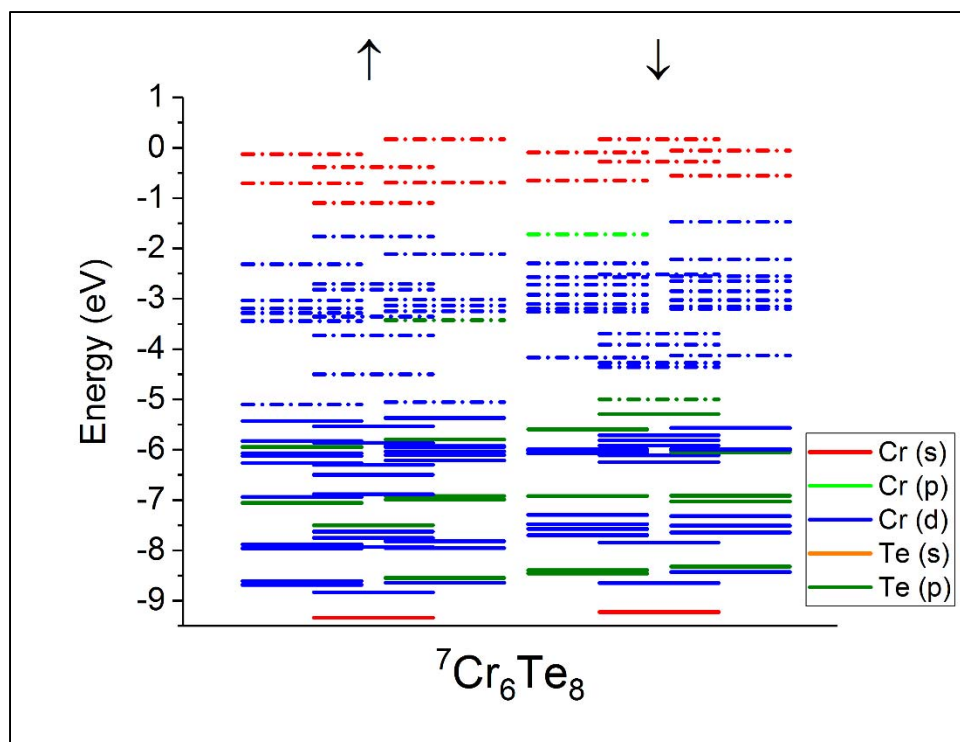


Figure 4-3. Atomic Orbital (AO) level diagram for ${}^7\text{Cr}_6\text{Te}_8$ as computed using the TZ2P (Large Core) basis set.

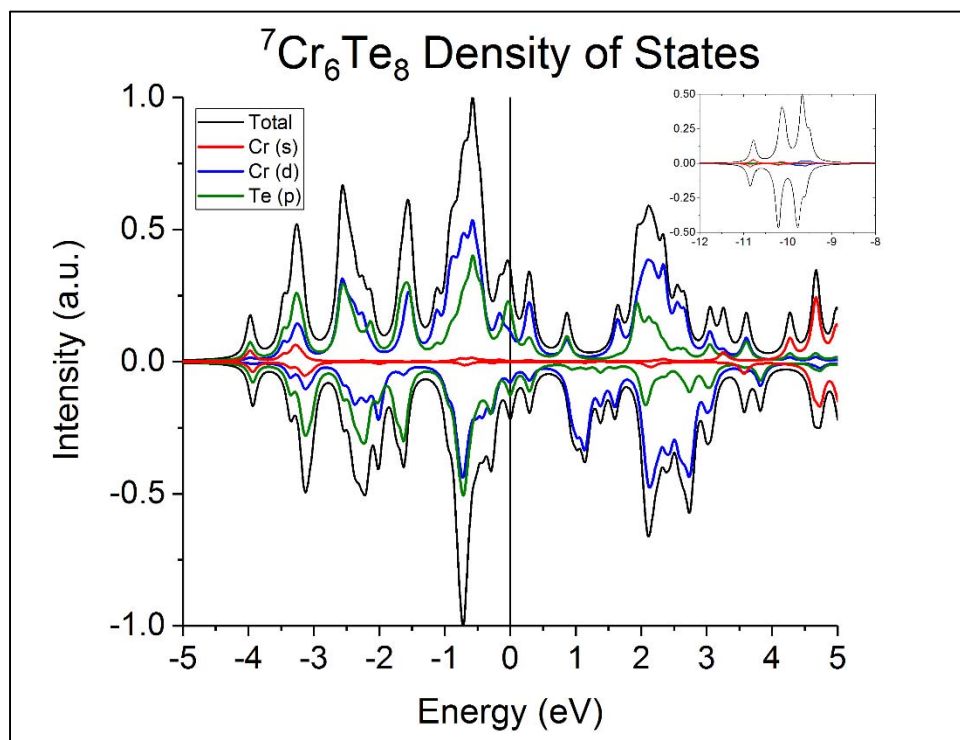


Figure 4-4. Density of States for the ${}^7\text{Cr}_6\text{Te}_8$ cluster as computed using the TZ2P (Large Core) basis set. (Inset shows location of Te(s). HOMO adjusted to zero eV.)

4.4 The ${}^7\text{Cr}_6\text{Te}_8(\text{PET}_3)_6$ Cluster

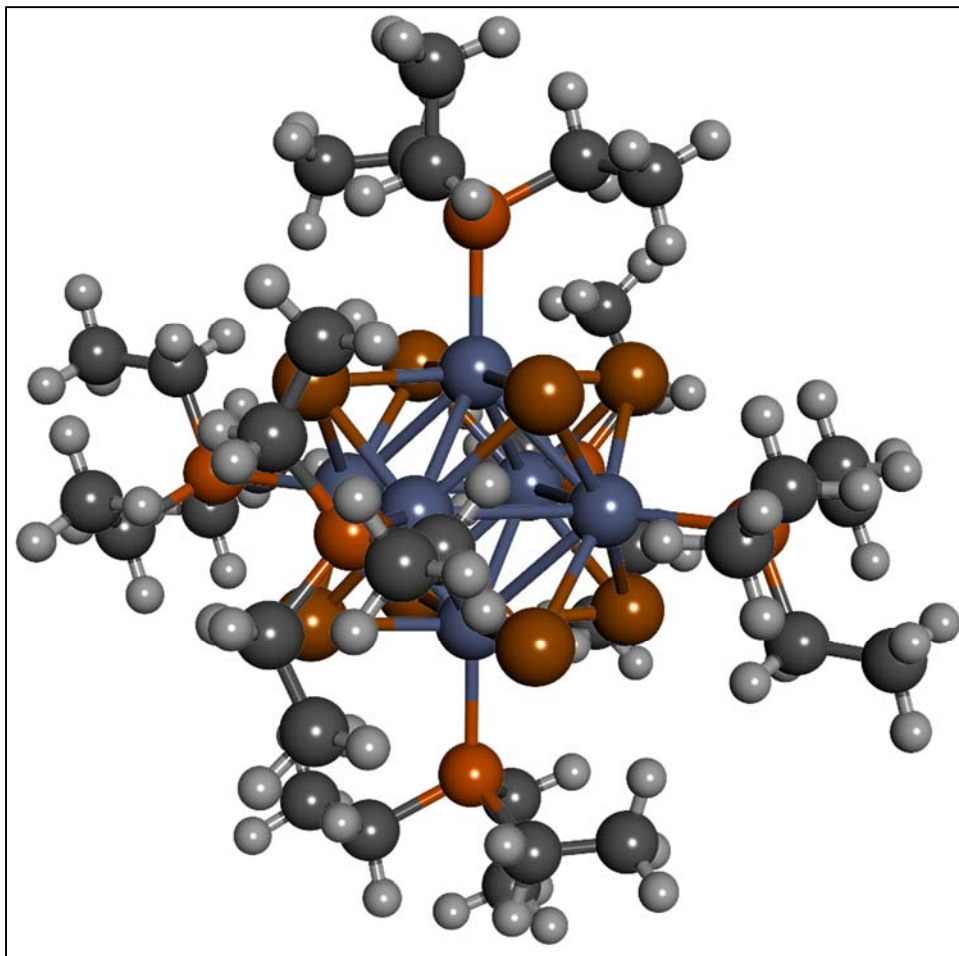


Figure 4-5. The groundstate structure of the ${}^7\text{Cr}_6\text{Te}_8(\text{PET}_3)_6$ cluster.

The stabilization of the Cr_6Te_8 structure as completed within the previous sections serves as the starting point for its passivation with various ligands. The groundstate structure for the ${}^7\text{Cr}_6\text{Te}_8(\text{PET}_3)$ cluster is shown above in **Figure 4-5**. More importantly, effects of introducing PET_3 onto the surface of ${}^7\text{Cr}_6\text{Te}_8$ can be seen below in **Figure 4-6 (A) and (B)**. The overall spin arrangement is maintained, across both Cr and Te atoms, with the spin up Cr atoms forming and maintaining the center Cr_4 subunit, with spin-down Cr atoms at the apex positions. We can see that upon passivation, the range in which we find the individual Cr spin moments has now narrowed and each fall between $| 2.99 - 3.21 \mu_B |$, respectively.

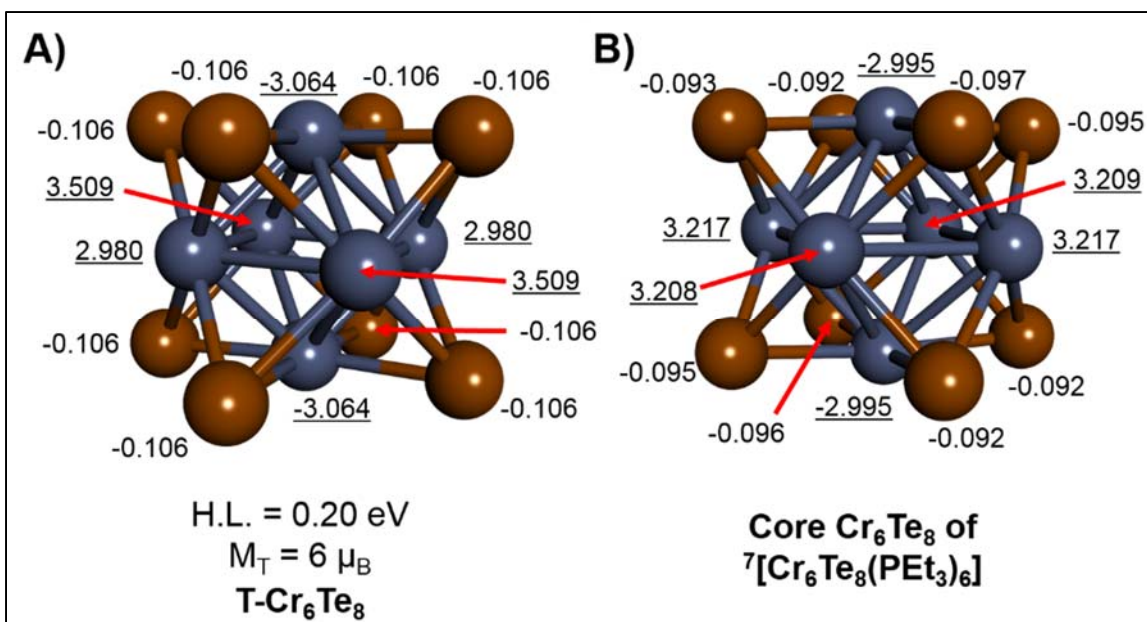


Figure 4-6. Groundstate geometries for ${}^7\text{Cr}_6\text{Te}_8$, and core of the ${}^7\text{Cr}_6\text{Te}_8(\text{PEt}_3)_6$ cluster. (A) and (B), respectively. (With HOMO-LUMO gap energies and individual spin moments. Cr spins are underlined.)

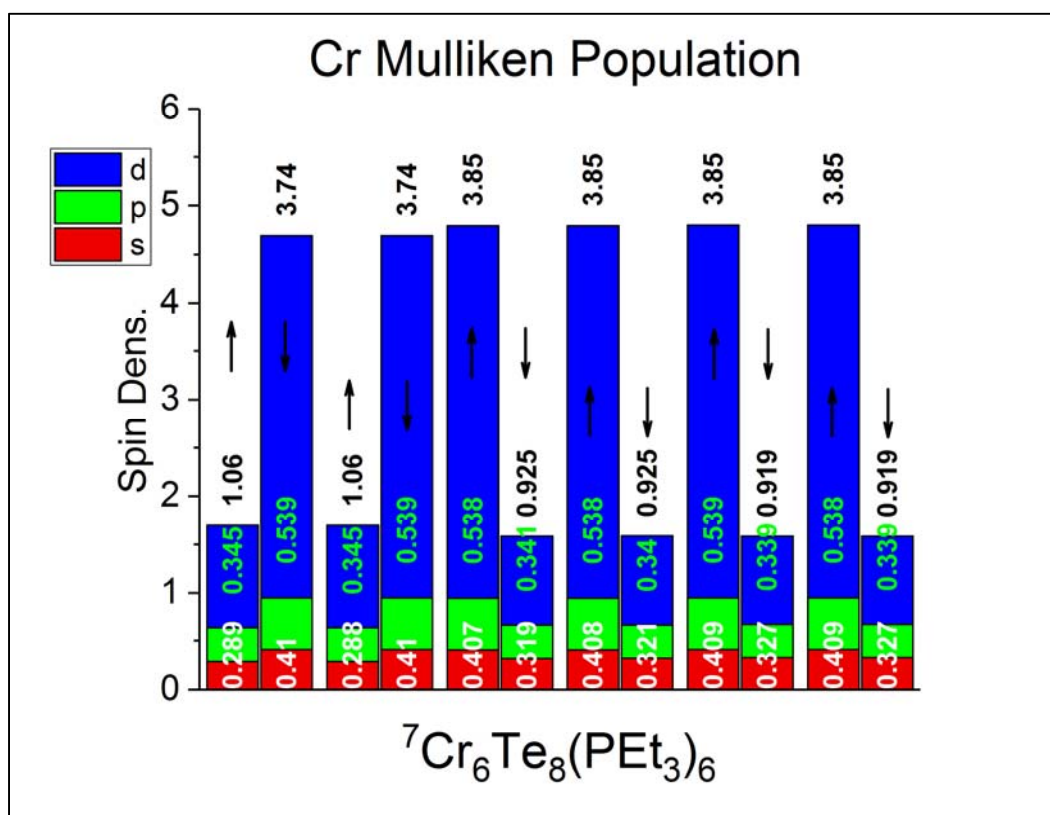


Figure 4-7. Mulliken spin populations for ${}^7\text{Cr}_6\text{Te}_8(\text{PEt}_3)_6$. (Arrows mark direction of both spin channels for each Cr atom, respectively.)

In comparing the Cr atom Mulliken populations of the ligated cluster in **Figure 4-7** with that of the bare ${}^7\text{Cr}_6\text{Te}_8$ (TZ2P-Large Core) cluster found in **Figure 4-2**, there is a clear difference. The PEt_3 ligands are bonding to Cr by way of both s and d -orbitals. Due to the introduction of electrons from PEt_3 ligand, the Cr (s) electrons no longer participate in the Cr-Cr bonding, and as a result there is an increase of the average bond distances between Cr atoms, to 3.050 Å. But, more importantly, the Cr atoms maintain their d -orbital spin density magnitudes to a relative degree in the spin up, and increase slightly in the spin-down. Confirmation of this effect caused by the added PEt_3 can be viewed within the clusters level diagrams and density of states, **Figure 4-8**, **Figure 4-9**, and **Figure 4-10**.

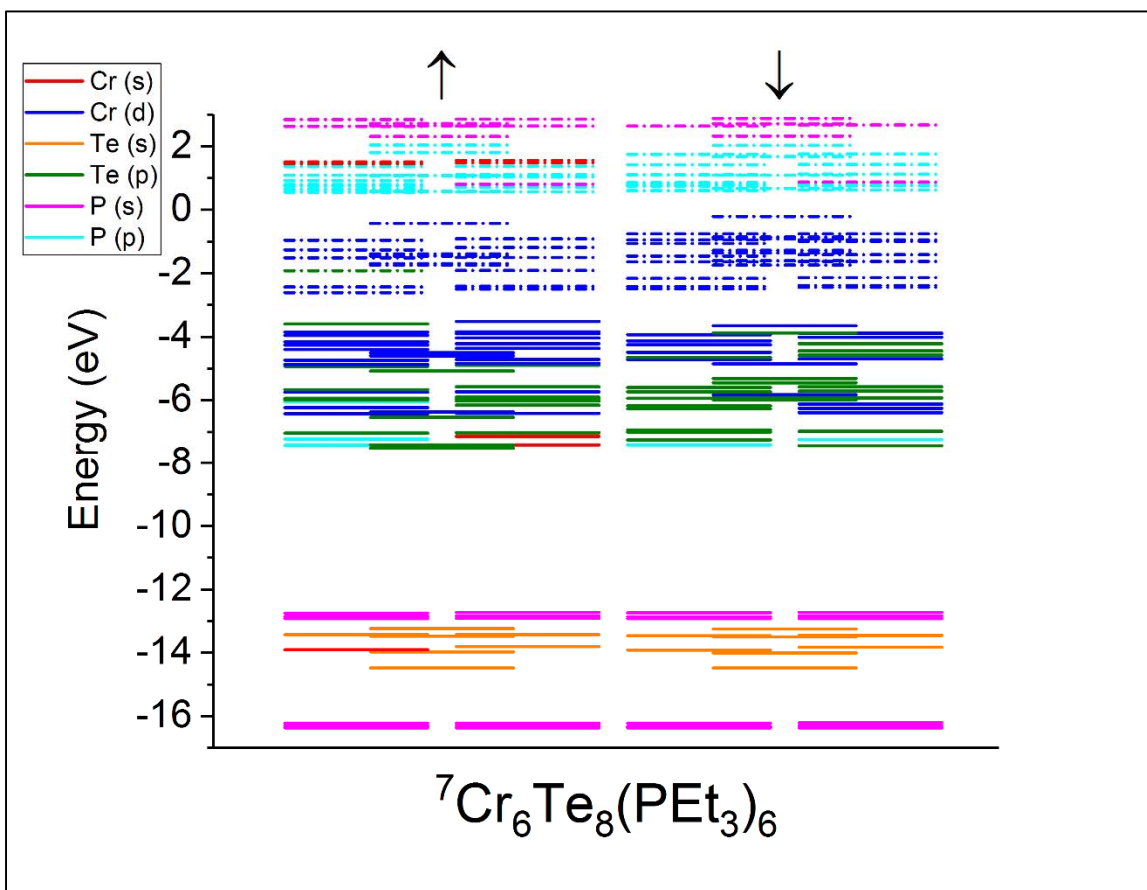


Figure 4-8. ${}^7\text{Cr}_6\text{Te}_8(\text{PEt}_3)_6$ Atomic Orbital (AO) level diagram, total.
(Carbon and Hydrogen orbitals removed for clarity.)

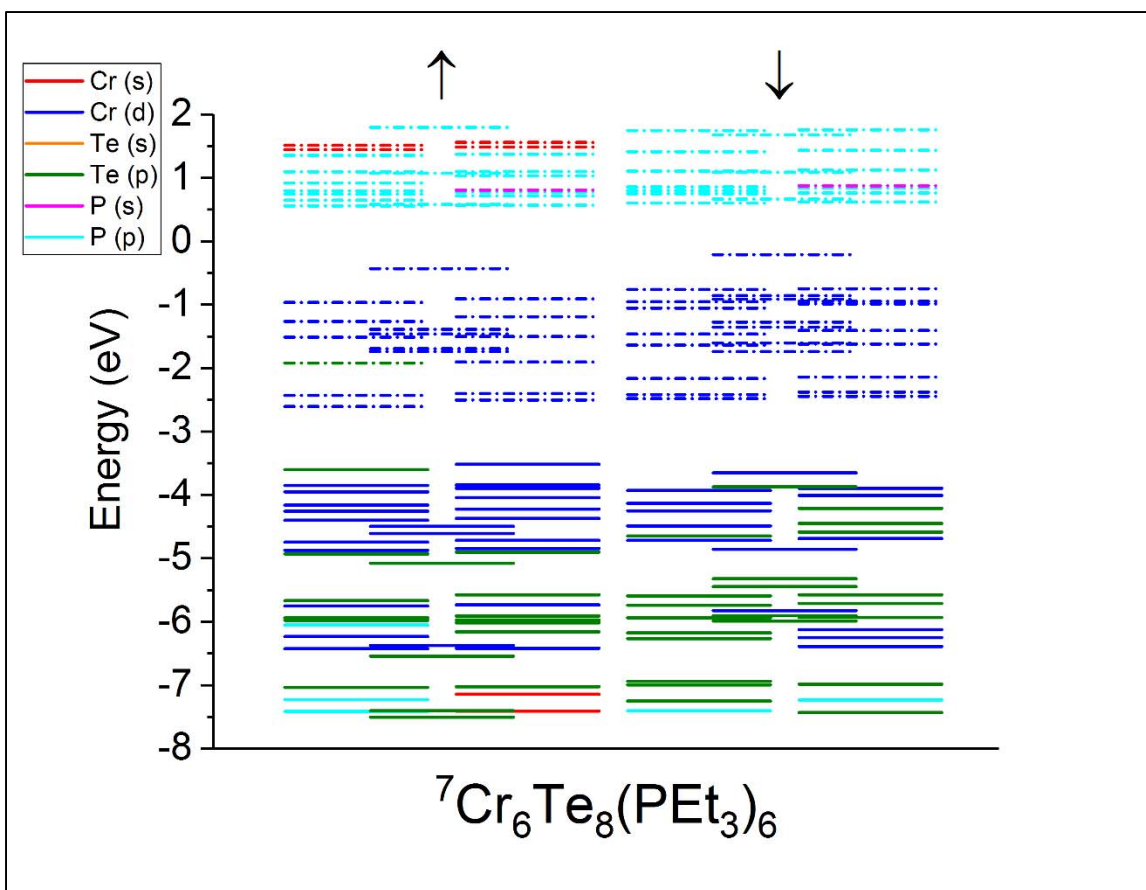


Figure 4-9. ${}^7\text{Cr}_6\text{Te}_8(\text{PEt}_3)_6$ Atomic Orbital (AO) level diagram, scaled.
(Carbon and Hydrogen orbitals removed for clarity.)

The level diagram of **Figure 4-9** clearly shows confirms our earlier assessment, but we find further that the P (p) orbitals are bonding with both the *d* and *s* orbitals of chromium. Specifically, in the region of -7 to -8 eV, the bonds are comprised of a mixture between Cr (s) – Te (p) – P (p), while the region of -5.5 to -6.5 eV comprises the region where the bonds are constructed of a mixture between Cr (d) – Te (p) – P (p). The total effect shifts the electronic levels upwards when compared with bare ${}^7\text{Cr}_6\text{Te}_8$ in **Figure 4-3**, note the scale used for both figures. Further evidence for the behavior between Cr_6Te_8 and PEt_3 continues within the density of states below in **Figure 4-10**. The donation of charge from PEt_3 is shown to reorganize the effective bonding orbitals involved between Cr (d) and Te (p). This also is another reason for

expansion in the bond distances between Cr-Cr atoms. Additional details regarding the electronic substructure of the ${}^7\text{Cr}_6\text{Te}_8(\text{PEt}_3)_6$ cluster will be elaborated upon below, in Sec. 4.5.

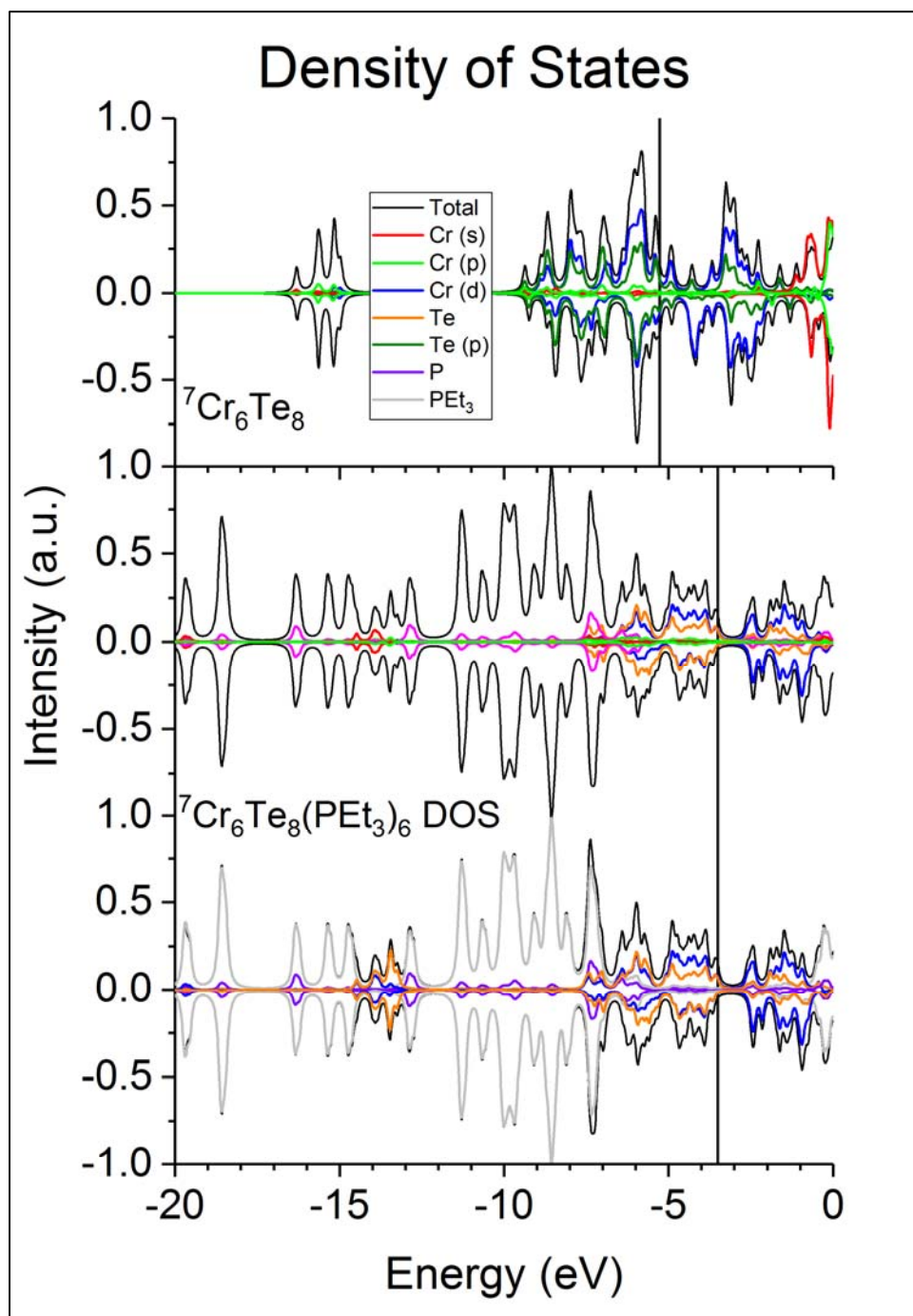


Figure 4-10. Density of states (DOS) for the Bare and PEt_3 ligated ${}^7\text{Cr}_6\text{Te}_8$ clusters. Top and Bottom, respectively. (Solid line represents HOMO of alpha spin channel.)

4.4.1 Robustness of $^7\text{Cr}_6\text{Te}_8(\text{PEt}_3)_6$

To verify the $M = 7$ multiplicity is truly the groundstate geometry for the ligated cluster, additional calculations have been performed. Specifically, in addition to the sequential series where the total magnetic moment of the system was varied, there are a handful of permutations regarding the arrangement of Cr spin moments that must be eliminated in terms of their energy. Due to the large, and more importantly, even number of Cr atoms present, these additional calculations are deemed necessary. Thus, these permutations strictly produce clusters where the Cr atoms are arranged antiferromagnetically throughout, and will then leave the overall cluster system in the singlet state, $M = 1$. In terms of calculation method, using the valence electrons, each individual Cr atom was given a maximal spin moment ($6 \mu_B$) which was then directed to point in either the spin-up or spin-down direction, together totaling a net $0 \mu_B$. From that point forward, the geometry is allowed to fully relax without restriction or constraints.

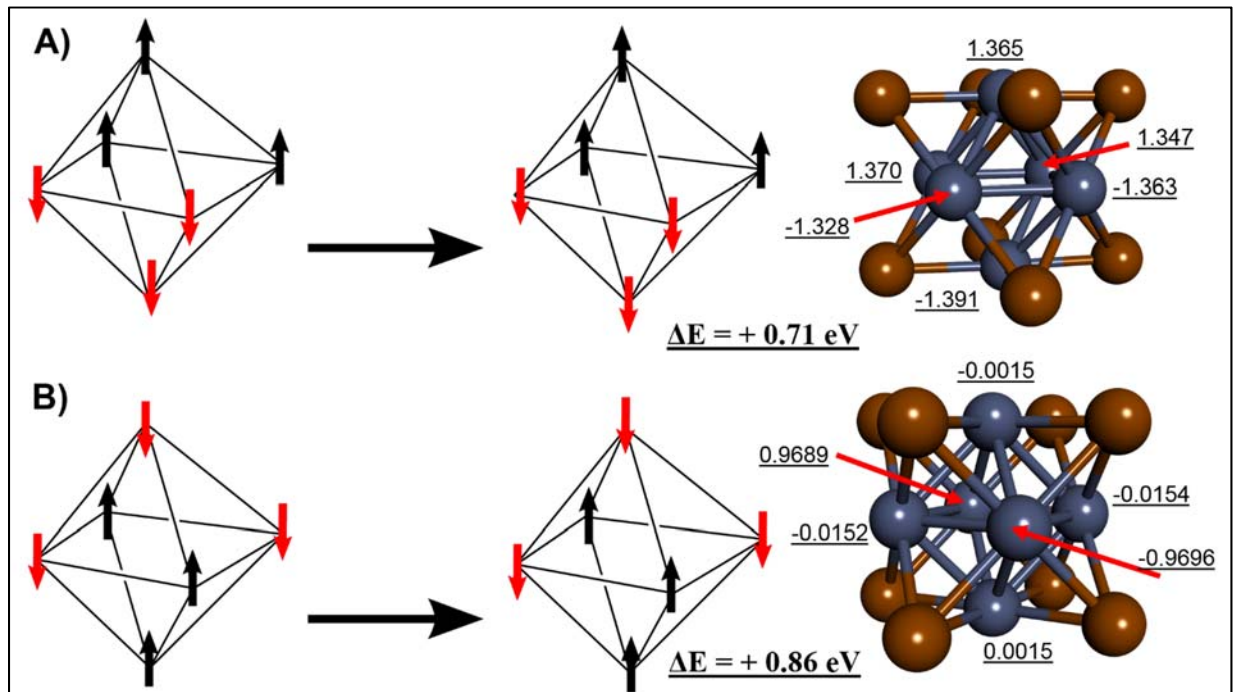


Figure 4-11. Starting and final Cr spin moment arrangements for the two singlet state permutations of $^1\text{Cr}_6\text{Te}_8(\text{PEt}_3)_6$. Each with distance in energy from groundstate, core geometry, and individual Cr moments labelled. (The PEt_3 ligands have been removed for clarity.)

Two permutations of spin moments have been calculated, and the results of this exercise are shown in **Figure 4-11 (A)**, and **(B)**. The first arrangement possible for the $M = 1$ configuration is two complexes of trigonal chromium coupling antiferromagnetically, effectively two faces of the Cr_6Te_8 core. The start (left) and final (middle) spin moment arrangement is shown for both, as well as the cluster geometry and labelled associated spin moments for the individual chromium atoms (right). The PEt_3 ligands have been removed for clarity.

In addition to the above verification process, the $\text{Cr}_6\text{Te}_8(\text{PEt}_3)_6$ cluster has also been found for a variety of spin moments. The energies for each, as they compare to the groundstate, can be seen below in **Figure 4-12**. Noting the scale, the figure clearly highlights a preference for the total cluster to remain in the central, 2, 4, and 6 μ_B spin states. Above, we have established the 0 μ_B antiferromagnetic spin state to be unfavorable, and we now confirm the same for the quenched singlet state. Moreover, the difference between high and low spin states, 6 and 4 μ_B , is approximately 0.20 eV.

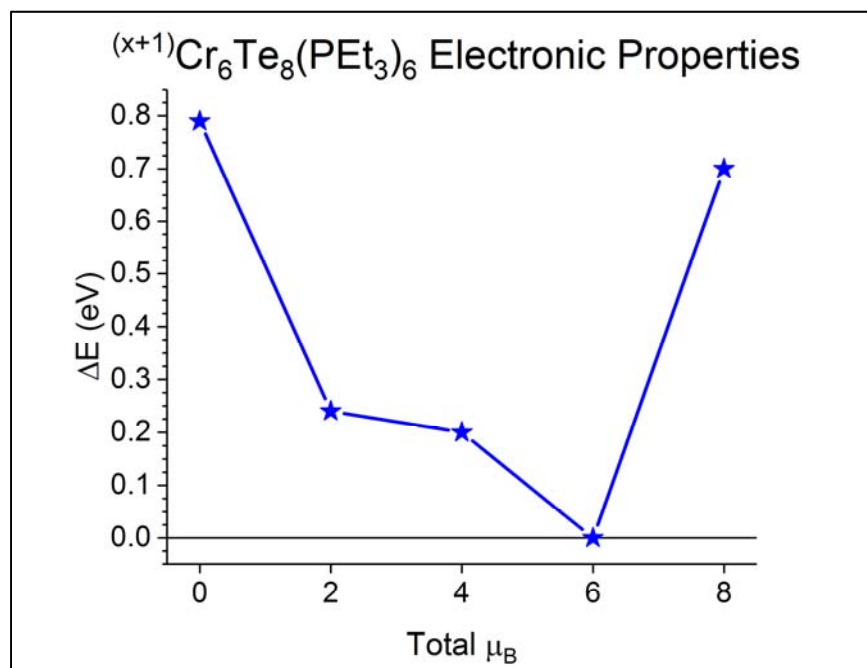


Figure 4-12. Cluster energetics for ${}^x\text{Cr}_6\text{Te}_8(\text{PEt}_3)_6$ across various values of total μ_B . Cluster energies have been normalized to groundstate.

4.5 Ligand Exchange

Recalling the discussion above in Chapter 1, where periodic solids are constructed through leveraging a clusters fundamental properties of ionization potential and electron affinity. Specifically, we can manipulate those properties through alteration of the clusters valence electron count. A particular strategy to tune electron count, as well as stabilize the cluster core, is to attach ligands. In addition to passivating the metallic core, ligands form covalent bonds that also change the valence electron count. This type of cluster electron count has been completed previously in the literature, where a large number of solids composed of pure or mixed ligated clusters of gold have been used as motifs who are subsequently arranged into periodic solids.^{15,17,41,66,214–218} The stability of these cluster motif systems is rationalized within the superatom framework.^{16,23} That is, the stable species formed from this process as its valence count obtains a value corresponding to a filled valence and large HOMO – LUMO gap.

Knowing now the structural form of ${}^7\text{Cr}_6\text{Te}_8$ cluster, as well as its counterpart within the ${}^7\text{Cr}_6\text{Te}_8(\text{PEt}_3)_6$, we aim to now demonstrate within this chapter that ligands can be used to significantly alter the ionization potential and electron affinity of the total cluster. In altering these properties, we can thereby enable this metallic core to behave as either an electron donor or acceptor. The study carried out within this chapter, utilizing the same formalisms established above, further incorporate a variety of alternate ligands, belonging to two different classes. The electron donor of PH_3 , and electron acceptors such as carbon monoxide (CO) and cyanide (CN). Note the chemical formula for cyanide is actually CN^- , but here we take the neutral, effectively the cation. The reason for this is to view any possible changes between the CO and CN decorated cluster by strategically removing a solitary electron from each bonding site. Once the calculations regarding the total cluster of ${}^7\text{Cr}_6\text{Te}_8(\text{PEt}_3)_6$ had been completed, it was a trivial

matter (in terms of setup, calculations, time, and resources) in exchanging the ligand for smaller versions. Our main objective is to now examine the effect of each ligand upon the electronic spectrum of the overall cluster. We can view these effects not only through spin population density, but also in the modification of the density of states, as we have done in the previous chapter.

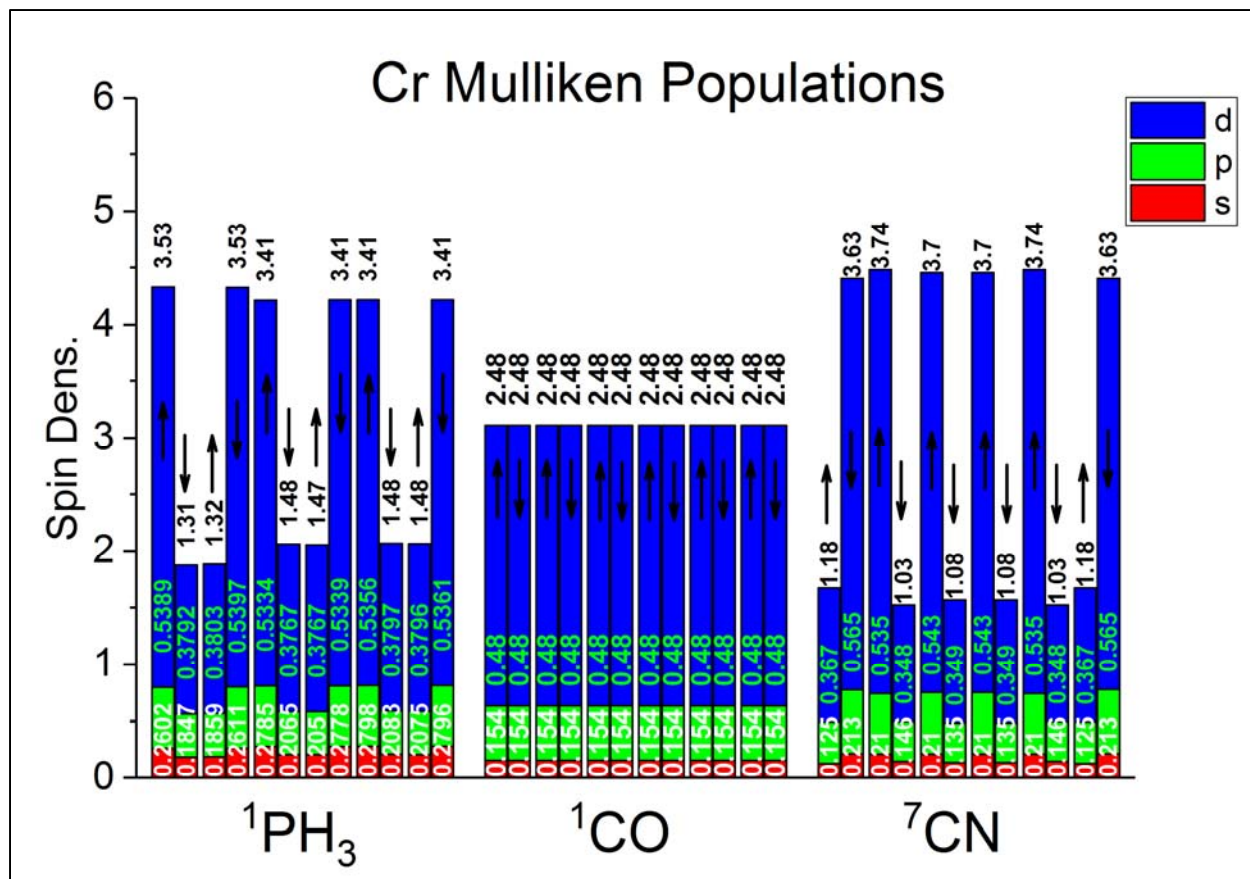


Figure 4-13. Mulliken spin populations for individual chromium atoms within the ligated systems of $L = \text{PH}_3$, CO , and CN . (left-to-right, respectively. Superscript designates total system multiplicity.)

An immediate change that is visible across these clusters is their total magnetic moment, and how that moment is comprised from the individual spin moments of the Cr atoms. We can see those changes above in **Figure 4-13**, for each of the ligands PH_3 , CO , and CN , left-to-right, respectively. There are immediately a few points to address, the first being the total absence of a total magnetic moment for both PH_3 and CO cluster variants. Moreover, that the Cr atoms

within the PH_3 cluster are antiferromagnetically arranged, while in the CO case, those same moments are quenched and thus totally absent. Additionally, the cluster decorated by CN maintains the original $M = 7$ groundstate found in the PEt_3 cluster. It should also be noted, that while the clusters of CO and PH_3 closely maintain the central core structure of the Cr and Te atoms, this is however not the case for the CN cluster whose core is now heavily distorted. Moreover, that the spin moments of the underlying Cr atoms now fall within the region of $|2.73 - 2.96| \mu_B$, which is only a slight difference from those found within the PEt_3 cluster, whose moments are in the range of $|3.00 - 3.22| \mu_B$.

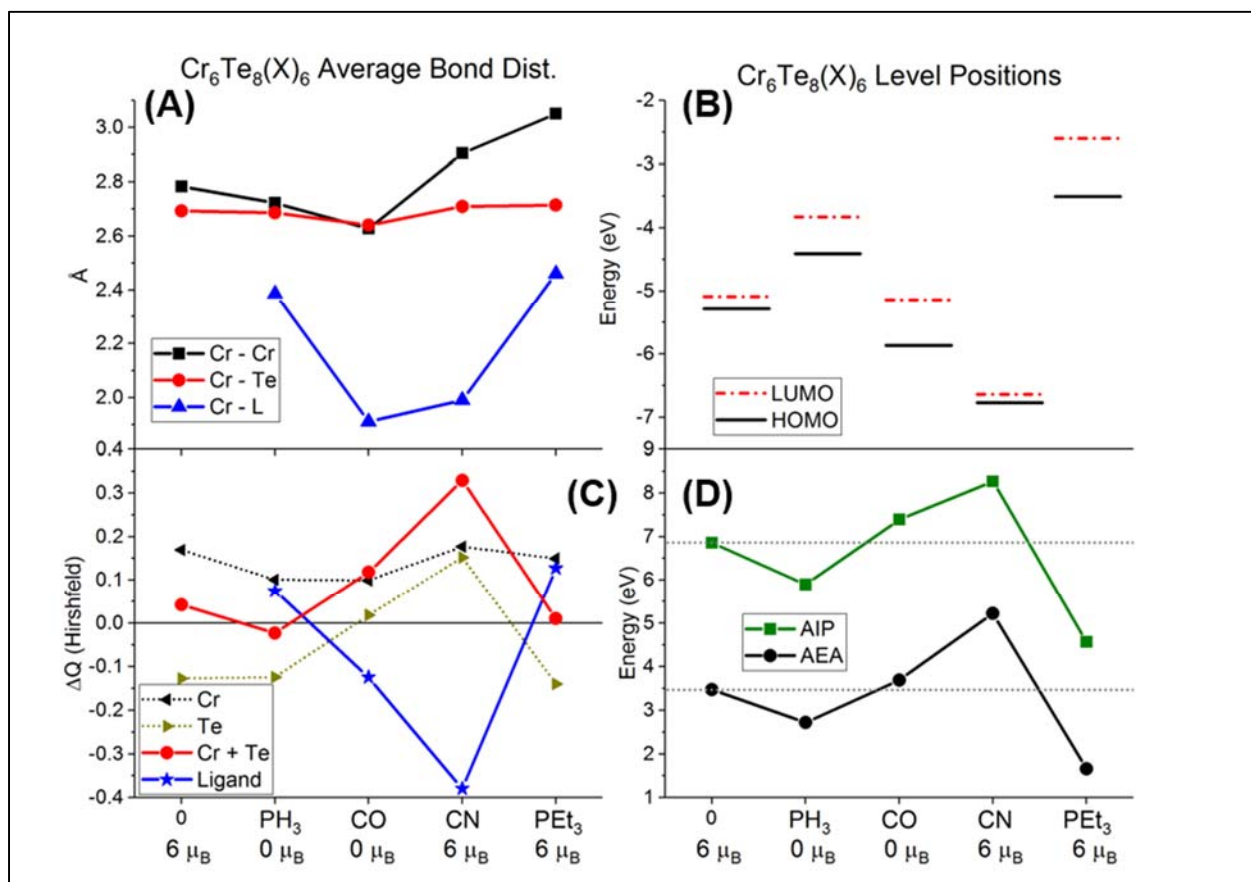


Figure 4-14. Average bond distances, HOMO-LUMO level positions, Hirshfeld Charge Density, Adiabatic Ionization Potential and Electron Affinity energies, for none and various ligands. (A) – (D), respectively. (Spin moments are in reference to the groundstate structure of that system.)

The plots of the basic electronic properties we aim to alter with ligand substitution are given above in **Figure 4-14**. Here we can see, the average bond lengths between Cr - Cr , Cr - Te

atoms, as well as the length between Cr and ligand. The associated HOMO and LUMO levels for all of our clusters. The change in Hirshfeld charge density for Cr, Te, and Ligand. Finally, the change in value for both ionization potential and electron affinity. In panel (A) of **Figure 4-14**, we can see the overall effect of the ligand upon the central cluster core. The most intriguing plot here is the average bond lengths between the Cr, which are significantly altered and highly dependent upon the type of ligand. Moreover, there is a significant difference between those bond lengths found when comparing PH₃ and PEt₃ cluster variants as well. Additionally, remembering from above, that although CN and PEt₃ clusters have large Cr bond distances, the CN cluster system does not maintain its geometry. The Cr bond distances for the PEt₃ cluster fall within the region of 2.972 – 3.153 Å, while for the CN geometry 2.678 – 3.068 Å, two wildly different ranges in length.

Despite these large variations in bond lengths between the Cr atoms, their Hirshfeld charge densities deviate the least when compared to the Te atoms and Ligands, **Figure 4-14 (C)**. Upon addition of PH₃ there is a slight decrease in charge density of the Cr, 0.169 to 0.101 e⁻, meaning there is a significant amount of donation from the ligand. This is confirmed by the positive density experienced by the PH₃ ligand. The addition of CO oddly does not modify the charge density of the Cr as compared to PH₃, but does drastically alter that of Te whose role has changed from charge removal to charge donation, from -0.125 to 0.019 e⁻. This charge movement is further maximized in the attachment of CN. Charges for both Cr and Te atoms are diminished, a net positive charge of 0.176 e⁻ for Cr, close to its value of the bare ⁷Cr₆Te₈ cluster, and 0.152 e⁻ for Te. These effects upon Cr and Te are exactly inverse to that of the ligand, of course, which for both CO and CN can be seen to be accepting this charge (blue line, **Figure 4-14 (C)**). Things appear to return to “normal” with the addition of PEt₃, where charge density

values return closely to those found in the bare and PH_3 ligated cores. Interestingly enough, the Hirshfeld charge density of the P atoms in both the PH_3 and PET_3 clusters are drastically different. Although in both systems it is donating charge, within the PH_3 system it has density of $0.080 e^-$, while in PET_3 it has a density of $0.206 e^-$. Highlighting the fact that these two ligands are not as similar as one might initially expect.

The bare ${}^7\text{Cr}_6\text{Te}_8$ cluster has a high ionization potential (IP) of 6.96 eV and electron affinity (EA) of 3.47 eV, **Figure 4-14 (D)**. Both of these number are some degree higher than those found in the literature for the bare ${}^7\text{Ni}_9\text{Te}_6$ cluster, 6.33 eV and 2.63 eV; and even more so for bare ${}^2\text{Co}_9\text{Te}_6$, 5.82 eV and 2.38 eV, respectively.⁸¹ We further find an IP of 5.95 eV and 2.72 eV EA values for the PH_3 system. An effective lowering from the bare cluster, resulting in the raising of the HOMO and LUMO levels, **Figure 4-14 (B)**. And, as expected, the raising of IP and EA values in both CO and CN systems, as well as the resultant lowering of their respective HOMO-LUMO levels. In CO, the IP has reached 7.39 eV and EA of 3.69 eV. This pales in comparison to the CN system, whose IP has value of 8.27 eV and an EA of 5.22 eV. We go further, and compare these values to the PET_3 system, which has IP of 4.49 eV and EA of 1.74 eV. Both numbers significantly smaller than its ligated counterparts. To give a frame of reference for these values, as a means of comparison, the IP of Sodium (Na) is 5.14 eV and EA of Chlorine (Cl) is 3.61 eV. We have focused our attention in these calculations to AEA and AIP, as these clusters will relax when paired with a counterion in forming a cluster assembly. Thus, across all of these calculated values and properties, it has been shown that these clusters are capable of such an assembly, in the role of either donor or acceptor.

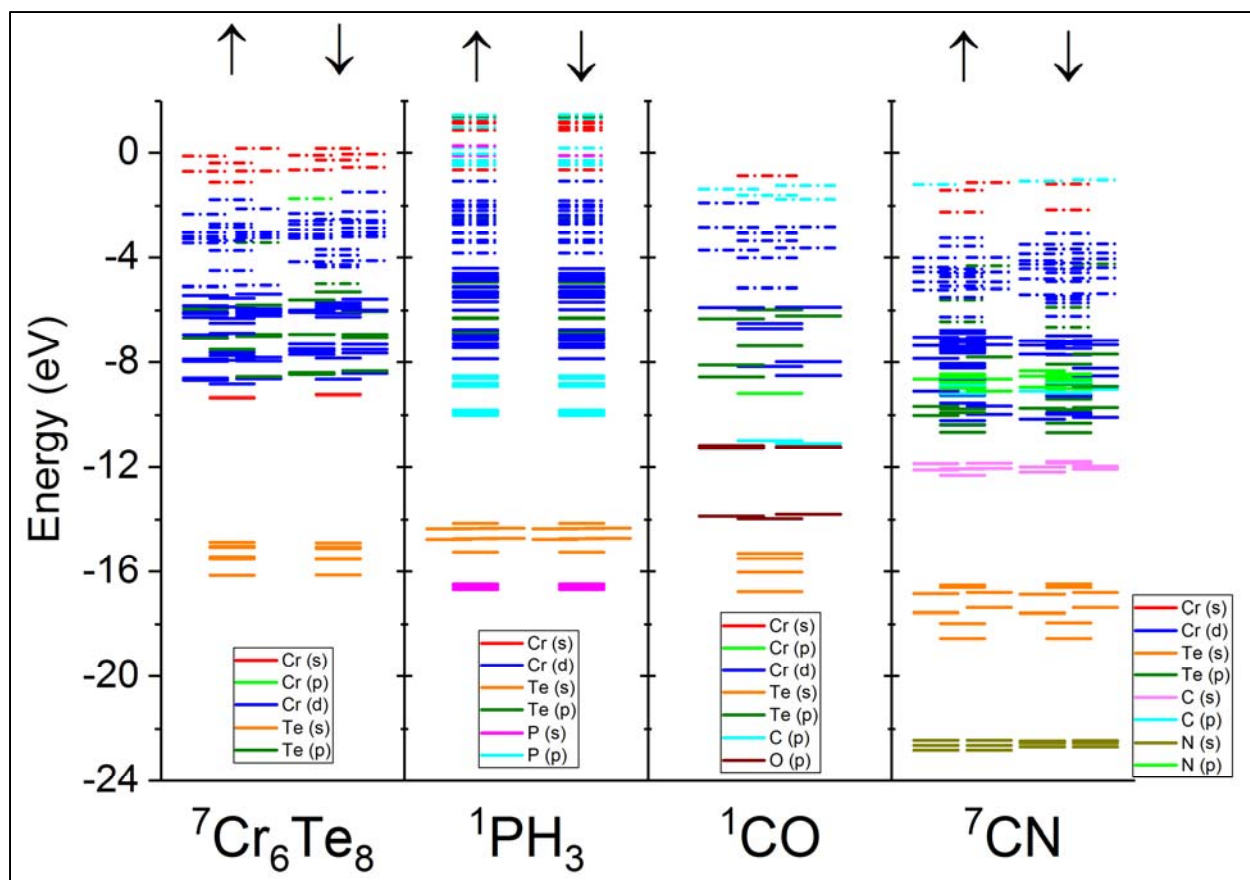


Figure 4-15. Atomic Orbital (AO) level diagrams for Bare and Ligated ${}^x\text{Cr}_6\text{Te}_8$ cluster cores. Bare ${}^7\text{Cr}_6\text{Te}_8$, with PH_3 , CO , and CN versions, left-to-right respectively. (Each with individual legend. Superscript designates total cluster multiplicity. Degeneracies of CO not labelled.)

In considering the atomic changes yielding these alterations to the IP and EA values, the entirety of the atomic orbital energy levels for each cluster, compared to those seen in **Figure 4-14 (C)**, have now been plotted in **Figure 4-15**. There are significant changes to these levels through the alteration of these ligands. The addition of PH_3 shifts upwards the HOMO and LUMO (HL) levels of the bare cluster from -5.29 eV and -5.09 eV, to -4.42 eV and -3.82 eV. The HL gap has now doubled in size. The addition of CO however lowers HOMO level of the bare cluster to -5.87 eV, and increases the HL gap to 0.73 eV. This lowering of the HOMO levels continues with the addition of CN , and can be found at -6.77 eV. But, the CN cluster now has a HL gap of 0.13 eV which is almost half of that in the bare cluster.

In addition to the one electron orbitals above, we can view the movement of the orbitals within the Density of States (DOS) plots of **Figure 4-16**. Within that figure, as well as the DOS plot of the bare and PEt_3 clusters in **Figure 4-10** above, we can readily see the lowering and alteration of the HOMO level (vertical line) through the addition of various ligands. Moreover, although the region near the HOMO level is still comprised of Cr (d) orbitals for all of these clusters, the diminishment of charge on the Te atom can readily be seen in the cluster of CN, where its contributions to the total system have now moved lower in energy.

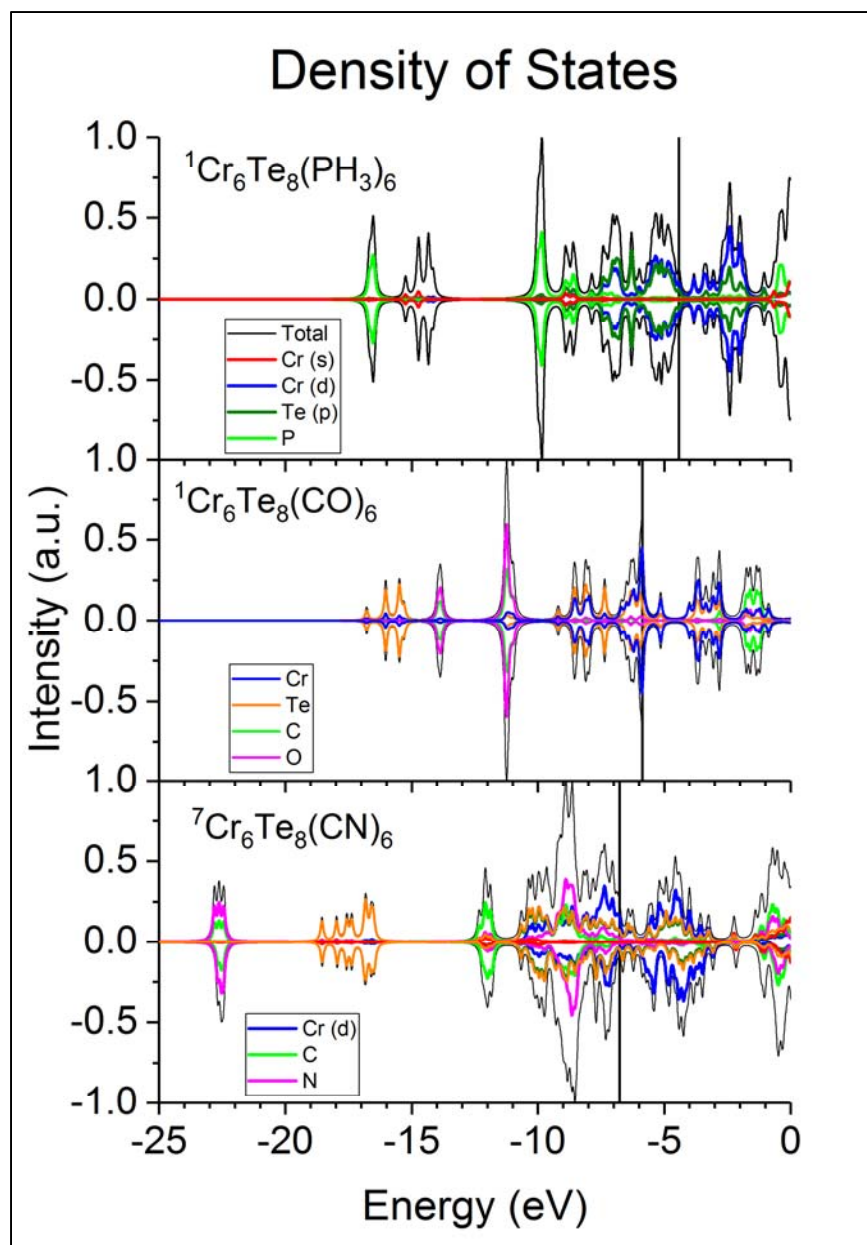


Figure 4-16. Density of States for various ligated $\text{Cr}_6\text{Te}_8(\text{L})_6$ clusters. $\text{L} = \text{PH}_3, \text{CO}, \text{CN}$; respectively. Solid line represents HOMO of alpha spin channel. (Colors from upper legend apply downwards, unless otherwise noted.)

4.6 Discussion & Conclusions

To summarize, the theoretical studies above have illustrated a number of points. The first being in regards to our original cluster of ${}^7\text{Cr}_6\text{Te}_8(\text{PEt}_3)_6$ and the bare ${}^7\text{Cr}_6\text{Te}_8$ core. The ligation of this core does not modify the overall magnetic moment, but does have an influence upon the bond lengths, ionization potential, and electron affinity. Moreover, despite this ligation the energy difference between the groundstate $6 \mu_B$ and next higher isomer of $4 \mu_B$, remains nearly the same in both of these systems at approximately 0.20 eV. Further adaptability of the bare cluster has been shown in the alteration of the attached ligand. We have shown how these ligands can be utilized in changing the strength of electron withdrawal or donation of the cluster. And, depending on the ligand, fundamentally alter both the physical and electronic structure of the total cluster. The addition of PH_3 and PEt_3 drive the cluster to electron donation, each to a differing degree, however, the addition of CO and CN ligands drives the total cluster toward electron acceptor.

Combining the information of the previous sections together, we have found the PEt_3 donor ligand to be the most desirable in this investigation. This is chiefly due to the bare cluster maintaining its large magnetic moment. But, also due to the fact that the cluster is now more stable after ligation, as well as a better electron donor. Two properties which further solidify it as a suitable building block in cluster assembled materials.

5 Summary & Future Directions

During this thesis we have focused on the evolution of bonding as the Cr atoms are mixed with Te so as to provide insight into the stability and magnetic properties of the $\text{Cr}_6\text{Te}_8(\text{PEt}_3)_6$ cluster that forms a periodic $[\text{Cr}_6\text{Te}_8(\text{PEt}_3)_6][\text{C}_{60}]$ cluster assembled solid. Our results on small Cr_xTe_y cluster indicate that while pure Cr_n clusters display antiferromagnetic coupling, the bonding and the nature of coupling evolve as Te is added. Furthermore, that the addition of Te results in a stronger binding with Cr that in turn destabilizes the weaker Cr-Cr metal bonds. Initially, the addition of Te leads to a Cr_2Te_3 cluster with quenched Cr spin moments. This situation only occurs in this particular size and changes as one goes to larger clusters where the Cr sites continue to carry spin magnetic moments.

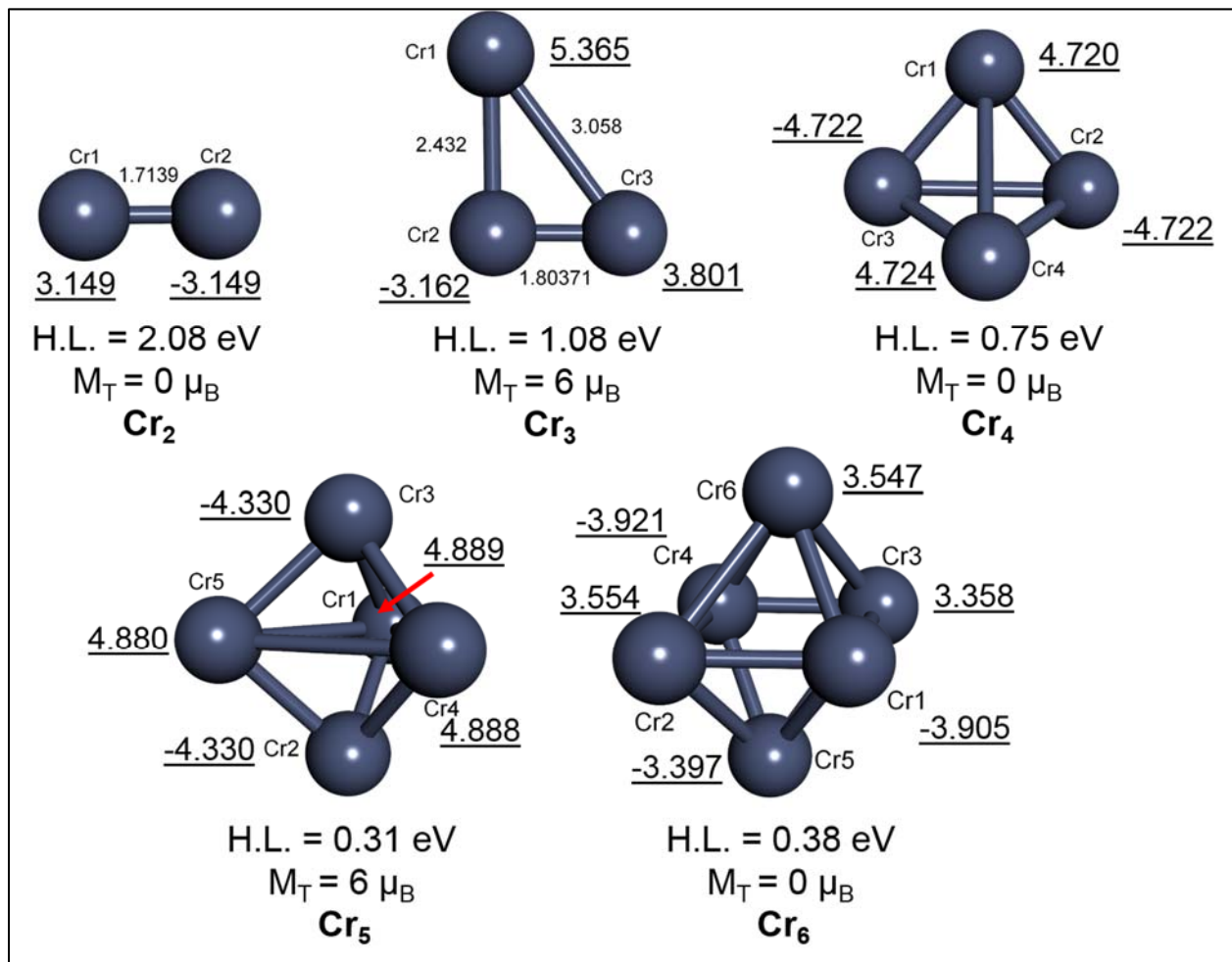
The manipulation of the underlying Cr cluster structure by the addition of Te atoms involves two aspects. The first, is the bonding of the incoming Te (p) orbitals upon those of Cr (d). The second, is the specific coordination of Te in forming either two or three bonds. Consequently, the bonding of Te results in cluster geometries consisting of two-coordinated, three-coordinated, and a mixture of both, depending on the size of the total cluster. In fact, as a general observation, clusters that contain an abundance of triply coordinated Te are the more stable. The twofold coordination of Te atoms is mostly seen in clusters of up to four Cr, for larger sizes, Te bonds with triple coordination. The balance between Cr and Te atoms exemplifies itself within the geometry of Cr_6Te_8 . Here, we have shown, that it has a high magnetization that can be linked to the symmetrical structure, which is reliant upon the equal number of Te atoms distributed around the cluster. Moreover, this cluster maintains its magnetization upon ligation with the triethylphosphine (PEt_3) ligands.

The studies upon the ligated cluster shows that the stability of the bare Cr_6Te_8 core carries over to the ligated species, making it a suitable building block for synthesis in constructing cluster assembled materials. This aspect was demonstrated within Chapter 4, where we investigated the stability of the properties found in the ligated cluster across a variety of ligands having donor or acceptor characteristics. In particular, the ${}^7\text{Cr}_6\text{Te}_8(\text{PEt}_3)_3$ cluster is not only highly stable, due to its large HOMO-LUMO gap, but also maintains its high magnetization within its first cation, $5 \mu_B$. This finding allows us to make a first step towards understanding the magnetic properties of the $[{}^7\text{Cr}_6\text{Te}_8(\text{PEt}_3)_3][\text{C}_{60}]$ periodic solid. Note that although ${}^7\text{Cr}_6\text{Te}_8(\text{PEt}_3)_3$ has a net magnetic moment, the local spins at two Cr sites are antiferromagnetically coupled to the remaining four. This inter-antiferromagnetic coupling is indicative of the clusters behavior after entering into a periodic solid with C_{60} . The previous studies upon the companion cluster system of $[\text{Ni}_9\text{Te}_6(\text{PEt}_3)_8][\text{C}_{60}]$ have shown only a weak antiferromagnetic coupling.²¹⁹ Although, we have not investigated this aspect within $[{}^7\text{Cr}_6\text{Te}_8(\text{PEt}_3)_3][\text{C}_{60}]$, the presence of a similar coupling could mark a system with both inter- and intra-antiferromagnetic coupling and as previous studies on perovskites have indicated, these types of systems can show an inverse susceptibility vs temperature plot which saturates at higher temperature. This could account for the observed saturation of the inverse susceptibility of the $[{}^7\text{Cr}_6\text{Te}_8(\text{PEt}_3)_3][\text{C}_{60}]$ system seen in experiment.

The implications of the theoretical results and studies found within the previous chapters can be summarized in two points. The first, knowing the history of two-dimensional CrTe solids with their numerous stoichiometric versions and properties, we can conclude that those properties continue downward into the atomic scale and their binary clusters. The number and arrangement of Te around Cr both play an important role. Additionally, the studies herein show

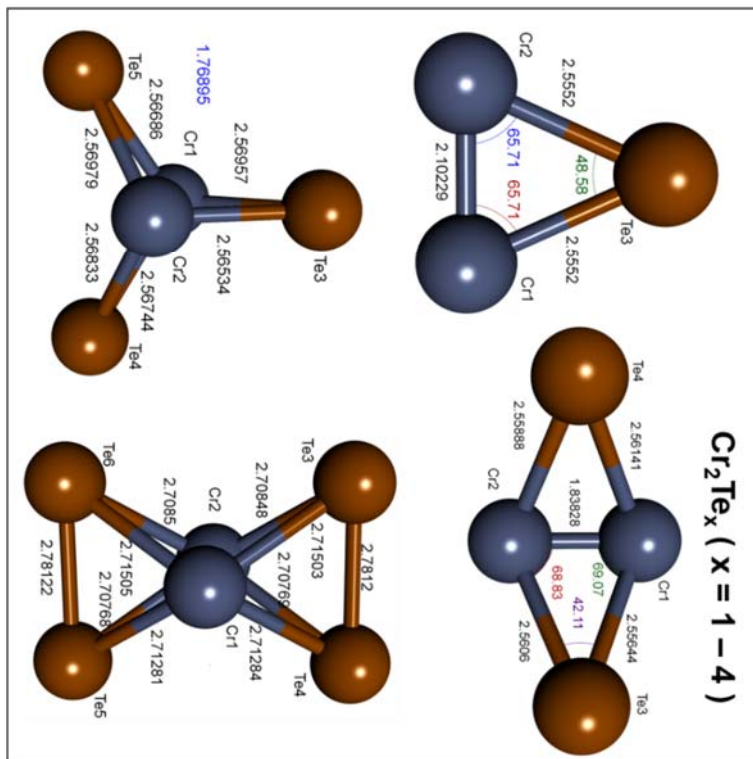
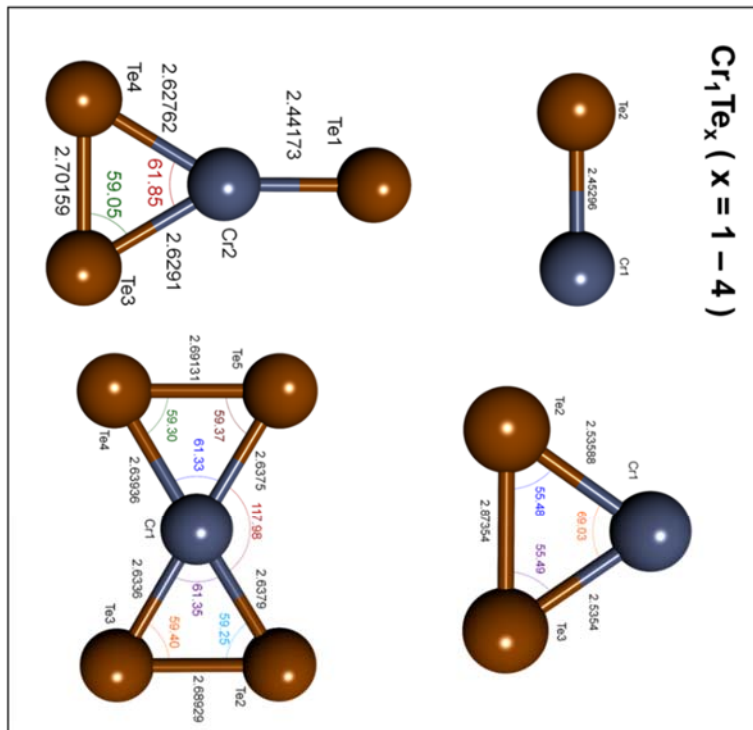
that the cluster of Cr_6Te_8 retains the flexibility in its properties most often seen within two-dimensional CrTe , and this flexibility and adaptability is now being exploited in a manner to construct novel materials.

Appendix A Cr_x Bond Lengths



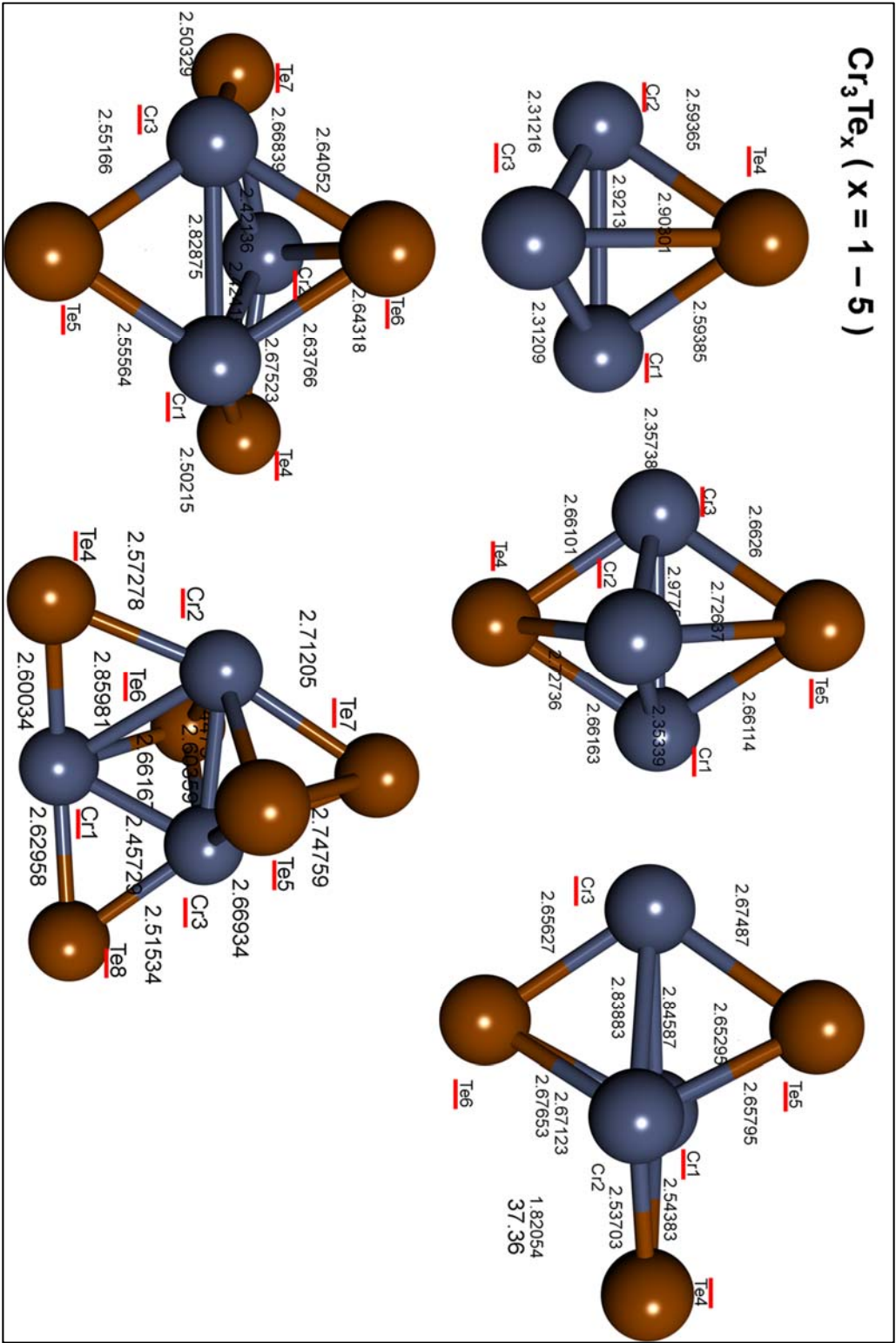
2		3		4	
Cr1-Cr2	1.7138	Cr1 - Cr3	3.0580	Cr1 - Cr2	2.3506
		Cr1 - Cr2	2.4320	Cr1 - Cr3	2.3473
		Cr3 - Cr2	1.8037	Cr1 - Cr4	3.0121
				Cr2 - Cr3	3.0118
				Cr4 - Cr2	2.3486
				Cr4 - Cr3	2.3518
5		6		7	
Cr1 - Cr2	2.3936	Cr3 - Cr4	2.3452	Cr6 - Cr1	2.4354
Cr3 - Cr1	2.4016	Cr4 - Cr2	2.3767	Cr3 - Cr1	2.4640
Cr3 - Cr4	2.3916	Cr2 - Cr1	2.3777	Cr5 - Cr1	2.4505
Cr3 - Cr5	2.3935	Cr3 - Cr1	2.3430	Cr3 - Cr6	2.8215
Cr4 - Cr1	3.0382	Cr6 - Cr3	2.5563	Cr4 - Cr3	2.2444
Cr4 - Cr2	2.4025	Cr6 - Cr4	2.3714	Cr4 - Cr6	2.4304
Cr5 - Cr1	3.0444	Cr2 - Cr6	2.7607	Cr2 - Cr4	2.8613
Cr5 - Cr2	2.3926	Cr6 - Cr1	2.3866	Cr2 - Cr6	2.4196
Cr5 - Cr4	3.0426	Cr1 - Cr5	2.3375	Cr5 - Cr2	2.4308
		Cr2 - Cr5	2.5562	Cr5 - Cr3	2.8205
		Cr4 - Cr5	2.3633	Cr5 - Cr4	2.4210
		Cr3 - Cr5	2.7068	Cr6 - Cr7	2.8241
				Cr7 - Cr1	2.4588
				Cr7 - Cr2	2.2580
				Cr7 - Cr5	2.8183

Appendix B Cr_xTe_y Bond Distances



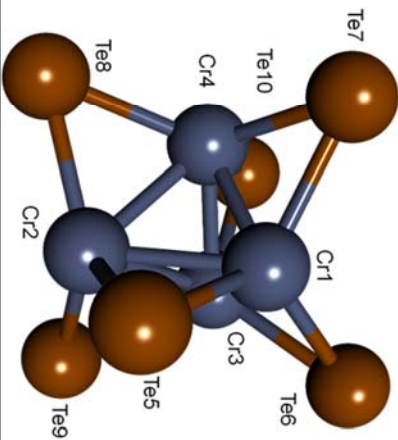
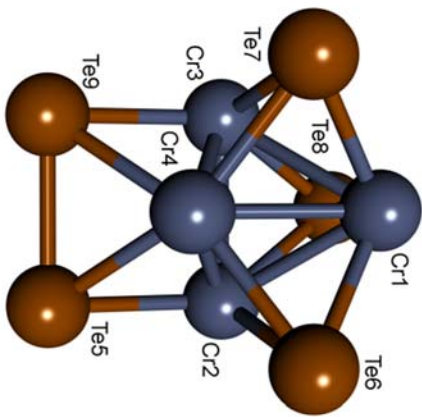
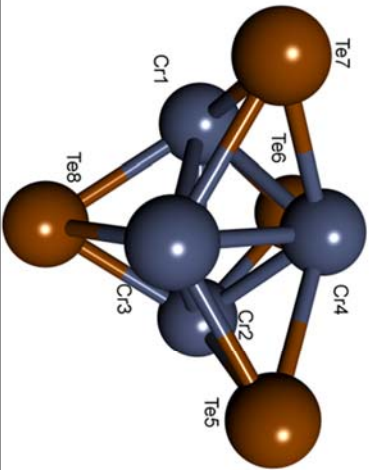
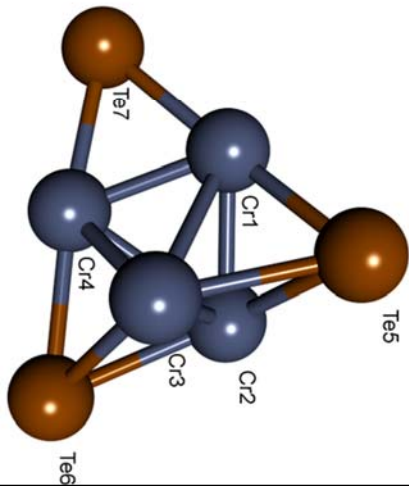
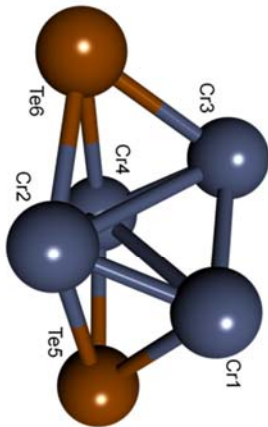
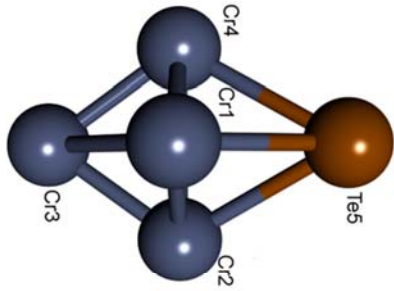
11		12		13		14	
Cr1 - Te2	2.453	Cr1 - Te2	2.536	Cr2 - Te3	2.629	Cr1 - Te3	2.634
		Cr1 - Te3	2.535	Cr2 - Te4	2.628	Cr1 - Te5	2.638
		Te2 - Te3	2.874	Te1 - Cr2	2.442	Te2 - Cr1	2.638
				Te3 - Te4	2.702	Te2 - Te3	2.689
						Te4 - Cr1	2.639
						Te4 - Te5	2.691
21		22		23		24	
Cr2 - Cr1	2.102	Cr1 - Cr2	1.838	Cr1 - Cr2	1.769	Cr2 - Cr1	1.79214
Cr2 - Te3	2.555	Te3 - Cr1	2.556	Cr1 - Te3	2.570	Te3 - Cr1	2.71503
Te3 - Cr1	2.555	Te3 - Cr2	2.561	Te3 - Cr2	2.565	Te3 - Cr2	2.70848
		Te4 - Cr1	2.561	Cr1 - Te4	2.567	Te3 - Te4	2.7812
		Te4 - Cr2	2.559	Cr2 - Te4	2.568	Te4 - Cr1	2.71284
				Cr1 - Te5	2.567	Te4 - Cr2	2.70769
				Cr2 - Te5	2.570	Te5 - Cr1	2.71281
						Te5 - Cr2	2.70768
						Te5 - Te6	2.78122
						Te6 - Cr1	2.71505
						Te6 - Cr2	2.7085

Cr₃Te_x (x = 1 - 5)



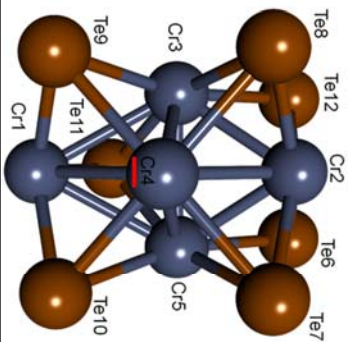
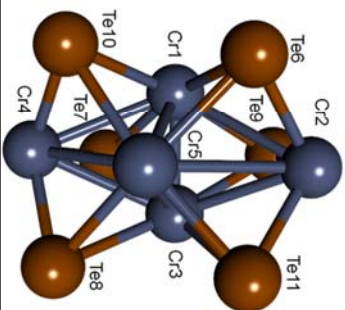
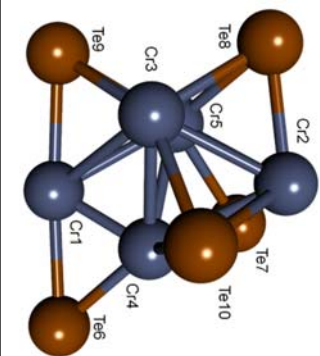
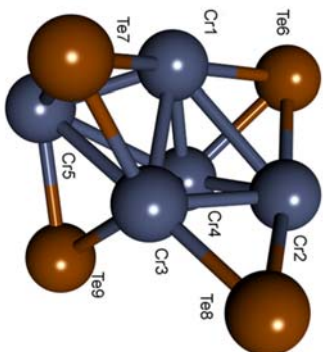
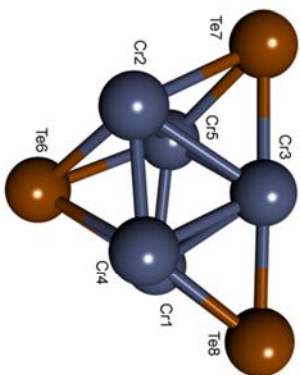
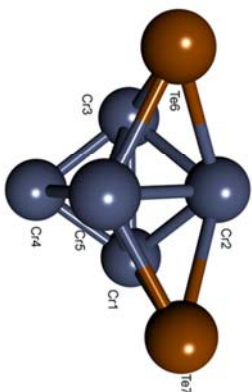
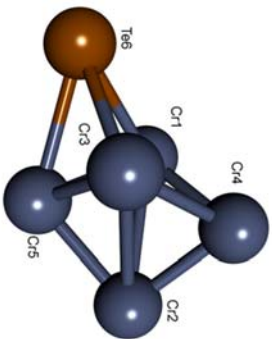
31		32		33		34		35	
Cr1 - Cr2	2.921	Cr1 - Cr2	2.353	Cr1 - Cr2	1.821	Cr3 - Cr1	2.829	Cr1 - Cr2	2.85981
Cr1 - Cr3	2.312	Cr1 - Cr3	2.978	Cr1 - Cr3	2.846	Cr3 - Cr2	2.421	Cr1 - Cr3	2.45729
Cr2 - Cr3	2.312	Cr3 - Cr2	2.357	Cr3 - Cr2	2.839	Cr2 - Cr1	2.424	Cr2 - Cr3	2.60359
Te4 - Cr2	2.594	Cr1 - Te4	2.662	Cr1 - Te4	2.544	Cr1 - Te5	2.556	Cr2 - Te5	2.71205
Te4 - Cr3	2.903	Cr3 - Te4	2.661	Cr1 - Te6	2.671	Cr3 - Te5	2.552	Cr2 - Te7	2.71205
Te4 - Cr1	2.594	Cr2 - Te4	2.727	Cr2 - Te6	2.677	Te6 - Cr3	2.641	Cr3 - Te5	2.66934
		Te5 - Cr3	2.663	Cr3 - Te6	2.656	Te6 - Cr2	2.643	Cr3 - Te7	2.72974
		Te5 - Cr1	2.661	Te5 - Cr1	2.658	Te6 - Cr1	2.638	Te4 - Cr1	2.60034
		Te5 - Cr2	2.726	Te5 - Cr3	2.675	Te4 - Cr1	2.502	Te4 - Cr2	2.57278
				Te5 - Cr2	2.653	Te4 - Cr2	2.675	Te5 - Te7	2.74759
				Te4 - Cr2	2.537	Te7 - Cr3	2.503	Te6 - Cr1	2.66167
						Te7 - Cr2	2.668	Te6 - Cr2	2.64475
								Te6 - Cr3	2.64333
								Te8 - Cr1	2.62958
								Te8 - Cr3	2.51534

Cr_4Te_x ($x = 1 - 6$)



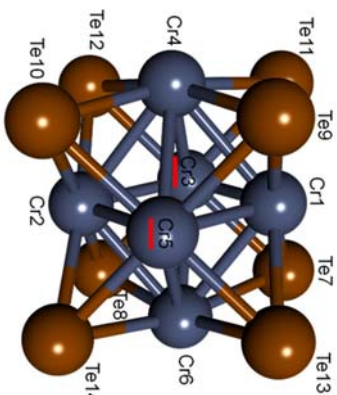
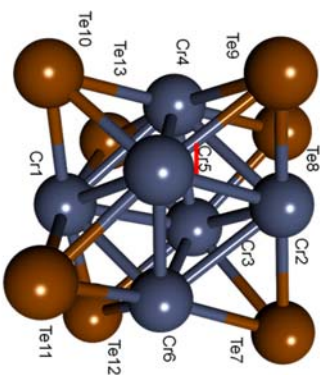
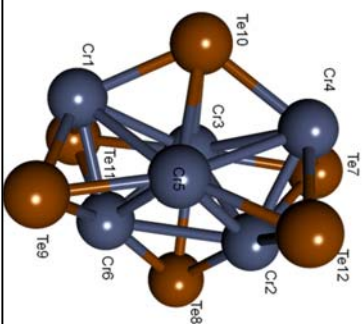
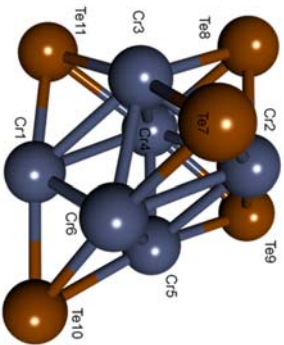
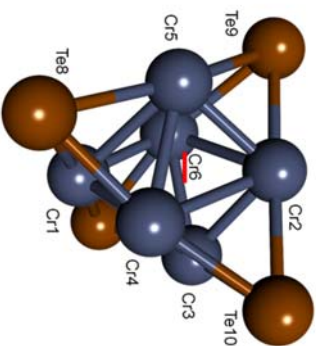
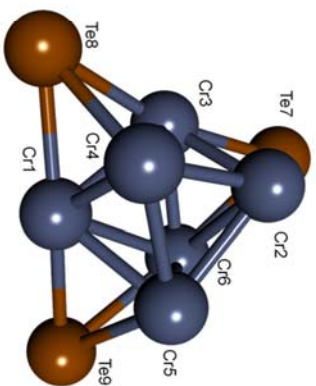
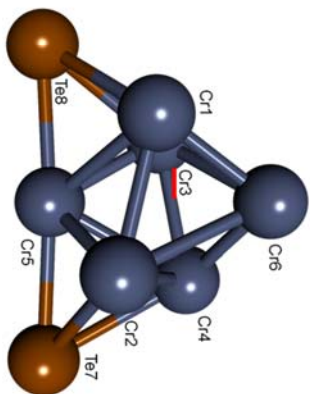
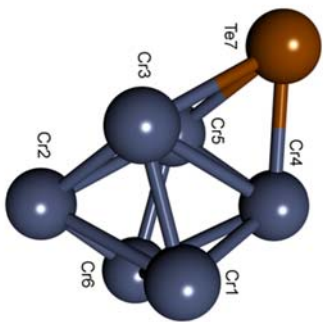
41		42		43	
Cr1 - Cr3	2.841	Cr2 - Cr3	3.014	Cr1 - Cr3	2.745
Cr2 - Cr3	2.331	Cr2 - Cr1	2.270	Cr1 - Cr4	2.409
Cr2 - Cr4	2.690	Cr1 - Cr3	2.465	Cr2 - Cr1	2.460
Cr4 - Cr1	2.330	Cr4 - Cr2	2.372	Cr2 - Cr4	2.748
Cr2 - Cr1	2.327	Cr4 - Cr3	2.273	Cr3 - Cr2	2.238
Cr4 - Cr3	2.328	Cr1 - Cr4	3.014	Cr3 - Cr4	2.460
Te5 - Cr2	2.746	Te5 - Cr2	2.791	Cr1 - Te7	2.575
Te5 - Cr4	2.748	Te5 - Cr1	2.610	Cr2 - Te6	2.716
Te5 - Cr1	2.640	Te5 - Cr4	2.666	Cr3 - Te6	2.675
		Cr4 - Te6	2.791	Cr4 - Te6	2.650
		Cr2 - Te6	2.670	Te5 - Cr1	2.651
		Cr3 - Te6	2.605	Te5 - Cr2	2.674
				Te5 - Cr3	2.717
				Te7 - Cr4	2.576
44		45		46	
Cr1 - Cr3	2.850	Cr1 - Cr3	2.931	Cr1 - Cr3	2.277
Cr2 - Cr1	2.852	Cr2 - Cr1	2.928	Cr1 - Cr2	2.465
Cr2 - Cr3	2.847	Cr2 - Cr4	2.354	Cr3 - Cr2	2.575
Cr3 - Cr4	2.449	Cr3 - Cr2	2.819	Cr4 - Cr3	2.275
Cr4 - Cr1	2.458	Cr3 - Cr4	2.362	Cr4 - Cr1	2.320
Cr4 - Cr2	2.450	Cr4 - Cr1	2.751	Cr4 - Cr2	2.467
Te5 - Cr2	2.648	Cr2 - Te5	2.688	Cr2 - Te8	2.505
Te5 - Cr3	2.643	Cr2 - Te6	2.670	Cr4 - Te8	2.526
Te5 - Cr4	2.704	Cr3 - Te9	2.691	Te5 - Cr2	2.506
Te6 - Cr1	2.648	Cr4 - Te5	2.717	Te5 - Cr1	2.527
Te6 - Cr2	2.647	Cr4 - Te9	2.713	Te7 - Cr1	2.510
Te6 - Cr4	2.700	Te6 - Cr1	2.594	Te7 - Cr4	2.511
Te7 - Cr1	2.644	Te6 - Cr4	2.717	Te10 - Cr4	2.509
Te7 - Cr3	2.649	Te7 - Cr1	2.593	Te10 - Cr3	2.516
Te7 - Cr4	2.704	Te7 - Cr3	2.673	Te6 - Cr1	2.509
Te8 - Cr1	2.654	Te7 - Cr4	2.715	Te6 - Cr3	2.516
Te8 - Cr2	2.652	Te8 - Cr1	2.653	Cr3 - Te9	2.532
Te8 - Cr3	2.652	Te8 - Cr2	2.688	Cr2 - Te9	2.511
		Te8 - Cr3	2.686		
		Te5 - Te9	2.807		

Cr_5Te_x (x = 1 - 7)



51	C2 - C1	2.83986	C1 - C3	2.780	C1 - C3	2.817	C1 - C5	2.332	C2 - C3	2.826	C2 - C5	3.296	C2 - C3	2.610
	C1 - C3	2.83067	C1 - C4	2.299	C1 - C4	2.370	C2 - C1	2.836	C2 - C4	2.881	C2 - C3	3.016	C2 - C4	2.763
	C2 - C3	2.8433	C3 - C4	2.306	C3 - C2	2.803	C2 - C3	2.457	C2 - C5	2.770	C3 - C1	2.482	C2 - C5	2.602
	C4 - C1	2.41487	C5 - C4	2.421	C3 - C4	2.454	C4 - C1	2.390	C3 - C4	2.740	C5 - C1	2.836	C3 - C1	2.928
	C4 - C2	2.27203	C2 - C5	2.253	C5 - C1	2.467	C4 - C2	2.249	C3 - C1	2.887	C2 - C1	3.287	C3 - C4	2.589
	C4 - C3	2.41858	C2 - C1	2.443	C3 - C5	2.407	C3 - C1	2.539	C3 - C5	2.056	C5 - C3	2.488	C3 - C5	2.852
	C2 - C5	2.39858	C2 - C3	2.448	C5 - C2	2.376	C4 - C3	2.656	C5 - C1	2.749	C3 - C4	3.149	C4 - C1	2.963
	C3 - C5	2.33463	C5 - C3	2.753	C2 - C4	2.464	C3 - C5	2.778	C4 - C1	2.225	C1 - C4	3.128	C4 - T ^e 9	2.760
	C1 - C5	2.33464	C5 - C1	2.750	C3 - T ^e 8	2.647	C4 - C5	2.972	C5 - C4	2.637	C5 - C4	3.129	C5 - C1	2.923
	T ^e 6 - C1	2.656	C5 - T ^e 6	2.704	C4 - T ^e 6	2.739	C1 - T ^e 7	2.670	T ^e 7 - C4	2.625	T ^e 6 - C5	2.819	C5 - C4	2.582
	T ^e 6 - C3	2.654	C2 - T ^e 6	2.727	C2 - T ^e 6	2.741	C3 - T ^e 7	2.619	T ^e 7 - C2	2.655	C2 - T ^e 6	2.593	T ^e 10 - C1	2.541
	T ^e 6 - C5	2.787	T ^e 7 - C1	2.650	C5 - T ^e 6	2.744	C5 - T ^e 7	2.645	T ^e 7 - C5	2.657	T ^e 6 - C1	2.815	T ^e 10 - C4	2.760
			T ^e 7 - C2	2.725	C1 - T ^e 6	2.745	T ^e 8 - C2	2.654	C5 - T ^e 9	2.683	C1 - T ^e 10	2.805	T ^e 10 - C5	2.725
			T ^e 7 - C5	2.707	T ^e 7 - C5	2.715	T ^e 8 - C3	2.491	C3 - T ^e 9	2.644	C5 - T ^e 10	2.799	T ^e 11 - C1	2.530
			T ^e 6 - C3	2.652	T ^e 7 - C2	2.706	C3 - T ^e 9	2.668	T ^e 9 - C1	2.680	T ^e 10 - C4	2.588	T ^e 11 - C3	2.747
					C3 - T ^e 7	2.652	C4 - T ^e 9	2.645	T ^e 6 - C4	2.471	C4 - T ^e 7	2.568	T ^e 11 - C5	2.747
					T ^e 8 - C1	2.705	T ^e 9 - C5	2.652	T ^e 6 - C1	2.687	C3 - T ^e 7	2.806	T ^e 12 - C2	2.652
					T ^e 8 - C4	2.719	T ^e 6 - C4	2.648	T ^e 10 - C2	2.677	C1 - T ^e 7	2.783	T ^e 12 - C3	2.745
							T ^e 6 - C2	2.700	T ^e 10 - C4	2.604	T ^e 9 - C3	2.787	T ^e 6 - C2	2.648
							T ^e 6 - C1	2.667	T ^e 10 - C3	2.695	T ^e 9 - C2	2.589	T ^e 6 - C5	2.741
									T ^e 8 - C5	2.662	T ^e 9 - C1	2.752	T ^e 6 - T ^e 12	2.813
									T ^e 8 - C2	2.629	T ^e 11 - C1	2.589	T ^e 7 - C2	2.588
									T ^e 10 - C3	2.643	T ^e 11 - C3	2.787	T ^e 7 - C4	2.757
									T ^e 8 - C3		T ^e 11 - C5	2.751	T ^e 7 - C5	2.703
											C5 - T ^e 8	2.780	T ^e 8 - C2	2.589
											C3 - T ^e 8	2.804	T ^e 8 - C3	2.703
											T ^e 8 - C4	2.567	T ^e 8 - C4	2.752
													T ^e 9 - C1	2.538
													T ^e 9 - C3	2.728

Cr_6Te_x ($x = 1 - 8$)



61	C1 - C3	2,489	C1 - C5	2,704	C2 - C3	2,661	C1 - C5	2,723	C5 - C1	2,734	C1 - C6	2,556	C2 - C3	2,561	C3 - C4	2,835
	C1 - C6	2,421	C1 - C3	2,322	C2 - C4	2,432	C1 - C3	2,725	C6 - C1	2,339	C2 - C3	2,455	C2 - C4	2,781	C4 - C5	2,835
	C1 - C4	2,371	C2 - C1	2,315	C3 - C5	2,356	C1 - C4	2,332	C3 - C1	2,760	C3 - C1	2,927	C2 - C5	2,693	C5 - C6	2,835
	C1 - C2	2,867	C4 - C2	2,317	C2 - C6	2,337	C2 - C5	2,437	C4 - C1	2,864	C3 - C5	2,923	C2 - C6	2,788	C3 - C6	2,835
	C3 - C3	2,342	Q2 - C5	2,296	C3 - C1	2,744	C2 - C3	2,464	C5 - C4	2,551	C3 - C6	2,450	C3 - C1	2,886	C1 - C3	2,539
	C3 - C4	2,307	C4 - C6	2,323	C3 - C4	2,286	C6 - C1	2,314	C4 - C3	2,459	C6 - C2	2,954	C3 - C4	2,714	C1 - C4	2,764
	C4 - C3	2,878	C6 - C1	2,328	C4 - C1	2,475	C6 - C5	2,525	C3 - C6	2,659	C4 - C2	2,553	C3 - C6	2,507	C1 - C5	2,539
	C5 - C6	2,519	C6 - C2	2,706	C4 - C5	2,706	C6 - C2	2,719	C5 - C6	2,372	C4 - C3	2,926	C4 - C1	2,785	C1 - C6	2,764
	C6 - C4	2,806	C4 - C3	2,512	C5 - C1	2,326	C6 - C3	2,554	C2 - C4	2,876	C4 - C5	2,850	C4 - C5	2,454	C2 - C5	2,539
	C3 - C2	2,429	C4 - C5	2,706	C5 - C6	2,666	C3 - C4	2,555	C2 - C5	2,651	C5 - C1	2,776	C5 - C1	2,776	C3 - C2	2,539
	C6 - C2	2,251	C6 - C3	2,700	C6 - C1	2,552	C2 - C4	2,720	C2 - C3	2,566	C5 - C2	2,581	C6 - C1	2,593	C6 - C2	2,764
	C5 - C2	2,744	C3 - C5	2,300	C6 - C3	2,387	C5 - C4	2,562	C2 - C6	2,824	C5 - C6	2,574	C6 - C5	2,649	C2 - C4	2,764
	Te1 - C5	2,681	C3 - Te8	2,648	Te1 - C2	2,768	Te7 - C1	2,636	Te1 - C2	2,645	Te10 - C1	2,660	C2 - Te9	2,648	C4 - Te10	2,661
	Te1 - C4	2,650	C1 - Te8	2,776	Te1 - C3	2,665	Te9 - C5	2,681	Te1 - C3	2,683	Te10 - C3	2,785	C3 - Te13	2,672	Te10 - C5	2,633
	Te1 - C3	2,755	C5 - Te8	2,672	Te7 - C6	2,622	Te9 - C2	2,626	Te7 - C6	2,646	Te10 - C4	2,659	C4 - Te10	2,643	Te10 - C2	2,659
			C5 - Te7	2,667	Te8 - C1	2,707	Te9 - C3	2,680	C6 - Te10	2,659	Te10 - C5	2,787	C4 - Te13	2,645	Te12 - C2	2,659
			C4 - Te7	2,777	Te8 - C3	2,651	Te7 - C3	2,719	Te10 - C1	2,656	Te11 - C1	2,576	C5 - Te11	2,676	Te12 - C4	2,661
			C2 - Te7	2,651	Te9 - C1	2,693	C6 - Te7	2,647	Te10 - C5	2,661	Te12 - C2	2,670	C6 - Te11	2,602	Te8 - C6	2,661
					Te9 - C5	2,661	C2 - Te10	2,637	C3 - Te11	2,692	Te12 - C4	2,648	Te10 - C1	2,678	Te8 - C2	2,659
					Te9 - C6	2,666	C4 - Te10	2,674	C4 - Te11	2,652	Te12 - C5	2,644	Te10 - C5	2,640	Te8 - C3	2,653
					C4 - Te8	2,687	C4 - Te10	2,676	Te11 - C1	2,648	Te7 - C2	2,687	Te11 - C1	2,713	C3 - Te12	2,633
							Te8 - C4	2,639	Te8 - C4	2,695	Te7 - C3	2,759	Te12 - C1	2,656	C5 - Te14	2,633
							C1 - Te8	2,637	Te8 - C2	2,653	Te7 - C4	2,577	Te12 - C3	2,699	C6 - Te14	2,661
							C1 - Te8	2,701	Te8 - C3	2,652	Te8 - C2	2,606	Te12 - C6	2,597	Te14 - C2	2,659
									Te9 - C2	2,707	Te8 - C6	2,606	Te12 - C1	2,665	Te7 - C3	2,653
									Te9 - C5	2,569	Te9 - C1	2,650	Te7 - C2	2,573	Te7 - C1	2,659
									Te9 - C4	2,791	Te9 - C6	2,673	Te7 - C3	2,844	Te7 - C6	2,661
											C3 - Te11	2,757	Te1 - C3	2,606	Te13 - C6	2,661
											C3 - Te8	2,889	Te8 - C2	2,619	Te13 - C1	2,659
											C5 - Te9	2,644	Te8 - C3	2,672	Te13 - C5	2,633
											C6 - Te11	2,688	Te8 - C4	2,691	Te9 - C4	2,661
													Te9 - C4	2,782	Te9 - C5	2,639
													Te9 - C1	2,573	C4 - Te11	2,661
													C4 - Te11	2,661	C4 - Te11	2,633
													Te11 - C3	2,633	Te11 - C1	2,659

References

- (1) Herzing, A. A.; Kiely, C. J.; Carley, A. F.; Landon, P.; Hutchings, G. J. Identification of Active Gold Nanoclusters on Iron Oxide Supports for CO Oxidation. *Science* **2008**, *321* (5894), 1331–1335 DOI: 10.1126/science.1159639.
- (2) Bergeron, D. E.; Castleman, A. W.; Morisato, T.; Khanna, S. N. Formation of Al13I-: Evidence for the Superhalogen Character of Al13. *Science* **2004**, *304* (5667), 84–87 DOI: 10.1126/science.1093902.
- (3) Reddy, B. V.; Khanna, S. N.; Dunlap, B. I. Giant magnetic moments in 4 *d* clusters. *Phys. Rev. Lett.* **1993**, *70* (21), 3323–3326 DOI: 10.1103/PhysRevLett.70.3323.
- (4) Liyanage, R.; Zhang, X.-G.; Armentrout, P. B. Activation of methane by size-selected iron cluster cations, Feⁿ⁺ (n=2–15): Cluster-CH_x (x=0–3) bond energies and reaction mechanisms. *J. Chem. Phys.* **2001**, *115* (21), 9747–9763 DOI: 10.1063/1.1413983.
- (5) Reilly, N. M.; Reveles, J. U.; Johnson, G. E.; del Campo, J. M.; Khanna, S. N.; Köster, A. M.; Castleman, A. W. Experimental and Theoretical Study of the Structure and Reactivity of Fe_mO_n⁺ (m = 1, 2; n = 1–5) with CO. *J Phys Chem C* **2007**, *111* (51), 19086–19097 DOI: 10.1021/jp0736239.
- (6) Baran, P.; Boča, R.; Chakraborty, I.; Giapintzakis, J.; Herchel, R.; Huang, Q.; McGrady, J. E.; Raptis, R. G.; Sanakis, Y.; Simopoulos, A. Synthesis, Characterization, and Study of Octanuclear Iron-Oxo Clusters Containing a Redox-Active Fe₄O₄-Cubane Core. *Inorg. Chem.* **2008**, *47* (2), 645–655 DOI: 10.1021/ic7020337.
- (7) *Quantum phenomena in clusters and nanostructures*; Khanna, S. N., Castleman, A. W., Eds.; Springer Series in Cluster Physics; Springer-Verlang: New York.

- (8) Kelly, K. L.; Coronado, E.; Zhao, L. L.; Schatz, G. C. The Optical Properties of Metal Nanoparticles: The Influence of Size, Shape, and Dielectric Environment. *J. Phys. Chem. B* **2003**, *107* (3), 668–677 DOI: 10.1021/jp026731y.
- (9) Smith, J. C.; Reber, A. C.; Khanna, S. N.; Castleman, A. W. Boron Substitution in Aluminum Cluster Anions: Magic Clusters and Reactivity with Oxygen. *J. Phys. Chem. A* **2014**, *118* (37), 8485–8492 DOI: 10.1021/jp501934t.
- (10) Zemski, K. A.; Justes, D. R.; Castleman, A. W. Studies of Metal Oxide Clusters: Elucidating Reactive Sites Responsible for the Activity of Transition Metal Oxide Catalysts. *J Phys Chem B* **2002**, *106* (24), 6136–6148 DOI: 10.1021/jp0142334.
- (11) Bunker, C. E.; Smith, M. J. Nanoparticles for hydrogen generation. *J Mater Chem* **2011**, *21* (33), 12173–12180 DOI: 10.1039/C1JM10856E.
- (12) Khanna, S. N.; Jena, P. Assembling crystals from clusters. *Phys. Rev. Lett.* **1992**, *69* (11), 1664–1667 DOI: 10.1103/PhysRevLett.69.1664.
- (13) Khanna, S. N.; Jena, P. Atomic clusters: Building blocks for a class of solids. *Phys. Rev. B* **1995**, *51* (19), 13705–13716 DOI: 10.1103/PhysRevB.51.13705.
- (14) Reber, A. C.; Khanna, S. N.; Castleman, A. W. Superatom Compounds, Clusters, and Assemblies: Ultra Alkali Motifs and Architectures. *J Am Chem Soc* **2007**, *129* (33), 10189–10194 DOI: 10.1021/ja071647n.
- (15) Claridge, S. A.; Castleman, A. W.; Khanna, S. N.; Murray, C. B.; Sen, A.; Weiss, P. S. Cluster-Assembled Materials. *ACS Nano* **2009**, *3* (2), 244–255 DOI: 10.1021/nn800820e.
- (16) Castleman, A. W.; Khanna, S. N. Clusters, Superatoms, and Building Blocks of New Materials†. *J Phys Chem C* **2009**, *113* (7), 2664–2675 DOI: 10.1021/jp806850h.

- (17) Turkiewicz, A.; Paley, D. W.; Besara, T.; Elbaz, G.; Pinkard, A.; Siegrist, T.; Roy, X. Assembling Hierarchical Cluster Solids with Atomic Precision. *J. Am. Chem. Soc.* **2014**, *136* (45), 15873–15876 DOI: 10.1021/ja508698w.
- (18) Jena, P.; Castleman, A. W. Clusters: A bridge across the disciplines of physics and chemistry. *Proc. Natl. Acad. Sci.* **2006**, *103* (28), 10560–10569 DOI: 10.1073/pnas.0601782103.
- (19) de Heer, W. A. The physics of simple metal clusters: experimental aspects and simple models. *Rev. Mod. Phys.* **1993**, *65* (3), 611–676 DOI: 10.1103/RevModPhys.65.611.
- (20) Akola, J.; Manninen, M.; Häkkinen, H.; Landman, U.; Li, X.; Wang, L.-S. Aluminum cluster anions: Photoelectron spectroscopy and ab initio simulations. *Phys. Rev. B* **2000**, *62* (19), 13216–13228 DOI: 10.1103/PhysRevB.62.13216.
- (21) Yamada, Y.; Castleman, A. W. The magic numbers of metal and metal alloy clusters. *J. Chem. Phys.* **1992**, *97* (6), 4543 DOI: 10.1063/1.463898.
- (22) Jena, P.; Khanna, S. n.; Rao, B. k. Designing clusters as superelements. *Surf. Rev. Lett.* **1996**, *03* (01), 993–999 DOI: 10.1142/S0218625X96001789.
- (23) Luo, Z.; Castleman, A. W. Special and General Superatoms. *Acc. Chem. Res.* **2014**, *47* (10), 2931–2940 DOI: 10.1021/ar5001583.
- (24) Zhang, X.; Wang, Y.; Wang, H.; Lim, A.; Gantefoer, G.; Bowen, K. H.; Reveles, J. U.; Khanna, S. N. On the Existence of Designer Magnetic Superatoms. *J. Am. Chem. Soc.* **2013**, *135* (12), 4856–4861 DOI: 10.1021/ja400830z.
- (25) Zhang, M.; Zhang, J.; Feng, X.; Zhang, H.; Zhao, L.; Luo, Y.; Cao, W. Magnetic Superatoms in VLi_n ($n = 1-13$) Clusters: A First-Principles Prediction. *J. Phys. Chem. A* **2013**, *117* (48), 13025–13036 DOI: 10.1021/jp410489g.

- (26) Rehm, E.; Boldyrev, A. I.; Schleyer, P. v R. Ab initio study of superalkalis. First ionization potentials and thermodynamic stability. *Inorg. Chem.* **1992**, *31* (23), 4834–4842 DOI: 10.1021/ic00049a022.
- (27) Reveles, J. U.; Khanna, S. N.; Roach, P. J.; Castleman, A. W. Multiple valence superatoms. *Proc. Natl. Acad. Sci.* **2006**, *103* (49), 18405–18410 DOI: 10.1073/pnas.0608781103.
- (28) Reveles, J. U.; Clayborne, P. A.; Reber, A. C.; Khanna, S. N.; Pradhan, K.; Sen, P.; Pederson, M. R. Designer magnetic superatoms. *Nat Chem* **2009**, *1* (4), 310–315 DOI: 10.1038/nchem.249.
- (29) Knight, W. D.; Clemenger, K.; de Heer, W. A.; Saunders, W. A.; Chou, M. Y.; Cohen, M. L. Electronic Shell Structure and Abundances of Sodium Clusters. *Phys. Rev. Lett.* **1984**, *52* (24), 2141–2143 DOI: 10.1103/PhysRevLett.52.2141.
- (30) Chou, M. Y.; Cleland, A.; Cohen, M. L. Total energies, abundances, and electronic shell structure of lithium, sodium, and potassium clusters. *Solid State Commun.* **1984**, *52* (7), 645–648 DOI: 10.1016/0038-1098(84)90725-7.
- (31) de Heer, W. A.; Knight, W. D.; Chou, M. Y.; Cohen, M. L. Electronic Shell Structure and Metal Clusters. In *Solid State Physics*; Turnbull, H. E. and D., Ed.; Academic Press, 1987; Vol. 40, pp 93–181.
- (32) Knight, W. D.; De Heer, W. A.; Saunders, W. A.; Clemenger, K.; Chou, M. Y.; Cohen, M. L. Alkali metal clusters and the jellium model. *Chem. Phys. Lett.* **1987**, *134* (1), 1–5 DOI: 10.1016/0009-2614(87)80002-7.

- (33) Brack, M. The physics of simple metal clusters: self-consistent jellium model and semiclassical approaches. *Rev. Mod. Phys.* **1993**, *65* (3), 677–732 DOI: 10.1103/RevModPhys.65.677.
- (34) Martins, J. L.; Car, R.; Buttet, J. Variational spherical model of small metallic particles. *Surf. Sci. Lett.* **1981**, *106* (1–3), A174 DOI: 10.1016/0167-2584(81)90335-2.
- (35) Clemenger, K. Ellipsoidal shell structure in free-electron metal clusters. *Phys. Rev. B* **1985**, *32* (2), 1359–1362 DOI: 10.1103/PhysRevB.32.1359.
- (36) Martin, T. P.; Bergmann, T.; Göhlich, H.; Lange, T. Observation of electronic shells and shells of atoms in large Na clusters. *Chem. Phys. Lett.* **1990**, *172* (3–4), 209–213 DOI: 10.1016/0009-2614(90)85389-T.
- (37) Nakajima, A.; Hoshino, K.; Naganuma, T.; Sone, Y.; Kaya, K. Ionization potentials of aluminum–sodium bimetallic clusters (Al_nNam). *J. Chem. Phys.* **1991**, *95* (10), 7061–7066 DOI: 10.1063/1.461434.
- (38) Selby, K.; Kresin, V.; Masui, J.; Vollmer, M.; de Heer, W. A.; Scheidemann, A.; Knight, W. D. Photoabsorption spectra of sodium clusters. *Phys. Rev. B* **1991**, *43* (6), 4565–4572 DOI: 10.1103/PhysRevB.43.4565.
- (39) Leuchtner, R. E.; Harms, A. C.; Castleman, A. W. Thermal metal cluster anion reactions: Behavior of aluminum clusters with oxygen. *J. Chem. Phys.* **1989**, *91*, 2753 DOI: 10.1063/1.456988.
- (40) Bergeron, D. E.; Roach, P. J.; Castleman, A. W.; Jones, N. O.; Khanna, S. N. Al Cluster Superatoms as Halogens in Polyhalides and as Alkaline Earths in Iodide Salts. *Science* **2005**, *307* (5707), 231–235 DOI: 10.1126/science.1105820.

- (41) Zheng, W.-J.; Thomas, O. C.; Lippa, T. P.; Xu, S.-J.; Bowen, K. H. The ionic KAl13 molecule: a stepping stone to cluster-assembled materials. *J. Chem. Phys.* **2006**, *124* (14), 144304 DOI: 10.1063/1.2184316.
- (42) Wang, H.; Zhang, X.; Ko, Y. J.; Grubisic, A.; Li, X.; Ganteför, G.; Schnöckel, H.; Eichhorn, B. W.; Lee, M.-S.; Jena, P.; et al. Aluminum Zintl anion moieties within sodium aluminum clusters. *J. Chem. Phys.* **2014**, *140* (5), 054301 DOI: 10.1063/1.4862989.
- (43) Kolobov, A. V.; Tominaga, J. *Chalcogenides: Metastability and Phase Change Phenomena*, 1st ed.; Wang, Z., Series Ed.; Springer Series in Materials Science; Springer-Verlag Berlin Heidelberg, 2012; Vol. 164.
- (44) Zallen, R. *The Physics of Amorphous Solids*; Wiley-Interscience, 1983.
- (45) Mott, N. F. Electrons in disordered structures. *Adv. Phys.* **2001**, *50* (7), 865–945 DOI: 10.1080/00018730110102727.
- (46) Jellinek, F. Transition metal chalcogenides. relationship between chemical composition, crystal structure and physical properties. *React. Solids* **1988**, *5* (4), 323–339 DOI: 10.1016/0168-7336(88)80031-7.
- (47) Sato, H.; Koyama, M.; Takada, K.; Okuda, H.; Shimada, K.; Ueda, Y.; Ghijsen, J.; Taniguchi, M. Electronic structure of chromium chalcogenides. *J. Electron Spectrosc. Relat. Phenom.* **1998**, *88*, 333–337.
- (48) Huisman, R.; de Jonge, R.; Haas, C.; Jellinek, F. Trigonal-prismatic coordination in solid compounds of transition metals. *J. Solid State Chem.* **1971**, *3* (1), 56–66 DOI: 10.1016/0022-4596(71)90007-7.

- (49) Hulliger, F. Crystal chemistry of the chalcogenides and pnictides of the transition elements. In *Structure and Bonding*; Springer Berlin Heidelberg: Berlin, Heidelberg, 1968; Vol. 4, pp 83–229.
- (50) Wells, A. F. *Structural Inorganic Chemistry*, 5th ed.; Oxford University Press: Oxford Oxfordshire : New York, 1984.
- (51) Hessen, B.; Siegrist, T.; Palstra, T.; Tanzler, S. M.; Steigerwald, M. L. Hexakis (triethylphosphine) octatelluridohexachromium and a molecule-based synthesis of chromium telluride, Cr₃Te₄. *Inorg. Chem.* **1993**, *32* (23), 5165–5169.
- (52) Steigerwald, M. L.; Rice, C. E. Organometallic synthesis of manganese telluride. Isolation and characterization of [(Et₃P)₂(CO)₃MnTe]₂. *J. Am. Chem. Soc.* **1988**, *110* (13), 4228–4231 DOI: 10.1021/ja00221a023.
- (53) Brennan, J. G.; Siegrist, T.; Carroll, P. J.; Stuczynski, S. M.; Brus, L. E.; Steigerwald, M. L. The preparation of large semiconductor clusters via the pyrolysis of a molecular precursor. *J. Am. Chem. Soc.* **1989**, *111* (11), 4141–4143 DOI: 10.1021/ja00193a079.
- (54) Steigerwald, M. L. Selective syntheses of iron monotelluride and iron ditelluride from organometallic precursors. Synthesis and pyrolysis of [Cp(Et₃P)(CO)Fe]₂(Te)_n. *Chem. Mater.* **1989**, *1* (1), 52–57 DOI: 10.1021/cm00001a014.
- (55) Brennan, J. G.; Siegrist, T.; Stuczynski, S. M.; Steigerwald, M. L. Cluster intermediates in an organometallic synthesis of palladium telluride PdTe. *J. Am. Chem. Soc.* **1990**, *112* (25), 9233–9236 DOI: 10.1021/ja00181a027.
- (56) Steigerwald, M. L.; Siegrist, T.; Stuczynski, S. M. Initial stages in the molecule-based growth of the solid-state compound cobalt telluride (CoTe). *Inorg. Chem.* **1991**, *30* (26), 4940–4945 DOI: 10.1021/ic00026a018.

- (57) Steigerwald, M. L.; Siegrist, T.; Stuczynski, S. M. Octatelluridohexakis(triethylphosphine)hexacobalt and a connection between Chevrel clusters and the NiAs structure. *Inorg. Chem.* **1991**, *30* (10), 2256–2257 DOI: 10.1021/ic00010a005.
- (58) Steigerwald, M. L.; Siegrist, T.; Stuczynski, S. M.; Kwon, Y. U. Iron telluride (Et₃P)₄Fe₄Te₄: an intermediate between molecular reagents and solid state products. *J. Am. Chem. Soc.* **1992**, *114* (8), 3155–3156 DOI: 10.1021/ja00034a081.
- (59) Brennan, J. G.; Siegrist, T.; Stuczynski, S. M.; Steigerwald, M. L. The transition from molecules to solids: molecular syntheses of Ni₉Te₆(PEt₃)₈, Ni₂₀Te₁₈(PEt₃)₁₂ and NiTe. *J. Am. Chem. Soc.* **1989**, *111* (26), 9240–9241 DOI: 10.1021/ja00208a023.
- (60) Fenske, D.; Ohmer, J.; Hachgenei, J. New Co and Ni Clusters with Se and PPh₃ as Ligands: [Co₄(μ₃-Se)₄(PPh₃)₄], [Co₆(μ₃-Se)₈(PPh₃)₆], [Co₉(μ₄-Se)₃(μ₃-Se)₈(PPh₃)₆], and [Ni₃₄(μ₅-Se)₂(μ₄-Se)₂₀(PPh₃)₁₀]. *Angew. Chem. Int. Ed. Engl.* **1985**, *24* (11), 993–995 DOI: 10.1002/anie.198509931.
- (61) Cecconi, F.; Ghilardi, C. A.; Midollini, S.; Orlandini, A.; Zanello, P. Redox behaviour of the iron–sulphur cluster [Fe₆(μ₃-S)₈(PEt₃)₆]²⁺. Synthesis and crystal structure of the new paramagnetic monocationic species [Fe₆(μ₃-S)₈(PEt₃)₆]⁺ as its [PF₆][–] salt. *J. Chem. Soc. Dalton Trans.* **1987**, No. 4, 831–835 DOI: 10.1039/DT9870000831.
- (62) Saito, T.; Yamamoto, N.; Yamagata, T.; Imoto, H. Synthesis of [Mo₆S₈(PEt₃)₆] by reductive dimerization of a trinuclear molybdenum chloro sulfido cluster complex coordinated with triethylphosphine and methanol: a molecular model for superconducting Chevrel phases. *J. Am. Chem. Soc.* **1988**, *110* (5), 1646–1647 DOI: 10.1021/ja00213a060.

- (63) Saito, T.; Yoshikawa, A.; Yamagata, T.; Imoto, H.; Unoura, K. Synthesis, structure and electronic properties of octakis(μ_3 -sulfido)hexakis(triethylphosphine)hexatungsten as a tungsten analog of the molecular model for superconducting Chevrel phases. *Inorg. Chem.* **1989**, *28* (18), 3588–3592 DOI: 10.1021/ic00317a037.
- (64) Diana, E.; Gervasio, G.; Rossetti, R.; Valdemarin, F.; Bor, G.; Stanghellini, P. L. Hexacarbonylocta(μ_3 -sulfido)hexacobalt.cntdot.tris(octasulfur). Structure, bonding, and vibrational analysis of an exceptionally electron-rich carbonyl cluster. *Inorg. Chem.* **1991**, *30* (2), 294–299 DOI: 10.1021/ic00002a026.
- (65) Saito, T.; Yamamoto, N.; Nagase, T.; Tsuboi, T.; Kobayashi, K.; Yamagata, T.; Imoto, H.; Unoura, K. Molecular models of the superconducting chevrel phases: syntheses and structures of $[\text{Mo}_6\text{X}_8(\text{PEt}_3)_6]$ and $[\text{PPN}][\text{Mo}_6\text{X}_8(\text{PEt}_3)_6]$ (X = S, Se; PPN = $(\text{Ph}_3\text{P})_2\text{N}$). *Inorg. Chem.* **1990**, *29* (4), 764–770 DOI: 10.1021/ic00329a039.
- (66) Mandal, S.; Reber, A. C.; Qian, M.; Weiss, P. S.; Khanna, S. N.; Sen, A. Controlling the Band Gap Energy of Cluster-Assembled Materials. *Acc. Chem. Res.* **2013**, *46* (11), 2385–2395 DOI: 10.1021/ar3002975.
- (67) Khanna, S. N.; Jena, P. Designing ionic solids from metallic clusters. *Chem. Phys. Lett.* **1994**, *219* (5), 479–483 DOI: 10.1016/0009-2614(94)00097-2.
- (68) Rao, B. K.; Khanna, S. N.; Jena, P. Designing New Materials Using Atomic Clusters. *J. Clust. Sci.* **1999**, *10* (4), 477–491 DOI: 10.1023/A:1021948806958.
- (69) Long, D.-L.; Burkholder, E.; Cronin, L. Polyoxometalate clusters, nanostructures and materials: From self assembly to designer materials and devices. *Chem. Soc. Rev.* **2006**, *36* (1), 105–121 DOI: 10.1039/B502666K.

- (70) Chevrel, R.; Sergent, M.; Prigent, J. Sur de nouvelles phases sulfurées ternaires du molybdène. *J. Solid State Chem.* **1971**, *3* (4), 515–519 DOI: 10.1016/0022-4596(71)90095-8.
- (71) Chevrel, R.; Sergent, M.; Prigent, J. Un nouveau sulfure de molybdene : Mo₃S₄ preparation, proprietes et structure cristalline. *Mater. Res. Bull.* **1974**, *9* (11), 1487–1498 DOI: 10.1016/0025-5408(74)90095-6.
- (72) Sergent, M.; Fischer, Ø.; Decroux, M.; Perrin, C.; Chevrel, R. Stabilization of Mo₆S₈ by halogens; new superconducting compounds: Mo₆S₆Br₂, Mo₆S₆I₂. *J. Solid State Chem.* **1977**, *22* (1), 87–92 DOI: 10.1016/0022-4596(77)90192-X.
- (73) Burdett, J. K.; Lin, J. H. The structures of Chevrel phases. *Inorg. Chem.* **1982**, *21* (1), 5–10 DOI: 10.1021/ic00131a002.
- (74) Ichitsubo, T.; Yagi, S.; Nakamura, R.; Ichikawa, Y.; Okamoto, S.; Sugimura, K.; Kawaguchi, T.; Kitada, A.; Oishi, M.; Doi, T.; et al. A new aspect of Chevrel compounds as positive electrodes for magnesium batteries. *J. Mater. Chem. A* **2014**, *2* (36), 14858–14866 DOI: 10.1039/C4TA03063J.
- (75) Choi, B.; Paley, D. W.; Siegrist, T.; Steigerwald, M. L.; Roy, X. Ligand Control of Manganese Telluride Molecular Cluster Core Nuclearity. *Inorg. Chem.* **2015**, *54* (17), 8348–8355 DOI: 10.1021/acs.inorgchem.5b01020.
- (76) Peña, O. Chevrel phases: Past, present and future. *Phys. C Supercond. Its Appl.* **2015**, *514*, 95–112 DOI: 10.1016/j.physc.2015.02.019.
- (77) Matthias, B. T.; Marezio, M.; Corenzwit, E.; Cooper, A. S.; Barz, H. E. High-Temperature Superconductors, the First Ternary System. *Science* **1972**, *175* (4029), 1465–1466 DOI: 10.1126/science.175.4029.1465.

- (78) Roy, X.; Lee, C.-H.; Crowther, A. C.; Schenck, C. L.; Besara, T.; Lalancette, R. A.; Siegrist, T.; Stephens, P. W.; Brus, L. E.; Kim, P.; et al. Nanoscale Atoms in Solid-State Chemistry. *Science* **2013**, *341* (6142), 157–160 DOI: 10.1126/science.1236259.
- (79) Lee, C.-H.; Liu, L.; Bejger, C.; Turkiewicz, A.; Goko, T.; Arguello, C. J.; Frandsen, B. A.; Cheung, S. C.; Medina, T.; Munsie, T. J. S.; et al. Ferromagnetic Ordering in Superatomic Solids. *J. Am. Chem. Soc.* **2014**, *136* (48), 16926–16931 DOI: 10.1021/ja5098622.
- (80) Chauhan, V.; Sahoo, S.; Khanna, S. N. Ni₉Te₆(PET₃)₈C₆₀ Is a Superatomic Superalkali Superparamagnetic Cluster Assembled Material (S3-CAM). *J. Am. Chem. Soc.* **2016**, *138* (6), 1916–1921 DOI: 10.1021/jacs.5b10986.
- (81) Chauhan, V.; Reber, A. C.; Khanna, S. N. Transforming Ni₉Te₆ from Electron Donor to Acceptor via Ligand Exchange. *J. Phys. Chem. A* **2016**, *120* (33), 6644–6649 DOI: 10.1021/acs.jpca.6b05701.
- (82) Chevreton, M.; Bertaut, E. F.; Jellinek, F. Quelques remarques sur le système Cr–Te. *Acta Crystallogr.* **1963**, *16* (5), 431–431 DOI: 10.1107/S0365110X63001134.
- (83) Van Con, K.; Suchet, J. Étude cristallographique et propriétés électriques des alliages de composition CrTe. *COMPTEs RENDUS Hebd. SEANCES Acad. Sci. Ser. B* **1963**, *256*, 2823–2826.
- (84) BERTAUT, E.; ROULT, G.; ALEONARD, R.; PAUTHENET, R.; CHEVRETON, M.; JANSEN, R. STRUCTURES MAGNETIQUES DE CR₃X₄(X=S,SE,TE). *J. Phys.* **1964**, *25* (5), 582–595 DOI: 10.1051/jphys:01964002505058200.
- (85) KHOI, L.; VEILLET, P. RESONANCE MAGNETIQUE NUCLEAIRE DANS CRTE ET CR₃TE₄. *COMPTEs RENDUS Hebd. SEANCES Acad. Sci. Ser. B* **1967**, *264* (15), 1154.

- (86) Dijkstra, J.; Weitering, H. H.; Bruggen, C. F. van; Haas, C.; Groot, R. A. de. Band-structure calculations, and magnetic and transport properties of ferromagnetic chromium tellurides (CrTe , Cr_3Te_4 , Cr_2Te_3). *J. Phys. Condens. Matter* **1989**, *1* (46), 9141 DOI: 10.1088/0953-8984/1/46/008.
- (87) Hashimoto, T.; Yamaguchi, M. Magnetic Properties of Cr_7Te_8 . *J. Phys. Soc. Jpn.* **1969**, *27* (5), 1121–1126 DOI: 10.1143/JPSJ.27.1121.
- (88) Hashimoto, T.; Hoya, K.; Yamaguchi, M.; Ichitsubo, I. Magnetic Properties of Single Crystals $\text{Cr}_{2-\delta}\text{Te}_3$. *J. Phys. Soc. Jpn.* **1971**, *31* (3), 679–682 DOI: 10.1143/JPSJ.31.679.
- (89) Hamasaki, T.; Hashimoto, T.; Yamaguchi, Y.; Watanabe, H. Neutron diffraction study of Cr_2Te_3 single crystal. *Solid State Commun.* **1975**, *16* (7), 895–897 DOI: 10.1016/0038-1098(75)90888-1.
- (90) Akram, M.; Nazar, F. M. Magnetic properties of CrTe , $\text{Cr}_{23}\text{Te}_{24}$, Cr_7Te_8 , Cr_5Te_6 , and Cr_3Te_4 compounds. *J. Mater. Sci.* **1982**, *18* (2), 423–429 DOI: 10.1007/BF00560631.
- (91) Klepp, K. O.; Ipser, H. CrTe_3 —A Novel Transition-Metal Polytelluride. *Angew. Chem. Int. Ed. Engl.* **1982**, *21* (12), 911–911 DOI: 10.1002/anie.198209111.
- (92) Yuzuri, M.; Kanomata, T.; Kaneko, T. The pressure effect on the Curie temperature and exchange striction of Cr_2S_3 and Cr_2Te_3 . *J. Magn. Magn. Mater.* **1987**, *70* (1), 223–224 DOI: 10.1016/0304-8853(87)90416-1.
- (93) Zhang, J. H.; Birdwhistell, T. L. T.; O'Connor, C. J. Magnetic and electrical properties of a new chromium telluride phase: CrTe_2 . *Solid State Commun.* **1990**, *74* (6), 443–446 DOI: 10.1016/0038-1098(90)90323-4.
- (94) Canadell, E.; Jobic, S.; Brec, R.; Rouxel, J. Electronic structure and properties of anionic mixed valence and layered CrTe_3 : The question of extended tellurium bonding in

- transition metal tellurides. *J. Solid State Chem.* **1992**, 98 (1), 59–70 DOI: 10.1016/0022-4596(92)90070-C.
- (95) Shimada, K.; Saitoh, T.; Namatame, H.; Fujimori, A.; Ishida, S.; Asano, S.; Matoba, M.; Anzai, S. Photoemission study of itinerant ferromagnet Cr(1- δ)Te. *Phys. Rev. B* **1996**, 53 (12), 7673–7683 DOI: 10.1103/PhysRevB.53.7673.
- (96) Bensch, W.; Helmer, O.; Näther, C. Determination and redetermination of the crystal structures of chromium tellurides in the composition range CrTe_{1.56}–CrTe_{1.67}: Trigonal di-chromium tri-telluride Cr₂Te₃, monoclinic penta-chromium octa-telluride Cr₅Te₈, and the five layer superstructure of trigonal penta-chromium octa-telluride Cr₅Te₈. *Mater. Res. Bull.* **1997**, 32 (3), 305–318 DOI: 10.1016/S0025-5408(96)00194-8.
- (97) Kanomata, T.; Sugawara, Y.; Kaneko, T.; Kamishima, K.; Aruga Katori, H.; Goto, T. Giant magnetovolume effect of CrTe. *J. Alloys Compd.* **2000**, 297 (1–2), 5–8 DOI: 10.1016/S0925-8388(99)00570-8.
- (98) Eto, T.; Ishizuka, M.; Endo, S.; Kanomata, T.; Kikegawa, T. Pressure-induced structural phase transition in a ferromagnet CrTe. *J. Alloys Compd.* **2001**, 315 (1–2), 16–21 DOI: 10.1016/S0925-8388(00)01237-8.
- (99) Ishizuka, M.; Kato, H.; Kunisue, T.; Endo, S.; Kanomata, T.; Nishihara, H. Pressure-induced magnetic phase transition in CrTe at approximately 7 GPa. *J. Alloys Compd.* **2001**, 320 (1), 24–28 DOI: 10.1016/S0925-8388(01)00927-6.
- (100) Kanchana, V.; Vaitheeswaran, G.; Rajagopalan, M. Pressure-induced structural and magnetic phase transition in ferromagnetic CrTe. *J. Magn. Magn. Mater.* **2002**, 250, 353–363 DOI: 10.1016/S0304-8853(02)00419-5.

- (101) Huang, Z.-L.; Bensch, W.; Benea, D.; Ebert, H. Anion substitution effects on structure and magnetism in the chromium chalcogenide Cr₅Te₈—Part I: Cluster glass behavior in trigonal Cr(1+x)Q₂ with basic cell (Q=Te, Se; Te:Se=7:1). *J. Solid State Chem.* **2004**, *177* (10), 3245–3253 DOI: 10.1016/j.jssc.2004.05.046.
- (102) Yaji, K.; Kimura, A.; Hirai, C.; Taniguchi, M.; Koyama, M.; Sato, H.; Shimada, K.; Tanaka, A.; Muro, T.; Imada, S.; et al. Electronic structure of Cr(1- δ)Te studied by Cr 2p soft x-ray magnetic circular dichroism. *Phys. Rev. B* **2004**, *70* (6), 064402 DOI: 10.1103/PhysRevB.70.064402.
- (103) Huang, Z.-L.; Bensch, W.; Mankovsky, S.; Polesya, S.; Ebert, H.; Kremer, R. K. Anion substitution effects on structure and magnetism of the chromium chalcogenide Cr₅Te₈—Part II: Cluster-glass and spin-glass behavior in trigonal Cr(1+x) Q₂ with basic cells and trigonal Cr(5+x) Q₈ with superstructures (Q=Te, Se; Te:Se=6:2). *J. Solid State Chem.* **2006**, *179* (7), 2067–2078 DOI: 10.1016/j.jssc.2006.04.001.
- (104) Youn, S. J.; Kwon, S. K.; Min, B. I. Correlation effect and magnetic moments in Cr₂Te₃. *J. Appl. Phys.* **2007**, *101* (9), 09G522 DOI: 10.1063/1.2713699.
- (105) Huang, Z.-L.; Kockelmann, W.; Telling, M.; Bensch, W. A neutron diffraction study of structural and magnetic properties of monoclinic Cr₅Te₈. *Solid State Sci.* **2008**, *10* (8), 1099–1105 DOI: 10.1016/j.solidstatesciences.2007.11.013.
- (106) Wontcheu, J.; Bensch, W.; Mankovsky, S.; Polesya, S.; Ebert, H.; Kremer, R. K.; Brücher, E. Anion substitution effects on the structure and magnetism of the chromium chalcogenide Cr₅Te₈—Part III: Structures and magnetism of the high-temperature modification Cr(1+x)Q₂ and the low-temperature modification Cr(5+x)Q₈ (Q=Te, Se;

- Te:Se=5:3). *J. Solid State Chem.* **2008**, *181* (6), 1492–1505 DOI: 10.1016/j.jssc.2008.03.021.
- (107) Polesya, S.; Mankovsky, S.; Benea, D.; Ebert, H.; Bensch, W. Finite-temperature magnetism of CrTe and CrSe. *J. Phys. Condens. Matter* **2010**, *22* (15), 156002 DOI: 10.1088/0953-8984/22/15/156002.
- (108) Ramasamy, K.; Mazumdar, D.; Bennett, R. D.; Gupta, A. Syntheses and magnetic properties of Cr₂Te₃ and CuCr₂Te₄ nanocrystals. *Chem. Commun.* **2012**, *48* (45), 5656 DOI: 10.1039/c2cc32021e.
- (109) Polesya, S.; Kuhn, G.; Benea, D.; Mankovsky, S.; Ebert, H. Electronic Structure and Magnetic Properties of Chromium Chalcogenides and Pnictides with NiAs Structure: Chromium Chalcogenides and Pnictides with NiAs Structure. *Z. Für Anorg. Allg. Chem.* **2013**, *639* (15), 2826–2835 DOI: 10.1002/zaac.201300314.
- (110) Bester, M.; Stefaniuk, I.; Kuzma, M. Quasi-Two-Dimensional Ferromagnetism in Cr₂Te₃ and Cr₅Te₈ Crystals. *Acta Phys. Pol. A* **2015**, *127* (2), 433–435 DOI: 10.12693/APhysPolA.127.433.
- (111) Kraschinski, S.; Herzog, S.; Bensch, W. Low temperature synthesis of chromium tellurides using superlattice reactants: crystallisation of layered CrTe₃ at 100°C and the decomposition into Cr₂Te₃. *Solid State Sci.* **2002**, *4* (10), 1237–1243 DOI: 10.1016/S1293-2558(02)00004-3.
- (112) Wontcheu, J.; Bensch, W.; Mankovsky, S.; Polesya, S.; Ebert, H. Effect of anion substitution onto structural and magnetic properties of chromium chalcogenides. *Prog. Solid State Chem.* **2009**, *37* (2–3), 226–242 DOI: 10.1016/j.progsolidstchem.2009.11.001.

- (113) Tripathi, T. S.; Tewari, G. C.; Rastogi, A. K.; Yadav, C. S.; Paulose, P. L. Magnetic properties of stuffed copper chromium tellurides $\text{Cu}_{1+x}\text{Cr}_{2+y}\text{Te}_4$ ($x=0-1$, $y < 0.3$). *J. Magn. Magn. Mater.* **2011**, 323 (17), 2300–2304 DOI: 10.1016/j.jmmm.2011.04.010.
- (114) Raveau, B.; Motin Seikh, M. Impact of Crystal Chemistry upon Spin Orientation Transitions in Magnetic Perovskites. *Z. Für Anorg. Allg. Chem.* **2014**, 640 (14), 2649–2657 DOI: 10.1002/zaac.201400348.
- (115) Harrison, N. M. An Introduction to Density Functional Theory. In *Computational Materials Science*; Catlow, Kotomin, Eds.; NATO Science Series III; IOS Press, 2003.
- (116) Levine, I. N. *Quantum Chemistry*, 7 edition.; Pearson: Boston, 2013.
- (117) Szabo, A.; Ostlund, N. S. *Modern Quantum Chemistry: Introduction to Advanced Electronic Structure Theory*; Dover: New York, 1996.
- (118) Parr, R. G.; Yang, W. *Density-Functional Theory of Atoms and Molecules*; International Series of Monographs on Chemistry; Oxford University Press: New York, 1989.
- (119) Eschrig, H. *The Fundamentals of Density Functional Theory*, Softcover reprint of the original 1st ed. 1996 edition.; Vieweg+Teubner Verlag: Stuttgart ; Leipzig, 1996.
- (120) Capelle, K. A bird's-eye view of density-functional theory. *ArXivcond-Mat0211443* **2002**.
- (121) Thomas, L. H. The calculation of atomic fields. *Math. Proc. Camb. Philos. Soc.* **1927**, 23 (5), 542–548 DOI: 10.1017/S0305004100011683.
- (122) Hohenberg, P.; Kohn, W. Inhomogeneous Electron Gas. *Phys. Rev.* **1964**, 136 (3B), B864–B871 DOI: 10.1103/PhysRev.136.B864.
- (123) Koch, W.; Holthausen, M. C. *A Chemist's Guide to Density Functional Theory*, 2nd Edition, 2 edition.; Wiley-VCH: Weinheim; New York, 2001.

- (124) Kohn, W.; Sham, L. J. Self-Consistent Equations Including Exchange and Correlation Effects. *Phys. Rev.* **1965**, *140* (4A), A1133–A1138 DOI: 10.1103/PhysRev.140.A1133.
- (125) Pielak, L. *Ideas of Quantum Chemistry, Second Edition*, 2 edition.; Elsevier: Amsterdam, 2013.
- (126) *Density Functional Theory and its Application to Materials: Antwerp, Belgium, 8-10 June 2000*, 1 edition.; Doren, V. V., Alsenoy, C. V., Geerlings, P., Eds.; American Inst. of Physics: Melville, N.Y, 2001.
- (127) Martin, R. M. *Electronic Structure: Basic Theory and Practical Methods*; Cambridge University Press: New York, 2004.
- (128) Vosko, S. H.; Wilk, L.; Nusair, M. Accurate spin-dependent electron liquid correlation energies for local spin density calculations: a critical analysis. *Can. J. Phys.* **1980**, *58* (8), 1200–1211 DOI: 10.1139/p80-159.
- (129) Perdew, J. P.; Zunger, A. Self-interaction correction to density-functional approximations for many-electron systems. *Phys. Rev. B* **1981**, *23* (10), 5048–5079 DOI: 10.1103/PhysRevB.23.5048.
- (130) Cole, L. A.; Perdew, J. P. Calculated electron affinities of the elements. *Phys. Rev. A* **1982**, *25* (3), 1265–1271 DOI: 10.1103/PhysRevA.25.1265.
- (131) Perdew, J. P.; Wang, Y. Accurate and simple analytic representation of the electron-gas correlation energy. *Phys. Rev. B* **1992**, *45* (23), 13244–13249 DOI: 10.1103/PhysRevB.45.13244.
- (132) Scuseria, G. E.; Staroverov, V. N. Progress in the development of exchange-correlation functionals. In *Theory and Applications of Computational Chemistry: The First Forty Years*; Elsevier Science, 2005; pp 669–724.

- (133) Mulliken, R. S. Electronic Population Analysis on LCAO–MO Molecular Wave Functions. I. *J. Chem. Phys.* **1955**, *23* (10), 1833–1840 DOI: 10.1063/1.1740588.
- (134) Mulliken, R. S. Electronic Population Analysis on LCAO-MO Molecular Wave Functions. III. Effects of Hybridization on Overlap and Gross AO Populations. *J. Chem. Phys.* **1955**, *23* (12), 2338–2342 DOI: 10.1063/1.1741876.
- (135) Mulliken, R. S. Electronic Population Analysis on LCAO–MO Molecular Wave Functions. II. Overlap Populations, Bond Orders, and Covalent Bond Energies. *J. Chem. Phys.* **1955**, *23* (10), 1841–1846 DOI: 10.1063/1.1740589.
- (136) Mulliken, R. S. Electronic Population Analysis on LCAO-MO Molecular Wave Functions. IV. Bonding and Antibonding in LCAO and Valence-Bond Theories. *J. Chem. Phys.* **1955**, *23* (12), 2343–2346 DOI: 10.1063/1.1741877.
- (137) Fonseca Guerra, C.; Handgraaf, J.-W.; Baerends, E. J.; Bickelhaupt, F. M. Voronoi deformation density (VDD) charges: Assessment of the Mulliken, Bader, Hirshfeld, Weinhold, and VDD methods for charge analysis. *J. Comput. Chem.* **2004**, *25* (2), 189–210 DOI: 10.1002/jcc.10351.
- (138) Hirshfeld, F. L. Bonded-atom fragments for describing molecular charge densities. *Theor. Chim. Acta* **1977**, *44* (2), 129–138 DOI: 10.1007/BF00549096.
- (139) Niessen, W. von. Density Localization of Atomic and Molecular Orbitals. I. *J. Chem. Phys.* **1972**, *56* (9), 4290–4297 DOI: 10.1063/1.1677859.
- (140) Wiberg, K. B.; Rablen, P. R. Comparison of atomic charges derived via different procedures. *J. Comput. Chem.* **1993**, *14* (12), 1504–1518 DOI: 10.1002/jcc.540141213.

- (141) De Proft, F.; Van Alsenoy, C.; Peeters, A.; Langenaeker, W.; Geerlings, P. Atomic charges, dipole moments, and Fukui functions using the Hirshfeld partitioning of the electron density. *J. Comput. Chem.* **2002**, *23* (12), 1198–1209 DOI: 10.1002/jcc.10067.
- (142) Saha, S.; Roy, R. K.; Ayers, P. W. Are the Hirshfeld and Mulliken population analysis schemes consistent with chemical intuition? *Int. J. Quantum Chem.* **2009**, *109* (9), 1790–1806 DOI: 10.1002/qua.21901.
- (143) Perdew, J. P.; Burke, K.; Ernzerhof, M. Generalized Gradient Approximation Made Simple. *Phys. Rev. Lett.* **1996**, *77* (18), 3865–3868 DOI: 10.1103/PhysRevLett.77.3865.
- (144) Baerends, E. J.; Ziegler, T.; Atkins, A. J.; Autschbach, J. ADF2016, SCM, Theoretical Chemistry, Vrije Universiteit, Amsterdam, The Netherlands, <http://www.scm.com>
<http://www.scm.com>.
- (145) Fonseca Guerra, C.; Snijders, J. G.; te Velde, G.; Baerends, E. J. Towards an order- N DFT method. *Theor. Chem. Acc. Theory Comput. Model. Theor. Chim. Acta* **1998**, *99* (6), 391–403 DOI: 10.1007/s002140050353.
- (146) te Velde, G.; Bickelhaupt, F. M.; Baerends, E. J.; Fonseca Guerra, C.; van Gisbergen, S. J. A.; Snijders, J. G.; Ziegler, T. Chemistry with ADF. *J. Comput. Chem.* **2001**, *22* (9), 931–967 DOI: 10.1002/jcc.1056.
- (147) Slater, J. C. Atomic Shielding Constants. *Phys. Rev.* **1930**, *36* (1), 57–64 DOI: 10.1103/PhysRev.36.57.
- (148) Belkić, D.; Taylor, H. S. A unified formula for the Fourier transform of Slater-type orbitals. *Phys. Scr.* **1989**, *39* (2), 226–229 DOI: 10.1088/0031-8949/39/2/004.

- (149) Cruz, S. A.; Cisneros, C.; Alvarez, I. Individual orbital contribution to the electronic stopping cross section in the low-velocity region. *Phys. Rev. A* **1978**, *17* (1), 132–140 DOI: 10.1103/PhysRevA.17.132.
- (150) Van Lenthe, E.; Baerends, E. J.; Snijders, J. G. Relativistic regular two-component Hamiltonians. *J. Chem. Phys.* **1993**, *99* (6), 4597 DOI: 10.1063/1.466059.
- (151) van Lenthe, E.; Baerends, E. J.; Snijders, J. G. Relativistic total energy using regular approximations. *J. Chem. Phys.* **1994**, *101* (11), 9783 DOI: 10.1063/1.467943.
- (152) van Lenthe, E.; Snijders, J. G.; Baerends, E. J. The zero-order regular approximation for relativistic effects: The effect of spin–orbit coupling in closed shell molecules. *J. Chem. Phys.* **1996**, *105* (15), 6505 DOI: 10.1063/1.472460.
- (153) van Lenthe, E.; van Leeuwen, R.; Baerends, E. J.; Snijders, J. G. Relativistic regular two-component Hamiltonians. *Int. J. Quantum Chem.* **1996**, *57* (3), 281–293 DOI: 10.1002/(SICI)1097-461X(1996)57:3<281::AID-QUA2>3.0.CO;2-U.
- (154) van Lenthe, E.; Ehlers, A.; Baerends, E.-J. Geometry optimizations in the zero order regular approximation for relativistic effects. *J. Chem. Phys.* **1999**, *110* (18), 8943 DOI: 10.1063/1.478813.
- (155) Van Lenthe, E.; Baerends, E. J. Optimized Slater-type basis sets for the elements 1-118. *J. Comput. Chem.* **2003**, *24* (9), 1142–1156 DOI: 10.1002/jcc.10255.
- (156) Hippel, A. von. Structure and Conductivity in the VIb Group of the Periodic System. *J. Chem. Phys.* **1948**, *16* (4), 372–380 DOI: 10.1063/1.1746893.
- (157) Akola, J.; Jones, R. O. Structure and dynamics in amorphous tellurium and Te_n clusters: A density functional study. *Phys. Rev. B* **2012**, *85* (13) DOI: 10.1103/PhysRevB.85.134103.

- (158) Becker, J.; Rademann, K.; Hensel, F. Electronic structure of selenium- and tellurium-clusters. *Z. Phys. At. Mol. Clust.* **1991**, *19* (1–4), 233–235 DOI: 10.1007/BF01448300.
- (159) Goddard, J. D.; Chen, X.; Orlova, G. Density Functional Study of Systems with Nondynamical Electron Correlation: The S₃, Se₃, and Te₃ Potential Energy Surfaces. *J. Phys. Chem. A* **1999**, *103* (20), 4078–4084 DOI: 10.1021/jp9847134.
- (160) Orlova, G.; Goddard, J. D. Density Functional Study of Tetra-Atomic Clusters and Complexes of the Group 16 Elements: Trends in Structure and Bonding. *J. Phys. Chem. A* **1999**, *103* (34), 6825–6834 DOI: 10.1021/jp990848d.
- (161) Pan, B. C. Geometric structures, electronic properties, and vibrational frequencies of small tellurium clusters. *Phys. Rev. B* **2002**, *65* (8), 085407 DOI: 10.1103/PhysRevB.65.085407.
- (162) Barlow, D. A.; Alvarez, P. K. Theoretical study of Te₅ rings. *Mol. Phys.* **2005**, *103* (5), 643–646 DOI: 10.1080/00268970412331327769.
- (163) Ghosh, P.; Bhattacharjee, J.; Waghmare, U. V. The Origin of Stability of Helical Structure of Tellurium. *J. Phys. Chem. C* **2008**, *112* (4), 983–989 DOI: 10.1021/jp077070d.
- (164) Igel-Mann, G.; Stoll, H.; Preuss, H. Structure and ionization potentials of clusters containing heavy elements. *Mol. Phys.* **1993**, *80* (2), 341–354 DOI: 10.1080/00268979300102301.
- (165) Chivers, T.; Laitinen, R. S. Tellurium: a maverick among the chalcogens. *Chem. Soc. Rev.* **2015**, *44* (7), 1725–1739 DOI: 10.1039/C4CS00434E.
- (166) Payne, F. W.; Jiang, W.; Bloomfield, L. A. Magnetism and Magnetic Isomers in Free Chromium Clusters. *Phys. Rev. Lett.* **2006**, *97* (19), 193401 DOI: 10.1103/PhysRevLett.97.193401.

- (167) Zamudio-Bayer, V.; Hirsch, K.; Langenberg, A.; Niemeyer, M.; Vogel, M.; Ławicki, A.; Terasaki, A.; Lau, J. T.; von Issendorff, B. Maximum Spin Polarization in Chromium Dimer Cations as Demonstrated by X-ray Magnetic Circular Dichroism Spectroscopy. *Angew. Chem. Int. Ed.* **2015**, *54* (15), 4498–4501 DOI: 10.1002/anie.201411018.
- (168) Yamada, Y.; Hongo, K.; Egashira, K.; Kita, Y.; Nagashima, U.; Tachikawa, M. Gold-standard coupled-cluster study of the ground-state chromium dimer cation. *Chem. Phys. Lett.* **2013**, *555*, 84–86 DOI: 10.1016/j.cplett.2012.11.017.
- (169) Ruiz-Díaz, P.; Ricardo-Chávez, J. L.; Dorantes-Dávila, J.; Pastor, G. M. Magnetism of small Cr clusters: Interplay between structure, magnetic order, and electron correlations. *Phys. Rev. B* **2010**, *81* (22), 224431 DOI: 10.1103/PhysRevB.81.224431.
- (170) Delley, B.; Freeman, A. J.; Ellis, D. E. Metal-Metal Bonding in Cr-Cr and Mo-Mo Dimers: Another Success of Local Spin-Density Theory. *Phys. Rev. Lett.* **1983**, *50* (7), 488–491 DOI: 10.1103/PhysRevLett.50.488.
- (171) Bauschlicher, C. W.; Partridge, H. Cr₂ revisited. *Chem. Phys. Lett.* **1994**, *231* (2), 277–282 DOI: 10.1016/0009-2614(94)01243-1.
- (172) Cheng, H.; Wang, L.-S. Dimer growth, structural transition, and antiferromagnetic ordering of small chromium clusters. *Phys. Rev. Lett.* **1996**, *77* (1), 51.
- (173) Reddy, B. V.; Khanna, S. N.; Jena, P. Structure and magnetic ordering in Cr₈ and Cr₁₃ clusters. *Phys. Rev. B* **1999**, *60* (23), 15597.
- (174) Wang, Q.; Sun, Q.; Rao, B. K.; Jena, P.; Kawazoe, Y. Nitrogen-induced magnetic transition in small chromium clusters. *J. Chem. Phys.* **2003**, *119* (14), 7124 DOI: 10.1063/1.1607958.

- (175) Hirsch, K.; Zamudio-Bayer, V.; Ameseder, F.; Langenberg, A.; Rittmann, J.; Vogel, M.; Möller, T.; v. Issendorff, B.; Lau, J. T. 2p x-ray absorption of free transition-metal cations across the 3d transition elements: Calcium through copper. *Phys. Rev. A* **2012**, *85* (6), 062501 DOI: 10.1103/PhysRevA.85.062501.
- (176) Huber, M. C. E.; Sandeman, R. J.; Tubbs, E. F. The Spectrum of Cr I between 179.8 and 200 nm Wavelengths, Absorption Cross Sections, and Oscillator Strengths. *Proc. R. Soc. Lond. Math. Phys. Eng. Sci.* **1975**, *342* (1630), 431–438 DOI: 10.1098/rspa.1975.0033.
- (177) Lau, J. T.; Hirsch, K.; Langenberg, A.; Probst, J.; Richter, R.; Rittmann, J.; Vogel, M.; Zamudio-Bayer, V.; Möller, T.; von Issendorff, B. Localized high spin states in transition-metal dimers: X-ray absorption spectroscopy study. *Phys. Rev. B* **2009**, *79* (24), 241102 DOI: 10.1103/PhysRevB.79.241102.
- (178) Michalopoulos, D. L.; Geusic, M. E.; Hansen, S. G.; Powers, D. E.; Smalley, R. E. The bond length of chromium dimer. *J. Phys. Chem.* **1982**, *86* (20), 3914–3916 DOI: 10.1021/j100217a005.
- (179) Anderson, A. B. Structures, binding energies, and charge distributions for two to six atom Ti, Cr, Fe, and Ni clusters and their relationship to nucleation and cluster catalysis. *J. Chem. Phys.* **1976**, *64* (10), 4046–4055 DOI: 10.1063/1.432013.
- (180) DiLella, D. P.; Limm, W.; Lipson, R. H.; Moskovits, M.; Taylor, K. V. Dichromium and trichromium. *J. Chem. Phys.* **1982**, *77* (11), 5263–5266 DOI: 10.1063/1.443794.
- (181) Andersson, K.; Roos, B. O.; Malmqvist, P.-Å.; Widmark, P.-O. The Cr₂ potential energy curve studied with multiconfigurational second-order perturbation theory. *Chem. Phys. Lett.* **1994**, *230* (4), 391–397 DOI: 10.1016/0009-2614(94)01183-4.

- (182) Andersson, K. The electronic spectrum of Cr₂. *Chem. Phys. Lett.* **1995**, 237 (3), 212–221
DOI: 10.1016/0009-2614(95)00328-2.
- (183) Weber, S. E.; Reddy, B. V.; Rao, B. K.; Jena, P. Chemically induced changes in the magnetic moments in transition metal monomers and dimers. *Chem. Phys. Lett.* **1998**, 295 (3), 175–180 DOI: 10.1016/S0009-2614(98)00947-6.
- (184) Desmarais, N.; Reuse, F. A.; Khanna, S. N. Magnetic coupling in neutral and charged Cr₂, Mn₂, and CrMn dimers. *J. Chem. Phys.* **2000**, 112 (13), 5576–5584 DOI: 10.1063/1.481183.
- (185) Casey, S. M.; Leopold, D. G. Negative ion photoelectron spectroscopy of chromium dimer. *J. Phys. Chem.* **1993**, 97 (4), 816–830 DOI: 10.1021/j100106a005.
- (186) Bondybey, V. E.; English, J. H. Electronic structure and vibrational frequency of Cr₂. *Chem. Phys. Lett.* **1983**, 94 (5), 443–447 DOI: 10.1016/0009-2614(83)85029-5.
- (187) Baykara, N. A.; McMaster, B. N.; Salahub, D. R. LCAO local-spin-density and X α calculations for Cr₂ and Mo₂. *Mol. Phys.* **1984**, 52 (4), 891–905 DOI: 10.1080/00268978400101641.
- (188) Simard, B.; Lebeault-Dorget, M.-A.; Marijnissen, A.; ter Meulen, J. J. Photoionization spectroscopy of dichromium and dimolybdenum: Ionization potentials and bond energies. *J. Chem. Phys.* **1998**, 108 (23), 9668–9674 DOI: 10.1063/1.476442.
- (189) Roos, B. O.; Borin, A. C.; Gagliardi, L. Reaching the Maximum Multiplicity of the Covalent Chemical Bond. *Angew. Chem. Int. Ed.* **2007**, 46 (9), 1469–1472 DOI: 10.1002/anie.200603600.
- (190) Pakiari, A. H.; Shariati, S. Geometry and electronic structure of ultrafine/nanoparticle chromium clusters (Cr_n, n=2–5) and their interaction with oxygen (triplet) and ethylene

- molecules: A DFT–NBO study. *Comput. Theor. Chem.* **2016**, *1084*, 169–178 DOI: 10.1016/j.comptc.2016.03.032.
- (191) Ge, G.; Jing, Q.; Luo, Y. A computational investigation of boron-doped chromium and chromium clusters by density functional theory. *Sci. China Phys. Mech. Astron.* **2010**, *53* (5), 812–817 DOI: 10.1007/s11433-010-0074-5.
- (192) López-Estrada, O.; López-Olay, S.; Aburto, A.; Orgaz, E. Unexpected High Spin Polarization in Cr₄ Cluster. *J. Phys. Chem. C* **2016**, *120* (41), 23892–23897 DOI: 10.1021/acs.jpcc.6b08575.
- (193) Würdemann, R.; Kristoffersen, H. H.; Moseler, M.; Walter, M. Density functional theory and chromium: Insights from the dimers. *J. Chem. Phys.* **2015**, *142* (12), 124316 DOI: 10.1063/1.4915265.
- (194) Kohl, C.; Bertsch, G. F. Noncollinear magnetic ordering in small chromium clusters. *Phys. Rev. B* **1999**, *60* (6), 4205.
- (195) Shah, E. V.; Kumar, V.; Roy, D. R. DFT investigation on structure, electronic and magnetic properties of Cr_n (n=2-8) clusters; American Inst. of Physics, 2016; Vol. 1728, p 020605.
- (196) Hilpert, K.; Ruthardt, R. Determination of the Dissociation Energy of the Cr₂ Molecule. *Berichte Bunsenges. Für Phys. Chem.* **1987**, *91* (7), 724–731 DOI: 10.1002/bbpc.19870910707.
- (197) Goodgame, M. M.; Goddard, W. A. The “sextuple” bond of chromium dimer. *J. Phys. Chem.* **1981**, *85* (3), 215–217 DOI: 10.1021/j150603a001.
- (198) Reed, A. E.; Weinstock, R. B.; Weinhold, F. Natural population analysis. *J. Chem. Phys.* **1985**, *83* (2), 735–746 DOI: 10.1063/1.449486.

- (199) Weinhold, F.; Landis, C. R. NATURAL BOND ORBITALS AND EXTENSIONS OF LOCALIZED BONDING CONCEPTS. *Chem. Educ. Res. Pract.* **2001**, 2 (2), 91–104 DOI: 10.1039/B1RP90011K.
- (200) Clark, A. E.; Sonnenberg, J. L.; Hay, P. J.; Martin, R. L. Density and wave function analysis of actinide complexes: What can fuzzy atom, atoms-in-molecules, Mulliken, Löwdin, and natural population analysis tell us? *J. Chem. Phys.* **2004**, 121 (6), 2563–2570 DOI: 10.1063/1.1766292.
- (201) Weinhold, F.; Landis, C. R. *Valency and Bonding: A Natural Bond Orbital Donor-Acceptor Perspective*, 1 edition.; Cambridge University Press: Cambridge, UK ; New York, 2005.
- (202) Glendening, E. D.; Landis, C. R.; Weinhold, F. Natural bond orbital methods. *Wiley Interdiscip. Rev. Comput. Mol. Sci.* **2012**, 2 (1), 1–42 DOI: 10.1002/wcms.51.
- (203) Weinhold, F. *Discovering Chemistry With Natural Bond Orbitals*, 1 edition.; Wiley: Hoboken, NJ, 2012.
- (204) Glendening, E. D.; Landis, C. R.; Weinhold, F. NBO 6.0: Natural bond orbital analysis program. *J. Comput. Chem.* **2013**, 34 (16), 1429–1437 DOI: 10.1002/jcc.23266.
- (205) Hobza, P.; Müller-Dethlefs, K. *Non-covalent Interactions: Theory and Experiment*; RSC Theoretical and Computational Chemistry Series; Royal Society of Chemistry, 2009.
- (206) Stone, A. *The Theory of Intermolecular Forces, 2nd Edition*, 2nd edition.; Oxford University Press: Oxford, 2013.
- (207) Jahn, H. A.; Teller, E. Stability of Polyatomic Molecules in Degenerate Electronic States. I. Orbital Degeneracy. *Proc. R. Soc. Math. Phys. Eng. Sci.* **1937**, 161 (905), 220–235 DOI: 10.1098/rspa.1937.0142.

- (208) Jahn, H. A. Stability of Polyatomic Molecules in Degenerate Electronic States. II. Spin Degeneracy. *Proc. R. Soc. Math. Phys. Eng. Sci.* **1938**, *164* (916), 117–131 DOI: 10.1098/rspa.1938.0008.
- (209) Griffith, J. S. *The Theory of Transition-Metal Ions*, 1 edition.; Cambridge University Press: Cambridge England, 1961.
- (210) Schläfer, H. L.; Gliemann, G. *Basic principles of ligand field theory*; Wiley-Interscience: London, New York, 1969.
- (211) *The Jahn-teller-effect: fundamentals and implications for physics and chemistry*; Köppel, H., Yarkony, D., Barentzen, H., Eds.; Springer series in chemical physics; Springer Verlag: Heidelberg ; New York , N.Y, 2009.
- (212) Bersuker, I. B. *Electronic structure and properties of transition metal compounds: introduction to the theory*, 2nd ed.; Wiley: Hoboken, N.J, 2010.
- (213) Khomskii, D. *Transition metal compounds*; Cambridge University Press: Cambridge, United Kingdom, 2014.
- (214) Neukermans, S.; Janssens, E.; Chen, Z. F.; Silverans, R. E.; Schleyer, P. v. R.; Lievens, P. Extremely Stable Metal-Encapsulated AlPb_{10}^{+} and AlPb_{12}^{+} Clusters: Mass-Spectrometric Discovery and Density Functional Theory Study. *Phys. Rev. Lett.* **2004**, *92* (16), 163401 DOI: 10.1103/PhysRevLett.92.163401.
- (215) Negishi, Y.; Iwai, T.; Ide, M. Continuous modulation of electronic structure of stable thiolate-protected Au₂₅ cluster by Ag doping. *Chem. Commun.* **2010**, *46* (26), 4713–4715 DOI: 10.1039/C0CC01021A.

- (216) Zhong, J.; Tang, X.; Tang, J.; Su, J.; Pei, Y. Density Functional Theory Studies on Structure, Ligand Exchange, and Optical Properties of Ligand-Protected Gold Nanoclusters: Thiolate versus Selenolate. *J. Phys. Chem. C* **2015**, *119* (17), 9205–9214 DOI: 10.1021/jp511615r.
- (217) Biltek, S. R.; Mandal, S.; Sen, A.; Reber, A. C.; Pedicini, A. F.; Khanna, S. N. Synthesis and Structural Characterization of an Atom-Precise Bimetallic Nanocluster, Ag₄Ni₂(DMSA)₄. *J. Am. Chem. Soc.* **2013**, *135* (1), 26–29 DOI: 10.1021/ja308884s.
- (218) Nakaya, M.; Iwasa, T.; Tsunoyama, H.; Eguchi, T.; Nakajima, A. Formation of a superatom monolayer using gas-phase-synthesized Ta@Si₁₆ nanocluster ions. *Nanoscale* **2014**, *6* (24), 14702–14707 DOI: 10.1039/C4NR04211E.
- (219) Sutradhar, P.; Chauhan, V.; Khanna, S. N.; Atulasimha, J. Magnetic behavior of superatomic-fullerene assemblies. *Phys. Chem. Chem. Phys.* **2017**, *19* (2), 996–1002 DOI: 10.1039/C6CP05196K.